THESIS

VARIATION IN CLINOPYROXENE TEXTURE, COMPOSITION, AND CRYSTALLIZATION DEPTH OF LATE CRETACEOUS TO EARLY EOCENE LAMPROPHYRIC ROCKS FROM ALKALINE CALC-ALKALINE MAGMATIC COMPLEXES OF MONTANA, USA.

Submitted by

Jacob McCane

Department of Geosciences

In partial fulfillment of the requirements

For the Degree of Master of Science

Colorado State University

Fort Collins, Colorado

Spring 2022

Master's Committee:

Advisor: John Ridley

Christopher Bareither
Kaleb Scarberry
Sally Sutton

ABSTRACT

VARIATION IN CLINOPYROXENE TEXTURE, COMPOSITION, AND CRYSTALLIZATION DEPTH OF LATE CRETACEOUS TO EARLY EOCENE LAMPROPHYRIC ROCKS FROM ALKALINE CALC-ALKALINE MAGMATIC COMPLEXES OF MONTANA, USA.

Lamprophyres are spatially and temporally associated with many types of hydrothermal ore deposits and have been argued to be a marker in mineral exploration. A reconnaissance study of lamprophyric rocks in central Montana, namely the Central Montana Alkalic Province (CMAP) is presented that details the variations of petrographic textures and clinopyroxene (Cpx) mineral chemistry from different Late Cretaceous to Early Tertiary aged alkalic to calc-alkaline magmatic complexes. Using current International Union of Geological Sciences (IUGS) standards, lamprophyric rocks studied from the Late Cretaceous Bull Mountain/Golden Sunlight mining operations are found to be predominately minette > vogesite > kersantite varieties of lamprophyres. The Highwood Mountains lamprophyric rocks of Eocene age are classified as vogesites > sannaites > minnettes ≈ spessartites. Crazy Mountain (Crazies) lamprophyric rocks of Eocene age are monchiquites > vogesites > kersantites > spessartites. The sapphire-bearing Yogo dyke lamprophyre of Eocene age is classified as an ouachitite. Lamprophyric rocks occur as dykes and display porphyritic and panidiomorphic textures with dominant macrocrysts of Cpx, biotite, with lesser olivine and hornblende that range in size from a few centimeters in length to microcrystalline (<10 μm) matrix constituents. Leucocratic circular ocelli structures as well as bent and strained crystals of biotite are present within all lamprophyric rocks from the CMAP.

Extreme heterogeneity exists within lamprophyres ranging from macroscale dyke swarm features to microscale Cpx macrocrysts assemblages captured in a single thin section. Cpx from every region of the CMAP display intricate optical zonations associated with complex compositional variations

across core to rim analytical traverses and display disequilibrium features like spongy textured melt pockets. Within the CMAP the Cpx classify as diopside, Fe-rich diopside, Ca-rich diopside or augite and do not contain uniform textures or zonations. Cpx of the Crazies are strictly diopsides and the only region with augite is Bull Mountain/Golden Sunlight. Cpx macrocrysts from each region of this study are separated into Types based off of differing textural features from back scatter electron imaging and under the petrographic microscope. All Types across the CMAP are predominately normally zoned and are interpreted as antecrysts or xenocrysts that host compositions and textures that record disequilibrium with the host magma during crystallization. B Types of Bull Mountain/Golden Sunlight are enriched in Cr_2O_3 and FeO. H Types from the Highwoods are similar to B Types but record Step-zoning characteristics and contain the greatest proportion of both normal and reverse zoning characteristics. C Types of the Crazies record lower values of TiO_2, Al_2O_3, CaO, and Fe^{2+} /Fe^{3+} ratios but have higher Na_2O levels than all other Types of the CMAP. Y Types of the Yogo Dyke host the most ultramafic signatures with elevated Mg#, TiO_2, Al_2O_3, Cr_2O_3, and CaO levels along with the lowest SiO_2 and FeO composition of all Types of the CMAP. Barometric estimates of the pressure of crystallization for Cpx are presented from the CMAP, mean crystallization estimates are as follows: Bull Mountain/Golden Sunlight = 15.1 ± 1.5 kbar (56 km), Highwood Mountains = 11.4 ± 1.5 kbar (42 km), Crazy Mountains = 7.1 ± 1.5 kbar (26 km), Yogo Dyke = 14.3 ± 1.5 kbar (53 km). Cpx macrocrysts crystalized near the lower crust-mantle boundary and barometry from Bull Mountain/Golden Sunlight likely records a deeper magma reservoir and plumbing system than previously thought for the Boulder Batholith. Lamprophyric rock petrogenesis cannot be explained by simple fractionation processes because the antecrysts do not follow regular fractionation trendlines. Multiple complex open system magmatic processes are likely at play when controlling lamprophyric magma composition. Drastically different compositional variations of C Types compared to others of the CMAP confirm that the parent magma of lamprophyric rocks originating from the Crazies is significantly different than other areas of this study. Primary melts from the Crazies and

the Highwoods likely had an enriched composition and heavy metasomatic influence. Evidence for multiple recharge and mixing events exists within all lamprophyric rocks of the CMAP. Hybridization of mafic and felsic magmas likely influenced the petrogenesis of lamprophyric rocks from Bull Mountain/Golden Sunlight, the Highwood Mountains, the Crazy Mountains, and the Yogo Dyke.

ACKNOWLEDGMENTS

This project was partially funded by the Tobacco Root Geological Society and the Wyoming Association of Geologists.

I would like to thank Phil Dalhoff for keeping me sane during our travels of Montana. I'm sorry you are still probably unearthing clumps of white fur from your truck. You were an excellent companion with a natural taste for finding well-hidden lamprophyre outcrops and delicious craft beers (the most important part). I would also like to thank Kaleb Scarberry, Fess Foster, Frank Dudas, Sandy Underwood, Susan Vuke, Dick Berg, and John Childs for their input and guidance. I would also like to thank Maui the Akbash for fending off any wildlife from our campsites during this study. Another thanks to John Ridley for his support during this project. Shout out to Aaron Bell, head of the Electron Microprobe facilities at CU Boulder for his help during stressful microprobe sessions. And finally, a special thanks to family, friends, and Erinn Johnson for tolerating nega-Jake.

DEDICATION

This work is dedicated to those who lost their way while struggling with mental health illnesses. No thesis, piece of paper, diploma, or personal failure is worth the value of your life.

TABLE OF CONTENTS

ABSTRACT ii
ACKNOWLEDGMENTS v
DEDICATION vi
TABLE OF CONTENTS vii
LIST OF TABLES ix
LIST OF FIGURES x
(1) Introduction 1
(1A) Lamprophyre Background 1
(1A.i) Lamprophyres and Ore Deposits 6
(1B) Petrogenetic Models of Lamprophyres 7
(1Bi) Mantle Metasomatism Model 8
(1Bii) Prostka Model 8
(1Biii) Cogne Model 9
(1C) Thesis Goals 10
2. Regional Geology 11
(2A) Tectonic Setting 11
(2B) Late Cretaceous to Eocene Volcanism and Magmatism in Montana 12
(2C) Bull Mountain Range 18
(2D) Highwood Mountain Range 20
(2E) Crazy Mountain Range 21
(2F) The Yogo Dyke Lamprophyre 22
3. Methods 24
(3A) Field Work 24
(3B) Petrography 25
(3C) Electron Microprobe 26
4. Data and Results 29
(4A) Field Observations 29
(4B) Petrography 35
(4B. i) Pyroxenes 36
(4B. ii) Melt Pockets 45
(4B. iii) Phlogopite/Biotite 49
(4B. iv) Olivine 55
(4B. v) Ocelli 57
(4B. vi) Xenoliths/ Mafic Enclaves 58
(4B vii). Accessory Minerals 60
(4C) Central-Montana Alkalic Province Lamprophyre Geochemical Signatures 60
(4C. i) Total Akali-Silica Diagram 61
(4C. ii) MORB Normalized Spider Diagram 62
(4C. iii) Harker Variation Diagrams 64
(4D) Pyroxene Mineral Chemistry 67
(4D. i) Bull Mountain Lamprophyre Mineral Chemistry 74
(4D. ii) Highwood Mountains Lamprophyre Mineral Chemistry 91
(4D. iii) Crazy Mountain Lamprophyre Mineral Chemistry 108
(4D. iv) Yogo Dyke Lamprophyre Mineral Chemistry 115

(4D. v) DS Plots 124
(4D. vi) CMAP Pyroxene Geothermobarometry 127
(5) Discussions 146
(5A) Petrology of the CMAP 146
(5B) Petrography of the CMAP 148
(5C) Clinopyroxene Mineral Chemistry of the CMAP 154
(5D) Clinopyroxene Geobarometry of the CMAP 180
(5E) Petrogenesis 184
(5F) Conclusions & Future Implications 193
References 201
Appendices 211
A. Modal Mineralogy of Thin Sections from Study 211
B. Select Hand Sample Descriptions 213
C. Select Thin Section Descriptions 219
D. Select Hand Sample Photographs 231
E. GPS Coordinates 240

LIST OF TABLES

Table 1 The present IUGS classification of lamprophyres (Le Bas and Streckeisen, 1991). 2
Table 2: Terminology when describing Greyscale BSE imagery 28
Table 3. Representative Pyroxene Mineral Chemistry 69
Table 4: Matrix Clinopyroxene Analysis.....71
Table 5: Summary of Petrography from Lamprophyric Rocks of the CMAP.....149
Table 6: Macrocryst Type BSE and Petrographic Textural Features 153
Table 7: Summary of Type Composition, Geothermobarometry Statistical Analysis, and Analytical Zoning Characteristics (determined by electron microprobe analysis). 157
Table 8: Summary of Lamprophyric and Clinopyroxene Variations for Bull Mountain/Golden Sunlight and the Highwood Mountains. 197
Table 9: Summary of Lamprophyric and Clinopyroxene Variations for the Crazy Mountains and the Yogo Dyke Lamprophyre.....198

LIST OF FIGURES

Figure 1: Hierarchical Structure of the Lamprophyre Clan 3
Figure 2: Lamprophyre Petrogenetic Models 7
Figure 3: Map Displaying Structural Features in Southwestern Montana 12
Figure 4: Geologic Map of the Boulder Batholith in Southwestern Montana 17
Figure 5: Volcanic and Plutonic Centers of the CMAP 24
Figure 6: EMP at CU Boulder 28
Figure 7: Lamprophyric Trend/Orientation Rose Diagrams 31
Figure 8: Lamprophyric Outcrop Field Habits from the Highwood Mtns. 32
Figure 9: Lamprophyric Outcrop Field Habits from Bull Mtn./Golden Sunlight 33
Figure 10: Lamprophyric Outcrop Field Habits from the Crazy Mtn. 34
Figure 11: BSE Example of Complexly Zoned Clinopyroxene 38
Figure 12: Photomicrographs of Clinopyroxenes from Bull Mountain/Golden Sunlight 40
Figure 13: Photomicrographs of Clinopyroxenes from the Highwood Mountains 42
Figure 14: Photomicrographs of Clinopyroxenes from the Crazy Mountains 44
Figure 15: BSEs of Spongy Texture Melt Pockets Within Clinopyroxene Crystals 47
Figure 16: Photomicrographs of Melt Pocket Behaviors Within Clinopyroxenes. 48
Figure 17: Yogo Dyke Phlogopite BSE with Ba Signature 51
Figure 18: Photomicrographs of Biotite from Bull Mtn., Yogo Dyke, and the Crazy Mtn. 52
Figure 19: Photomicrographs of Biotite from the Highwood Mtns. 53
Figure 20: Photomicrographs of Biotite from the Crazy Mountains 54
Figure 21: Photomicrographs of Olivine from Lamprophyric Rocks of the CMAP 56
Figure 22: Ocelli Within Lamprophyric Rocks of the CMAP 57
Figure 23: Xenolithic Fragments Within Lamprophyric Rocks of the CMAP 59
Figure 24: Total-Alkalis-Silica Diagram of Lamprophyres from the CMAP 62
Figure 25: Lamprophyre MORB Normalized Spider Diagram from the CMAP 64
Figure 26: Compositional Harker Variation Diagrams of Lamprophyres of the CMAP 65
Figure 27: Pyroxene Ternary Diagram and Quadrilateral 67
Figure 28: Pyroxene CAL, AL, UML, and LL Discrimination Diagram 72
Figure 29: Pyroxene Al2O3 vs TiO2 (wt. %) Discrimination Plot. 73
Figure 30: BSE and Ternary Diagram for the analytical traverse of crystal 1A, Slide J06, Bull Mtn. 80
Figure 31: BSE and Ternary Diagram for the analytical traverse of crystal 2A, Slide J06, Bull Mtn. 81
Figure 32: BSE and Ternary Diagram for the analytical traverse of crystal 3A, Slide J06, Bull Mtn. 82
Figure 33: BSE and Ternary Diagram for the analytical traverse of crystal 5A, Slide J06, Bull Mtn. 83
Figure 34: BSE and Ternary Diagram for the analytical traverse of crystal 8A, Slide J06, Bull Mtn. 84
Figure 35: BSE and Ternary Diagram for the analytical traverse of crystal 1A, Slide J12, Bull Mtn. 85
Figure 36: BSE and Ternary Diagram for the analytical traverse of crystal 3A, Slide J12, Bull Mtn. 86
Figure 37: BSE and Ternary Diagram for the analytical traverse of truncated crystals 4A, Slide J12, Bull Mtn... 87
Figure 38: Compilation of pyroxene ternary diagrams from Bull Mountain. 88
Figure 39: Lamprophyre J06 of Bull Mtn. Mineral Chemistry Analytical Traverses 89
Figure 40: Lamprophyre J12 of Bull Mtn. Mineral Chemistry Analytical Traverses 90
Figure 41: BSE and Ternary Diagram for the analytical traverse of crystal 1A, Slide J18, Highwood Mtns. 97
Figure 42: BSE and Ternary Diagram for the analytical traverse of crystal 2A, Slide J18, Highwood Mtns. 98
Figure 43: BSE and Ternary Diagram for the analytical traverse of crystal 4A, Slide J18, Highwood Mtns. 99
Figure 44: BSE and Ternary Diagram for the analytical traverse of crystal 6A, Slide J18, Highwood Mtns. 100
Figure 45: Compilation of pyroxene ternary diagrams from lamprophyre J18 of the Highwood Mtns. 101
Figure 46: BSE and Ternary Diagram for the analytical traverse of crystal 1A, Slide J24, Highwood Mtns. 102
Figure 47: BSE and Ternary Diagram for the analytical traverse of crystal 4A, Slide J24, Highwood Mtns. 103
Figure 48: BSE and Ternary Diagram for the analytical traverse of crystal 6A, Slide J24, Highwood Mtns. 104
Figure 49: Compilation of pyroxene ternary diagrams from lamprophyre J24 of the Highwood Mtns. 105

Figure 50: Lamprophyre J18 of the Highwood Mtns. Mineral Chemistry Analytical Traverses. 106
Figure 51: Lamprophyre J24 of the Highwood Mtns. Mineral Chemistry Analytical Traverses. 107
Figure 52: BSE and Ternary Diagram for the analytical traverse of crystal 2A, Slide J32_3, Crazy Mtns. 110
Figure 53: BSE and Ternary Diagram for the analytical traverse of crystal 4A, Slide J32_3, Crazy Mtns. 111
Figure 54: BSE and Ternary Diagram for the analytical traverse of crystal 3A, Slide J36, Crazy Mtns. 112
Figure 55: Compilation of pyroxene ternary diagrams from lamprophyres J32_3 and J36 of the Crazy Mtns. 113
Figure 56: Lamprophyre J32_3 and J36 of the Crazy Mtns. Mineral Chemistry Analytical Traverses 114
Figure 57: BSE and Ternary Diagram for the analytical traverse of crystal 1A, Slide Yogo 118
Figure 58: BSE and Ternary Diagram for the analytical traverse of crystal 4A, Slide Yogo 119
Figure 59: BSE and Ternary Diagram for the analytical traverse of crystal 5A, Slide Yogo 120
Figure 60: BSE and Ternary Diagram for the analytical traverse of crystal 6A, Slide Yogo 121
Figure 61: Compilation of pyroxene ternary diagrams from lamprophyre Yogo Dyke. 122
Figure 62: Lamprophyre YOGO of the Yogo Dyke. Mineral Chemistry Analytical Traverses. 123
Figure 63: DS Variations of Al2O3, TiO2, CaO, and Mg# for samples analyzed from the CMAP 126
Figure 64: Box and Whisker Plots Depth of Crystallization 129
Figure 65: Clinopyroxene Barometry and Thermometry of Clinopyroxenes from the CMAP 131
Figure 66: Clinopyroxene Barometry from Bull Mountain/Golden Sunlight lamprophyres J06 and J12. 134
Figure 67: Clinopyroxene Barometry from Highwood Mountain lamprophyres J18 and J24 139
Figure 68: Clinopyroxene Barometry from Crazy Mountain lamprophyres J32_3 and J36 142
Figure 69: Clinopyroxene Barometry from the Yogo Dyke lamprophyre 145
Figure 70: Pyroxene Ternary Diagram of the CMAP 155
Figure 71: Clinopyroxene Elemental Bivariate Diagrams vs Mg# by Macrocryst Type 158
Figure 72: Box and Whisker Plots (Mg#, FeO, Al2O3, TiO2, Cr2O3) 167
Figure 73: Pyroxene FeO vs SiO2 (wt.%) Variation Diagram 170
Figure 74: Clinopyroxene Normalized Fe2+ vs Fe3+ by Region of the CMAP 171
Figure 75: Clinopyroxene Fe2+/(Fe3++Fe2+) Variation of the CMAP 172
Figure 76: Clinopyroxene Na2O vs Distance analytical traverses from the CMAP 173
Figure 77: Clinopyroxene Fe2+/(Fe3++Fe2+) analytical traverses from the CMAP 174
Figure 78: CMAP Clinopyroxene Macrocryst Type Depth of Crystallization 183
Figure 79: Conceptual Schematic of Magmatic Processes of the CMAP 192

(1) Introduction

(1A) Lamprophyre Background

Understanding of the petrogenesis of lamprophyric rocks is poor compared to most igneous rocks and their relationships with other rock and magma types remains an enigma (Prelevic et al., 2004). Lamprophyres are treated if at all, as an afterthought in most geologic texts and some petrological descriptions of alkaline provinces tone down any importance of lamprophyric components (Mitchell, 1994). In some cases, lamprophyric rocks were viewed as obscure and subsequently misunderstood, disregarded completely, or simply labeled as basalt or hornblende diorites to avoid further confrontation with these bizarre rocks (Spry et al., 1997; Rock, 1991). To many geologists long ago, it seems the old moniker, 'Ignorance is bliss', applies to the study of lamprophyres throughout history. Despite this, lamprophyres should be treated as an exploration tool because their association with gold deposits has been the topic of many studies (Rock, et al. 1987, 1988, 1989; Rock and Groves, 1988; Wyman and Kerrich 1988, 1988 b, 1989).

The term "lamprophyre" was first devised by Gümbel in 1874 and predates other terms in geology, such as ophiolite or komatiite, by a full century (Rock,1991). The name itself is derived from the Greek words "***lampros porphyros***", meaning 'glistening porphyry' or 'purple rock', and was originally used because of the large, glistening biotite phenocrysts that occur in the rocks of Fichtelgebirge, Germany (Rock, 1987). Thus, when observed in the field, lamprophyres can often be identified by their porphyritic and panidiomorphic nature (having coarse and euhedral constituents), unlike many fine grained widespread alkalic rocks. In the years following the lamprophyre's introduction, its meaning was broadened to encompass a wider variety of hypabyssal rocks containing ferromagnesian phenocryst phases (Mitchell, 1994). In the early rush of classification and nomenclature, it was recognized that lamprophyres portray abnormalities compared to most alkalic or calc-alkaline rocks, and thus type

locality terms for lamprophyric rocks sprang up overnight. The influx of type locality terms, such as Jerseyite, Tjosite, Garganite, or Odinite (I really wish this one stuck around), just to name a few, led to a legion of obscure rock types named after equally obscure European villages and settlements (Rock, 1991). This outdated and imprecise nomenclature system has been a burden to petrologists because rocks of diverse origins were all lumped under one petrographic banner, known as, the lamprophyre clan (Rock, 1987; Mitchell, 1994).

During this study, the definition proposed by Streckeisen (1979) and the IUGS (Le Maitre et al. 1989; Le Bas and Streckeisen, 1991) is used when naming and classifying the lamprophyric rocks of this study (see Table 1 below). The IUGS recommended using the general heading "lamprophyric rocks" for calc-alkaline, alkaline, ultramafic, lamproite, and kimberlite rocks because the standard QAPF classification scheme does not work well for lamprophyres due to their mineralogy. In 1991, the IUGS commissioned a working group to try and resolve several differing opinions that exist on lamprophyres, particularly opinions expressed by Rock (1991) (Le Bas and Streckeisen, 1991). Lamprophyric rocks are generally dyke rocks that are not simply textural varieties of common plutonic or volcanic rocks. They are mesocratic to melanocratic rocks of porphyritic texture which contain essential biotite, and/or amphibole, clinopyroxene, and olivine.

Table 1 The present IUGS classification of lamprophyres (Le Bas and Streckeisen, 1991).

Light-coloured constituents		Predominant mafic minerals			
Feldspar	Foid	Biotite, diopsidic augite, (±olivine)	Hornblende, diopsidic augite, (±olivine)	Amphibole, (barkevikite, kaersutite), Ti-augite, olivine, biotite	Melilite, biotite, ±Ti-augite, ±olivine, ±calcite
or > pl	—	Minette	Vogesite	—	—
pl > or	—	Kersantite	Spessaritite	—	—
or > pl	Feld > foid	—	—	Sannaite	—
pl > or	Feld > foid	—	—	Camptonite	—
—	Glass or foid	—	—	Monchiquite	Polzenite
—	—	—	—	—	Alnöite

Or, alkali feldspar; pl, plagioclase; feld, feldspar; foid, feldspathoid. (After Le Maitre *et al.* 1989).

In an attempt to give lamprophyres their rightful place in geologic literature, Rock (1977, 1981, 1984, 1987, and 1991) expanded upon Streckeisen (1979) and coined the lamprophyre clan while attempting to discern different chemical and textural observations between each variation of lamprophyre. The classification devised by Rock was divided into five main lamprophyric 'families' that made up the whole of the lamprophyric clan. Those being the calc-alkaline (often called shoshonitic) lamprophyres (CAL), the alkaline lamprophyres (AL), the ultramafic lamprophyres (UML), the kimberlites (KIL), and finally the lamproites (LL) (Figure 1).

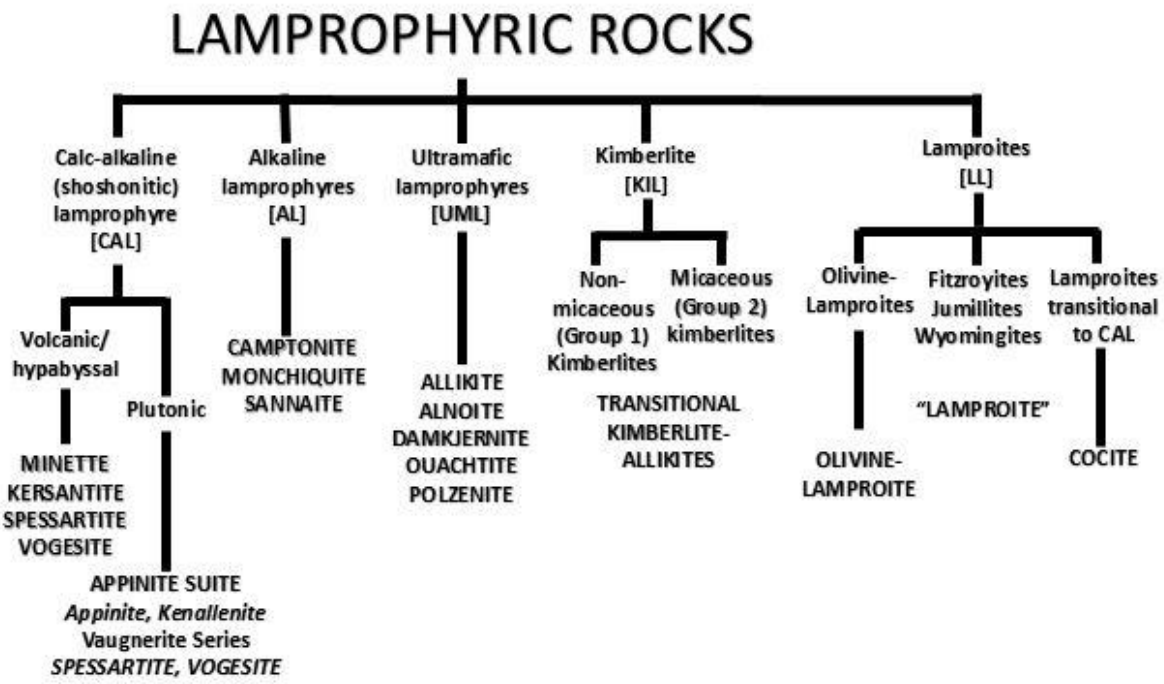

Figure 1: Hierarchical structure of Rocks' rendition of the lamprophyre clan (expanded from Streckeisen 1979).

Lamprophyric rocks have many distinctive geochemical and geological characteristics, these include: (1) their common occurrence as dykes, sheets, sills, pipes, and diatremes; (2) having primitive compositions, as represented by high Mg# (where Mg# = $Mg/(Mg+Fe^{2+}$); (3) rich in Cr, V, and Ni contents; (4) high in large ion lithophile elements (LILE) , such as K, Rb, Sr, and Ba; (5) elevated levels of

light rare-earth elements (LREE) and volatiles such as CO_2 , H_2O, F, and Cl (Currie and Ferguson, 1970; Rock et al., 1988; Müller and Groves, 2016;).

Other common characteristics of lamprophyres include: (1) the presence of xenoliths in dykes, (2) the panidiomorphic (often completely euhedral phenocrysts) nature of crystals, (3) the abundance of apatite phenocrysts, (4) the presence of leucocratic globular structures termed “ocelli”, which are most commonly found in syenite or carbonatite rocks, (5) the abundance of biotite, hornblende, or other volatile bearing phases such as carbonates, sulfates, or zeolites, (6) fractured or bent biotite phenocrysts, and (7) complexly and unusually zoned phenocrysts.

The late Dr. Nick Rock was a strong proponent of continuing research on lamprophyres and brought about a discussion of their importance to the greater geologic community. His efforts were commendable and any petrologist or geologist who studies lamprophyres, will undoubtedly be indebted to him for his contribution because Rock rekindled interest in lamprophyres by linking them with numerous economic deposits. Rock’s concept of the lamprophyre clan has since been questioned by some (Mitchell and Bergman, 1991; Mitchell, 1994a) who claim that members of the ‘lamprophyre clan’ are not ultimately genetically unrelated; the lamprophyre clan merely serves to link rocks that have crystallized under volatile-rich conditions.

The discrepancies and inadequacies of Rock’s lamprophyre clan are best shown by some definitions of members within his clan diagram (Figs. 1 and 2) Rock defined a minette as, a calc-alkaline volcanic variety of lamprophyre on his adapted diagram, as “consisting of phenocrysts of phlogopite-biotite, with or without subordinate calcic or alkali amphibole, forsteritic olivine or diopsidic clinopyroxene set in a groundmass of the same plus alkali feldspar and subordinate plagioclase” (Rock, 1991). Mitchell (1994) argues that this definition is so broad that multitudes of rocks could be defined as minettes when in actuality, they may have similar mineralogical features, it is doubtful that a “diverse” grouping of minettes could be genetically related to one another.

A revised definition for 'lamprophyre' was proposed by Mitchell (1994). Mitchell stated that, "Lamprophyres are rocks which are characterized by the presence of euhedral to subhedral phenocrysts of mica and/or amphibole together with clinopyroxene and/or melilite set in a groundmass which may consist (either singly or in various combinations) of plagioclase, alkali feldspar, feldspathoids, carbonate, monticellite, melilite, mica, amphibole, pyroxene perovskite, Fe-Ti oxides and glass". Note that olivine has evaded this definition. This is because although olivine is widely present in a majority of lamprophyres, its presence does not indicate unusual crystallization conditions (Mitchell, 1994; Hatch et al., 1972).

It is apparent that lamprophyres can occur in many different forms (extrusive and intrusive varieties), thus it becomes increasingly more difficult to classify lamprophyres into a petrogenetic clan. While intrusive lamprophyres are more common and widespread, extrusive lamprophyres have also been documented. Eocene minette lavas of the Colima Graben, Mexico, and the presence of ultrapotassic lavas of the Paleoproterozoic Baker Lake Group, Northwest Territories, are two such examples (Luhr and Carmichael, 1980 & 1981; Peterson, 1992). Mitchell (1994) argues that a lamprophyric facies would be more appropriate.

The adjective "lamprophyric" should be used to describe (facies of) rocks derived from an individual parent magma which may have crystallized under different conditions than other similar or neighboring rocks (Mitchell, 1994). The term lamprophyric then designates observable field characteristics, such as a porphyritic or panidiomorphic textures, that can easily be differentiated from other rocks they might be associated with in the field. It should be stressed that the petrogenesis of lamprophyric rock facies is commonly not known, but merely, the term aids to draw attention to rocks that must have formed by different and/or specific magmatic processes than other members of their co-magmatic suite (Mitchell, 1994).

(1A.i) Lamprophyres and Ore Deposits

From an economic and exploration front, lamprophyres are known to be closely associated with numerous gold and base metal deposits (Rock, 1991; Rock and Groves, 1988; Wyman and Kerrich, 1988). In this study, lamprophyre samples were collected and analyzed from four different sites. One site from the Golden Sunlight Mining district of Whitehall, Montana is a major hydrothermal ore deposit. Total estimated pre-mining resource of the Golden Sunlight gold-silver-telluride deposit contains 3.8 million ounces of gold grading at 0.054 ounces per ton, with total estimated reserves of 70.8 million tons (Spry et al., 1997). These lamprophyres crosscut the deposit and postdate the age of mineralization, closely bracketing mineralization by ˜2 Ma (De Witt et al., 1996; Oyer et al., 2014) The timing of lamprophyric emplacement and mineralization is peculiar but their importance within the mining operations is but a mere afterthought. Another site from this study is the famous sapphire-bearing Yogo Dyke lamprophyre which is also associated with hydrothermal activity.

The most common types of economic deposits hosting lamprophyres are known to be epithermal Au, porphyry Cu-Au, or kimberlitic diamond deposits (Rock, 1991). Some evidence suggests that lamprophyre related deposits may be enriched in platinum group elements (PGEs) as well as Au (Müller et al. 1992). Rock and Groves (1988) reported the average Au abundance of lamprophyres compared to common igneous rocks is at least an order of magnitude higher. Studies from Rock and others (1988) speculated a closer genetic relationship between Au mineralization and lamprophyres than previously thought. They proposed that many syenitic and granitic plutons could be the product of various types of interactions between mantle derived lamprophyric melts and crustal rocks. Rock and others (1988) summarized this relationship as, "… lamprophyres can satisfactorily account for the often-observed indirect relationship between gold and felsic intrusions, if the lamprophyres acted as both the ultimate source of the Au and the parent magma to the intrusions". In contrast, Kerrich and Wyman (1994) reported that lamprophyres of the Superior Province of Canada are not intrinsically enriched in

Au or Au-affiliated elements typically found within mesothermal Au deposits, and thus lamprophyres are not the preferred source rock of Au, nonetheless, they concluded that lamprophyres are genetically related in space and time to mesothermal Au deposits within the Superior Province. Understanding how lamprophyres originate and interact with other rock types could potentially aid in understanding the genesis of Au deposits or potentially locating new economic deposits (Rock et al., 1989).

(1B) Petrogenetic Models of Lamprophyres

There are three competing models for the petrogenesis of lamprophyres. These are termed here the mantle metasomatism, Prostka, and Cogne models. Note that these are not the formal names of these petrogenetic models as they merely denote the author who most contributed to their origins (Mantle Metasomatism left as is due to multiple authors). The figure below depicts all three models simultaneously.

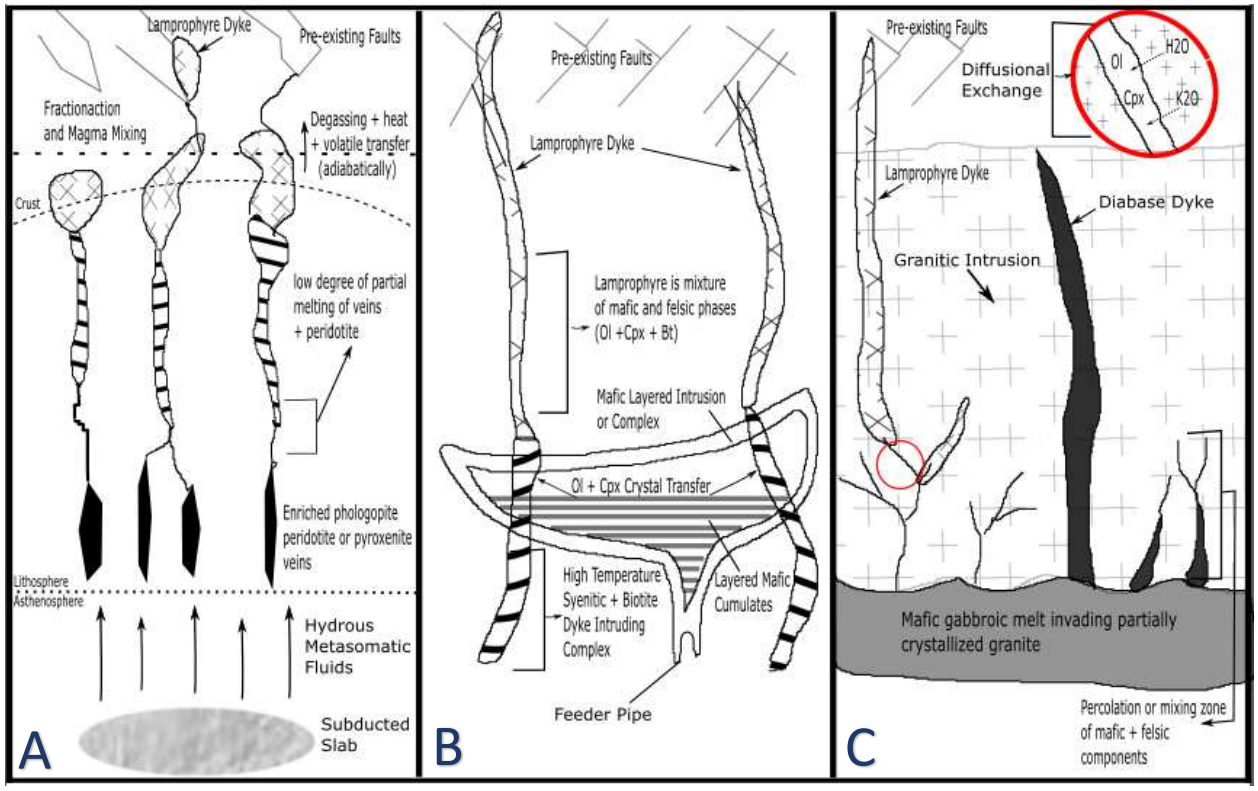

Figure 2: (A) - Mantle Metasomatism Model. (B) - Prostka Model. (C) - Cogne Model. Cross sectional view.

(1Bi) Mantle Metasomatism Model

The petrogenetic model that is the most widely accepted is currently the mantle metasomatic model after the work of Rock (1984), Perring and others (1989), Foley and Peccerillo (1992), and Peccerillo (1992). The model proposes that lamprophyres are products of low degrees of partial melting (<1%) of volatile rich metasomatized primitive mantle as deep as 100-150 km depth (Fig. 2A). Characteristic mineral phases of lamprophyres and common metasomatic minerals in the mantle and within lamprophyric rocks include amphiboles, apatites, and micas (Ma et al., 2015). The components needed to make these lamprophyre minerals could originate well below the lithosphere-asthenosphere boundary where mantle wedges or melting lithospheric slabs release hydrous metasomatic fluids at depth. Metasomatic fluids could interact with mantle rocks to produce enriched (in incompatible elements) phlogopite bearing peridotite or pyroxenite veining or veinlets. Low degrees of partial melting of the resultant peridotite or veins coupled with fractionation, addition of heat, degassing, and adiabatic rise after volatiles are transferred into the lamprophyric melt, could drive the bizarre melt towards the crust from the depths of the lithosphere and mantle. Lamprophyric melt would preferentially search for passageways to the surface in the form of faults or other conduits. This model is the only one of the three to incorporate recycled fluids and material from subducted matter, plus, there is no way to tell how much time the original wedge metasomatic fluids were coupled with melts and mixed with one another countless times at depth. Evidence for metasomatic influence exists in elevated Mg#, hydrous bearing phenocrysts, and increased concentration of LREEs and other incompatible elements.

(1Bii) Prostka Model

Prostka (1973) interpreted that lamprophyric rocks from the Absaroka Volcanic Field (AVF) of Wyoming and Montana as the product of hybridization between syenitic and gabbroic magmas (Fig. 2B). The origin of the lamprophyre, according to Prostka, is as follows. Large crystals of feldspar, augite, olivine, Fe-Ti oxides, and other mafic components crystallized plutonically as cumulates from a calc-

alkaline magma. The cumulates could be hosted within a mafic layered intrusion or complex, with the mineralogy of the layering differing slightly as mafic phases crystallized out preferentially and settled at the bottom of the mafic igneous complex. He surmised that there was a high temperature syenitic liquid that must have invaded the cumulates, disaggregated them, and partially assimilated them. Prostka does go on to state that the proportions of syenite to gabbro could have been highly variable in the resulting mixture. To explain some of the variation between different lamprophyre dykes, he stated that, if the gabbroic material was not homogeneous, and came from a series of layered intrusions or complexes, the relative proportion of mafic minerals to each other and to plagioclase would vary greatly. Crystal transfer of mafic phases (olivine and clinopyroxene) into a mixture of syenitic plus gabbroic melt may result in the creation of a lamprophyric composition (Bowen, 1928). Evidence for hybridization and crystallization in these environments exists in lamprophyric mineralogical complexities such as mineral resorption, complex zoning of crystals, and disequilibrium mineral assemblages (Mitchell, 1994).

(1Biii) Cogne Model

Cogne (1962) surmised a potential origin of lamprophyres based on petrographic and field observations of xenoliths centered on the mixing of mafic and felsic components along with diffusional exchange (Fig. 2C). The model, in broadest terms, could be viewed as the foil to Prostka's model. In it, a mafic gabbroic melt invades a partially crystalline granitic complex or intrusion at depth. Near the boundary where the mafic and felsic exchange occurs, percolation and mixing of the two magmas would undoubtedly transpire. Coupled with hybridization, selective diffusion is a critical component of the Cogne model, where felsic components such as K_2O or H_2O housed in mineral phases of the granitic intrusion could diffuse into the resulting mixed magma, thus bringing about the typical lamprophyric assemblage of olivine + pyroxene + biotite + other hydrous or metasomatic phases. The pressure differential of a lamprophyric melt and the surrounding magma would vary greatly and lamprophyric

melts under the right conditions could ascend via preexisting faults or conduits within the crust. Cogne used textural and mineralogical evidence of felsic minerals and crustal xenoliths rimmed by biotite rich haloes near lamprophyre dyke contacts to support mixing and diffusional exchange.

(1C) Thesis Goals

By analyzing the mineral chemistry, comparing field and petrographic textural variations of calc-alkaline to alkaline widespread lamprophyric rocks of Late Cretaceous to Early Eocene age within the Central Montana alkalic province (CMAP), this project aims to:

1. Document differences or similarities between lamprophyric rocks in alkalic to calc-alkaline magmatic complexes across Montana:
    a. By comparing field data and petrographic details of lamprophyric rocks from each study location,
    b. And by evaluating microprobe data of pyroxenes from representative samples from each area.
2. Discern if there is any evidence to suggest that these lamprophyric rocks were the product of hybridization of different magmas, and if there is, determine if the Prostka, Cogne, or the metasomatism model is more relevant:
    a. By evaluating textural petrographic data,
    b. By evaluating mineral geochemical variations of disequilibrium features such as bizarre, unusual mineral zonations or melt pockets found within major macrocrysts.

2. Regional Geology

(2A) Tectonic Setting

Volcanic fields and plutonic bodies of southwestern and central Montana are aligned along several broad ranging structural lineaments or belts (Chadwick, 1981; Winston, 1986; O'Neill, 1988; Berger et al., 2011) (Fig. 3). The Great Falls tectonic zone (GFTZ) is a northeast trending deformation zone, approximately 1,500 km long and 200 km wide, which formed during the suturing of Paleoproterozoic and Archean cratons at ~ 1.8 Ga. In ~ 1.5 Ga a northwest trending depositional trough began forming across the GFTZ known as the Belt Basin. Within this basin, the Lewis and Clark Line (also referred to as the Montana lineament in older literature), a series of northwest striking faults of Proterozoic ancestry are exposed in the west-central and southeast portions of the basin. The Belt Basin also contains the Helena embayment, an east-west fault belt with normal sense displacement.

During the Laramide orogenic period, from the beginning of the Late Cretaceous to Early Eocene, there existed significant tectonic stress and subsequent igneous activity in southwestern Montana. Berger and others (2011) summarized the Late Cretaceous tectonics in southwest Montana. An east to west compressional regime caused N - NW striking thrust faults that age younger progressing eastward. A thrust front north of the Boulder Batholith, termed the Montana Disturbed Belt, corresponds to the northeastern edge of the Belt Basin. The Helena Embayment's north and south fault boundaries, east of the Boulder Batholith, were reactivated as strike-slip to reverse-slip fault zones. These transverse fault zones form the Helena structural salient of the frontal thrust zone. Northwest striking, strike slip faults of the Helena structural salient thrust front advanced further east, and reactivated faults northwest of the Boulder Batholith along the Lewis and Clark Line (Hobbs et al., 1965; Reynolds, 1979).

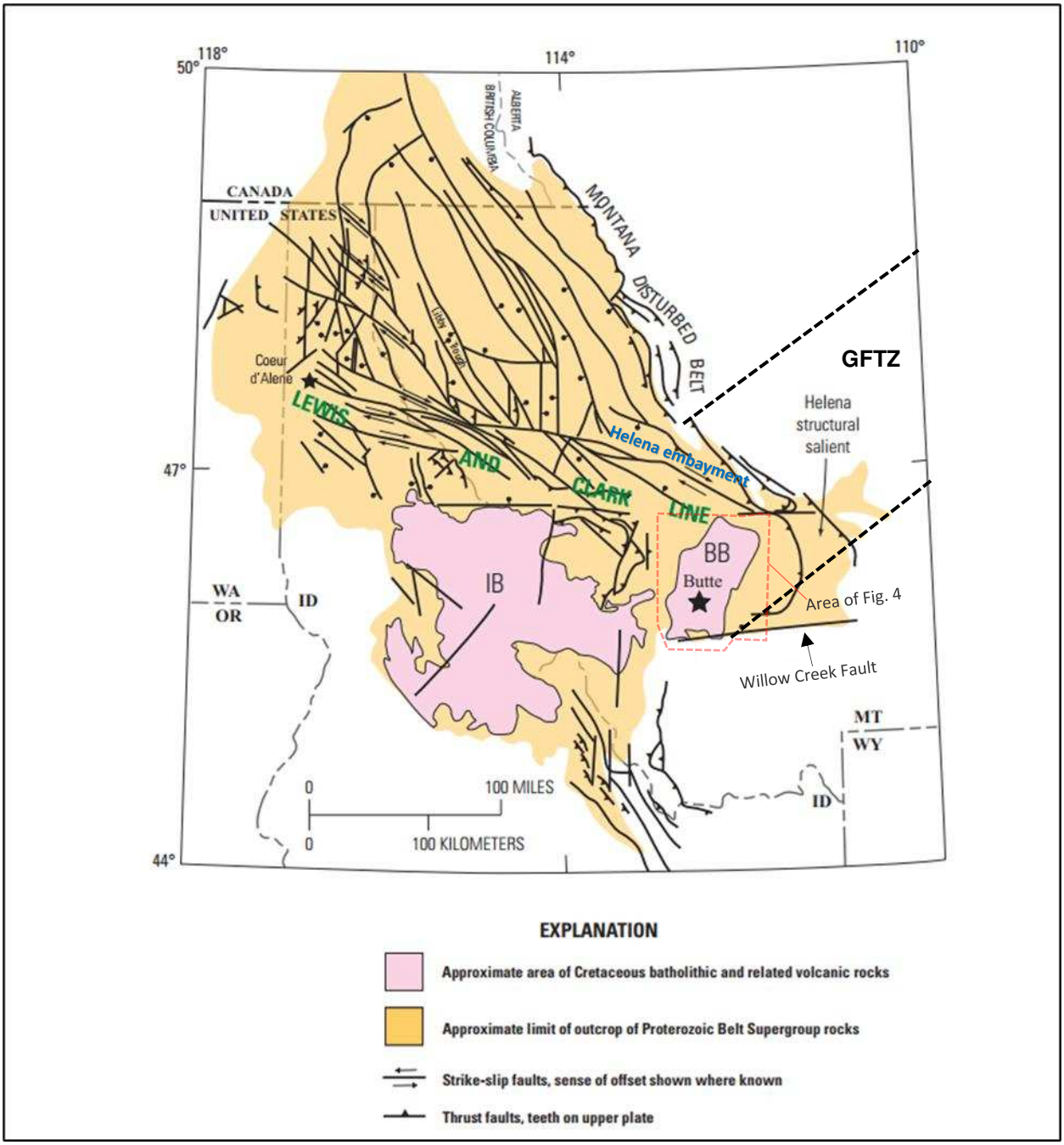

Figure 3: Map displaying the distribution structural features influencing Cretaceous volcanism and plutonism, the extent of the Belt Supergroup, and the major faults and structural features in southwest Montana. (After Berger et al., 2011)

(2B) Late Cretaceous to Eocene Volcanism and Magmatism in Montana

Volcanism and magmatism in southwestern and central Montana peaked during the Late Cretaceous and in the Early to Middle Eocene. Episodes of intense volcanism and plutonism accompanied folding, thrusting, and foreland basement deformation in response to subduction of the

eastward dipping Farallon oceanic plate underneath the western margin of the North American continent (Burchfiel and Davis, 1975). Scarberry and others (2020) summarize that the batholiths, plutons, and related volcanic rocks of Late Cretaceous age are a record of arc magmatism that formed in an evolving thrust wedge during contractional deformation, as opposed to the extensional regime that was present in the Cenozoic as the result of the Cordilleran arc collapse. Houston and Dilles (2013) inferred Paleocene uplift and subsequent erosion of cogenetic volcanics from the top of batholiths and plutons in southwestern Montana by radiometric ages, hornblende barometry, fluid inclusion pressure estimates, and geologic relationships.

Igneous activity was continuous from the Late Cretaceous to Paleogene time with periods of high magmatic flux occurring from 85-70 Ma and 55-45 Ma (Chadwick, 1981; Robinson et al., 1962; Scarberry et al., 2020). The Boulder Batholith and its associated satellites (plutons and batholiths) were emplaced during this 85-70 Ma period in response to: (1) Sevier-Laramide plate subduction (from 110 – 87 Ma); (2) crustal thickening and attendant crustal melting (from 83-54 Ma) (Scarberry et al., 2020). During the 55-45 Ma period of igneous activity, there was a shift from contraction-related magmatism (from 54-43 Ma) to magmatism associated with extensional collapse of overthickened crust (du Bray et al., 2012; Scarberry et al., 2020).

The Late Cretaceous Boulder Batholith is composed of the famed Butte Granite and is bordered by fifteen intrusions of similar composition (granodiorite, monzogranite, and minor syenogranite) (du Bray et al., 2012; Scarberry et al., 2020). The Boulder Batholith is a composite mass exposed over a 4500 km^2 area, elongate north northeastward (Fig. 4). The plutons associated with the batholith range in composition from syeno-gabbro to alaskite (leuco-alkali-feldspar granite), but the majority are dominated by quartz monzonite or granodiorite (Klepper et al., 1971; du Bray et al., 2012). The quartz monzonite, dubbed the “Butte Quartz Monzonite” or “Butte Granite”, because it houses the acclaimed ‘Richest Hill on Earth’, and is entrenched within the history of Butte, Montana where copper, gold, and

molybdenum have been extracted since 1864 and extraction continues to this day in the Continental and Berkeley pits. The Butte Quartz Monzonite, comprising the majority of the Boulder Batholith, is dated at 72 to 76 Ma (Tilling et al., 1968; du Bray et al., 2012). Roughly coeval with the batholith's intrusion large volumes of volcanics were erupted in the Livingston and Elkhorn Mountain volcanic fields.

The preserved roof of the batholith consists of welded tuffs correlated to be that of the middle and lower unit of the Elkhorn Mountain Volcanics. Age dating of the lower unit (78 Ma) is the same as the compositionally similar earlier plutons of the Boulder Batholith (Hamilton and Myers, 1974). K-Ar dating of rocks within the plutons indicate the entire batholith and its surrounding complexes were emplaced within 10 million years (Klepper et al., 1971), but others suggest the age of emplacement took place within a period of about 6 million years (Tilling et al., 1968, and Hamilton and Myers, 1974). More recent dating from zircon U-Pb geochronology of the Butte Granite depicts two episodes of magmatism at 76.7 ± 0.5 Ma and 74.7 ± 0.6 Ma; additionally, the peripheral Boulder Batholith plutons were emplaced from 81.7 ± 1.4 Ma to 73.7 ± 0.6 Ma (du Bray et al., 2012). The depth and thickness of the pluton is thought to be 5 km thick; however, gravity data suggests that thickness of the batholith to be 15 km thick or so (Hamilton and Myers, 1974, and Klepper et al., 1971). Geophysical depth estimates of the floor of the batholith coupled with hornblende barometric data from exposed granite at the surface yields a thickness of the Boulder Batholith ranging from 15 to 22 km (Houston and Dilles, 2013). The red demarcated zone on Figure 4 corresponds to an area known as Bull Mountain, a satellite intrusion of the Boulder Batholith. During this study, lamprophyres were collected and sampled throughout the Bull Mountain Range. The Livingston volcanics were originally named the Livingston Formation by Weed (1993) and first mapped by Parsons (1942). The Livingston Volcanics (Formation) were modified to the Livingston Group by Roberts (1963) and is a 4000 m thick sequence of epiclastic volcanic sedimentary rocks that filled the subsiding Crazy Mountain Basin (Scarberry et al., 2020). Parsons (1942) noted that

numerous pipes, plugs, dikes, and laccoliths are associated with the Livingston volcanic strata, and were deemed to be contemporaneous with the volcanic strata of andesitic breccias, conglomerates, tuffs, and lava flows. Andesitic dykes and dioritic plutons were dated at 82 Ma, which makes the Livingston volcanic field the earliest preserved volcanic center in southwestern Montana (Chadwick, 1981). The Livingston Group consists of deposits of epiclastic volcanic conglomerate, sand, silt (and mud), and intercalated bentonite ash beds and ignimbrite deposits (Scarberry et al., 2020). Four formations comprise the Livingston Group, from oldest to youngest, they are the Cokedale, the Miner Creek, the Billman Creek, and Hoppers Formations. Contemporaneous with the Livingston volcanics is the Elkhorn Mountain Volcanics.

The Elkhorn Mountain Volcanic (EMV) field represents a vast sequence of andesitic-rhyolite flows, breccias, tuffs, and ash flow tuffs that was first described by Klepper and others (1957). Rocks of the EMV cover an area of 25,000 km^2 and includes both the flank and roof pendants of the Boulder Batholith (Scarberry et al., 2020). Age dating of the EMV's middle member on the eastern flank of the Boulder Batholith yielded deposition ages of 84 to 82 Ma (Olson et al., 2016). Scarberry (2016) mapped rhyolite tuffs of the EMV middle member to the west of the Boulder Batholith which were dated at 79 to 78 Ma by Korzeb and others (2018). The Elkhorn Mountain volcanics contains three units (lower, middle, and upper) of varying thickness. The lower unit (650 m thick) (1) is categorized as containing dacitic, andesitic, and basaltic volcaniclastics and autobrecciated flows; the middle unit (1650 m thick) (2) contains interbedded rhyolite welded tuff sheets, epiclastic pyroclastics derived from erosion of the lower member, and autobrecciated flows; and finally, the upper unit (600m thick) (3) is dominated by bedded and water-lain tuffs and andesitic epiclastic volcanic rocks (Smedes, 1966; Hamilton and Myers, 1974; Chadwick, 1981; Scarberry et al., 2020). The Elkhorn Mountain Volcanics are thought to be a preliminary phase of the Boulder Batholith magmatism. The upper EMV member is best exposed in roof pendants of the Boulder Batholith found between Butte and Helena (Scarberry et al., 2020). The

batholith is proposed to have invaded a cover of its own volcanic deposits, and there is considerable amount of overlap in the time of emplacement. But the consensus is that the climax of plutonism followed that of volcanism (Chadwick, 1981, and Klepper and others, 1971).

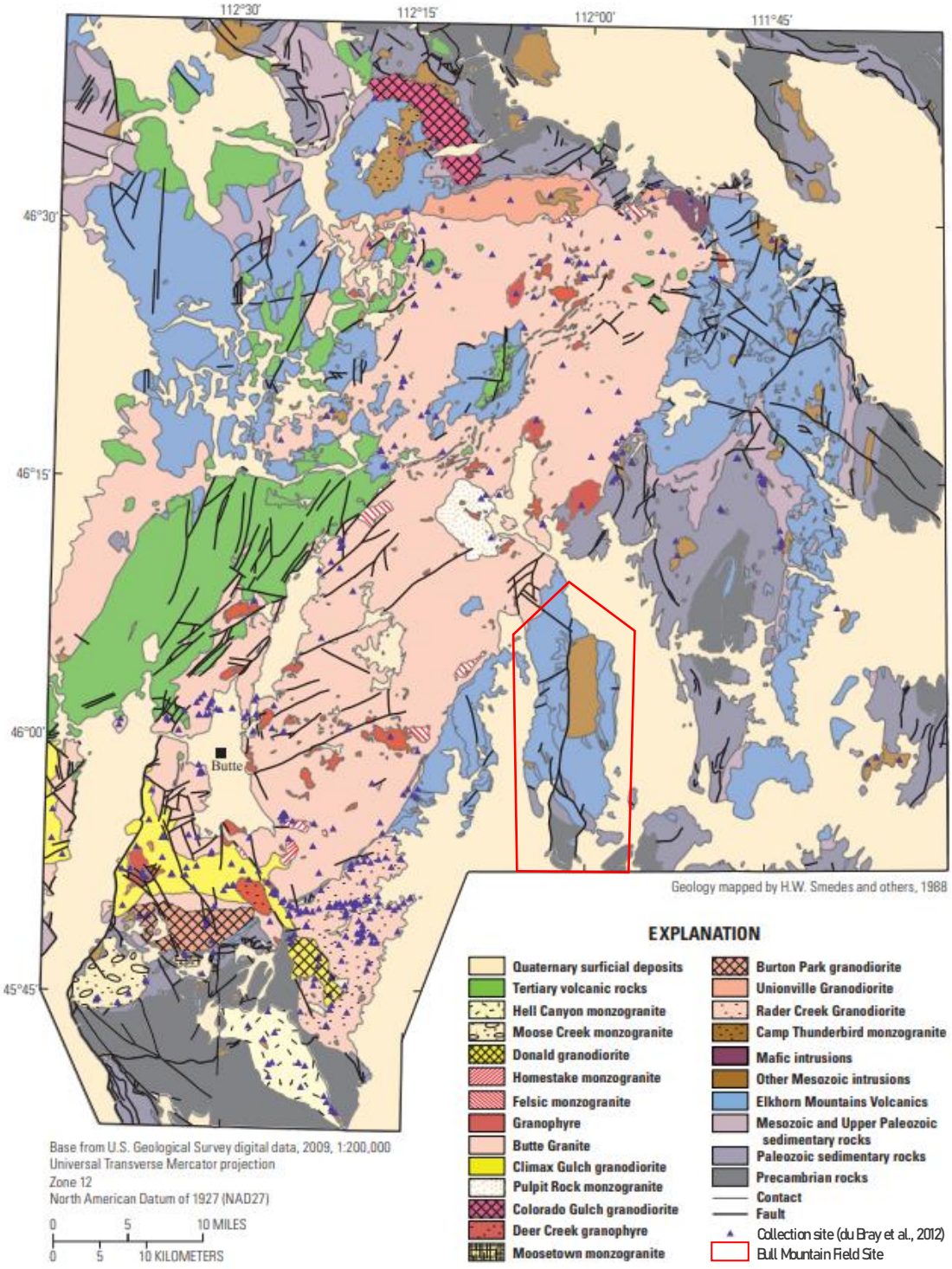

Figure 4: Geologic Map of the Boulder Batholith in southwestern Montana. Red outline depicts the Bull Mountain field area for this study. (Map after du Bray et al., 2012; Area Mapped by Smedes et al., 1988).

Following the igneous activity during the Cretaceous was another voluminous period in Montana during the Paleocene to Eocene of the Paleogene period. Radiometric information suggests another volcanic and plutonic maximum during the Early-Middle Eocene (54-45 Ma) within the Central-Montana alkalic province (CMAP) (Chadwick, 1981). This alkalic province includes the Highwood Mountains, Bearpaw Mountains, Eagle Buttes, the Crazy Mountains, and the Sweetgrass Hills of central Montana. The province consists of distinctly potassic, mafic to felsic rocks of Eocene age. Volcanic and intrusive rocks consist of latite, minette, or mafic phonolites along with their felsic byproducts (O'Brien et al., 1991). The Highwood Mountains are a deeply incised volcanic edifice dated at 54-50 Ma, that has dimensions of approximately 30 x 20 km, and are associated with widespread Eocene volcanism throughout south-western to central Montana (Marvin et al., 1980). Eocene volcanic and intrusive deposits include the Bearpaw Mountains (53-50 Ma), the Highwood Mountains (47-45 Ma), the Crazy Mountains associated with the Big Timber Stock (49 Ma), and the Gallatin Range-Northern Absaroka Mountains (53-48 Ma) (Chadwick, 1981, and du Bray et al., 2006). Lamprophyres from the Absarokas were analyzed by Prostka (1973) and led to his hybridization model for petrogenesis. The Highwood Mountains and Crazy Mountains were chosen as collection sites because they house lamprophyre dyke swarms, are roughly coeval with the Absaroka volcanism of the Wyoming-Montana Alkalic Province (of which the CMAP is part of).

(2C) Bull Mountain Range

Bull Mountain is a component of the aforementioned Late Cretaceous Elkhorn and Livingston Volcanics and is a satellite intrusion of the Boulder Batholith. The north-south oriented range is located approximately 40 km west of Butte, Montana. Bull Mountain is best known for accommodating the Golden Sunlight gold-silver-telluride deposit, owned by Barrick Gold Corporation in the Whitehall mining district, Jefferson County. The mine permanently closed in 2019 when gold production at the site was deemed no longer economically viable. During its 40 years of operation the mine is estimated to have

produced 3 million ounces of Au (mining.com, 2021). Golden Sunlight is hosted in a mineralized breccia pipe that cuts through the faulted west limb of a north-plunging syncline of sedimentary rocks of the Middle Proterozoic Belt Supergroup and sills of Late Cretaceous rhyolite porphyry (De Witt et al., 1996). The Proterozoic rocks, within and surrounding the mine area, can be subdivided into basin plane, outer fan, middle fan, inner fan, submarine canyon, and slope/shelf facies associations that prograde in a northerly direction (Foster et al., 1993; Spry et al., 1997). Within the Proterozoic, is the older LaHood Formation and the Greyson Formation, which consists of arkoses, sandstones, conglomerates, carbonaceous black shales, and the Bull Mountain Group. The Bull Mountain group, informally named, includes laminated siltstones, shales, rhythmically laminated siltstone and shales, synsedimentary sulfides, carbonate and silicate concretions, and olistostromes (Foster, 1991). Unconformably overlying the Proterozoic sedimentary rocks are quartzites, arkoses, and glauconite bearing sandstones of the Cambrian Flathead Formation (Spry et al., 1997).

Multiple magmatic alkalic to sub-alkalic suites are located in the vicinity of the mining district and the surrounding Bull Mountain Range to the north, the most notable of them is the aforementioned Elkhorn Mountain Volcanics associated with Boulder Batholith plutonism. These rocks consist of dykes, sills, and stock like bodies of quartz monzodiorite, latite, rhyolite porphyry, potassic trachybasalts, basaltic andesites, and lamprophyres (originally termed basalts in this area) (Spry et al., 1997). Lamprophyres in this region range in composition from CO_2 poor (0.2 weight percent CO_2) to CO_2 rich (20 weight percent CO_2) (De Witt et al., 1996). From biotite separate samples, from two different lamprophyre bodies, found within the Golden Sunlight Mining district, the age of emplacement was gathered. K-Ar dating using conventional methods yielded ages of 76.9 ± 0.5 Ma for the lamprophyres, making lamprophyric emplacement roughly coeval with the Boulder Batholith intrusion (De Witt et al., 1996).

Lamprophyre dykes are emplaced along structural features that contain earlier gold mineralization at Golden Sunlight; this indicates that early mineralization started with the intrusion of the main porphyry stock and continued during emplacement of the lamprophyre dykes and sills (Scarberry, 2016). Some lamprophyre dykes cut the mineralized breccia pipe and their spatial relationship with late shear zones and veins that produced high-grade gold has led to some speculation regarding a possible genetic connection between the timing of gold deposition and lamprophyre emplacement (Childs, Personal Com., 2017). A total of 21 lamprophyre samples were analyzed for their Au content by De Witt and others (1996) and only two samples yielded results more than 0.05 ppm Au. Regardless of this, the presence of magnesite as a gangue mineral in the mineralized breccia pipe and as replacement products of olivine and pyroxene in the lamprophyres may suggest that the latest stages of Au mineralization occurred during the same time as lamprophyre emplacement (De Witt et al., 1996).

(2D) Highwood Mountain Range

The Highwood Mountain potassic volcanic complex of Eocene age (52 ± 1 Ma) (O'Brien et al. 1991), (and the neighboring Beartooth Mountains) belong to the Central-Montana alkalic province and was first described by Weed and Pirsson (1895). The Highwoods contain stocks, dykes, and laccoliths of shonkinitic and monzonitic composition (Chadwick, 1981). The Highwood Mountain magmatic history started with the eruption and subsequent emplacement of ˜350 m of quartz latite lavas, tuffs, and breccias onto Cretaceous sediments (Henderson et al., 2012). Mafic phonolite, minette (lamprophyre), and syenite dykes ranging in size from 10 cm to 5 m in width crosscut the host volcanics and stocks (O'Brien et al., 1988). After a long period of erosion, a second eruption of potassic rich, SiO_2 undersaturated mafic rich phonolitic material took place, followed by the intrusion of stocks, sills, and radial dyke suites. The potassium rich rocks are host to leucite, pseudoleucite, or abundant biotite. The intrusion of stocks, up to 5 km across, led to deformation and faulting in the form of an upward doming of the adjacent sedimentary sequence (O'Brien et al., 1988). Finally, late-stage hydrothermal alteration

and recrystallization is thought to have occurred with the introduction of Na, K, Ca, Fe, and Si (Henderson, et al., 2012). Radiometric isotope and trace element research have concluded that the formation of magmas involved the interactions between different sources, including Archaean asthenopsheric mantle material and subduction related potassic metasomatic events in the lithosphere (Henderson et al., 2012). The primary magma in this complex and the parent of undersaturated magmas in this complex is of olivine minette (lamprophyre) composition and interpreted to form at depths of 150-200 km (O'Brien et al., 1991). Lamprophyres within the Highwoods are most common as dykes or sills; however, O'Brien and others (1991) identified two separate minette lava flows within younger volcanic series of primarily mafic phonolitic composition.

(2E) Crazy Mountain Range

The Crazy Mountain Range (often called the Crazies by locals of the area) is located in south central Montana and lies east of the Rocky Mountain front and north of the Archean Beartooth Block (Dudas, 1991). Like the Highwood Mountains, the Crazies span a distance of ~64 km and belong to the Central-Montana alkalic province, an extensive zone of potassic, mafic, and felsic rocks of Eocene age. The mountain range resides within the Crazy Mountains basin, a structural relief zone that is an east to west trending syncline of Cretaceous to early Tertiary origin (Hearn, 1989; and Dudas, 1991). The Crazy Mountains Basin is bounded by the Nye-Bowler lineament to the south, the Lake Basin Fault Zone to the north, and the Fromberg Fault to the east (Hearn, 1989). Igneous rocks in the range occur along the western portion of the Crazy Mountain Basin and are emplaced into Cretaceous and Paleocene sedimentary strata. Both alkalic and subalkalic volcanic rock suites exist in the Crazies. Basalt, andesite, and rhyolite of the subalkalic series encompass the largest intrusions of the Crazy Mountain Range, those being the Big Timber and Loco Mountain stocks. The dykes are more alkalic than the stocks, and it is possible that late-stage magmatic hydrothermal processes could have altered the composition of the dykes (du Bray et al., 2006). A prominent feature of these stocks is the presence of radial swarms of

dykes of varying composition (calk-alkaline to alkalic) as well as numerous dykes cross cutting the stocks. Dudas (1991) notes there are basalt, andesite, rhyolite, and lamprophyre dykes spatially associated with the Big Timber and Loco Mountain stocks. Zircon age dating in one latite dyke gave an age of 58 ± 6 Ma, thus intrusion is probably early Tertiary in age (Larsen and Simms, 1972). The underlying basement of the Crazy Mountains is Archean, and it is not exposed, but it is sometimes found in volcanic pipes and dykes as crustal xenoliths (Hearn, 1989). Trace element studies of abundant dyke swarms associated with the Big Timber stock, after the work of Pearce and others (1984), suggest that the ratios of Rb, Y, and Nb within the dykes are similar to rocks that are related to subduction-related volcanic arc rocks (du Bray et al., 2006). Dudas (1991) speculated the main driving mechanism for the Eocene magmatism within the alkalic province could be related to the heating of the lithospheric mantle by upwelling asthenosphere or by regional decompression.

(2F) The Yogo Dyke Lamprophyre

One sample analyzed in this study originates from the Tertiary aged Yogo Gulch sapphire deposit. Yogo is unique in that is the only known economic lamprophyre hosted sapphire deposit (Palke et al., 2016). The Yogo Gulch deposit is located in the Little Belt Mountains of central Montana, in Judith Basin County, some 75 km south of Lewiston and 95 km southeast of Great Falls, and roughly 20 km east of the Little Belt Mountains. In this area, syenites, monzonites, shonkinites, and lamprophyres of the Central-Montana alkalic province are common (Meyer and Mitchell, 1988). The dyke resides in the Central Montana alkalic province (Larson, 1940). Guylaine (1995) states the dyke shows similar characteristics to ouachitite, damkjernite, and aillikite of the ultramafic lamprophyre group because the rock is silica poor and rich in Ca, Mg, Cr, Ba, and Sr. The lamprophyre, under Rock's (1991) mineral and chemical classification, should be classified as an ultramafic lamprophyre, termed an ouachitite (Gauthier, 1995). The Yogo dyke is roughly 9 km in length in an east-west direction and varies in thickness between 2 to 7 m (Meyer and Mitchell, 1988).

The vertical dyke intrudes into the Madison Formation (a massive Mississippian limestone) and the Amsden Formation (Mississippian and Pennsylvanian shales) (Claybaugh, 1952). Radiometric age dating has bracketed 44 to 57 Ma, based off of biotite and hornblende in lamprophyre sills within the nearby Little Belt Mountains (Marvin et al., 1973). Guylaine (1995) dated the Yogo lamprophyre more precisely at 48 ± 1.3 Ma and Harlan (1996) dated phlogopite at 48.62 ±0.09 Ma. Thus, the Yogo lamprophyre is Eocene, or early Tertiary in age.

3. Methods

(3A) Field Work

During the Summer of 2017, three major alkalic to calc-alkaline magmatic complexes were identified as areas of interest based on previous records of lamprophyric rocks. The Bull Mountain, Highwood Mountain, and Crazy Mountain ranges were selected because they are coeval with abundant volcanic alkaline activity during the Late Cretaceous to Early Eocene periods within central Montana. The Yogo Dyke lamprophyre was of interest to this study not only because of its acclaimed history, but because it is of similar age to the other lamprophyres focused on during this study. Dr. John Childs provided the sample from the historic Yogo site. Figure 5 below shows their spatial distribution with regards to one another. With the aid of some friendly geologists from the Montana Bureau of Mines and Geology (MBMG) of Butte, Montana (Kaleb Scarberry, Susan Vuke, and Dick Berg), these targets were identified after studying geologic maps of the areas. Emphasis was put on sites with a high density of lamprophyric dyke swarms and sills.

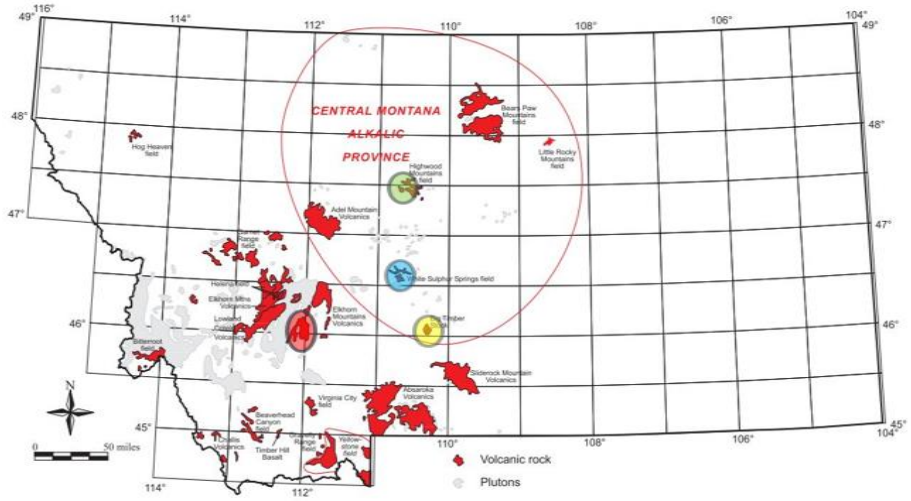

Figure 5: Volcanic and plutonic centers of Montana. The small transparent red zone is the Bull Mountain region, the yellow zone is the Crazy Mountain range, the green is the Highwood Mountain range, and the blue is the location of the Yogo Dyke (after Vuke et al., 2007).

Rocks bearing resemblance to the classic 'glistening porphyry' panidiomorphic texture were collected from field sites. Lamprophyric rocks identified in the field were porphyritic, displaying a fine-grained grey to greenish colored groundmass along with coarse mafic megacrysts, usually mica (biotite or phlogopite), clinopyroxene, or hornblende. Spotting micaceous macrocrysts in the field proved difficult at first but became easier once the eyes were attuned to spotting dykes and sills through shrubbery. Most areas were accessible by vehicle through unpaved back roads or jeep trails maintained by the US Forest Service but hiking off trail was necessary to access most of the lamprophyric outcrops. As lamprophyric rocks were collected and bagged, the location of the outcrops was logged using a Garmin 64st Topo U.S GPS (these GPS coordinates can be found in Appendix E). Field notes and pictures of select outcrops were taken, samples were labeled and collected for further analysis. The orientation of each dyke or sill was recorded using a Brunton compass or the FieldMoveClino professional geologist app on an iPhone 6S cellular device. Degree variation from the Brunton to the Clino app was less than five degrees, thus the app was deemed an acceptable and sometimes easier way to record orientation field datum than the traditional Brunton compass.

(3B) Petrography

Fifty-four samples of lamprophyric rocks from Bull Mountain, Highwood Mountains, Crazy Mountains, Yogo 'sapphire' dyke, a noted lone lamprophyre discovered at the Broadway Au-Cu skarn deposit in Silver Star, Montana, and three others from a MBMG sponsored fieldtrip in southwestern Montana were sent to Paula Leek Petrographics, and standard thin sections were created (See Appendices A and B). Using transmitted light from a Leica DM-EM microscope at the CSU Geosciences Department, thin sections were analyzed for mineralogy and textural features. A greater emphasis was placed on clinopyroxene phenocrysts as it would become the preferred target of the following mineral chemistry analysis. Sixteen samples were selected based off of the presence of disequilibrium features, i.e. spongy textured clinopyroxenes, abundant zoned micas, and unique zonations present within

pyroxenes. These samples were again sent to Paula Leek Petrographics, and 100 µm polished sections were created in preparation for mineral chemistry electron microprobe analysis.

(3C) Electron Microprobe

Clinopyroxene major element compositions were determined by electron microprobe (EMP) at the University of Colorado Boulder Electron Microprobe Laboratory, using a JEOL JXA-8230/8530 (TCP/IP Socket and EIKS) model equipped with a LaB6 electron gun and five tunable wavelength dispersive spectrometers (Fig. 6). Operating conditions were 40 degrees takeoff angle, and a beam energy of 15 KeV. The beam current was 20 nA, the beam diameter was 2 microns. Elements and radiation lines were acquired using analyzing crystals LIFL for Fe, Cr, Mn, Ni, PETL for Ti, K, Ca, TAPL for Al, Na, Mg, and TAP for Si. The standards were Almandine NY for Al and Fe, Chromite for Cr, Diopside for Si, Jadeite for Na, Labradorite for Ca, Rhondonite for Mn, Pentlandite for Ni, and Rutile for Ti. Standards originate from Astimex Minerals (std serial 1CH). Localities are as follows for the standards: Almandine (New York State, USA), Chromite (New South Wales, Australia), Diopside (Wakefield, Quebec, Canada), Jadeite (China), Labradorite (Sonora, Mexico), Rhodonite (British Columbia, Canada), Pentlandite (Sudbury Igneous Complex, Canada), and Rutile (Synthetic, CERAC Inc., USA).

X rays were measured simultaneously and are the average of five separate dispersive spectrometers. Detection limits ranged from 0.004 weight percent Mg, 0.006 weight percent Na, 0.010 weight percent Ti, 0.017 weight percent for Cr, and 0.02 weight percent for Ni. Beam count time was 30 seconds for all elements. The off-peak counting time was 30 seconds for all elements. The off-peak correction method was linear for all elements. Unknown and standard intensities were corrected for dead time. Analytical sensitivity (at the 99% confidence level) ranged from 0.203 percent relative for Si to 0.243 percent relative for Mg to 1.572 percent relative to Ti, to 12.568 percent relative to Mn, to 23.00 percent relative to Ni. Microprobe analyses were recalculated as cations based on six oxygens. Anomalous stoichiometry can be readily identified and likely represent accidental mixed point analyses

(see Table 3, analysis for J18_4A traverse # 9 & Yogo_4A traverse # 2) It should be noted that iron microprobe compositional analysis results were provided in FeO (Fe^{2+}). The matrix correction method was ZAF or Phi-Rho-Z calculations and the mass absorption coefficients dataset was FFAST. The ZAF or Phi-Rho-Z algorithm utilized was after Pouchou and Pichoir-Full (PAP). For more information on microprobe methodology and techniques used, see Armstrong (1988).

As clinopyroxene responds texturally and compositionally to changes in magmatic environments, crystal growth stratigraphy records information about past magmatic history and compositions (Ginibre et al., 2007). As the electron microprobe beam analyzes pre-selected traverses or points along the crystal, based on preliminary assessment of polished sections, an analytical core-rim compositional traverse is created with the data. The shape and form of these analytical core-rim traverses are characterized and aid in determining what processes the crystals underwent during crystallization from the melt. The primary focus of the study was large clinopyroxene macrocrysts, but few groundmass clinopyroxenes analyzed originate from Yogo Dyke, J18 & J24 of the Highwood Mountains. KeV graphs, X-ray energy spectra, were used on occasion in attempts to define mineral phases as inclusions or confined to disequilibrium features like spongy texture. Although not nearly as accurate as detailed SEM work, microprobe KeV graphs are semi-quantitative and can be generated quickly. KeV graphs show emitted X-ray wavelengths that can be matched to elements and can be used to determine (on a quick pass) which phases are present by working backwards to decipher the minerals basic formula (Bell. Personal. Com., 2019)

Back scattered electron (BSE) imaging collected from electron microprobe sessions were all collected under constant conditions to ensure that the grey scale colors are the same. BSEs provide a rich host of compositional data because the fluctuations of the greyscale imaging and observed intensity of these greyscale images reflect differences in mean atomic weight of the minerals observed (Blundy

and Cashman, 2008 & Streck, 2008). Compositional changes within minerals lead to changes in mean atomic weight, and these variations are identifiable as zonations and zoning patterns on BSE images.

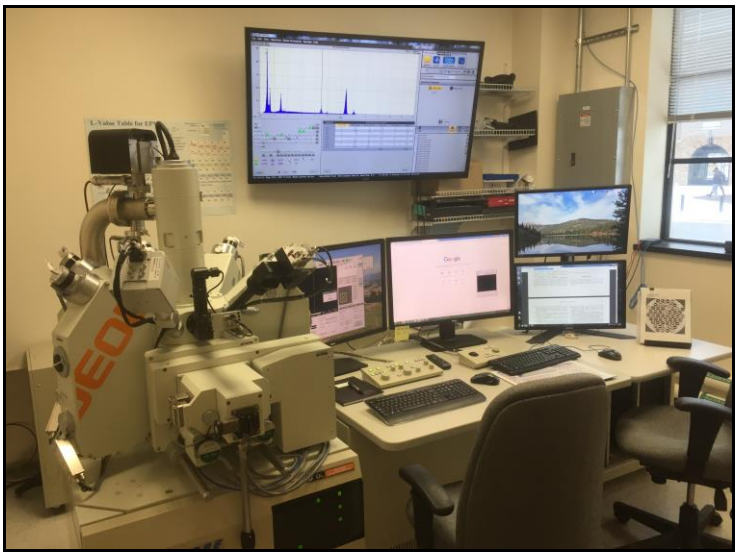

Figure 6: EMP at CU Boulder in action analyzing some lamprophyre samples.

Note: The author of this work has minor blue-grey color blindness, thus, when describing the color of greyscale zonations on BSEs the author uses classical HTML shades of grey terminology (Table 2). Do note that the location of grey is actually "darker" than dark grey on this scale. Each change in hue of grey along this greyscale corresponds to a qualitative change in pyroxene chemical composition. Quantitative changes are easily observed in microprobe transects across crystals.

Table 2: Terminology when describing Greyscale BSE imagery

	Color	Name	Hex	RGB
0	0	white	#FFFFFF	rgb(255,255,255)
1	1	whitesmoke	#F5F5F5	rgb(245,245,245)
2	2	gainsboro	#DCDCDC	rgb(220,220,220)
3	3	light grey	#D3D3D3	rgb(211,211,211)
4	4	silver	#C0C0C0	rgb(192,192,192)
5	5	dark grey	#A9A9A9	rgb(169,169,169)
6	6			
7	7			
8	8	grey	#808080	rgb(128,128,128)
9	9	dimgrey	#666666	rgb(102,102,102)
10	10	darkslategrey	#444444	rgb(68,68,68)
11	11			
12	12			
13	13			
14	14	black	#000000	rgb(0,0,0)

4. Data and Results

(4A) Field Observations

Lamprophyric rocks investigated in this study formed dykes, sills, or sheets (Figs. 8, 9, and 10). These often occurred together within each of the field areas, but dykes were the most common mode of lamprophyric emplacement found in this study (and often the easiest to locate!). Dykes and sills measured from this study ranged from 0.1 m to 12 m in width. Smaller 1 m wide dykes were the most common, and larger dykes and sills over 10 m were rarer. The longest lamprophyre traced during this study was roughly 25 m in length. Rock (1991) states a "keen eye" is needed by a geologist seeking lamprophyres in the field. After unsuccessfully hunting for lamprophyric outcrops one evening, the author and his field assistant stopped for some sustenance only to realize they had rested on an allusive lamprophyre outcrop. Lamprophyric rocks are notorious for weathering easily, thus finding fresh rock that is relatively unaltered proved to be a daunting task when collecting samples. In some worst-case scenarios, the fresh rock was up to a meter below the topsoil horizons and had to be excavated to yield "fresher" samples. When outcrops were completely weathered, the soil was dark grey, brown, or black in color with crystals of biotite or phlogopite often visible from afar within the soil top layer. The author does not advise continuing field research at night during the cover of darkness, but a flashlight was found to be an invaluable tool for locating some mica bearing lamprophyres as the micas would refract the light nicely for easy detection.

Lamprophyric dykes within the field did not behave similarly to other dykes of varying rock composition that were present in each area. The margins of lamprophyres when in contact with the host displayed chilled margins, contact alteration or hornfels development, abundant faulting, angular to sharp brecciation features, or no contact features whatsoever. The randomness with which these features were present in these lamprophyric rocks cannot be overstated. For example, at one

lamprophyric dyke within the Highwood mountains, near Highwood Baldy, chilled margins and faulting were present along margins of dykes, but less than 20 m away at an adjacent dyke, there were no signs of these features. The margins of dykes were also rarely uniform. Lamprophyric dykes often pinch or swell, tapering into snake like features with irregular branching patterns. Sometimes, discrete 'blobs' or 'circular to ellipsoidal bombs' were present separated from dykes within the host rock and could be pepperite (Ridley, 2021). These typically ranged in size from 0.1 m to 1 m in the field. Bizarre features along the emplacement margins of lamprophyric rocks within each field area were observed to be the norm rather than anomalies. Rock (1991) argued that strange features and the variation of intrusive forms within lamprophyric rocks are so bizarre, that they could be considered diagnostic features of lamprophyres.

Lamprophyric dykes within the Golden Sunlight open pit were the least altered or weathered, thus yielding the freshest of all samples collected during this study. Some of these lamprophyres showed small scale banding parallel to the margins, while others showed no signs of this. There were areas of macroscopically distinct bands of minerals and textures going from margin to the center of the lamprophyres. Golden Sunlight lamprophyres displayed less of a concentration of mafic phenocrysts in the margins, and a greater proportion of these phenocrysts were present in the center of dykes. A few dykes displayed grain size changes moving from the edge of the dykes to the center, with phenocryst size increasing moving towards the center of the dykes or sills, similar to features observed by Menezes and others (2015) in Cretaceous alkaline lamprophyres in SE Brazil. This behavior was not present to the north of Bull Mountain outside of the confines of the Golden Sunlight mining operations.

Field orientation data were collected when the author and his assistant were confident enough that the trend of emplacement could accurately be recorded. Many lamprophyric rocks were collected without orientation data but were still marked via GPS coordinates during this study. Directional Rose diagrams generated for lamprophyric rocks from each field area are present on Figure 7. Most dykes are

emplaced subvertically with exception of few sill-like bodies within Golden Sunlight. Orientation data from Bull Mountain lamprophyres shows a north-south trend. Highwood and Crazy Mountain lamprophyres exhibit a more radial style of emplacement. One would expect a radial pattern of dyke swarms around a central intrusion; thus, it is curious that Bull Mountain lamprophyres do not as it is a satellite intrusion of the Boulder Batholith. It is possible the observed dyke orientations do record regional tectonic stresses. It is possible that not enough orientation data was collected, and more is needed on the North end of the Bull Mountain Range as most of the samples from originate from the southern portion and the Golden Sunlight mining district. The Yogo Dyke lamprophyre orientation data was not collected in the field, as the author was not given access to that private property, but trend data was acquired by Mychaluk (1992) and Dahy (1991).

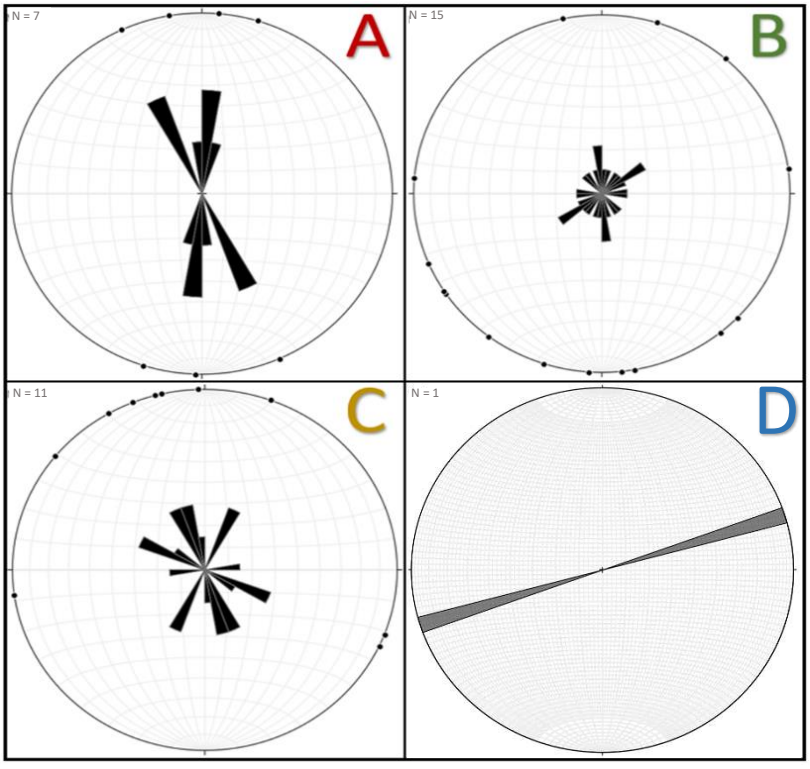

Figure 7: Lamprophyric trend/orientation data for fresh samples of collected lamprophyres from (A) Bull Mountains, (B) Highwood Mountains, (C) Crazy Mountains, and (D) The Yogo Dyke. Data plotted on Rose Diagrams. Note that N denotes how many instances of data were used to comprise each stereo net.

Figure 8: Lamprophyric outcrop field habits from the Highwood Mountains. The red lines demarcate the outcrop dimensions and orientation. Rock Hammer and a Field Assistant for scale. Host rock is likely monzonite. (Top Left) Outcrop depicts snake like dyke occurrence (Top Right) Outcrop contains both an irregular and a gradational margin with the country rock. (Bottom Left) Different colored soil with mica flakes which leads to a small outcropping of pseudo-fresh lamprophyric rock. Note the change in vegetation near the outcrop dimensions. (Bottom Right) Common mottled surface of a weathered lamprophyre with mica fragments in soil around collection site.

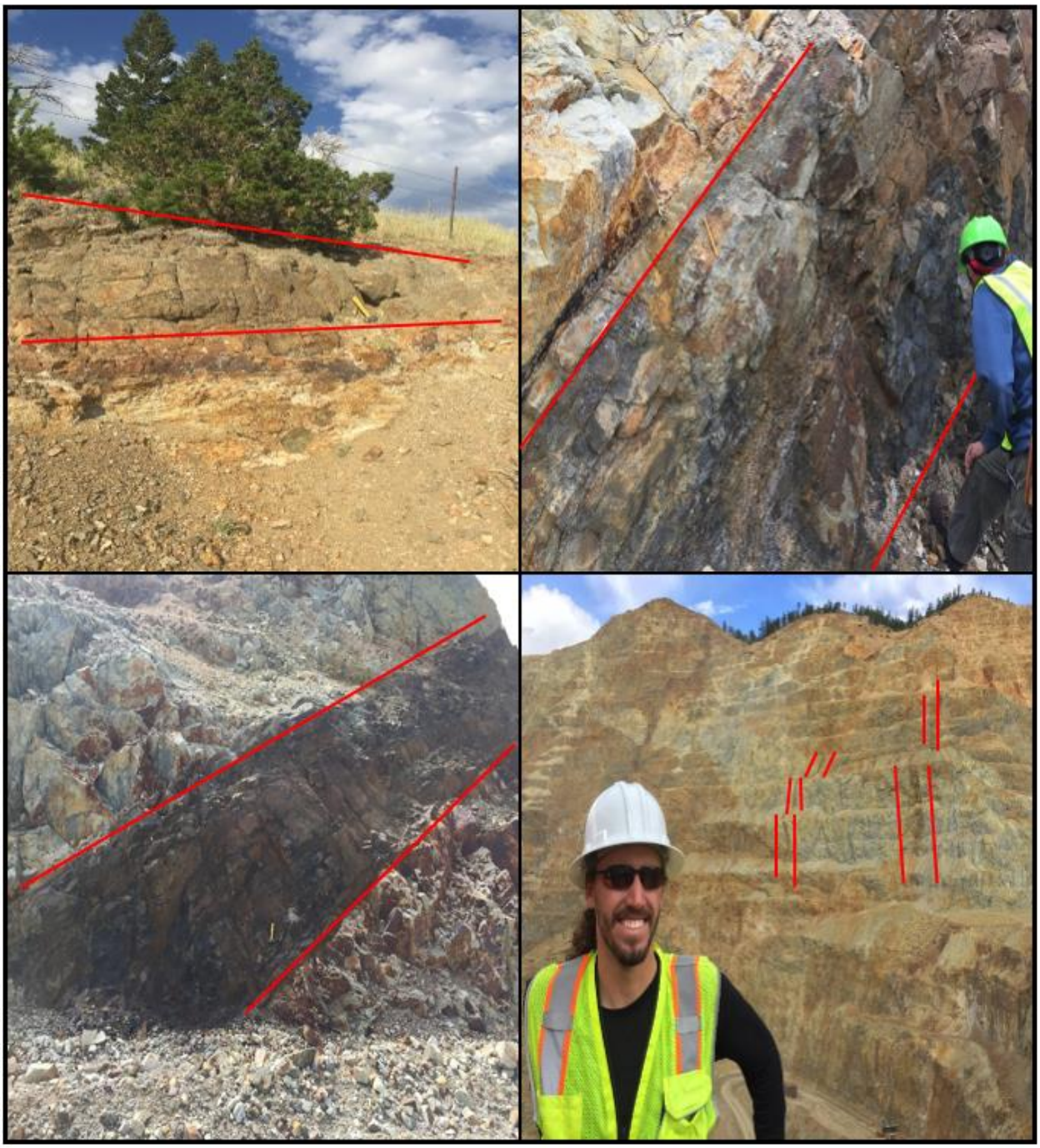

Figure 9: Lamprophyric outcrop field habits in the Bull Mountain area and the Golden Sunlight Mine. Red lines demarcate outcrop dimensions and shape. Hammer and humans for scale. Lamprophyric dykes cut through both the mineralized breccia pipe, belt supergroup, and the porphyritic rhyolite. (Top Left) Slightly weathered lamprophyre north of Golden Sunlight where heavy alteration occurs with margin of belt supergroup rocks. (Top Right) Faulting and fault brecciation occurring along upper margin of lamprophyre and host rock (Belt Supergroup). (Bottom Left) One of the freshest samples collected from within the Golden Sunlight mine cutting through Mesoproterozoic Belt supergroup rocks. (Bottom Right) Darker colored lamprophyre dykes offset by faulting in the Golden Sunlight main pit, Note size of the haul truck for comparison.

Figure 10: Lamprophyric outcrop habits in the Crazy Mountains. Red lines demarcate outcrop dimensions and shape. Hammer and field assistant for scale. Note the change in color between weathered and fresh outcrops. (Top Left) Classic lamprophyric dark colored mica rich soil adjacent to gabbroic rocks. The freshest of samples would crumble apart on transport. (Top Right) Sharp contact of a lamprophyric dyke with nepheline syenite margins. Note the pinched margin at the top of the dyke. (Bottom Left) The "Blink and you miss it" type of lamprophyre as termed by Francis Dudas present in photo. (Bottom Right) Lamprophyric dyke with irregular shaped pods or blebs of coarser/ altered lamprophyre material.

(4B) Petrography

Select lamprophyric hand sample descriptions from this study from the Yogo Dyke Lamprophyre, the Bull Mountains, the Highwood Mountains, and the Crazy mountains can be found in the appendices of this work. In general, hand specimens that are fresher (less weathered and altered) are dark grey to slightly green in color. The best samples show the 'glistening porphyry' porphyritic nature of the mafic crystals of phlogopite/biotite, clinopyroxene, and lesser amphiboles within a fine-grained aphanitic groundmass. Large mafic crystals are termed "macrocrysts" because they are 1-12mm in size (commonly 4-5 mm), but some of the crystals are greater than ~ 1cm and could technically be termed "megacrysts"; for simplicity, the author refers to all large crystals as macrocrysts. With a hand lens one can see the prismatic shape of the pyroxenes and even the internal zonations of some crystals. Several samples taken from the field were completely altered, crumbly, dark red to brown in color, and mica fragments would break apart from the rock and settle at the bottom of sample collection bags. These samples while collected, are omitted because they don't serve a purpose when fresher, pristine samples of lamprophyric rock exist.

Modal mineralogy for those sections is present in the appendices of this project (Appendix A). Select in depth descriptions of thin sections can be found in the appendices of this project (Appendix C). Note that some of these rocks do contain feldspar macrocrysts. Rock (1987) states that lamprophyres should be mesotype, melanocratic, and porphyritic with no feldspar or quartz phenocrysts. While some of the samples analyzed do contain microcrystalline to medium/coarse grained feldspars, it is unlikely that they are phenocrysts. These outliers are probably shonkinites or similar alkaline mafic igneous rock due to the presence of coarse potassium feldspar (mostly sanidine) and foid bearing phases within thin sections (Dudas. Personal. Com., 2017). Thus, not every rock within this study is technically a lamprophyre. Samples that could be easily identified with lamprophyric characteristics were looked at in

further detail and rocks not considered 'lamprophyric' (containing abundant feldspar or quartz phenocrysts) were not looked at further during this study.

Attention is needed when describing crystals within the lamprophyres during this study. With rocks as complex as lamprophyres, the chosen prefix implies knowledge of a genetic history pertaining to that specific crystal, which is not always abundantly clear. Because of these complexities, the author refers to all mafic phases as crystals in the data and results section of this work. Crystals will be more clearly defined based on their textural and chemical evidence within the discussions of this work.

Based on both petrography and BSE imagery, the thin sections depict strongly porphyritic and panidiomorphic textures. The largest crystals (macrocrysts) are clinopyroxenes and micas (phlogopite and biotite) commonly set in a fine grained or aphanitic ground mass of pyroxene, mica, olivine, feldspars, plagioclase, feldspathoids, carbonates, glass, and opaques. The rocks contain recognized lamprophyric characteristics such as bent crystals, ocelli or globular structures, and abundant xenoliths/xenocrysts. Notable minerals and features present in these lamprophyric rocks are described below. Disequilibrium freatures such as corroded crystal margins, evidence of strong mineral replacement, mineral embayment, spongy texture within crystals, and complex zonations are abundant within lamprophyric rocks of this study. Thin sections displaying strong disequilibrium features would go on to become the focus of this study with regards to mineral chemistry data collection.

(4B. i) Pyroxenes

Pyroxenes, more precisely clinopyroxene (augite-diopside) are the dominant mafic phase in most of the sections, and the author will use pyroxene and clinopyroxene interchangeably. Coarse pyroxene crystal populations far exceeded that of any other mafic phase. Clinopyroxene was found in rocks from every region of this study, although a few contained rare orthopyroxenes. Orthopyroxene phenocrysts are extremely rare within lamprophyres and are usually present in reaction rims or as xenocrysts (Fisera, 1974; Mitchell, 1985). Orthopyroxene was identified in a few xenolithic fragments as

well as within reaction rims of olivine. In thin section, clinopyroxenes appear colorless, pale yellow, pale green, to green in color when viewed in plane polarized light. Clinopyroxenes originating from the Highwood Mountains were greener than clinopyroxenes from Bull Mountain, the Crazy Mountains, or the Yogo Dyke Lamprophyre. Highwood Mountain pyroxenes occasionally displayed pleochroism from dark green to lighter green in plane polarized light. In thin section optical distinguishing features of clinopyroxene include characteristic inclined extinction, 2nd order interference colors, optically positive, stubby rectangular prisms elongated on the C-axis, occasional twins (not always present), and complex zonations.

Pyroxene zoning from every major site in this study varies from slight zonations to heavily or complexly zoned as seen by differing birefringences. Pyroxenes can display a range of internal zoning patterns from: concentric, patchy, or sector zoning. Heavily zoned pyroxenes are more common in akalic (AL) or ultramafic lamprophyres (UML) (Rock, 1991), but lamprophyres from alkalic to calc-alkaline magmatism from this study also displayed complex zonations. Often within a single thin section, pyroxene macrocrysts are not uniform in regard to zonations. Figure 11 is a back-scattered electron image that depicts the complexity of the zonation, within a single crystal, concentric zoning and patchy zoning can coexist.

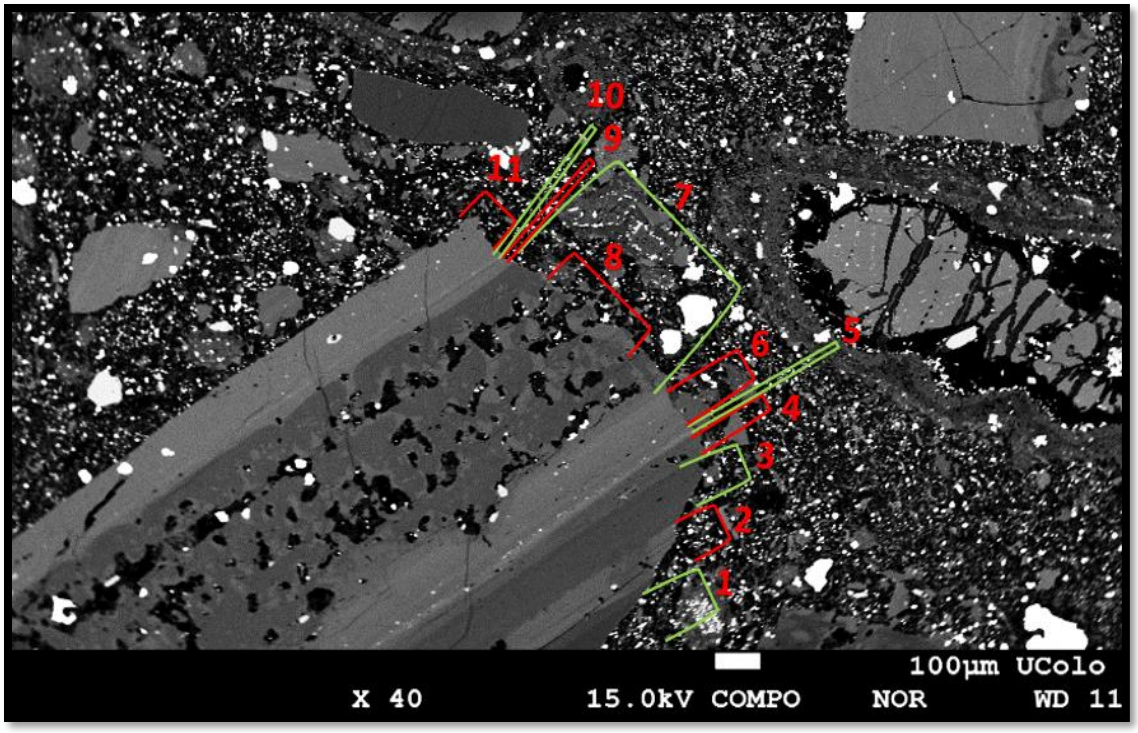

Figure 11: BSE concentric zoning and spongy texture present in a select grain of clinopyroxene from J06 a vogesite from Golden Sunlight. Note the many different compositional and truncated bands. This pyroxene grain is rich with inclusions inside melt pockets within bands 7 and 8. Band 5 contains abundant apatite inclusions. This truncated crystal lacks typical panidiomorphic shape associated with mafic phenocrysts of lamprophyric rocks.

Clinopyroxenes from Bull Mountain samples (Fig. 12) from this study are often the coarsest and most abundant mafic phase present. The crystals are porphyritic ranging in size from a few cm long tabular crystals to few microns sized crystals held within the groundmass. The crystals are often euhedral (panidiomorphic), display twins, and are complexly zoned (often displaying both concentric and patchy zoning patterns) (Fig. 12 a, b). Acicular apatite inclusions are common (Fig. 11). Subhedral varieties of pyroxene do exist as well as medium sized crystals residing in the same thin section as very coarse euhedral pyroxene crystals. These subhedral, subrounded pyroxene crystals are often embayed and fractures within the crystal are full of micas or carbonate infillings (Fig. 12 e). The margins of pyroxene crystals are often rimmed by rings of fine-grained opaques, micas, or other pyroxenes (Fig. 12 b). Enclosed crystals of biotite are common within pyroxene crystals (Fig. 12 f). Pyroxene macrocrysts ranged from broken and truncated aggregates (Fig. 11), or coarse cumulophyric clusters radiating out

from a central point. Dissolution features are common in Bull Mountain clinopyroxenes. Resorbed rims of crystals as well as the presence of spongy textured melt pockets are the most common disequilibrium features (Fig. 12 a, b, c). The spongy texture is either pervasive throughout the entire crystal or restricted to the cores of pyroxene crystals.

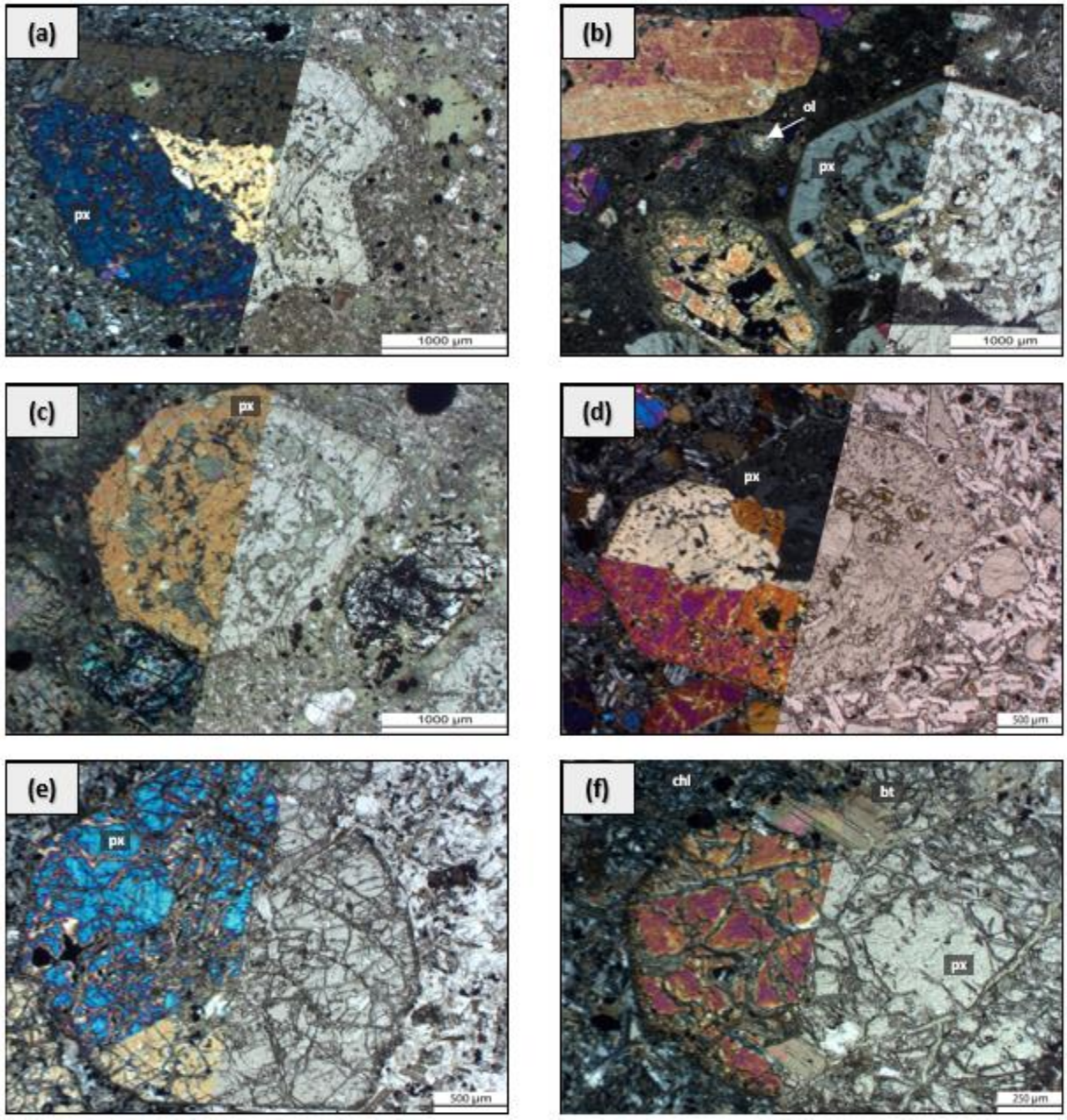

Figure 12: Photomicrographs of the studied samples from the Bull Mountain Range. Cross polarized light (left) and plane polarize light (right). Images show lamprophyre porphyritic texture with large clinopyroxene (px) crystals and variation of dissolution features present. (a) [J03-vogesite] Euhedral shaped arrowhead like crystal with slightly resorbed rim and spongy textured core. Note the presence of enclosed minerals. (b) [J06-vogesite] Section showing twinning and with pervasive spongy texture adjacent to anhedral px crystal surrounded by reaction rim of opaques. (c) [J03-vogesite] Px with melt pockets and enclosed crystals. White anhedral crystal is altered olivine. (d) [J12-minette] Spongy texture concentrated along the rim of the crystal rather than the core. (e) [J09-minette] *Subrounded embayed px without traces of spongy texture, fractures within crystal harbor carbonate infillings. (f) [J10-kersantite] Px crystal with partially and fully enclosed micas. Fractures are filled with chlorite.*

Clinopyroxene from lamprophyric rocks of the Highwood Mountains (Fig. 13) are surprisingly different from those of Bull Mountain. Pyroxene is often porphyritic (extremely coarse up to 2 cm in length to <20 microns in the groundmass) and panidiomorphic (Fig. 13 d). Crystals are frequently euhedral, display more of a variety in the form of spongy texture melt pockets, rich with fine grained apatite inclusions (some leucite was identified as well), and rich with melt or fluid inclusions in concentrically zoned intermediate portions of crystals (Fig 13 f). Crystals are occasionally twinned and very rarely exsolution lamellae were present in a few crystals. Pyroxene crystals are often longer prismatic-rectangular, or tabular shaped. Stubby prisms of pyroxene arranged in glomerophyric star like patterns exist, often radiating and growing out from a central host crystal that contains cores of patchy zonations. Some pyroxene crystals that exhibit concentric zoning have 'parasitic growths' along their margins seemingly fused to the host crystals (Fig 13 b, c). These growths display similar zoning habits and tendencies to the host crystals. Sector zoning is more prevalent of pyroxenes from the Highwood Mountains than other areas from this study. Patchy zoning is common in areas exhibiting spongy texture, while concentric zoning is common in the mantle or intermediate segments of crystals. Spongy textured melt pockets are often abnormally shaped within Highwood Mountain pyroxene crystals forming long worm-like features >1500 um in length (Fig 13 f). Spongy texture is observed aligned all in one direction, as pervasive growths throughout the entire crystal, emplaced within lighter bands of concentric zoning (Fig 13. d) or contained solely to the cores of crystals (Fig 13 b). Partial inclusions of olivine and phlogopite exist within clinopyroxene crystals while pyroxene is often included within phlogopite macrocrysts.

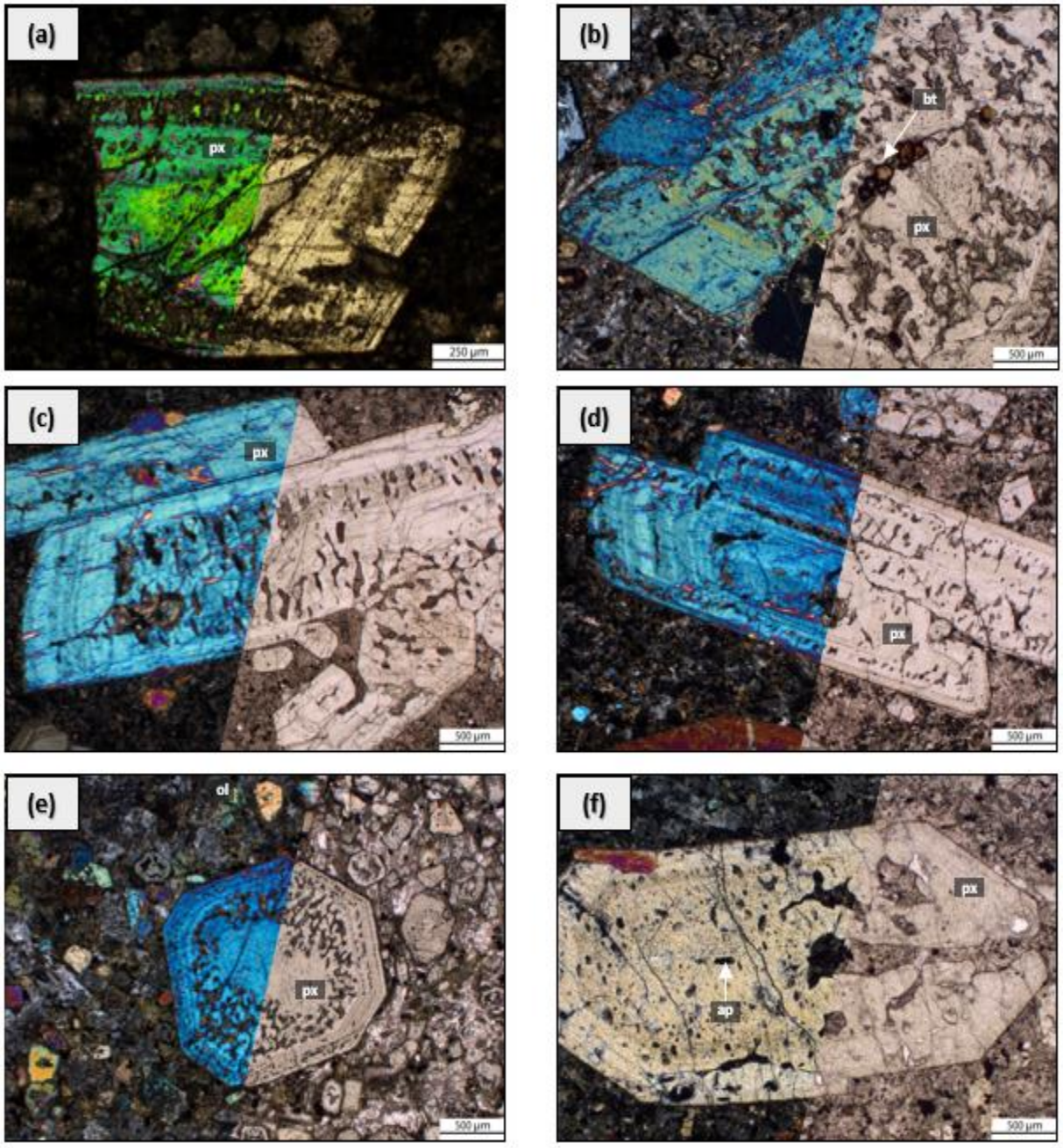

Figure 13: Photomicrographs of the studied samples from the Highwood Mountains. Cross polarized light (left) and plane polarize light (right). Images show lamprophyre porphyritic texture with large clinopyroxene (px) and variation of dissolution features present. (a) [J26-vogesite] Sector zoned truncated px crystal with intense zones of spongy texture near the mantle and rim. (b) [J22-sannaite] Px crystal with spongy textured core with inclusions of micas. (c) [J23B-vogesite] Prism shaped px crystal with melt pockets contained within the core that are aligned in one direction perpendicular to the C-axis. Note spongy texture in the parasitic px growth (d) [J21-vogesite] Prism shaped px crystal with multiple layers of melt pockets contained within higher birefringent zones. (e) [J26-vogesite] Complexly zoned basal px crystal with layered zones of spongy texture. (f) [J23A-vogesite] Px basal crystal full of apatite (ap) inclusions and spongy texture within the core and worm-like elongated melt pocket.

Clinopyroxenes from lamprophyric rocks of the Crazy Mountains (Fig. 14) depict crystals that are strongly resorbed and out of equilibrium with the melt. Crystals are slightly pale green to colorless in thin section and range in size from coarse to fine grained (within the groundmass). Pyroxene can be subhedral to anhedral with resorbed rounded edges of the crystals often hosting longer worm-like spongy texture running the length of the crystal (Fig 14. f). Stubby prisms are more common than long tabular sections of crystals. These stubby prisms are sometimes corroded to the point where ovate shaped pyroxene crystals can be observed. Twinning occurs more frequently in clinopyroxenes from the Crazies compared to the other regions of this study. Another unique feature is that the internal zonations of crystals are commonly rounded and rich with inclusions (Fig. 14 b). The core and intermediate segments of crystals often depict circular and irregular shaped zones of birefringence with spongy texture and patchy zoning (Fig. 14 c). Complexly zoned crystals exist where patchy zonation and repeated, concentrically zoned bands occur separate from one another, but yet within the same crystal. Partially enclosed crystals of olivine, hornblende, and biotite are common within clinopyroxene crystals of the Crazy Mountains (Fig. 14 e). Spongy textured melt pockets are either pervasive throughout the entire crystal (Fig. 14 d), present in the core and rim (Fig. 14 b), or only present in the intermediate/mantle portions of crystals along layers of concentrically banded zones. Where patchy zoning does exist, these areas are commonly more inclusion rich than their concentrically zoned counterparts. Some crystals not exhibiting signs of spongy texture host inclusion rich bands within concentric zones of differing birefringence (Fig. 14 a) The crystals are often “dirtier” in appearance than other pyroxenes from this study, often peppered with inclusions, opaques, or fractures that have been infilled by replacement assemblages. Ovate medium to fine grained pyroxene within the groundmass occasionally displays cores with spongy texture.

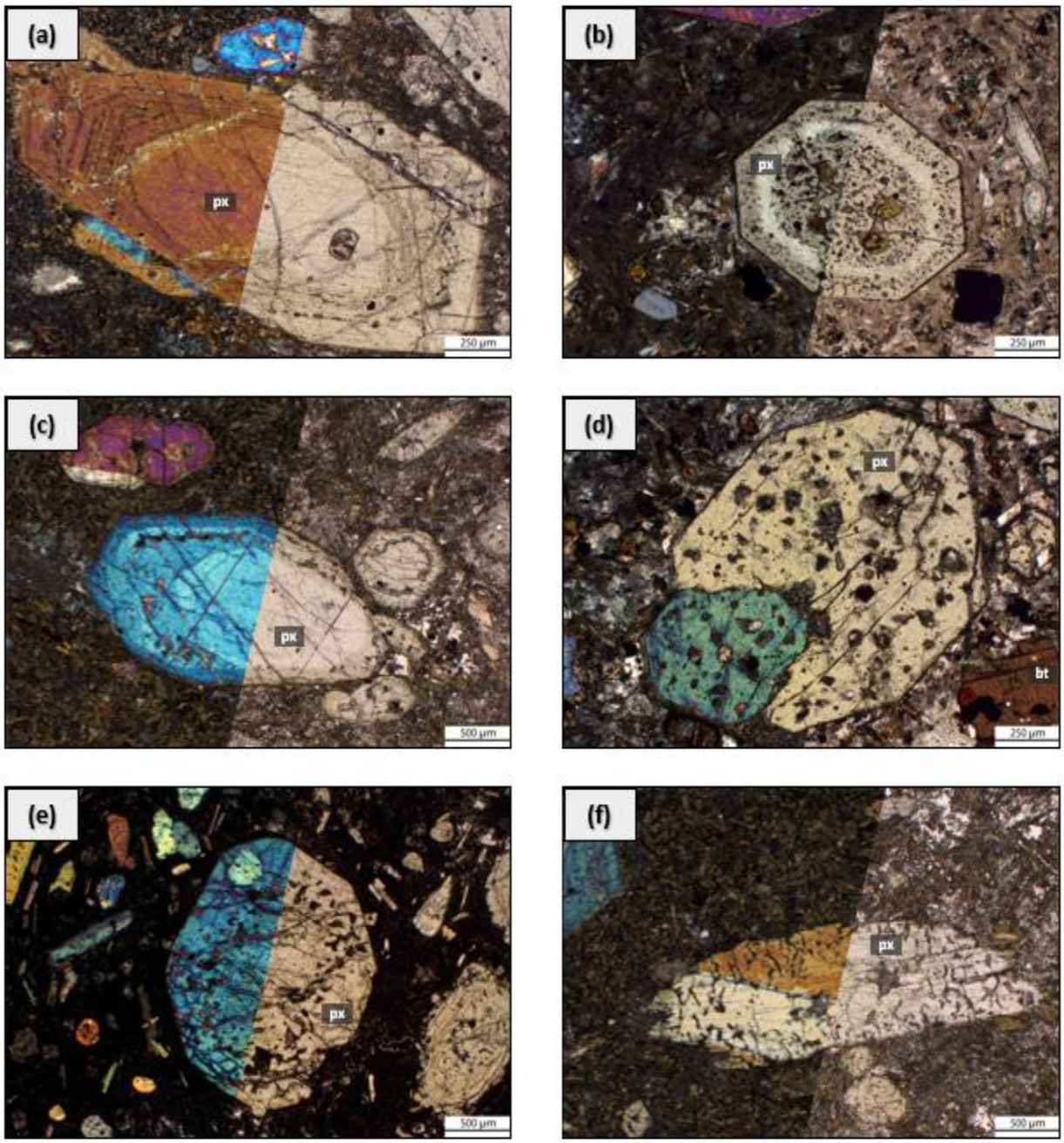

Figure 14: Photomicrographs of the studied samples from the Crazy Mountain Range. Cross polarized light (left) and plane polarize light (right). Images show lamprophyre porphyritic texture with clinopyroxene (px) macrocrysts, and variations of dissolution features present. (a) [J40-monchiquite] Concentrically zoned pyroxene rich with inclusions that follow orientation of zoning. (b) [J43-spessartite] Complexly zoned crystal that displays inclusion rich core with spongy texture in both the core and rim. This Disequilibrium texture is not within lighter colored intermediate portion of the crystal. (c) [J39-monchiquite] Circular and irregular shaped zones of birefringence with spongy texture in the intermediate zone of the crystal. (d) [J38-vogesite] Patchy zoned crystal with pervasive spongy texture. (e) [J32-1-monchiquite] Subhedral megacryst of pyroxene with spongy texture and enclosed crystal of olivine next to anhedral, corroded crystals of pyroxene within the groundmass. (f) [J39-monchiquite] Twinning prism shaped crystal with long connected vermiform shaped spongy texture. Note crystal is anhedral with corroded rims.

The Yogo Dyke lamprophyre contains crystals of pyroxene that are fine (within the groundmass) to coarse grained, subhedral to euhedral, and display spongy textured melt pockets that are more prevalent in the core than the rim of crystals (Figs. 56,57,58,59). There seems to be another population of coarse pyroxene crystal that is also euhedral but does not exhibit signs of spongy texture. These crystals are commonly fractured, overprinted by alteration minerals, corroded, and rimmed by biotite crystals. The coarsest pyroxene crystals are rich with apatite inclusions. Finer grained pyroxenes within the Yogo groundmass also exhibit spongy textured melt pockets.

(4B. ii) Melt Pockets

As previously described, spongy textures (sometimes referred to as spongy, cellular or sieve textured, are common disequilibrium features within pyroxenes from every region of this study. Associated with these spongy phases are fine grained patches of irregularly shaped blebs, termed melt pockets in this study. Within lamprophyric rocks from every region of this study, clinopyroxene is the dominant crystal displaying spongy features but other minerals host pockets (frequency of spongy texture →clinopyroxene>phlogopite>olivine). These melt pockets are host to fine grained mineral assemblages as well as empty void space. These pockets are usually found within the core region of pyroxenes, but they are visible within the outer rim or intermediate zones of these crystals, but to a much lesser extent (Figs. 15, 16). In pockets that are large enough, their phase constituents look similar to the matrix of thin section, but on a much smaller scale, as the majority of pockets are between 10-30 microns in size. Identifying the mineral assemblage within the pocket is a daunting task because of how fine grained the minerals can be.

Glass, apatite, plagioclase, biotite, phlogopite, leucite, pyroxene, sulfides, barite, carbonates, and pyroxene phases were identified during this study within melt pockets by both petrography and microprobe BSE imagery coupled with single spot spectrometer analysis (Fig. 15). In one melt pocket

analyzed within a pyroxene from Golden Sunlight (Fig. 15 a) six different phases coexist within a single pocket, where Fe Cr oxide, titanite, plagioclase, feldspathoids, chlorapatite, and Fe Cu sulfides reside.

The shape of the melt pockets in these lamprophyric rocks is highly variable (Fig. 16). Melt pockets vary from rounded, to more commonly elongate in shape, or chain like features. The melt pockets are often isolated from each other, but in some cases, the melt pockets are connected and networked with adjacent, neighboring pockets forming worm-like vermiform pockets. Melt pockets can be isolated to select compositional concentric bands within the intermediate zones of major mafic phases. At the boundary between the melt pocket and the encompassing pyroxene crystals, the boundary is often gradational with patchy zonation, with clear changes in coloration (and birefringence) viewed in thin section and BSE imaging. In most cases, the surrounding rim of the melt pocket is often lighter in color than the crystal core.

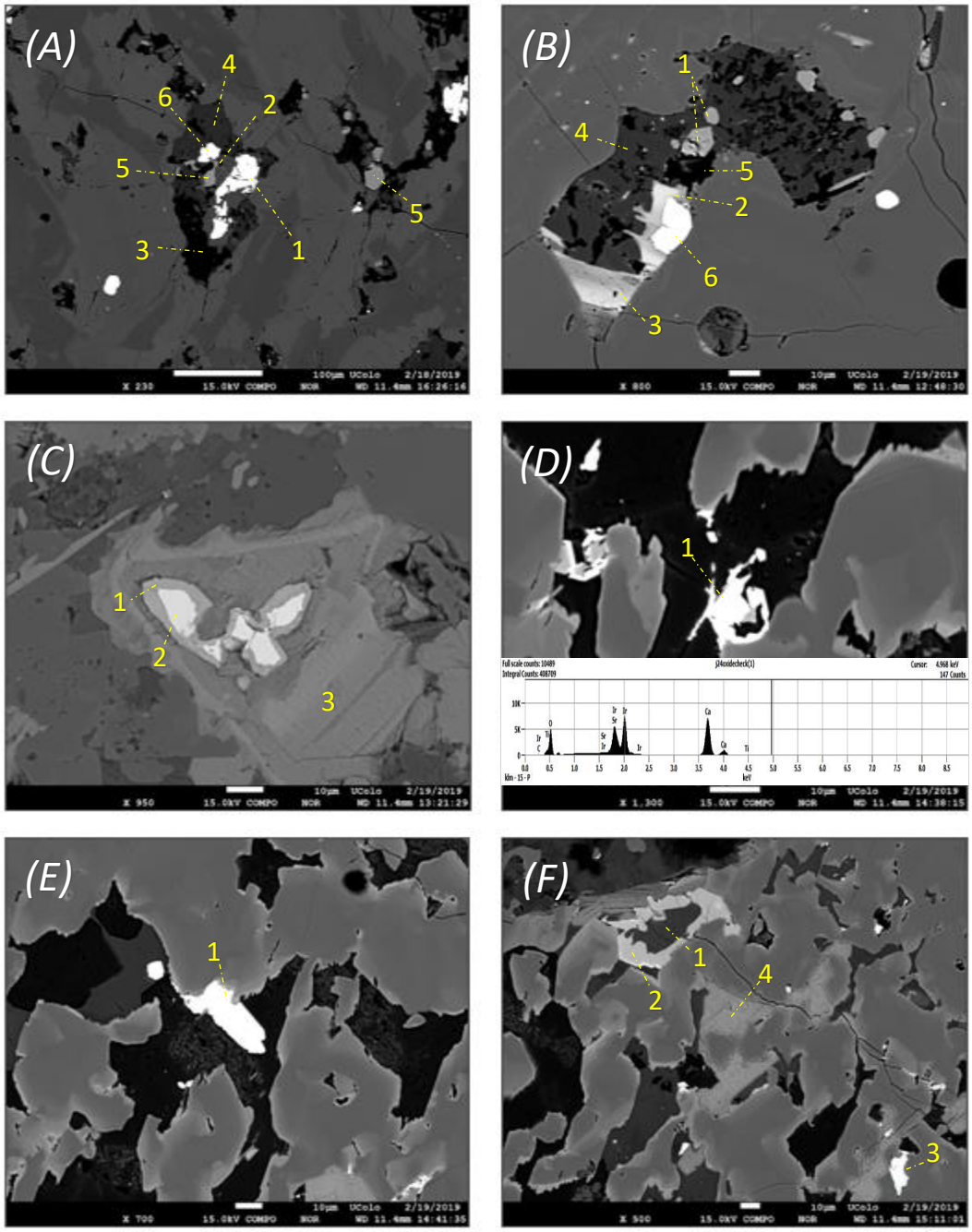

Figure 15: Enhanced BSE images of spongy texture melt pockets contained within clinopyroxene crystals. (a) [J06-vogesite] (b) [J24-Sannaite] (c) [J18-sannaite] (d) [Yogo-ouachitite] along with spectra analysis of phase 1(e) [Yogo-ouachitite] (f) [Yogo-ouachitite]. Key available on table 3. Melt Pocket Phases are as follows: (a) 1=Fe-Cr oxide, 2 =titanite, 3= plagioclase, 4= feldspathoid, 5= chlorapatite, 6= Cu-Fe sulfide; (b) 1= apatite, 2= Ba rich mica, 3= mica, 4= feldspathoid, 5= plagioclase, 6= unknown; (c) 1= Fe-Cu silicate?, 2= Cu-Fe Sulfide, 3= Ba rich mica; (d) 1= Sr-Ir phase; (e) 1= baryte; (f) 1= feldspathoid, 2= carbonate, 3= Ir-Tl phase, 4= mica.

While spongy texture is present in every region of this study, the Highwood, and Crazy Mountain lamprophyric rocks displayed the largest density of pyroxene macrocrysts with this type of disequilibrium feature. A common feature of the melt pockets is alignment and growth perpendicular to pyroxene crystallographic axis' (in an ideal crystal, the [C-axis] represents the longest dimensional plane of that crystal). Note the direction of the C-axis' in Figure 16. Some of these melt pockets are similar to negative crystals, wherein irregular shaped cavities aligned within the structure of the crystal can be filled with fluid, gas, or solid inclusions. Much like other features of lamprophyres, one cannot overlook the degree of randomness in which the melt pockets are shaped, aligned, and located in their host crystals. It is possible that each megacryst while crystallizing in the melt recorded varying stages of melt pocket growth. In extreme cases where melt pockets run through the entirety of the crystal, once the melt pockets are large enough to coalesce together, the grain seems to be caught in the process of disaggregating and breaking down. This is evident in crystals where truncated or corroded sections of pyroxene macrocrysts exist near the greatest density of melt pockets.

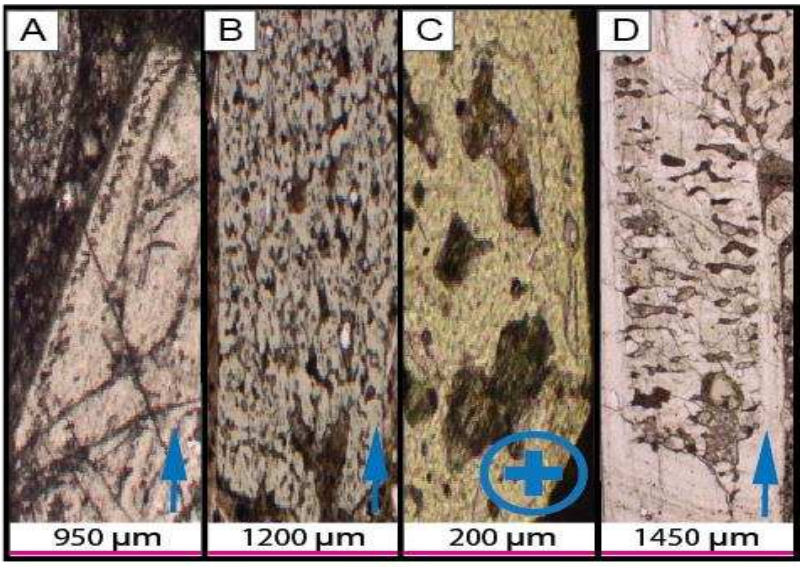

Figure 16: Photomicrographs of melt pocket behaviors within pyroxenes. Note that the blue arrows indicate which direction the crystallographic axis is oriented. (A) irregular melt pockets forming within the outer most rim of the pyroxene. (B) Pervasive spongy textured melt pocket growth from core to rim. (C) Irregularly shaped pockets of unusually large size (up to ~200 microns in length) and the point of view is looking down the C-axis. (D) Vermiform or 'worm-like' spongy texture confined to the core, most pockets are aligned perpendicular to the C-axis.

(4B. iii) Phlogopite/Biotite

The presence of micas (phlogopite/biotite) is characteristically what gave lamprophyres their 'glistening porphyry' etymology. Pyroxenes were the main target of this study with regards to mineral chemistry, thus, in order to find the exact composition of the micas within this study to differentiate between phlogopite and biotite, additional mineral chemical studies are needed. The names phlogopite and biotite will hence be used interchangeably, and both refer to the porphyritic (sometimes idiomorphic) and groundmass micas found within lamprophyric rocks from this study. The size of micas ranged from 1-2 cm to <20 micron very fine-grained sized groundmass crystals. Figures 18 and 19 depict the habits, zonations, and dissolution features present in micas from this study.

Color of micas ranged from dark reddish-brown, to tan, to colorless. In thin section these micas were identified by their micaceous or tabular crystal habit, characteristic mottled birds eye extinction, strong pleochroism, and 3rd to 4th order interference colors. Zoning was common of micas from each field area. Rock (1991) describes characteristic zonation within phlogopite phenocrysts as having pale yellow cores and transitioning to a reddish-brown pleochroic rim. As one would expect, higher Fe and Ti, and lower Mg values exist within the darker redder rims as recognized by absorption spectra. The rims within other lamprophyric phlogopite also commonly display elevated Mn, Ba, REE, Ni, Cr, and F. Micas from the Yogo dyke lamprophyre follow this trend of Ba enrichment along the rims (Fig. 17), unfortunately micas from other regions were not analyzed.

Yogo Dyke micas exhibit a darker colored inner core with an anhedral zonal interface and a lighter colored outer rim (Fig. 17 & Fig. 18 a). Some of the micas within the groundmass are zoned in a similar manner but the majority of crystals lack zonations. Micas within the Yogo displayed deformation characteristics such as kinking or bending. Reaction rims of biotite and opaques enshrouding the periphery of pyroxene crystals is common and chloritization of biotite and phlogopite crystals exists.

Bull Mountain micas (Fig. 18 b, d, e, and f) commonly exhibit a lighter colored inner core and a darker colored rim, as is typical with lamprophyres, some crystals contradict this and contain dark cores and lighter rims. Dissolution features such as anhedral zonal interface rounding of the cores, resorption along the edges of crystals (Fig. 18 b), as well as rounding of micas are common. Glomerophyric (clustering of crystals into aggregates or crystal clots) structures are common with micas enshrouding pyroxene or presumably altered olivine (Fig. 18 e). Micas associated with these structures are commonly rounded and have irregular internal zonations. Bent and kinked micas are present (Fig. 18 a, f) and birefringence differs along kinked segments of crystals.

Phlogopites from the lamprophyric rocks of the Highwood Mountains display a wide range of textural and dissolution features (Fig. 19). Both macrocrysts and finer grained micas within the groundmass exhibit bent features with birefringence differing along stressed areas of the crystals (Fig. 19 b). There are large extremely coarse, porphyritic, and idiomorphic crystals of micas which display no signs of disequilibrium textures (Fig. 19 d) and there are others that are strongly resorbed, often displaying rounded rims (Fig. 19 e). Glomerophyric masses of crystals are present with biotite enshrouding pyroxene which is then being replaced by leucite (Fig. 19 c). Enclosed crystals of olivine, pyroxene, and clinozoisite (?) are found within tabular porphyritic crystals of biotite (Fig. 19 d). Inclusions or pockets of minerals within the encapsulating mica often display a fine-grained darkened overgrowth rim. Groundmass crystals within the Highwood lamprophyres are often redder (more Fe and Ti rich) than the coarser, porphyritic micas (Fig. 19 f).

Compared to the other regions of this study, the coarse crystals of pyroxene observed from the Crazies show the greatest propensity for dissolution features (Fig. 20). Populations of phlogopites display dark rounded cores with lighter rims (Fig. 20 a), lighter cores with darker rims (Fig. 20 b), or light cores with reddish brown Ti-Fe rich rims (Fig. 18 c). Glomerophyric radiating clusters of biotite are common (Fig. 20 c) often with inclusions of pyroxene and feldspathoid at the center. Partially and fully

enclosed crystals of olivine are visible within anhedral resorbed crystals of biotite (Fig. 20 a). Much like the pyroxenes from this region, the biotite is often “dirtier” than that from other regions and is full of inclusions, altered chloritized segments, and spongy textured melt pockets. In some uncommon occurrences of tabular sub-anhedral biotites there exists complete replacement of biotite by an unidentified phase intimately interlayered with the original crystal (Fig. 20 b). Similar to micas of the Highwoods, both coarse and groundmass scale micas can be bent. Thin acicular blades of mica are commonly bent within the groundmass.

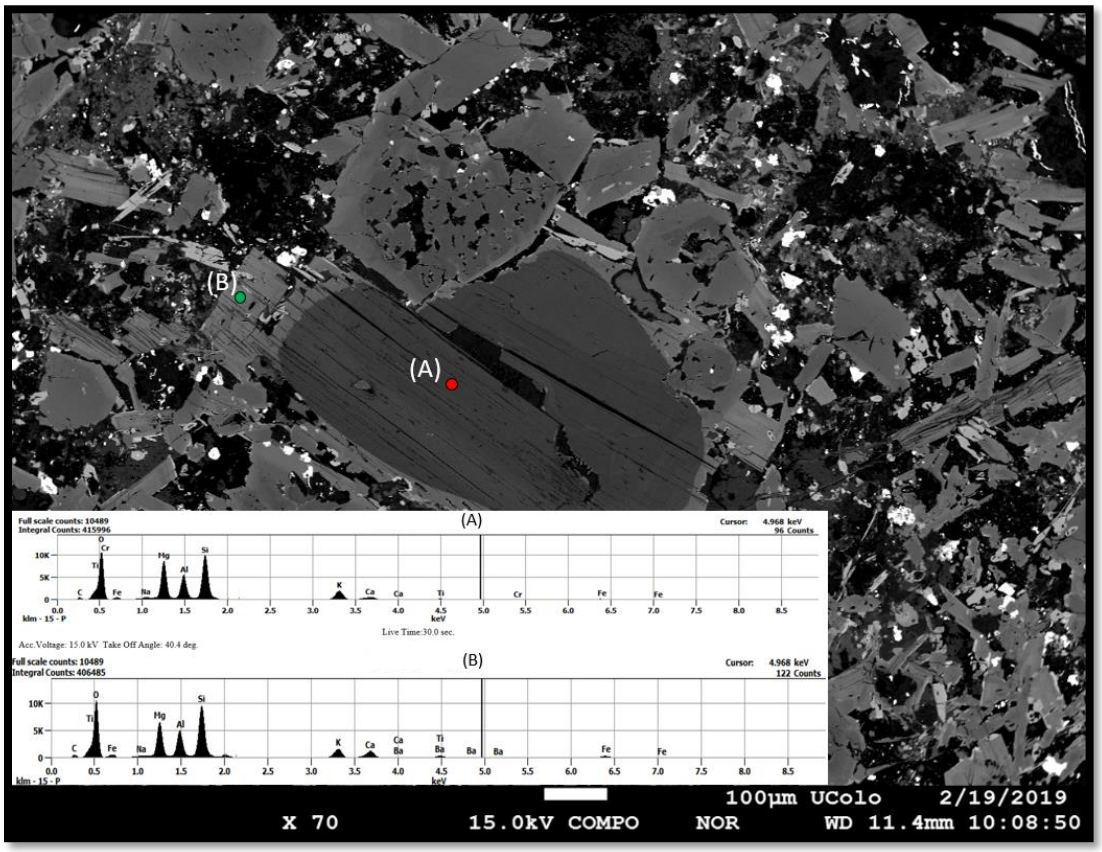

Figure 17: Yogo Dyke Phlogopite BSE with Ba Signature. Centered in this BSE is a partially corroded phlogopite crystal exhibiting rounding of the darker inner core. Point (A), represented in red, corresponds to Kev graph (A), while point (B), represented in green, corresponds to Kev graph (B). Note that Ba spikes on point B and the lighter colored outer rim, and there is a slight Cr spike in the inner core at point A.

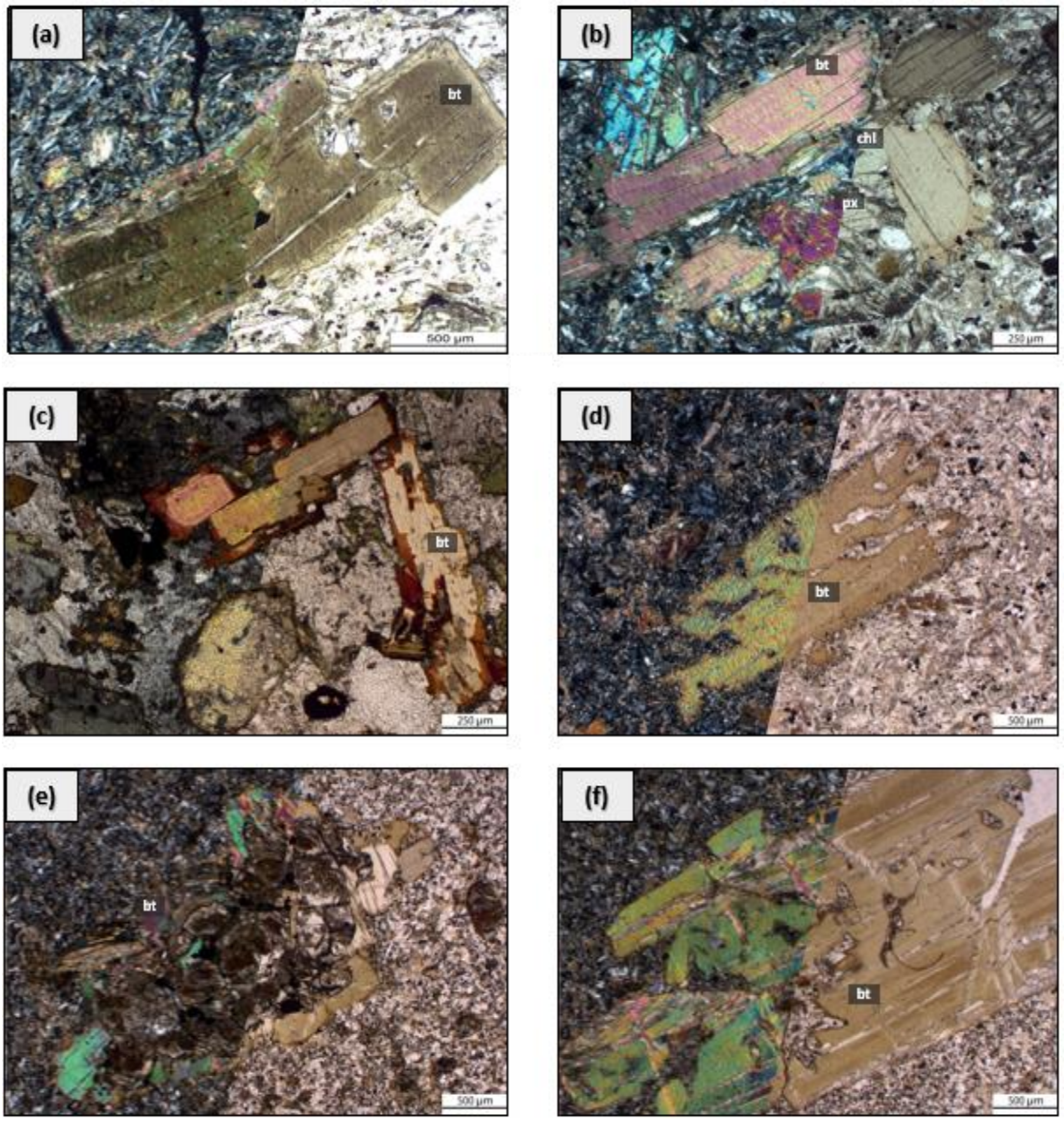

Figure 18: Photomicrographs of the studied samples from the Bull Mountain Range (b, d, e, f), Yogo Lamprophyre Dyke (a), and the Crazy Mountains (c). Cross polarized light (left) and plane polarize light (right). Images show lamprophyre porphyritic texture with large biotite/phlogopite micas (bt) and the variation of dissolution features present. (a) [Yogo-ouachitite] Bent tabular section with a rounded dark colored core and lighter rim. (b) [J10-kersantite] Common glomerophyric texture where pyroxene, biotite, and other minerals are clustered together. Mica displays lighter colored, rounded core with darker colored rims. (c) [J32-C-vogesite] Light colored rim with Fe Ti rich darker colored core. (d) [J10-1-kersantite] Tabular section with opaque reaction rim and resorbed edges/interior. (e) [J13-minette] Glomerophyric cluster of crystals with completely replaced and altered basal shaped crystals on inside with bt rich rim. (f) [J13-minette] Irregularly zoned mica megacryst with kinked zones of differing birefringence.

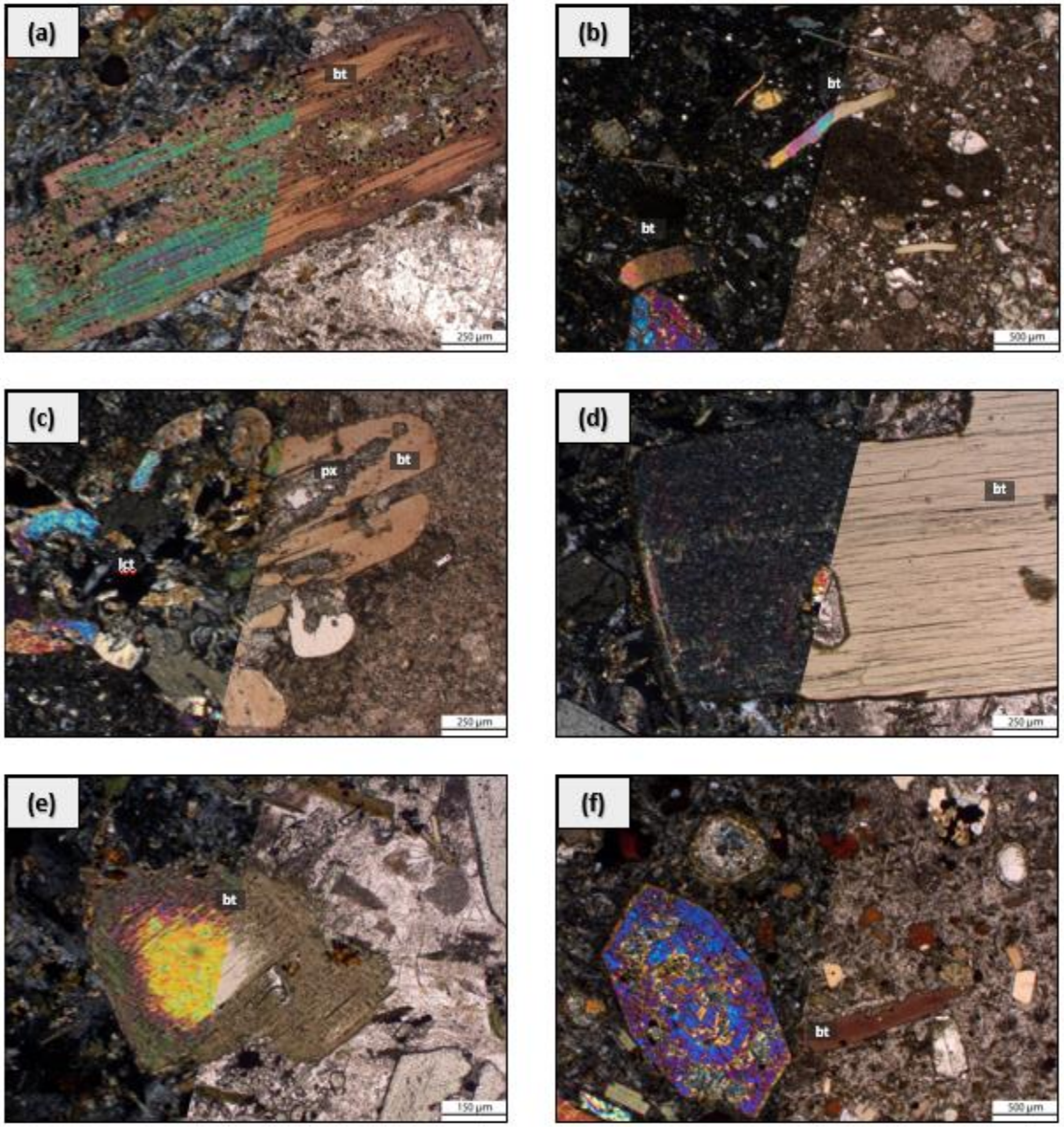

Figure 19: Photomicrographs of the studied samples from the Highwood Mountains. Cross polarized light (left) and plane polarize light (right). Images show lamprophyre porphyritic texture with large biotite/phlogopite micas (bt) and variation of dissolution features present. (a) [J25-vogesite] Euhedral, tabular section rich with opaque inclusions and melt pockets. Inner core zones are lighter in color whereas the rims are darker. (b) [J20-minette] Porphyritic micas that are bent. Bent and kinked micas also exist within the groundmass. (c) [J19-minette] Strange glomerophyric cluster of replacement occurring with rounded biotite on rim, grading into pyroxenes, and the innermost portion is composed of leucite. (d) [J17-vogesite] Large enclosure of crystals within tabular mica megacryst absent of melt pockets. (e) [J17-vogesite] Completely corroded, rounded, and resorbed embayed mica. (f) [J24-sannaite] Dark Fe-rich biotite with other micas in groundmass.

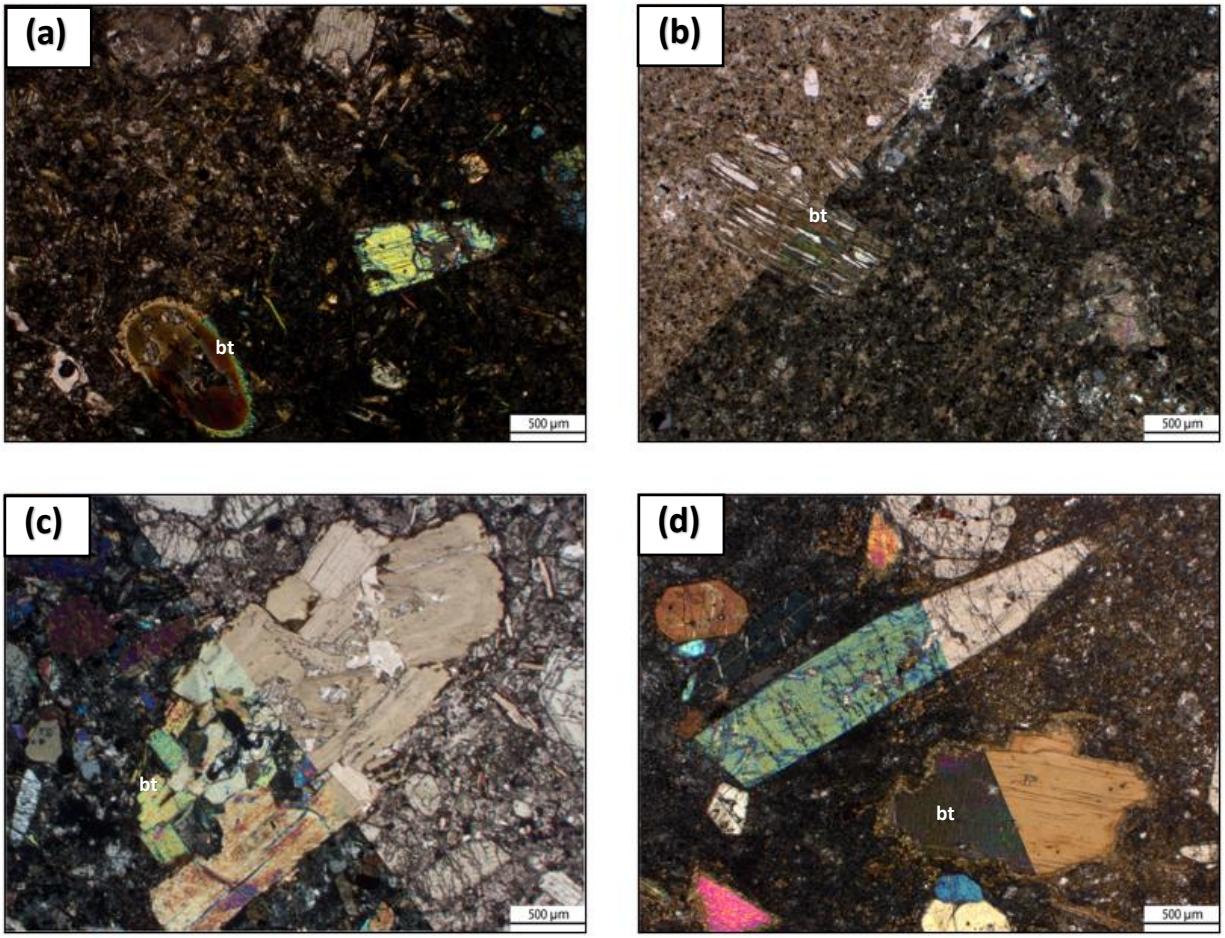

Figure 20: Photomicrographs of the studied samples from the Crazy Mountains. Cross polarized light and plane polarize light. Images show lamprophyre porphyritic texture with large biotite/phlogopite micas (bt) and variation of dissolution features present. (a) [J39-1-monchiquite] Resorbed bt crystal with dark inner core hosting enclosed olivine spongy texture and a lighter rim. Groundmass micas are slightly bent. (b) [J40-monchiqute] bt crystal being replaced by an unidentified phase. Carbonate blebs also present. (C) [J36-sannaite] bt cumulophyric cluster enclosing pyroxene. (d) [J32-2-monchiqute] bt crystal with darker outer core and resorbed margins.

(4B. iv) Olivine

Olivine is a common mafic phase of lamprophyric rocks from this study. Olivine is highly susceptible to weathering and alteration (hydrothermal and metasomatic), thus finding fresh, unaltered olivine was rather difficult (especially in the field!). In thin section olivine was identified by second order and higher interference colors, lack of cleavage, distinctive fracturing pattern, and affinity for intense alteration (Fig. 21 b, Fig. 12 c). Where completely altered, iddingstite, white micas (possibly talc?), chlorite, oxides-opaques, serpentine, and carbonate were identified as replacement assemblages (Fig. 21 b).

Reaction rims are common on olivine from every region of this study. Reaction rims ranged from: (1) biotite only rim, (2) pyroxene → opaques → white micas, and (3) opaque only rim. When biotite is rimming the olivine in a reaction rim, the biotite is commonly brownish red rather than pale in color (Fig. 21 a). Olivine ranges in size from 1cm to groundmass sized fragments of <25 microns. Partial inclusions of olivine within pyroxene and biotite exist (Fig. 12 f). Completely altered olivines are readily identifiable by complex assemblages of alteration minerals inside a typical granular, pseudo-hexagonal shaped shell of opaques. In some cases, the original idiomorphic olivine structure remains even though olivine may be pervasively altered.

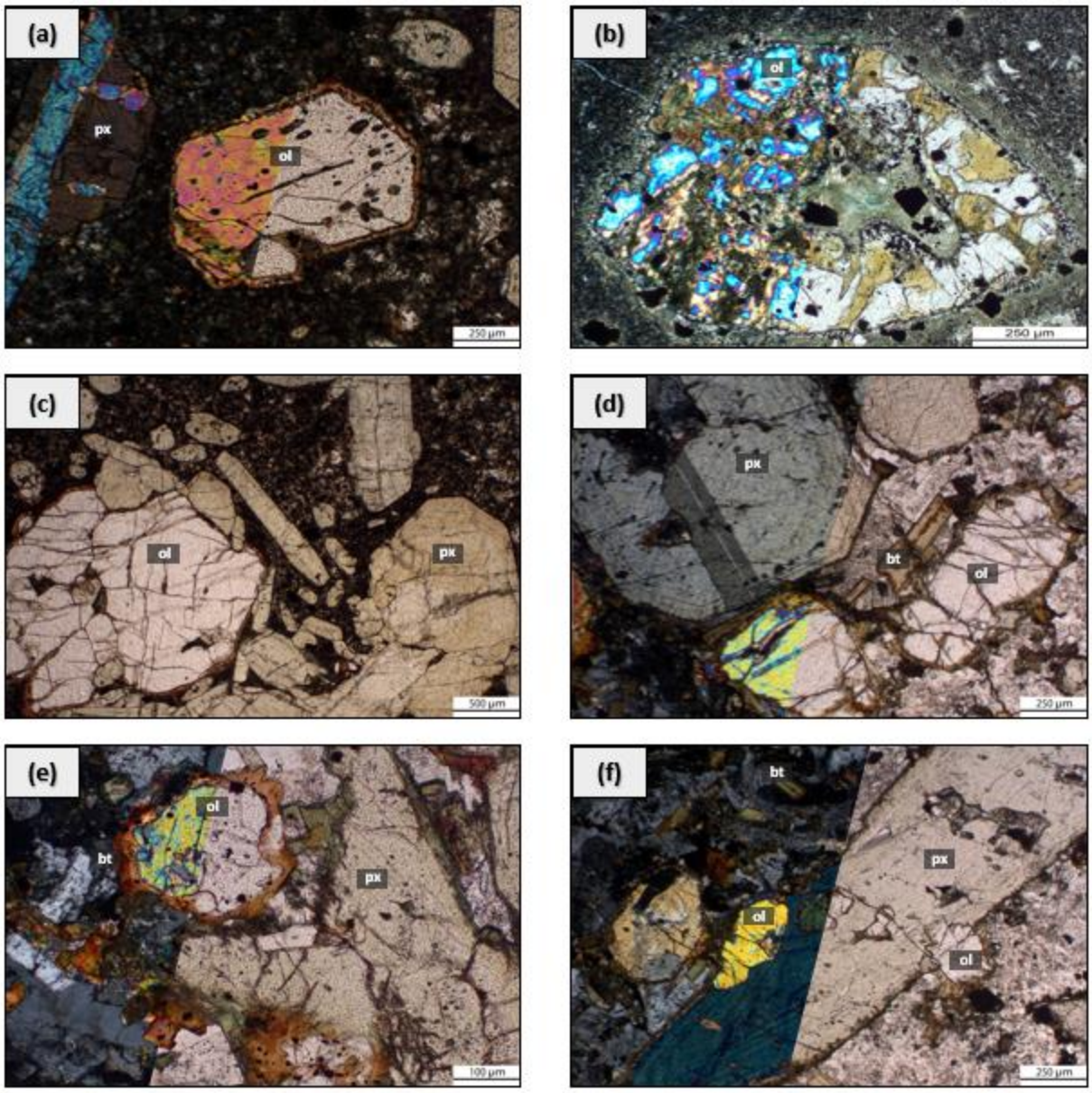

Figure 21: Photomicrographs of olivine (ol) from porphyritic lamprophyric rocks of this study. Cross polarized light (left) and plane polarize light (right). (a) [J33-1-monchiquite; Crazy Mtn.] ol tabular crystal rich with red-brown colored biotite reaction rim. (b) [J06-vogesite; Bull Mtn.] ol caught in process of alteration and replacement with fine grained opaque, pyroxene, and white mica reaction rim. (c) [J33-1-monchiquite; Crazy Mtn.] Coarse intergrowth of ol and pyroxenes. (d) [J18-sannaite; Highwood Mtns.] Classical fractured ol rimmed by zoned micas. Two crystals of ol intergrown together. (e) [J15-spessartite; Highwood Mtns.] ol habit within the groundmass is commonly displays red-brown biotite rim. (f) [J18-sannaite; Highwood Mtns.] ol crystals enclosed within coarse pyroxene crystal.

(4B. v) Ocelli

A notable characteristic of lamprophyric rocks is the presence of leucocratic, globular, spherical structures termed ocelli. Other names synonymous with ocelli in lamprophyre literature include: amygdules, patches, varioles, globules, ovoids, and schlieren; these structures are reported in roughly 40% of lamprophyre descriptions (Rock, 1987, 1991). These large structures (~10 mm in select samples) were identified by their round and elliptical outline, as well as their distinctly different coloration of minerals within plane polarized light when compared to the groundmass (Fig. 22 c). Ocelli occasionally show internal zonation (Fig. 22 a) of minerals from the margins to the center of the ocelli. Two types of ocelli were identified during this study, (1) a quartz, calcite, pyroxene, and epidote assemblage (Fig. 22 a), and the other a (2) dirty calcite (possibly Fe bearing) and chlorite rich assemblage (Fig. 22 b).

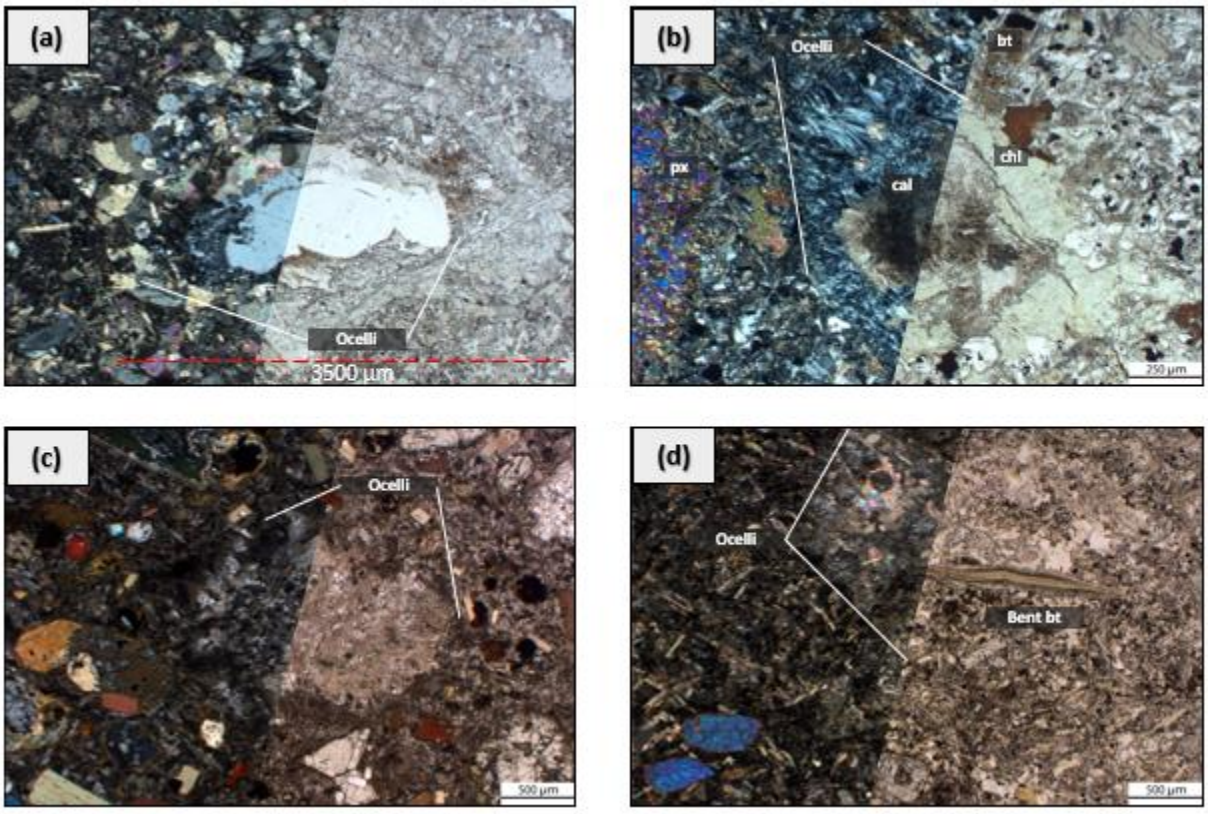

Figure 22: Ocelli within lamprophyric rocks of this study. Cross polarized light (left) and plane polarize light (right). (a) [Yogo-ouachitite] Quartz, calcite, pyroxene ocelli. The quartz grain exhibits undulose extinction. (b) [J10-kersantite; Bull Mtn.] Dirty calcite and chlorite ocelli. (c) [J25-vogesite; Highwood Mtns.] A fine grained internally zoned globular ocelli within glassy matrix. (d) [J33-2-monchiquite; Crazy Mtn.] A more elongate shaped carbonate bearing ocelli that has a bent phlogopite grains along its margin.

(4B. vi) Xenoliths/ Mafic Enclaves

Figure 23 depicts presumed xenoliths that are not of similar mineralogy to the macrocrysts which are the focus of this study. For example, some of these aggregates contain epidote (Fig. 23 b), coarse quartz or carbonate (Fig. 23 a), or abundant hornblende clusters residing within leucocratic coarse blebs (Fig. 23 c). There is a distinct color variation between these features and the hypocrystalline groundmass of the lamprophyric rocks of this study from the Crazies (Fig. 23 e). The margins of the xenoliths do not commonly display corrosion. Felsic and mafic components of xenoliths were identified. While amphiboles were identified in some of the lamprophyric rocks (more common in Crazies), none were as coarse as the hornblendes found within presumed mafic enclaves. These enclaves were irregularly shaped and contained micas, hornblende, and what looks to be altered olivines or some other mafic phase (Fig. 23 e).

A strange feature observed in one thin section (J27-vogesite) is a sharp boundary between the groundmass of one magma and what is presumed to be another of similar composition (Fig. 23 d). The left side of the image depicts a hypocrystalline glassy, darker groundmass with a coarse grained, idiomorphic pyroxene exhibiting spongy texture right in contact with a definite kink or S shaped bend separating two distinct groundmass populations. The other side displays pyroxenes which do not show signs of cored spongy texture and displays rounded crystal margins.

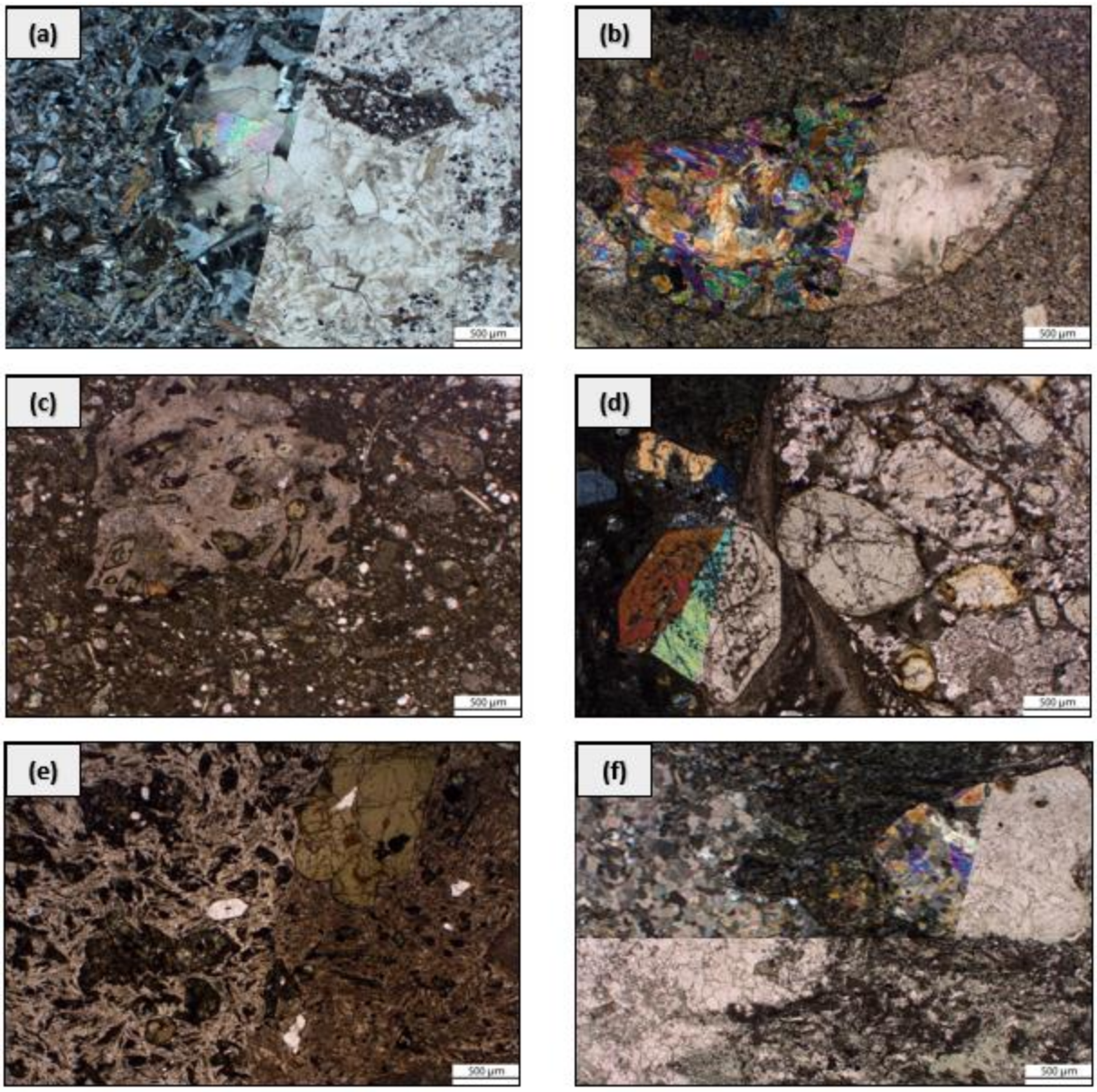

Figure 23: Xenolithic fragments and mafic enclaves found within lamprophyres from this study. (a) [J09-1-minette; Bull Mtn.] A coarse carbonate, replaced olivine, plagioclase, and quartz bearing xenolith. (b) [J11-kersantite; Bull Mtn.] An epidote and chlorite bearing xenolith. (c) [J20-minette; Highwood Mtns.] Hornblende bearing xenolith. Note the difference between this feature and the hypocrystalline groundmass common to lamprophyric rocks of this study. (d) [J27-vogesite; Highwood Mtns.] A bizarre S shaped sharp contact separating two distinct groundmasses and mineral assemblages. One is full of a glassy darker matrix and the other hosts an alkali feldspar dominated groundmass. Note that spongy texture exists in pyroxenes to the left of the contact but not the right. (e) [J35-monchiquite; Crazy Mtn.] A presumed mafic enclave with hornblende and biotite crystals. (f) [J45-minette] Two xenoliths next to each other, one is pyroxene/epidote bearing and the other is composed of equigranular carbonates.

(4B vii). Accessory Minerals

Accessory minerals encountered as inclusions in macrocrysts or within the groundmass include leucite, titanite, apatite, zeolite, magnetite, chromite, sulfides, glass, and clinozoisite. Glass of the groundmass was found crystalized into chlorite and other white micas/secondary products that are nigh indistinguishable when using a petrographic microscope. Apatite is the most common accessory mineral from every region of this study from Bull Mountain, the Highwoods, the Crazies, and the Yogo Dyke lamprophyre. Apatite is observed as low birefringent hexagonal prisms or elongate acicular needles with high relief. Acicular needles of apatite are common inclusions in the innermost cores of clinopyroxenes that display complex zonations. Clinopyroxenes that experienced pervasive spongy textured melt pocket growth and patchy zoning patterns, are rich with apatite inclusions from core to rim.

Major mineral accessory phases within the Yogo lamprophyre include phlogopite, clinopyroxene with analcime, nepheline, calcite, magnetite, apatite, zircon, pyrite, zeolites, corundum, and spinel (Dahy, 1988; Palke et al., 2016). Clinopyroxene and biotite constitute approximately 50 and 20 percent of the modal percentage of the lamprophyre, respectively (Claybaugh, 1952). Within the lamprophyre, the dominant phases are subhedral set in a finer groundmass of predominately mica, clinopyroxene, titaniferous magnetite, chlorite, calcite, serpentine, analcime, feldspathoids, and K-rich feldspars (Meyer & Mitchell, 1988).

(4C) Central-Montana Alkalic Province Lamprophyre Geochemical Signatures

Pyroxene mineral chemistry and its variations within lamprophyric rocks of the CMAP was the focus of this study. Due to financial restraints, whole rock geochemical analysis of lamprophyric rocks from this study was unattainable, but fortunately, other works within the CMAP have recorded whole rock geochemical data on select lamprophyres. The following authors published whole rock geochemical and/or trace element data on lamprophyres from the CMAP; Golden Sunlight and Bull Mountain (De Witt et al. 1996), Highwood Mountains (Henderson et al., 2012; O'Brien et al., 1991; O'Brien et al.,

1995), Crazy mountains (Dudas, 1991), and the Yogo Dyke (Gauthier, 1995). Their data was used when constructing the diagrams below (Figs. 24, 25, and 26) and pyroxene barometry in Section 7D. vi.

(4C. i) Total Akali-Silica Diagram

The Total-Alkalis-Silica diagram of lamprophyres from the CMAP is plotted on Figure 24. Any calk-alkaline to alkaline whole rock geochemical data that matched with Rock's (1991) classification scheme was used in the diagram. Bull Mountain and Golden Sunlight lamprophyres, represented in red, plot outside of the basalt fields and should be classified as foidites. Golden Sunlight lamprophyres are clearly low silica as their silica content is less than 45 percent. The Highwood lamprophyres, represented in green, are richer in Na_2O and K_2O content plotting between 6 to 8 percent, falling in the basanite/tephrite, trachybasalt, phonotephrite, and trachyandesite fields. One lamprophyre from the Highwoods is low silica (~42% SiO_2) while the others are more basic to intermediate. Much like the Highwood lamprophyres, the Crazy Mountain lamprophyres are more sodic and potassic than the Bull Mountain lamprophyres, ranging from 4 to 12 percent Na2O + K2O. The lamprophyres from the Crazies, represented in yellow, are more of basaltic composition plotting within the basalt, trachybasalt, basanite/tephrite, phonotephrite, and even the foidite fields. The Yogo Dyke lamprophyre samples range from ~2 to 6 percent Na2O + K2O and their silica content plots in ultrabasic and basic basaltic composition. Yogo samples plot within the basanite/tephrite, basalt, trachybasalt, basaltic trachyandesite, and the basaltic andesite fields. When comparing the CMAP lamprophyre data on Figure 23 to Rock's (1991) TAS diagrams, they align with the alkaline and calk-alkaline fields of lamprophyre.

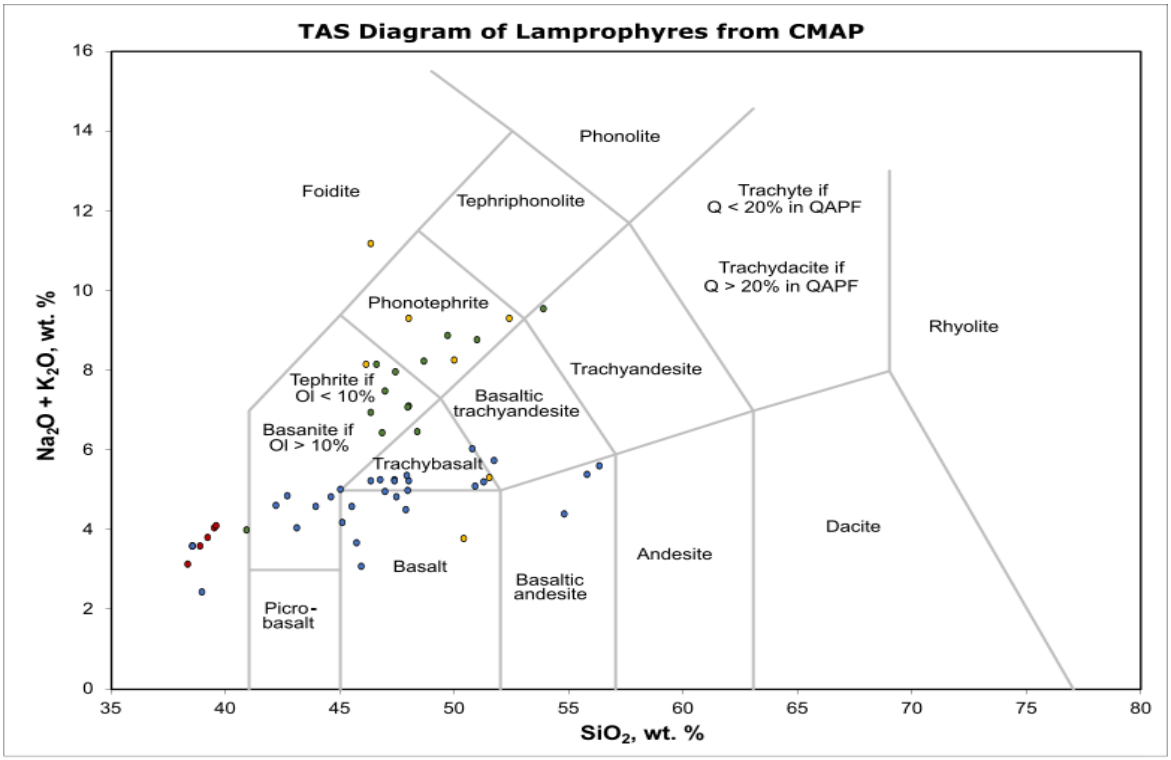

Figure 24: Total-Alkalis-Silica Diagram of Lamprophyres from the CMAP. The chemical classification and proper nomenclature of volcanic rocks from the CMAP. Note that correcting for volatile content in lamprophyres would alter datum positions by a few percentages. Red = Bull Mountain/Golden Sunlight, Green = Highwood Mountain, Yellow = Crazy Mountain, Blue = Yogo Dyke. Note that Q = quartz and Ol = olivine. Data from De Witt et al. 1996; Dudas, 1991; Gauthier, 1995; Henderson et al., 2012; O'Brien et al., 1991, O'Brien et al., 1995.

(4C. ii) MORB Normalized Spider Diagram

The trace element data available from lamprophyres of each region of the CMAP were collected and normalized against mid ocean ridge basaltic composition (MORB) for comparison on a spider diagram (Fig. 25). This particular MORB normalized spider diagram is slightly augmented with the loss of Thalium (not enough data collected) and the addition of Sc, Cr, and Ni after Rock (1991). Note that some trace element data is unavailable which is why there are breaks in data plots, with Golden Sunlight lamprophyres being the worst offender of this. LIL elements (Sr, K, Rb, Ba) may be mobilized by hydrous phases, the HFS elements (Th, Nb, Ce, P, Zr, Hf, Sm, Ti, Y, Yb) are more likely to be controlled by source region and mineral/melt fractionation during magma evolution (Rollinson, 2013; Winter, 2010). In ideal cases of partial melting from a mantle source, the spidergram plots should peak at Rb and Ba and

progressively decrease in slope towards the HFS elements, but this is not the case, likely indicating a more complex genetic history of these lamprophyres. Compared to alkali basalt, lamprophyres from the Highwoods, Crazies, and Yogo have similar Ba enrichment levels. Lamprophyres from Golden Sunlight plot noticeably lower than lamprophyres from other locations in regard to Ba enrichment. High Ba and Rb may reflect metasomatism (hydrous phases) or contamination by a crustal component. Yogo and Crazy lamprophyres display similar levels of Nb enrichment, while Highwood lamprophyres are identical to akali basalt, but in Golden Sunlight lamprophyres, Nb does not follow this trend plotting significantly lower than all other locations. This Nb anomaly is likely a signature of magmatism caused by convergent regimes (i.e., the subduction of the Farallon plate). Ce enrichment levels behave similarly to Nb across lamprophyres from all locations. When compared to typical alkali-basalt all lamprophyres from this study plot lower in regard to Zr enrichment. This Zr trough could imply a primitive source of the magmas. The Y anomaly present in the Crazies could represent partitioning of amphibole or apatite. Disparity exists between the Crazy Mountains lamprophyres and the other lamprophyre locations with regards to Cr and Ni enrichment, with the Crazies plotting significantly lower than the others. Sc, Cr, and Ni concentrations likely indicate pyroxene fractionation. Rocks displaying similar peaks and troughs from same province suggests a common parent, process, or contaminant (Winter, 2010).

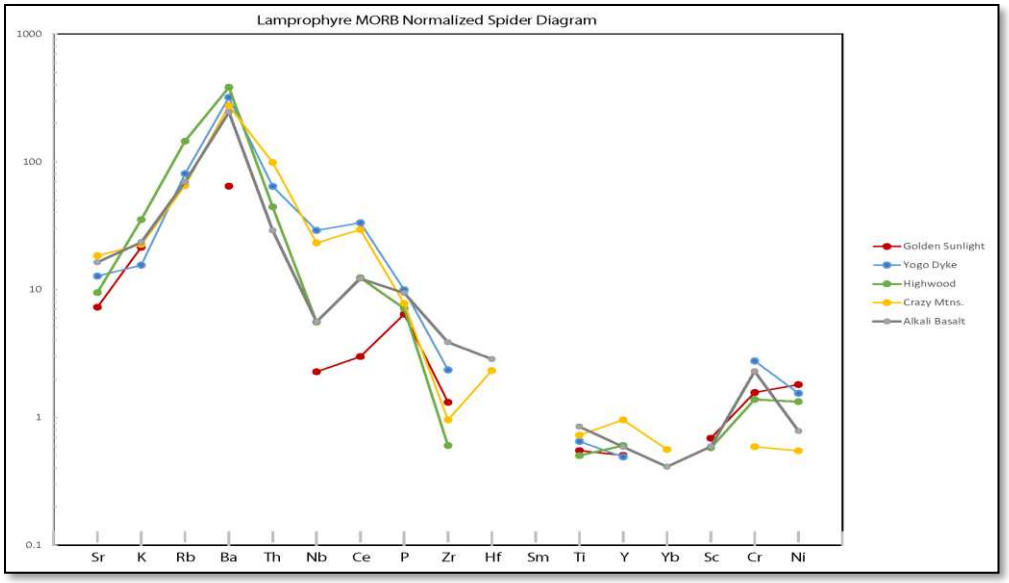

Figure 25: Lamprophyre MORB Normalized Spider Diagram from CMAP. Data from De Witt et al. 1996; Gauthier, 1995; Henderson et al., 2012; O'Brien et al., 1995; O'Brien et al., 1991; Dudas, 1991; Pearce, 1983; and Bevins et al., 1984.

(4C. iii) Harker Variation Diagrams

Variation diagrams (Harker Diagrams) are useful when determining what geochemical processes have influenced a suite of igneous rocks. Lamprophyric rocks from Bull Mountain (Golden Sunlight), the Highwoods, the Crazies, and Yogo Dyke are juxtaposed against a typical alkali basalt of Kalauea, Hawaii (from Richter and Moore, 1966) (Fig. 26). As the magma evolves fractional crystallization occurs which creates fractionation or mixing trends on SiO_2 Harker diagrams. These trends are visible on Figure 26 by the grey data points and the solid black trend (fractionation) line. Lamprophyric suites from every region of this study do not display simple or curved fractionation patterns on any of the Harker variation diagrams (Al_2O_3, TiO_2, CaO, FeOT, Mg#, MgO, P_2O, and K_2O). This alludes to a more complex history for the lamprophyric suites that cannot simply be explained by fractional crystallization.

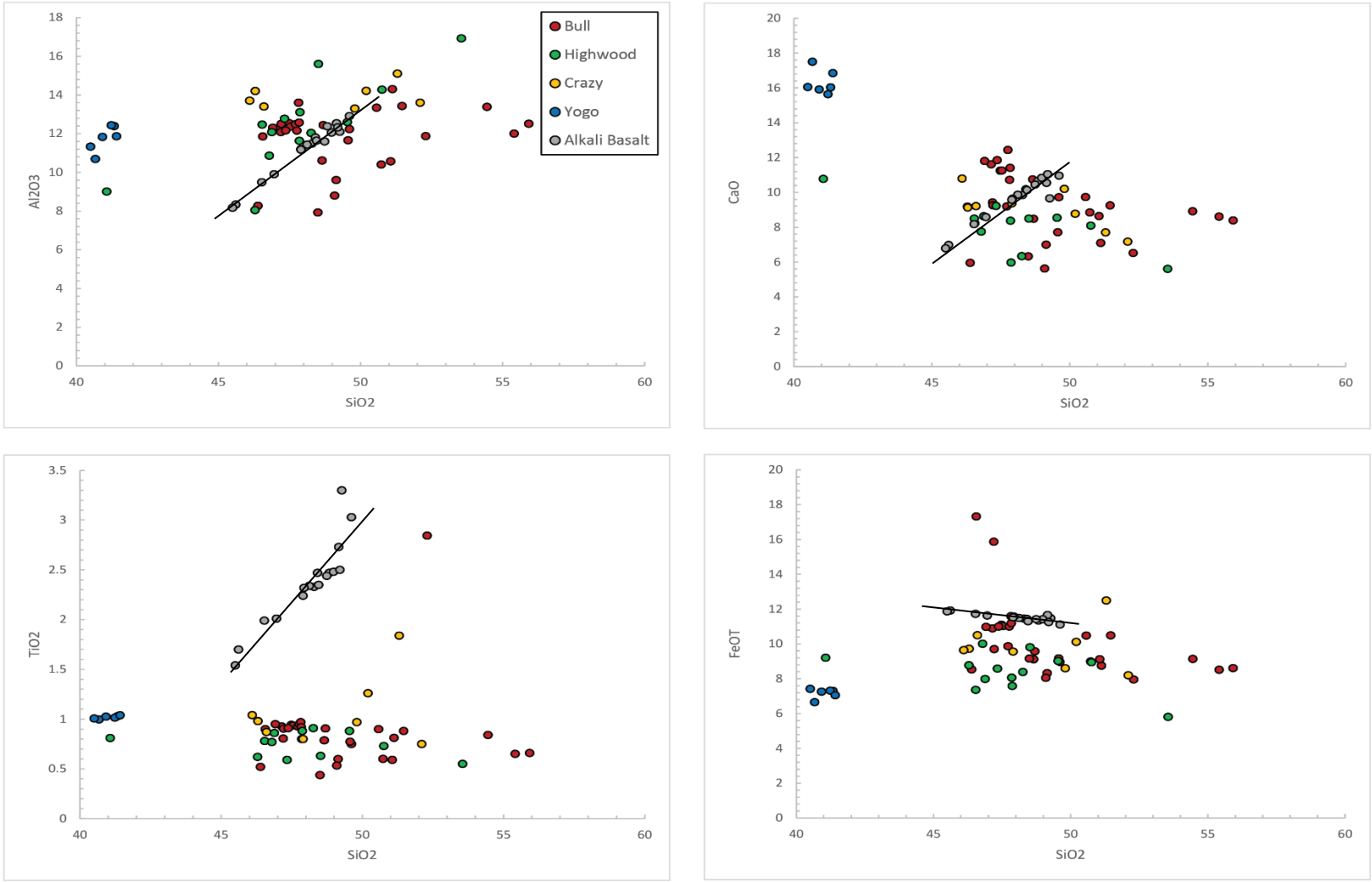

Figure 26: Harker Diagrams of Al2O3, TiO2, CaO, and FeOT vs SiO2 from lamprophyric rocks of the Central-Montana alkalic province with akali basalt from Hawaii (Richter and Moore, 1966). Bull Mountain/Golden Sunlight data from De Witt et al. 1996. Highwood Mountain data Henderson et al., 2012; O'Brien et al., 1991; O'Brien et al., 1995. Crazy Mountain data from Dudas. 1991. Yogo lamprophyre data from Gauthier, 1995.

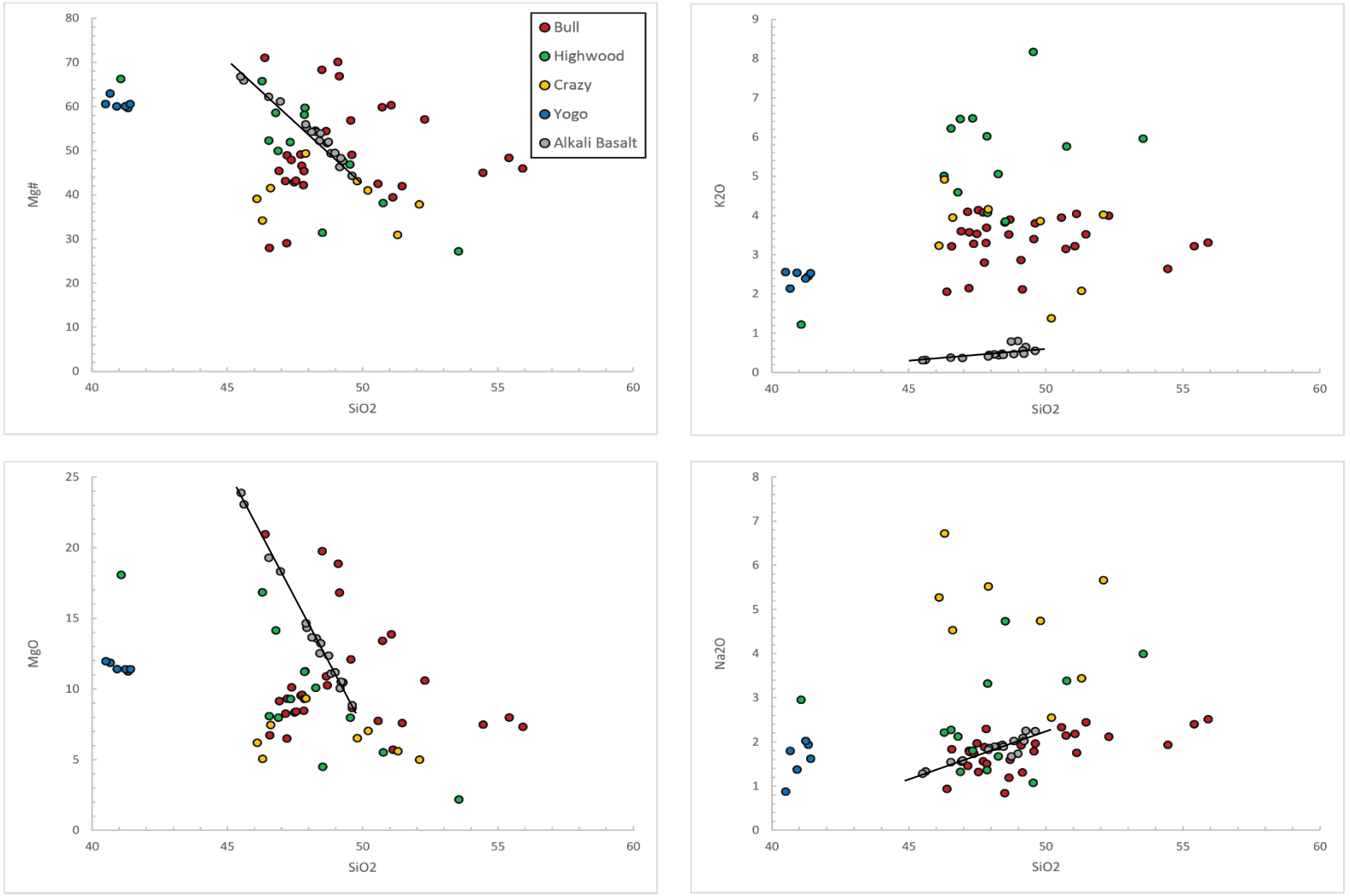

Figure 26 (Continued): Harker Diagrams of MgO, Mg#, K2O, and Na2O vs SiO2 from lamprophyric rocks of the Central-Montana alkalic province with akali basalt from Hawaii (Richter and Moore, 1966). Bull Mountain/Golden Sunlight data from De Witt et al. 1996. Highwood Mountain data Henderson et al., 2012; O'Brien et al., 1991.; O'Brien et al., 1995. Crazy Mountain data from Dudas. 1991. Yogo lamprophyre data from Gauthier, 1995.

(4D) Pyroxene Mineral Chemistry

Pyroxene solid solution are viewed on the pyroxene compositional ternary diagram or the pyroxene quadrilateral (Fig. 27). The general formula for a pyroxene is $XYSi_2O_6$, (where X = Na, Ca, Mg, and Fe^{2+}, and Y = Mg, Fe^{2+}, Al) and varies depending on end member composition of the pyroxene. End members on the ternary pyroxene compositional diagram are the following: Enstatite ($Mg_2Si_2O_6$), Ferrosilite ($Fe_2Si_2O_6$), and Wollastonite ($Ca_2Si_2O_6$). Fe Mg bearing pyroxenes with more than 50% Ca do not usually exist within nature, thus the top of the ternary diagram is cut off, creating the pyroxene quadrilateral. Typical pyroxene compositions of Na poor pyroxenes (<2 wt. % Na_2O) in lamprophyric rocks (calc-alkaline, alkaline, ultramafic, and lamproites), are expected to plot within the diopside or augite field of the pyroxene quadrilateral (Rock, 1991). The red polygon on Figure 27 demarcates this area. Compositional data collected from analytical transverses from every region in this study plot within this area (see Fig. 69).

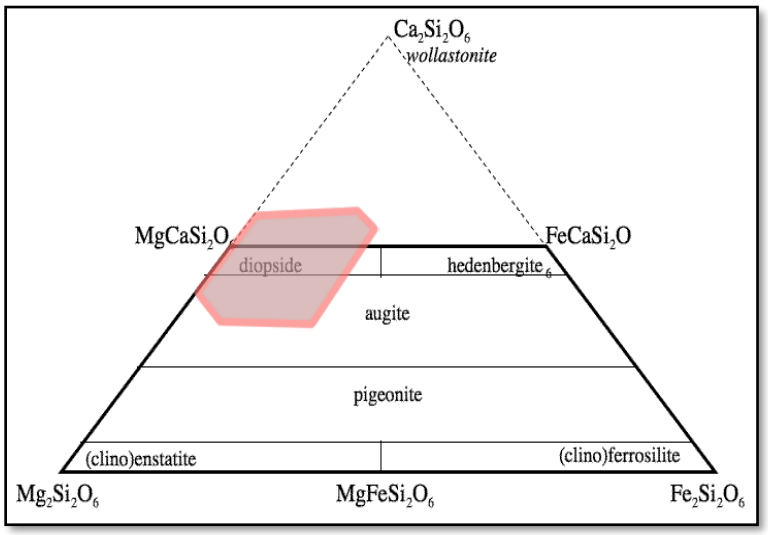

Figure 27: Pyroxene Ternary Diagram and Quadrilateral. Red area after (Rock, 1991) where Lamprophyric clinopyroxenes compositions concentrate from calc-alkine, alkaline, and ultramafic lamprophyres.

Due to the variability of zoning patterns within lamprophyric clinopyroxenes in this study, a summary is needed for classifying the various types of zonations viewed in thin section and through BSE images. Normal zoning refers to crystals that have compositional changes from core to rim, along the

crystal stratigraphy, that would be induced by compositional changes in the melt as it follows a liquid line of descent during cooling (Streck, 2008). Typical normal zoning in clinopyroxenes is evident by compositional changes (Mg# ↓, Mg ↓, Fe ↑, Na ↑, Al ↑, and Ti↑) from core to rim (Rock, 1991). One would expect Cr and Ni to follow suit with the same compositional trends as Mg# because more primitive magmas would be enriched with characteristic mafic elements (Cr, Ni, and V). More incompatible elements like Al and Ti are expected to increase in concentration during normal zoning as they are more characteristic of evolved magmas. As the melt solidifies in a closed system, changing mineral compositions during crystallization reflect the progressively evolving composition of the original melt. Thus, reverse zoning is any compositional inversion, or change that occurs from core to the rim of a single crystal, from what would be expected to result from crystallization in a closed system (Streck, 2008). Typical reverse zoning in clinopyroxene crystals from lamprophyres is evident by compositional changes (Mg# ↑, Mg ↑, Fe ↓, Na ↓, Al ↓, and Ti ↓) from core to rim (Rock, 1991). Inverse zoning is possible (usually Mg# ↓ and Na↓) within clinopyroxenes studied from alkaline and ultramafic lamprophyres and denotes any zonation where element changes of normal and reverse zoning exist together (Rock, 1991).

Representative electron microprobe analysis of clinopyroxenes from Bull Mountain, the Highwood Mountains, the Crazy Mountains, and Yogo Dyke is given on the Table 3 below. Each datum represents a specific location that was analyzed with the microprobe along a transect from core to rim of selected pyroxene crystals. The entirety of the data from each region from this study is available in the online supplemental appendices of this work. Groundmass or matrix clinopyroxenes analysis is given on Table 4 below.

Table 3. Representative Pyroxene Mineral Chemistry

Crystal	J06_1A								J18_1a							
traverse #	1	2	3	4	5	6	7	8	1	2	3	4	5	6	7	8
SiO2	50.27	51.25	48.49	50.77	50.47	50.42	46.32	46.93	51.45	51.56	54.75	51.63	50.43	49.02	50.00	47.55
TiO2	0.37	0.28	0.65	0.29	0.31	0.43	0.91	0.79	0.64	0.66	0.17	0.63	0.82	1.15	0.87	1.47
Al2O3	3.70	2.16	4.57	2.58	2.75	2.39	6.05	5.19	3.09	2.76	1.04	2.79	4.10	5.05	4.15	5.84
Cr2O3	0.31	0.25	0.13	0.47	0.48	0.15	0.03	0.02	0.06	0.01	0.15	0.13	0.06	0.13	0.24	0.00
FeO	6.63	5.01	7.39	5.23	5.24	5.83	8.29	7.83	6.83	6.66	3.29	5.55	6.49	7.44	6.45	8.86
MnO	0.15	0.09	0.14	0.14	0.12	0.12	0.17	0.16	0.12	0.12	0.08	0.13	0.11	0.09	0.11	0.16
MgO	15.11	16.21	14.22	15.86	15.74	15.75	13.18	13.77	14.39	14.57	17.55	15.20	14.34	13.45	14.22	12.32
CaO	22.27	23.24	22.18	23.06	22.96	23.06	22.59	22.48	23.23	23.49	23.81	23.69	23.60	23.32	23.71	23.25
Na2O	0.35	0.23	0.41	0.26	0.25	0.19	0.31	0.33	0.43	0.36	0.17	0.29	0.32	0.37	0.31	0.41
NiO	0.01	0.02	0.01	0.03	0.02	0.01	0.01	0.00	0.03	0.03	0.04	0.01	0.03	0.01	0.00	0.01
Total	99.17	98.74	98.18	98.68	98.35	98.37	97.85	97.50	100.27	100.23	101.06	100.05	100.31	100.03	100.07	99.86
Mg #	80.24	85.23	77.42	84.39	84.28	82.81	73.92	75.83	78.97	79.59	90.48	83.00	79.76	76.31	79.71	71.25
Normalized Analyis																
Si	1.88	1.91	1.84	1.90	1.90	1.90	1.78	1.81	1.91	1.91	1.97	1.91	1.87	1.83	1.86	1.80
Ti	0.01	0.01	0.02	0.01	0.01	0.01	0.03	0.02	0.02	0.02	0.00	0.02	0.02	0.03	0.02	0.04
Al (IV)	0.12	0.09	0.16	0.10	0.10	0.10	0.22	0.19	0.09	0.09	0.03	0.09	0.13	0.17	0.14	0.20
Al (VI)	0.04	0.01	0.05	0.02	0.02	0.01	0.06	0.04	0.04	0.03	0.02	0.03	0.05	0.05	0.04	0.06
Cr	0.01	0.01	0.00	0.01	0.01	0.00	0.00	0.00	0.00	0.00	0.00	0.00	0.00	0.00	0.01	0.00
Fe 3+	0.11	0.10	0.14	0.11	0.10	0.12	0.19	0.19	0.07	0.07	0.01	0.07	0.09	0.11	0.10	0.14
Fe 2+	0.21	0.16	0.24	0.16	0.16	0.18	0.27	0.25	0.21	0.21	0.10	0.17	0.20	0.23	0.20	0.28
Mn	0.00	0.00	0.00	0.00	0.00	0.00	0.01	0.01	0.00	0.00	0.00	0.00	0.00	0.00	0.00	0.01
Mg	0.84	0.90	0.81	0.89	0.88	0.88	0.76	0.79	0.79	0.80	0.94	0.84	0.79	0.75	0.79	0.69
Ca	0.89	0.93	0.90	0.93	0.92	0.93	0.93	0.93	0.92	0.93	0.92	0.94	0.94	0.93	0.94	0.94
Na	0.03	0.02	0.03	0.02	0.02	0.01	0.02	0.02	0.03	0.03	0.01	0.02	0.02	0.03	0.02	0.03
Tot. Cat.	4.04	4.03	4.05	4.04	4.04	4.04	4.07	4.06	4.02	4.02	4.00	4.02	4.03	4.04	4.03	4.05
Ideal Cat.	4.00	4.00	4.00	4.00	4.00	4.00	4.00	4.00	4.00	4.00	4.00	4.00	4.00	4.00	4.00	4.00
Tot. Oxy.	6.00	6.00	6.00	6.00	6.00	6.00	6.00	6.00	6.00	6.00	6.00	6.00	6.00	6.00	6.00	6.00

Table 3 (Cont.). Representative Pyroxene Mineral Chemistry

Crystal	J36_3a									yogo_6a						
traverse #	1	2	3	4	5	6	7	8	9	1	2	3	4	5	6	7
SiO2	53.94	53.04	52.42	52.24	53.16	51.54	52.36	53.33	53.29	55.36	53.70	46.01	53.96	52.34	50.17	47.11
TiO2	0.26	0.46	0.44	0.43	0.30	0.41	0.40	0.39	0.31	0.04	0.25	2.07	0.05	0.50	1.05	1.80
Al2O3	1.32	0.96	0.86	1.57	1.28	2.26	1.72	1.10	1.42	1.40	2.36	7.78	1.77	4.32	4.74	6.76
Cr2O3	0.83	0.01	0.12	0.04	0.08	0.02	0.07	0.00	0.81	0.01	1.60	0.88	0.00	0.10	0.90	0.74
FeO	2.86	6.12	5.47	6.23	4.33	6.05	4.45	4.57	3.03	1.88	3.05	5.46	5.30	4.51	3.94	5.15
MnO	0.04	0.16	0.12	0.17	0.13	0.11	0.06	0.11	0.08	0.13	0.10	0.05	0.60	0.17	0.03	0.05
MgO	16.59	14.68	14.13	14.70	16.15	14.75	15.83	15.89	16.73	18.07	17.21	12.79	15.22	15.60	14.71	13.31
CaO	24.10	23.25	23.36	23.49	24.09	23.65	24.49	24.43	24.00	23.54	21.05	24.07	22.74	21.26	24.23	24.34
Na2O	0.49	0.93	0.97	0.68	0.36	0.63	0.41	0.44	0.50	0.32	0.77	0.27	0.51	0.87	0.27	0.25
NiO	0.04	0.00	0.00	0.01	0.00	0.01	0.00	0.00	0.02	0.00	0.03	0.02	0.00	0.02	0.01	0.01
Total	100.46	99.62	97.88	99.56	99.87	99.44	99.79	100.26	100.19	100.74	100.11	99.39	100.16	99.69	100.04	99.53
Mg #	91.18	81.04	82.16	80.78	86.93	81.29	86.37	86.10	90.78	94.50	90.95	80.69	83.65	86.06	86.95	82.16
Normalized Analyis																
Si	1.96	1.97	1.98	1.95	1.96	1.92	1.93	1.96	1.95	1.98	1.95	1.73	1.98	1.92	1.85	1.76
Ti	0.01	0.01	0.01	0.01	0.01	0.01	0.01	0.01	0.01	0.00	0.01	0.06	0.00	0.01	0.03	0.05
Al (IV)	0.04	0.03	0.02	0.05	0.04	0.08	0.07	0.04	0.05	0.02	0.05	0.27	0.02	0.08	0.15	0.24
Al (VI)	0.02	0.01	0.02	0.02	0.01	0.02	0.01	0.01	0.01	0.04	0.05	0.07	0.06	0.10	0.05	0.06
Cr	0.02	0.00	0.00	0.00	0.00	0.00	0.00	0.00	0.02	0.00	0.05	0.03	0.00	0.00	0.03	0.02
Fe 3+	0.03	0.08	0.07	0.09	0.06	0.11	0.09	0.07	0.06	0.00	0.00	0.11	0.00	0.02	0.05	0.10
Fe 2+	0.09	0.19	0.17	0.19	0.13	0.19	0.14	0.14	0.09	0.06	0.09	0.17	0.16	0.14	0.12	0.16
Mn	0.00	0.01	0.00	0.01	0.00	0.00	0.00	0.00	0.00	0.00	0.00	0.00	0.02	0.01	0.00	0.00
Mg	0.90	0.81	0.80	0.82	0.89	0.82	0.87	0.87	0.91	0.97	0.93	0.72	0.83	0.85	0.81	0.74
Ca	0.94	0.93	0.95	0.94	0.95	0.95	0.97	0.96	0.94	0.90	0.82	0.97	0.89	0.83	0.96	0.98
Na	0.03	0.07	0.07	0.05	0.03	0.05	0.03	0.03	0.04	0.02	0.05	0.02	0.04	0.06	0.02	0.02
Tot. Cat.	4.01	4.03	4.02	4.03	4.02	4.04	4.03	4.02	4.02	4.00	4.00	4.04	4.00	4.01	4.02	4.03
Ideal Cat.	4.00	4.00	4.00	4.00	4.00	4.00	4.00	4.00	4.00	4.00	4.00	4.00	4.00	4.00	4.00	4.00
Tot. Oxy.	6.00	6.00	6.00	6.00	6.00	6.00	6.00	6.00	6.00	6.00	6.00	6.00	6.00	6.00	6.00	6.00

Table 4: Matrix Clinopyroxene Analysis

Crystal	J24_matrix_pyx			J18_matrix_pyx			yogo_matrix_pyx			
#	1	2	3	1	3	4	1	2	3	4
SiO2	50.62	49.70	49.12	50.95	50.56	50.60	52.27	48.03	49.81	53.06
TiO2	0.70	0.66	0.82	0.61	0.76	0.58	0.28	1.45	1.03	0.32
Al2O3	3.00	3.57	4.21	2.83	2.85	2.93	2.98	5.83	4.06	3.19
Cr2O3	0.04	0.00	0.02	0.16	0.00	0.20	0.32	0.71	0.36	0.24
FeO	6.60	7.52	7.48	6.08	7.35	5.80	3.13	4.61	4.20	4.03
MnO	0.16	0.17	0.19	0.11	0.20	0.11	0.08	0.07	0.09	0.15
MgO	14.95	14.40	13.85	15.13	14.14	15.20	16.84	14.02	14.95	16.82
CaO	22.67	22.34	22.38	23.56	23.59	23.70	22.51	24.23	24.35	21.24
Na2O	0.40	0.40	0.55	0.29	0.32	0.27	0.59	0.26	0.21	0.72
NiO	0.03	0.01	0.00	0.02	0.03	0.00	0.05	0.02	0.02	0.04
Total	99.17	98.78	98.61	99.74	99.79	99.40	99.04	99.24	99.08	99.81
Mg #	80.15	77.34	76.76	81.61	77.44	82.37	90.57	84.43	86.38	88.14
Normalized Analyis										
Si	1.90	1.88	1.86	1.90	1.48	1.89	1.92	1.80	1.86	1.93
Ti	0.02	0.02	0.02	0.02	0.00	0.02	0.01	0.04	0.03	0.01
Al (IV)	0.10	0.12	0.14	0.10	0.52	0.11	0.08	0.20	0.14	0.07
Al (VI)	0.03	0.04	0.05	0.02	0.00	0.02	0.05	0.05	0.04	0.07
Cr	0.00	0.00	0.00	0.00	0.00	0.00	0.01	0.02	0.01	0.01
Fe (3+)	0.10	0.12	0.13	0.10	1.38	0.10	0.06	0.10	0.08	0.03
Fe (2+)	0.21	0.24	0.24	0.19	0.63	0.23	0.10	0.14	0.13	0.12
Mn	0.00	0.01	0.01	0.00	0.01	0.01	0.00	0.00	0.00	0.00
Mg	0.83	0.81	0.78	0.84	2.38	0.79	0.92	0.78	0.83	0.91
Ca	0.91	0.90	0.91	0.94	0.02	0.95	0.89	0.97	0.97	0.83
Na	0.03	0.03	0.04	0.02	0.00	0.02	0.04	0.02	0.01	0.05
Tot. Cat.	4.03	4.04	4.04	4.03	4.52	4.03	4.02	4.03	4.03	4.01
Ideal Cat.	4.00	4.00	4.00	4.00	4.00	4.00	4.00	4.00	4.00	4.00
Tot. Oxy.	6.00	6.00	6.00	6.00	6.00	6.00	6.00	6.00	6.00	6.00
Crystallization										
Calc T (C)	1231.35	1236.85	1252.05	1213.25	1209.45	1208.05	1330.58	1289.62	1273.11	1349.11
Calc P (kbar)	12.80	13.30	15.10	10.80	10.40	10.20	16.50	11.60	10.11	18.00
Calc P (Km)	47.36	49.21	55.87	39.96	38.48	37.74	61.04	42.91	37.41	66.59

Pyroxene mineral chemistry data collected from crystal transects of lamprophyric rocks from this study are plotted on a pyroxene discrimination diagram (Fig. 28) after Rock (1991). As expected from the Central-Montana alkalic province, the alkaline (AL) and calk-alkaline (CAL) fields are the most densely populated. Compared to the other regions, the Yogo Dyke pyroxenes plot nearer the ultramafic lamprophyre field and some pyroxenes plot within the ultramafic lamprophyre (UML) field.

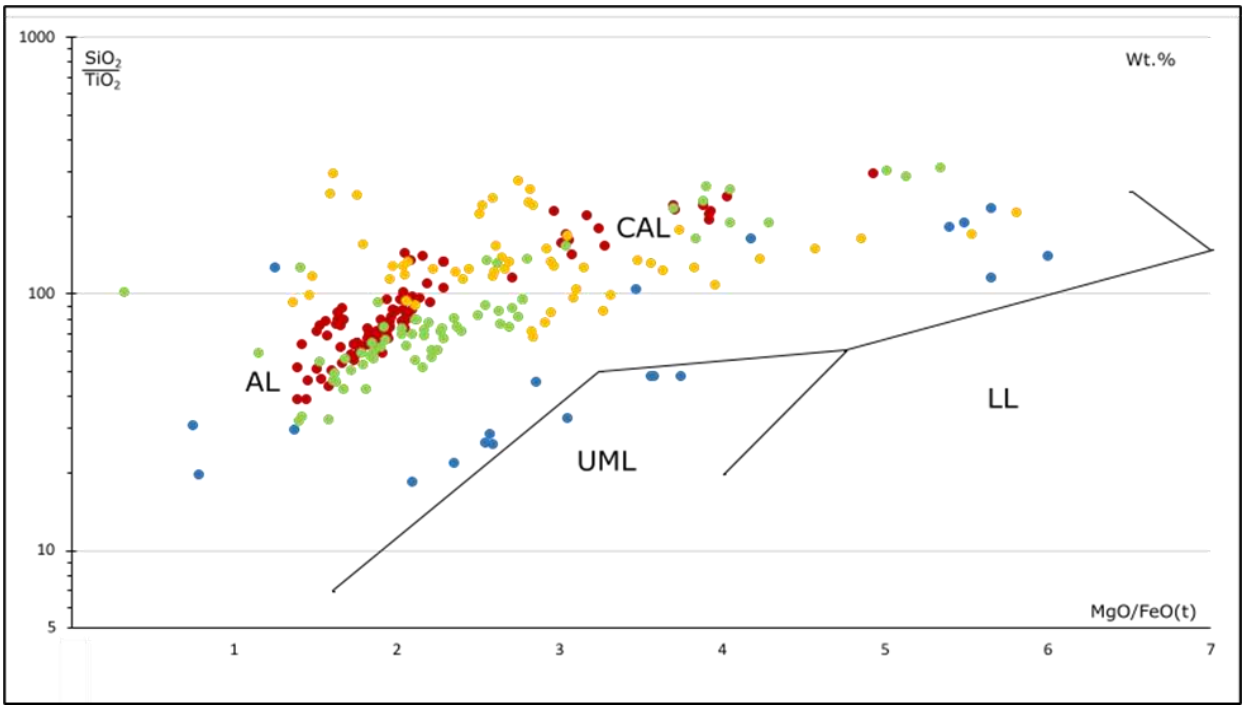

Figure 28: Pyroxene CAL, AL, UML, and LL Discrimination Diagram. Based off of Rock (1991). Note logarithmic scales and wt.% oxides used in ratios. Red points represent Bull Mountain and Golden Sunlight pyroxene data. Green points represent Highwood Mountain pyroxene data. Yellow points represent Crazy Mountain pyroxene data. Blue points represent Yogo Dyke pyroxene data. As expected, the pyroxenes plot within the calk-alkaline (CAL) and alkaline (AL) discrimination fields. Yogo Dyke pyroxene data plot near and within the ultramafic (UML) discrimination field.

This ultramafic trend within the Yogo Dyke pyroxenes is more apparent in the Al_2O_3 vs. TiO_2 discrimination diagram (Fig. 29). Rock (1991) used 1,095 pyroxene analyses and interpreted that 'typical' clinopyroxenes in calk-alklaline and lamproite lamprophyres are low Al-Ti diopsidic augites, but in alkalic and ultramafic lamprophyres the clinopyroxenes are often high Al-Ti Mg-rich diopsides. There exists some overlap between the Bull Mountain/Golden Sunlight and the Highwood Mountain lamprophyre pyroxene discrimination fields, whereas the Crazy Mountain lamprophyric pyroxenes display low Al-Ti pyroxene values. This is unusual, because the Crazy Mountain pyroxene discrimination field aligns more with lamproite lamprophyre analysis from Rock (1991).

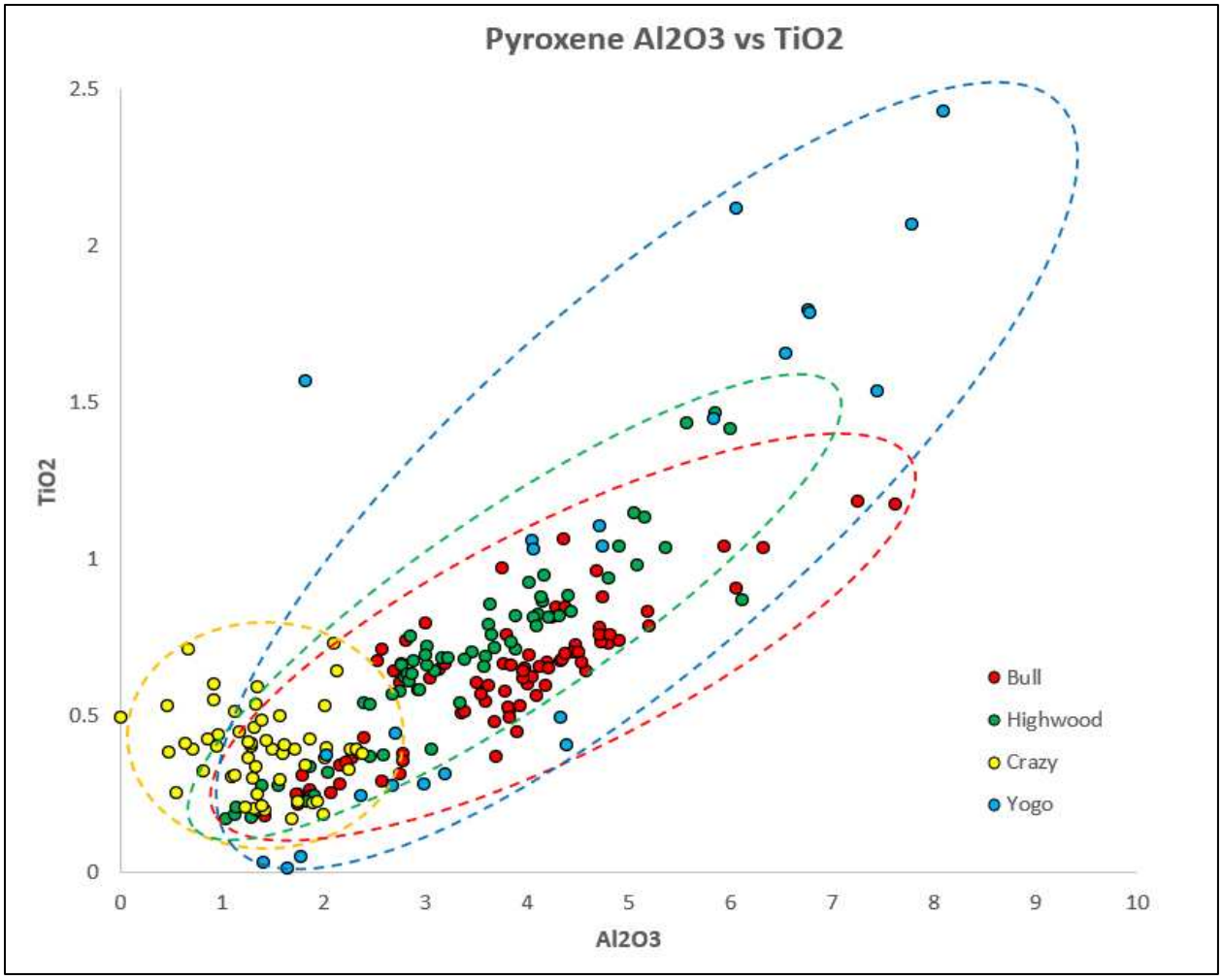

Figure 29: Pyroxene Al_2O_3 vs TiO_2 (weight %) Discrimination Plot.

Zoning within pyroxenes in lamprophyres can vary from minor, to major, and finally to complex (Rock, 1991). Within alkaline lamprophyres, Bedard et al. (1988) noted that clinopyroxene phenocrysts exhibit complex zoning patterns that can vary from dyke to dyke and from crystal to crystal within individual dykes. This is also characteristic of clinopyroxene crystals originating from lamprophyres of this study that have more of a calc-alkaline affinity than strictly alkaline. Zoning is the expression of compositional variability within a single crystal (Streck, 2008). It is common of minerals belonging to a solid solution series (commonly plagioclase and pyroxenes) to display zonations during crystal growth.

Progressive (also known as direct) zoning occurs when the traverse produces a smooth profile where compositions gradually change from core to rim. Step zoning occurs when chemical zoning

displays a series of compositional steps which are commonly associated with observable morphological features within crystals (Streck, 2008). Discontinuous zoning is similar to step zoning but occurs when chemical zoning shows a sudden or abrupt change in composition along an analytical traverse. Oscillatory zoning is common of clinopyroxenes and exists when composition oscillates in a regular fashion through the crystal. Shore and Fowler (1996) define oscillatory zoning as "…compositionally varying growth-shells (or layers) that are generally parallel to crystallographic planes of low Miller indices and have a thickness ranging from tens of nanometers to several tens of micrometers". Within alkaline and ultramafic lamprophyre varieties, pyroxenes displaying oscillatory zoning will often show Al and Ti content fluctuations (Rock, 1991). Banding is indicative of concentric zoning, whereas patchy zoning occurs when there exists irregularly shaped patterns or patches where compositional information can be difficult to interpret. Hourglass shaped sector zoning can occur in pyroxenes as well.

Pyroxenes targeted and analyzed during this study were selected off the following criteria: (1) coarse crystals large enough for desired analytical traverses, (2) crystals displaying prominent zoning patterns, (3) crystals with disequilibrium features (resorbed margins, reaction rims, rounding, spongy textured melt pockets, etc.), (4) crystals with presumed parasitic growths, and (5) if able, a wide variety of pyroxenes were analyzed from the same lamprophyre if pyroxene crystals did not behave uniformly.

Do note that analytical traverse data for Mg#, Cr_2O_3, NiO, TiO_2, Al_2O_3 are present at the end of the next sub chapters, while Na_2O and Fe^{3+}/Fe^{2+} traverse data are present on Figure 75 and 76 respectively in section 8C.

(4D. i) Bull Mountain Lamprophyre Mineral Chemistry

Five pyroxene crystals from one sample (J06-vogesite) were analyzed with mineral chemistry transects. The BSE image of Bull Mountain lamprophyre slide J06 (vogesite), crystal 1A (Fig. 30) shows a euhedral, complexly zoned pyroxene, and shows little sign of resorption along the rim of the crystal. Crystal 1A displays a dark dimgrey core that has an ovate shaped zone of patchy zoning and spongy

texture surrounding it. Point 3 is a lighter colored grey zone around the melt pockets (spongy texture). The outer core is dimgrey with a euhedral internal boundary between outer core margin and the intermediate zone. There is a dark grey colored intermediate (mantle) zone displaying spongy texture and inclusions. Outside that, a concentrically zoned rim with lighter dark grey color and the outermost band of the rim (blue points on Fig. 30) is grey in color. The inception of spongy textured pockets looks to be formed within the outermost portion of the grey colored rim. The pyroxene ternary diagram depicts the innermost core (point 1) decreasing in Fe content from points 1 to 2 within the ovate patchy zone contained within the spongy textured core. Point 3 increases in Fe content inside the grey lighter portion of ovate spongy texture. At Point 5, the rim of the outer core, the composition regresses to more a Mg rich diopside decreasing in Fe content. Point 6 increases in Fe, progressing to a more Fe rich diopside. The rim (points 7 and 8) depicts a significant jump in Fe content of the pyroxene shifting towards the hedenbergite compositional line. The analytical traverse of this crystal (Fig. 39 a) depicts Mg#, NiO, and Cr_2O_3 decreasing overall from core to rim. TiO_2, Al_2O_3, and Na_2O increase overall from core to rim. The crystal based off the compositional data and traverse structure is classified as a normally zoned crystal exhibiting patchy, oscillatory, and discontinuous features. The spongy bleb with lighter color (point 3) displays Mg#, Cr_2O_3, and NiO decreasing whereas TiO_2, Al_2O_3, and Na_2O greatly increase.

A second BSE of the same Bull Mountain lamprophyre shows a contrasting euhedral sector zoned pyroxene, crystal 2A (Fig. 30). The crystal consists of a patchy zoned inner dimgrey core with irregular shaped spongy texture, dark irregular zones within the patchy zonation are darkslate grey in color, and lighter areas around melt pockets are grey. There exists a sharp subhedral, sub-rounded edge of internal zonation between the core and intermediate zone. The intermediate dimgrey zone displays some oscillatory concentric zoning with thin grey bands, with a darker dimgrey colored rim. The outermost portion of the crystals rim when in contact with the groundmass shows a thin band of grey.

The ternary diagram for this crystal displays an Fe depleted core compared to the intermediate/mantle and rim. The rim regresses in Fe diopsidic composition when compared to the intermediate zone of the crystal. Along the analytical traverse (Fig. 38 b), the Mg#, Cr_2O_3, and NiO content decrease from core to rim, whereas TiO_2, Al_2O_3, and Na_2O increase from core to rim with higher values in the lighter colored mantle segment of the crystal. There exists a slight increase in Mg#, Cr_2O_3, and NiO and a decrease in TiO_2, Al_2O_3, and Na_2O content at the edge of the inner core. Based off of compositional data and the structure of the analytical traverse, this crystal is classified as normally zoned and shows both patchy, oscillatory, and discontinuous zoning patterns.

Figure 32 displays crystal 3A of slide J06 (vogesite) of the Bull Mountain range. Unfortunately, only traverse data exists for the dimgrey core. The cores margin is rounded, and the core contains patchy zoned lighter areas around dark colored melt pockets. The ternary diagram for pyroxene composition plots the crystal in the diopside field and the innermost core is Mg rich while the outer core decreases in Mg and increases in Ca and Fe content. This crystal is very similar in appearance to crystal 5A of the same thin section.

Crystal 5a of lamprophyre J06 of the Bull Mountain Range (Fig. 33) displays a subhedral crystal with minor rounding of the crystal's exterior. The crystal has a broad darker dimgrey colored core with rounded edges and lighter colored rim. The core region displays patchy zoning with grey lighter irregular shaped patches around melt pockets. Some of the melt pockets are sinuous in nature. Point 2 along the traverse is located within one of these lighter grey colored spongy textured areas within the core and exhibits a decrease in Mg# and an increase in Al_2O_3 and TiO_2 content. Faint oscillatory zoning exists within the rim alternating from grey to dimgrey thin individual bands. Along the analytical traverse (Fig. 39 c) Mg#, Cr_2O_3, and NiO decrease from core to rim. Al_2O_3, TiO_2, and Na_2O increase from core to rim. The analytical data presents a sharp contrast in data between the core to rim margin. The ternary diagram of this crystal shows that the Fe content of diopside decreases from the middle of the core to

the spongy textured melt pocket (point 2), then increases in Fe content from the outer core to the rim. Across the analytical traverse, this crystal is classified as normally zoned and shows both patchy and discontinuous zoning patterns.

Crystal 8A of lamprophyre J06 (vogesite) of the Bull Mountain Range (Fig. 34) is euhedral and contains a small dark dimgrey core with spongy melt pockets. The crystal has a broad concentrically zoned intermediate zone that oscillates from bands of dimgrey to grey. The core contains a thin dimgrey rim which houses a large 100 µm wide growth of spongy texture. Much like other pyroxenes of the same sample, inclusions are present throughout the entirety of the crystal. The ternary diagram is unusual compared to other crystals from lamprophyre J06. The diagram depicts no significant compositional change from core to rim. There might be a slight Ca increase in the core, but the effect is marginal. The Mg#, NiO, and Cr_2O_3 decrease in content from core to rim. TiO_2, Al_2O_3, and Na_2O increase slightly from core to rim. The range of data from the analytical traverse is distinctly different from other crystals from this slide (Fig. 39 d). This crystal is classified as normal oscillatory zoned.

A second lamprophyre analyzed from Bull Mountain was J12 (minette). Crystal 1A (Fig. 35) is euhedral and displays few signs of dissolution or resorption. The BSE image of 1A shows a darker slate grey inner core (red points along analytical traverse) that has many inclusions and faint growth of spongy texture. The outer core is darkslategrey with angular edges (orange points along analytical traverse), while the intermediate zone is dimgrey with a rounded margin along the intermediate-rim boundary. The rim is grey and has few inclusions. The Mg#, Cr_2O_3, and NiO content decrease from core to rim, while Al, Ti, and Na increase from core to rim. The analytical traverse (Fig. 40 a) contains a discontinuous margin from inner to outer core (between point red to orange point boundary). In this area the Mg#, TiO_2, Al_2O_3, Cr_2O_3, NiO, and Na_2O all display sharp increases in content. The ternary diagram of the crystal exhibits an overall Fe depleted core, with not much diopsidic variation from inner to outer core. The crystal progressively becomes more Fe rich in pyroxene composition from

intermediate zone to the rim. Based on the criteria above, the crystal is classified as normal discontinuously step zoned.

Crystal 3A of the same minette from the Bull Mountain Range (Fig. 36) shows a euhedral pyroxene crystal that is a pristine example of sector zoning. The core (red line on traverse) is grey and rich with acicular apatite inclusions. The intermediate zone (yellow line on traverse) oscillates from concentrically zoned dimgrey bands to grey bands. The outer rim is grey in color. The ternary diagram of this crystal depicts the diopside crystal becoming progressively more Mg rich from core to rim. On the analytical traverses (Fig. 40 b), Mg# and Na_2O content are constant and neither increase or decrease significantly. Al_2O_3 and TiO_2 content decrease from core to rim while the data fluctuates and oscillates. Curiously, Cr_2O_3 decreases while NiO increases at the boundary the core and intermediate zones. It should be noted that the range of Mg# values of this crystal are not as high as other crystals from the same thin section. For example, the Mg# range of crystal 3A is around 70-74, while crystal 1A of the same slide was around 88-72. This pyroxene crystal is classified as being reverse oscillatory sector zoned.

Crystal 4a of the same minette of the Bull Mountain Range (Fig. 37) is not a single crystal, but rather a cluster of three truncated and disaggregated pyroxene crystals that were analyzed separately (red, blue, and yellow are used to differentiate between the crystals). It is unclear if these truncated crystals were originally part of the same crystal. Textural and zonation patterns on the BSEs suggest that they did not originate from the same crystal. Even though the crystals are fragmented, they do possess euhedral margins. The crystal with red points depicts a patchy zoned inner core. Zonation ranges from darkslategrey to grey in the surrounding areas adjacent to the melt pockets (point 2 along the red traverse). The rest of the crystal is grey from the core to the rim. The second crystal (blue traverse) has a core that is dimgrey with a rounded core margin that is devoid of any signs of spongy texture. Outside that there is a grey colored intermediate zone with dark grey bands that appear concentrically zoned. The third crystal (orange traverse) is a truncated crystal depicting three definite compositional variations

moving from a dimgrey core to an intermediate grey zone, and finally to an inclusion bearing dark grey rim. On the ternary diagram for these crystals, every crystal behaves similarly to one another, even though the crystals display different extents of zonations. The diopside composition of the crystals starts Mg rich and becomes progressively more Fe rich towards the rims. The analytical traverses (Fig. 40 (c)) show Mg#, Cr_2O_3, and NiO decrease from cores to rims. TiO_2, Al_2O_3, and Na_2O increase from cores to rims. Unlike other crystals from Bull Mountain, the lighter portion of the inner core surrounding melt pockets (point 2 on red) does not vary significantly from the rest of the data, however, there exists a small Na_2O composition spike. All the crystals of 4A show typical signs of normal zoning. The red crystal displays concentric and patchy zoning while the blue and orange show signs of concentric zoning.

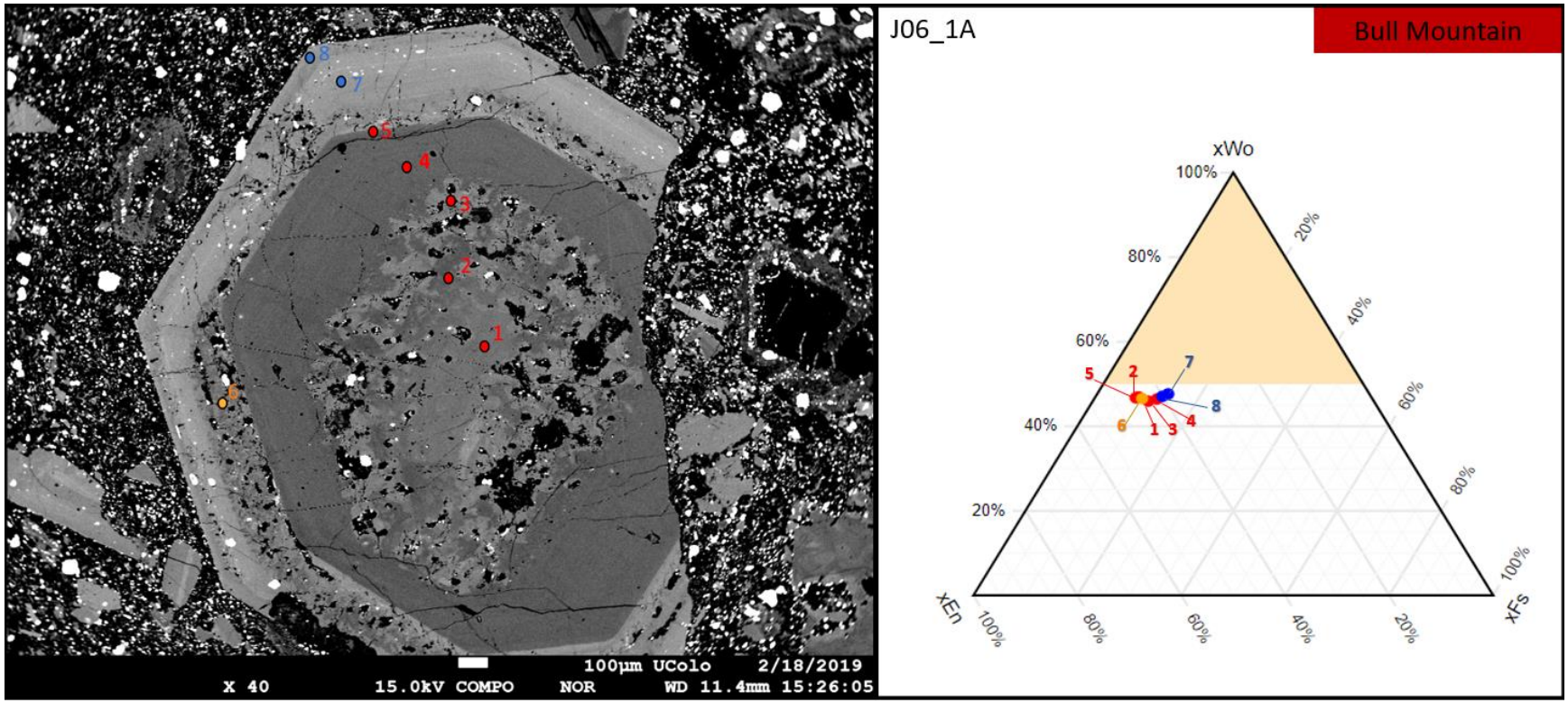

Figure 30: BSE and Ternary Diagram for the analytical traverse from core to rim across pyroxene crystal 1A, Slide J06, from the Bull Mountain Range.

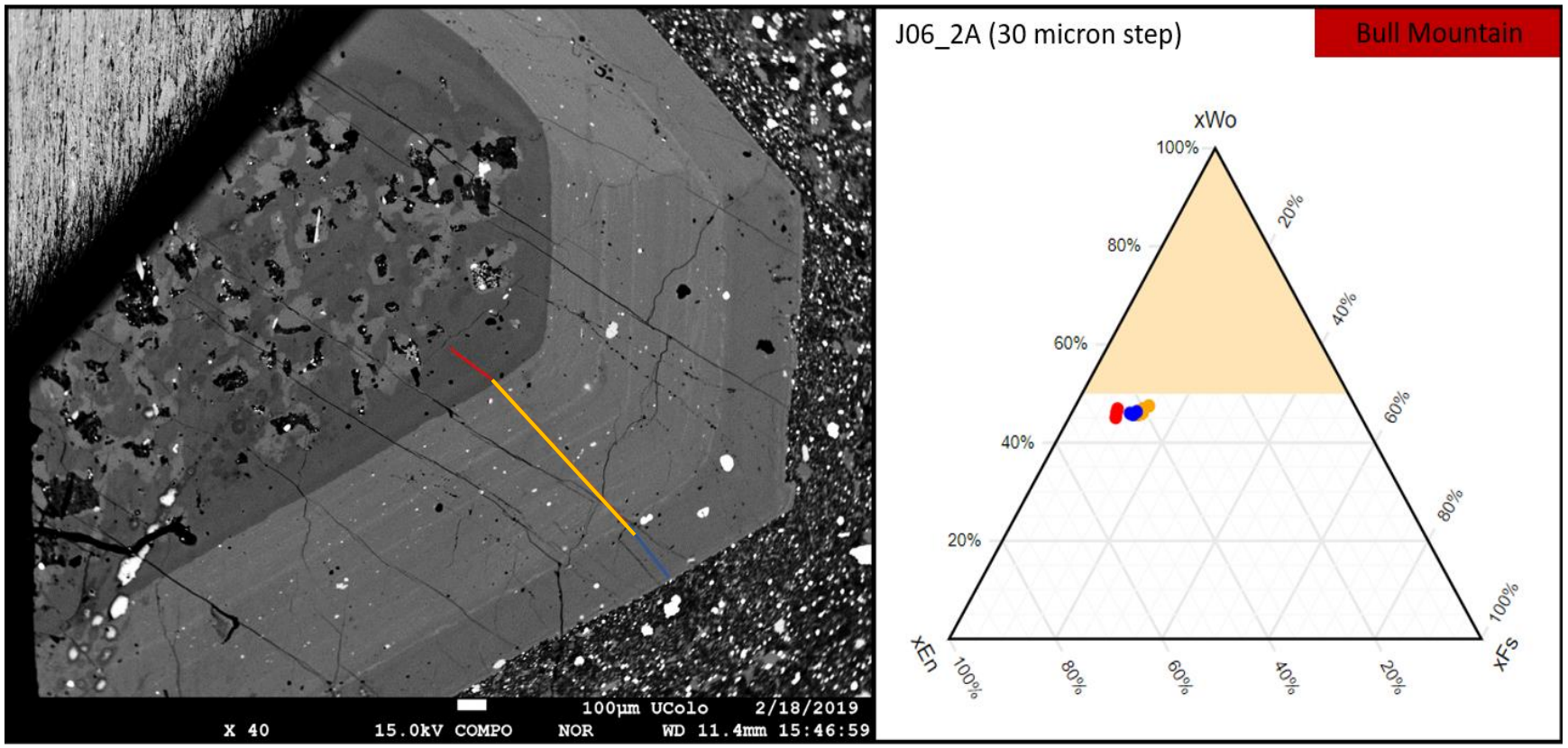

Figure 31: BSE and Ternary Diagram for the analytical traverse from core to rim across pyroxene crystal 2A, Slide J06, from the Bull Mountain Range. Traverse utilized a 30-micron step.

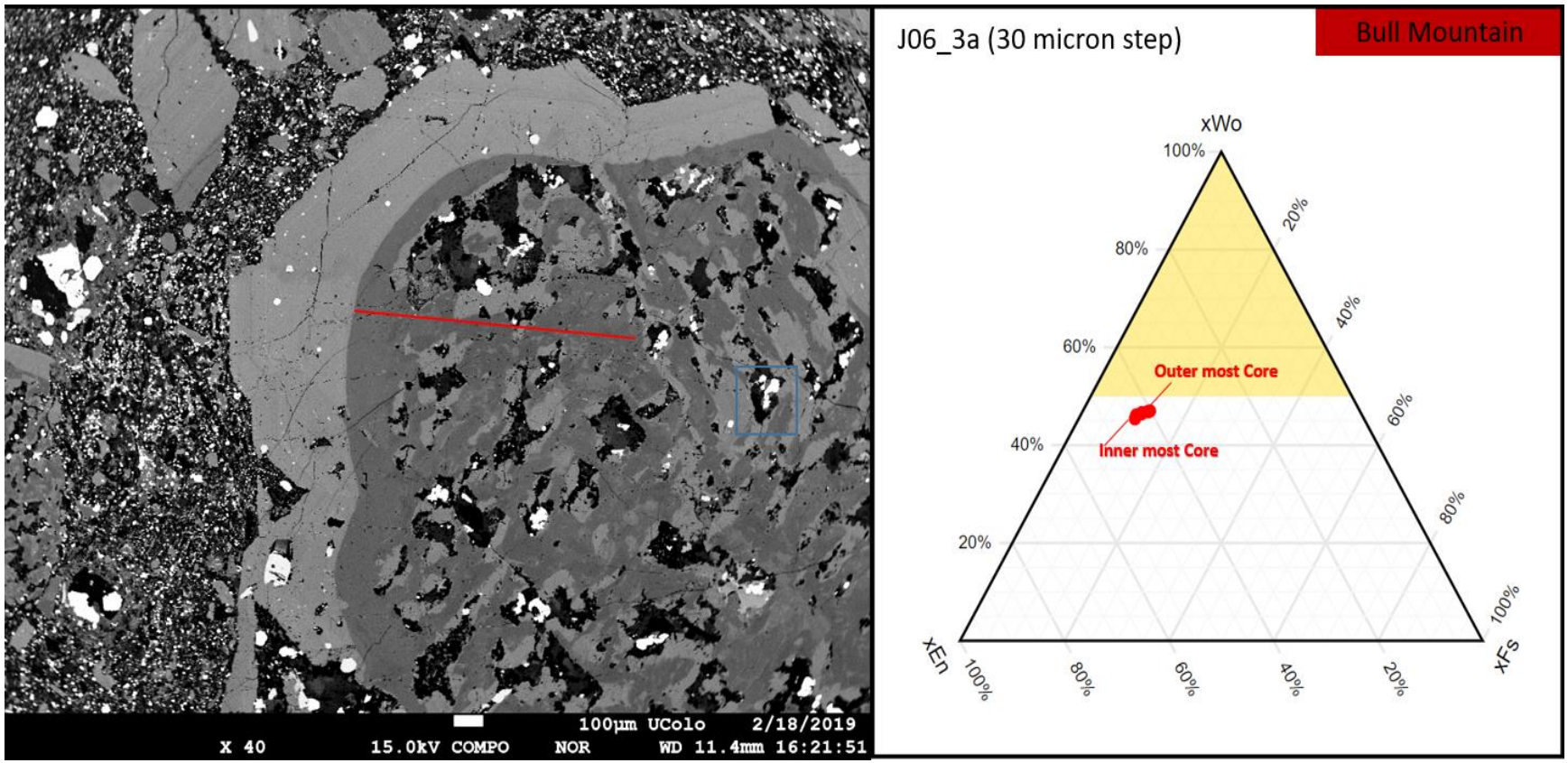

Figure 32: BSE and Ternary Diagram for the analytical traverse from inner to outer core across pyroxene crystal 3A, Slide J06, from the Bull Mountain Range. Traverse utilized a 30-micron step. Blue box corresponds to BSE melt pocket figure 15 (e)

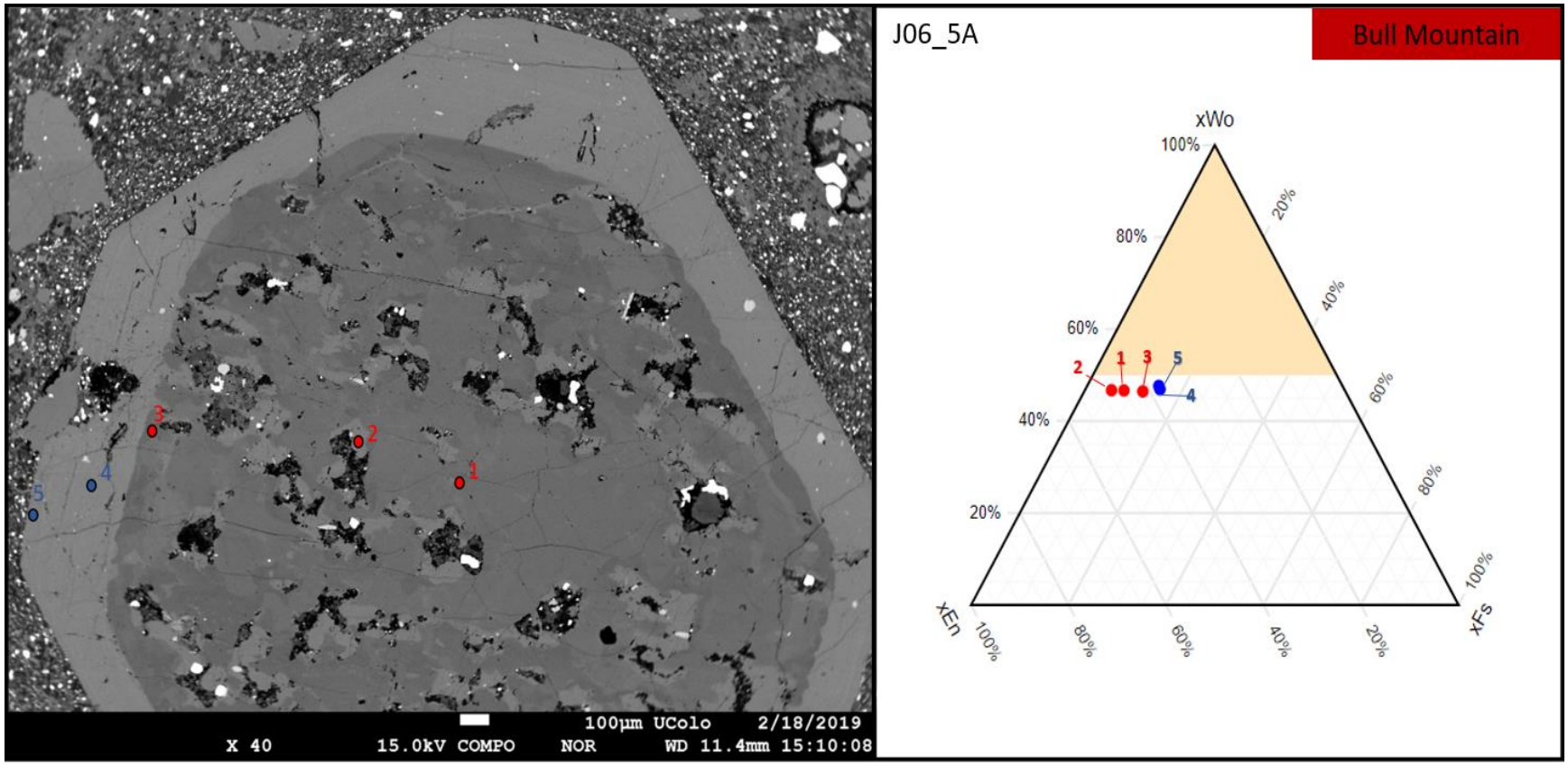

Figure 33: BSE and Ternary Diagram for the analytical traverse from core to rim across pyroxene crystal 5A, Slide J06, from the Bull Mountain Range.

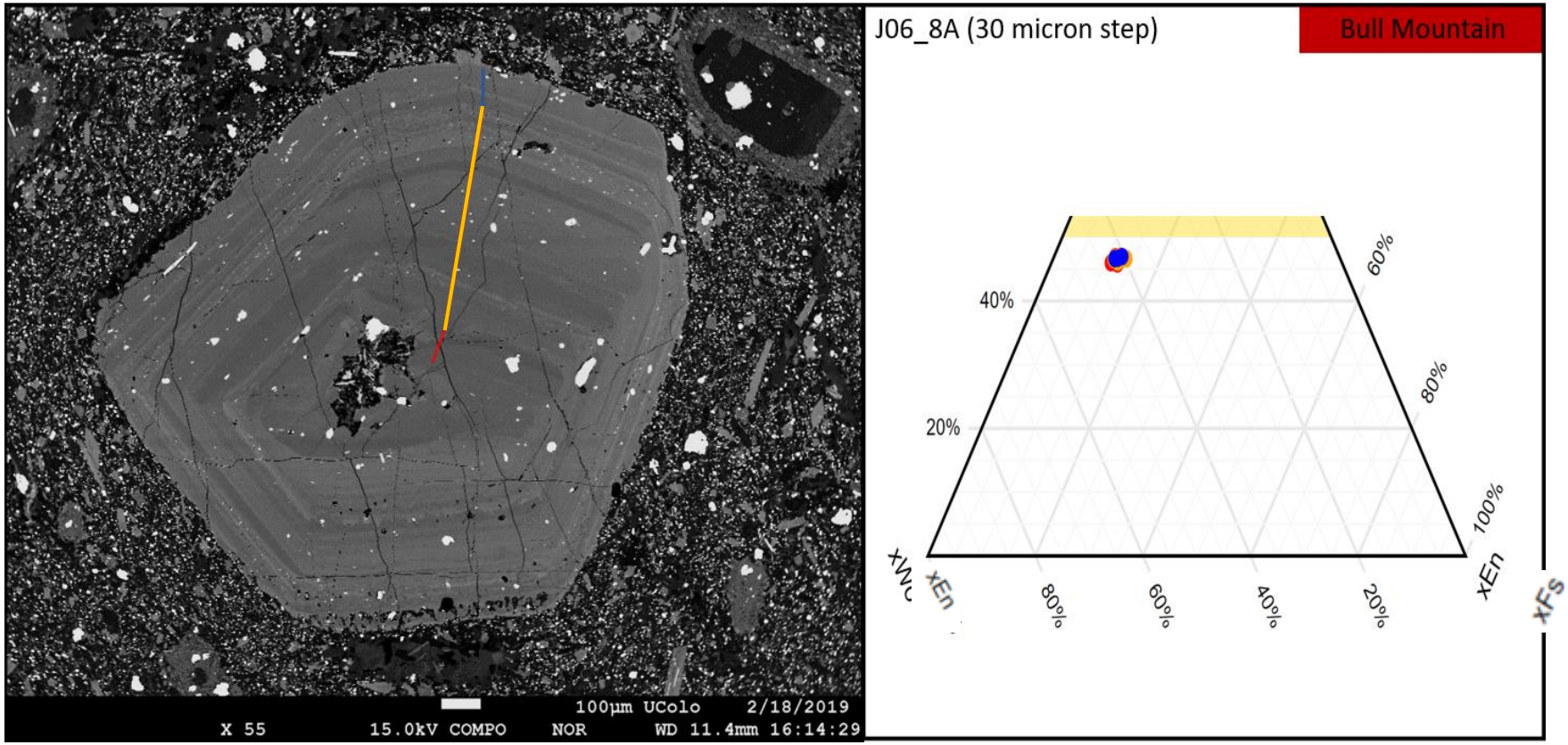

Figure 34: BSE and Ternary Diagram for the analytical traverse from core to rim across pyroxene crystal 8A, Slide J06, from the Bull Mountain Range. Traverse utilized a 30-micron step.

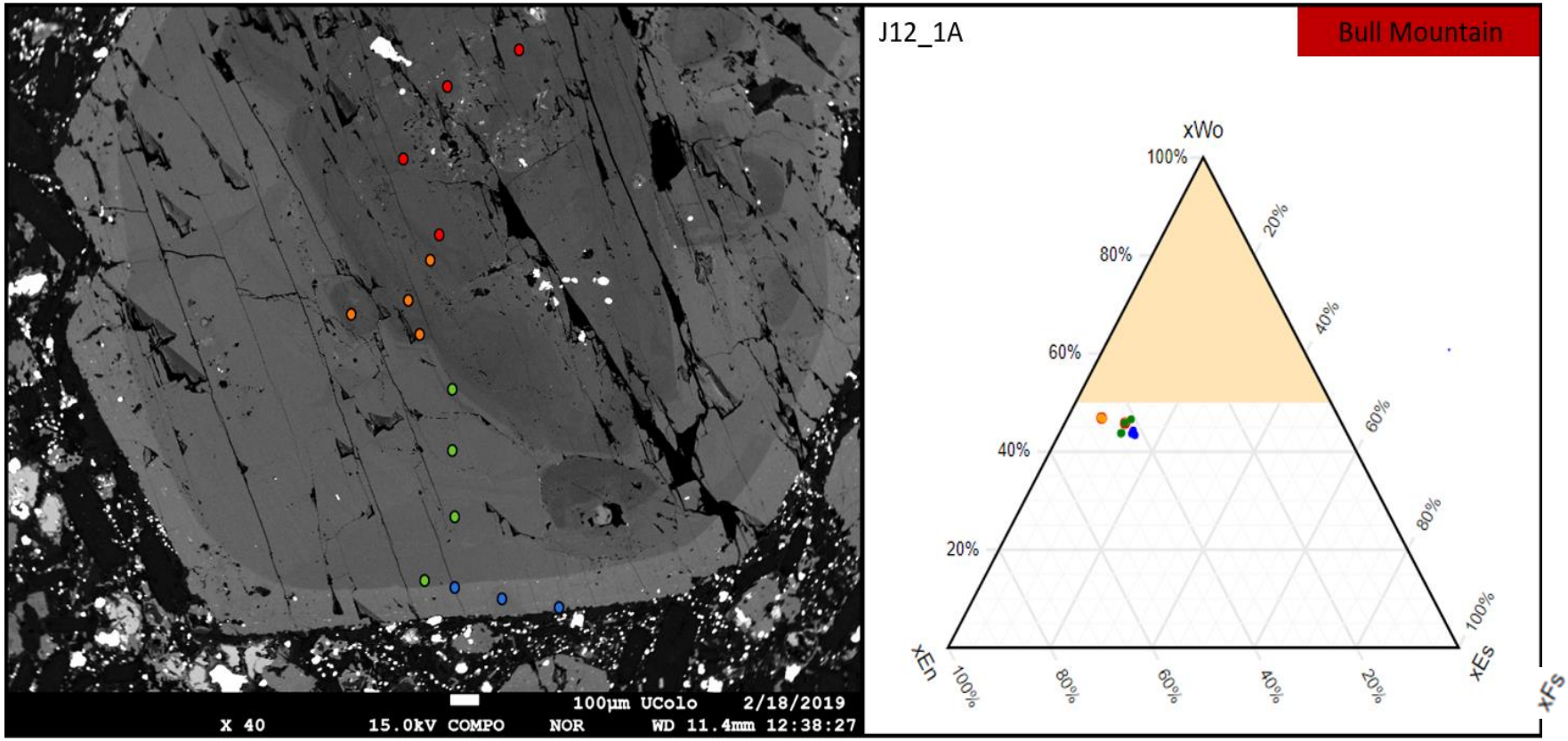

Figure 35: BSE and Ternary Diagram for the analytical traverse from core to rim across pyroxene crystal 1A, Slide J12, from the Bull Mountain Range.

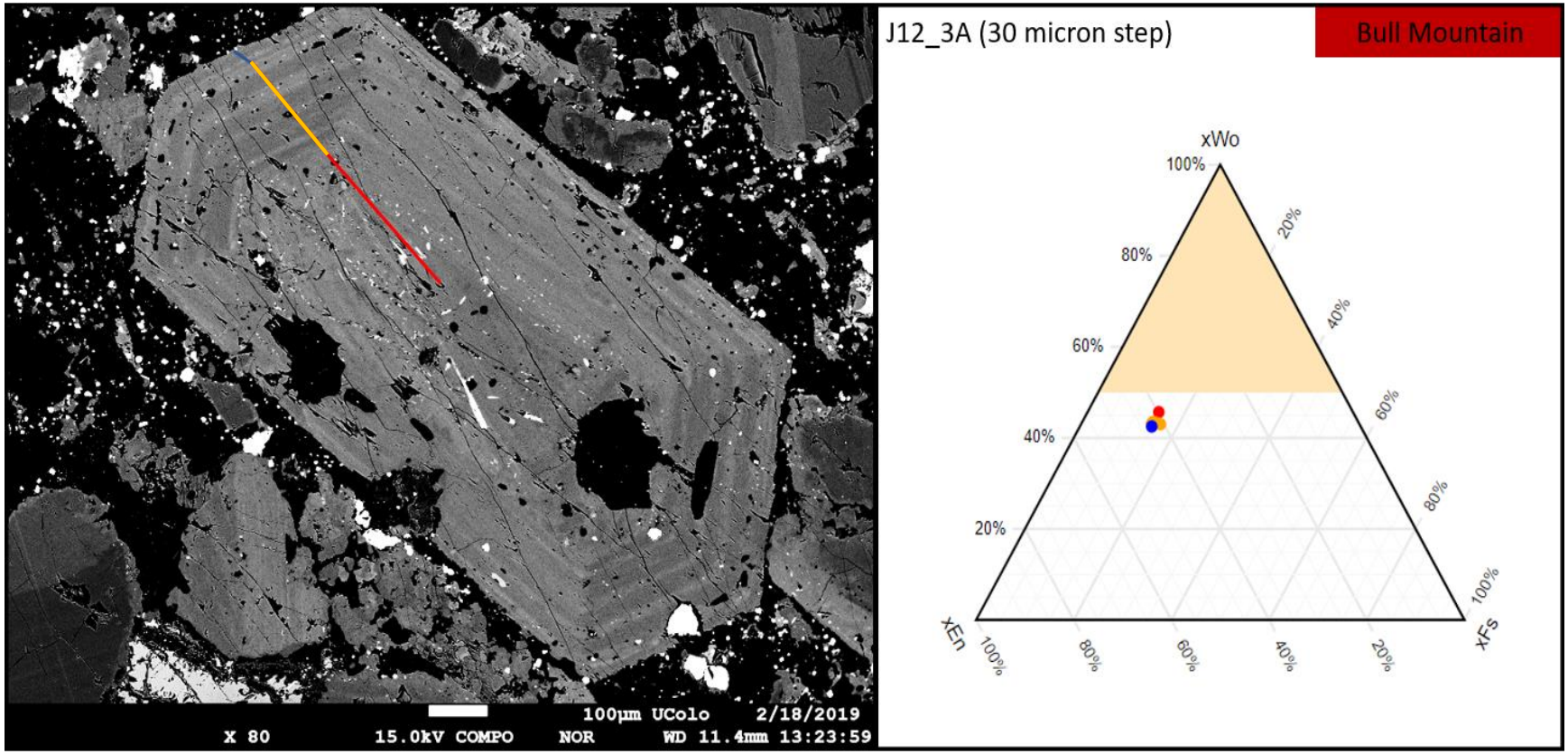

Figure 36: BSE and Ternary Diagram for the analytical traverse from core to rim across pyroxene crystal 3A, Slide J12, from the Bull Mountain Range. Traverse utilized a 30-micron step.

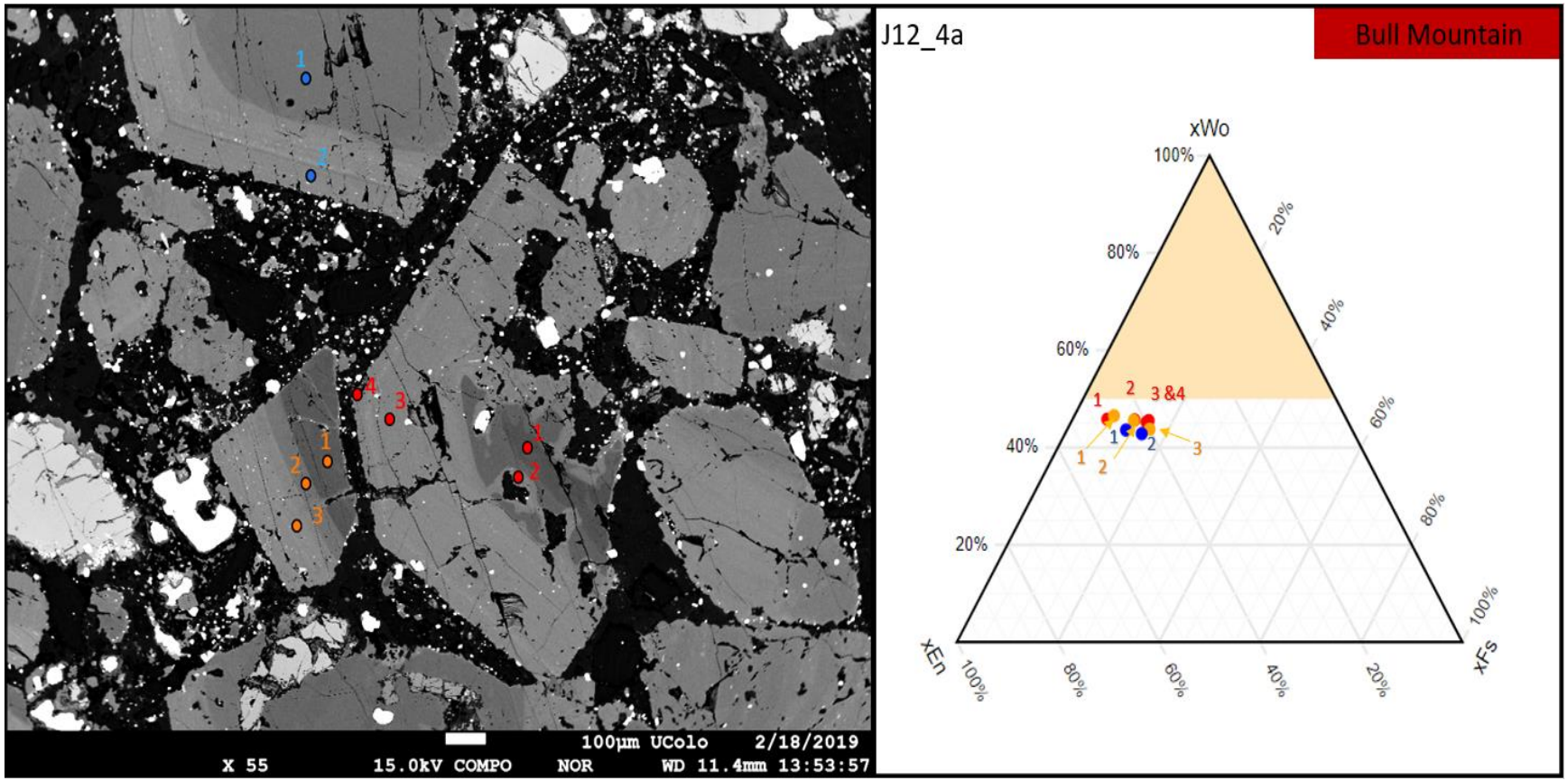

Figure 37: BSE and Ternary Diagram for the analytical traverse from core to rim of three different truncated crystals denoted as 4A, Slide J12, from the Bull Mountain Range.

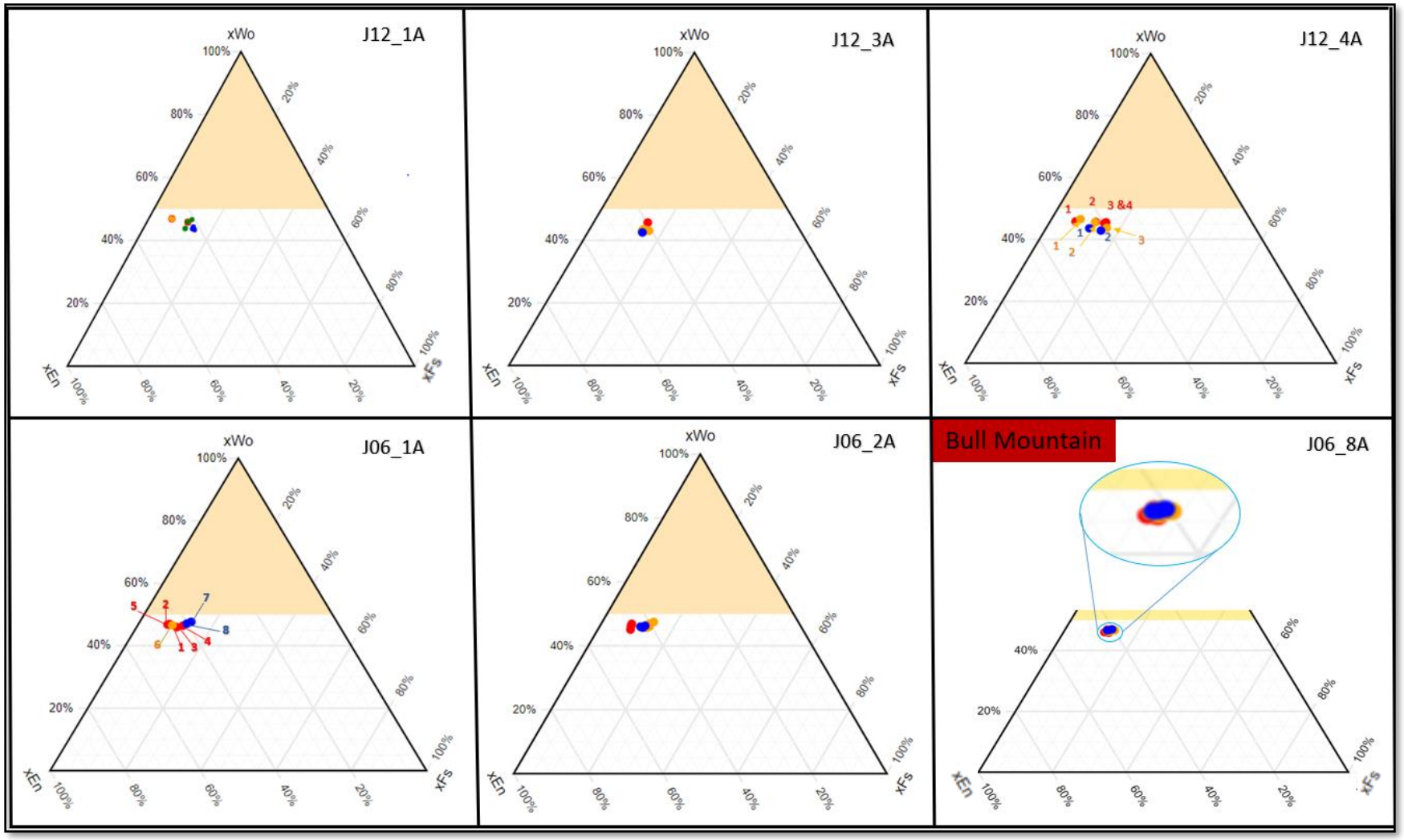

Figure 38: Compilation of pyroxene ternary diagram from Bull Mountain.

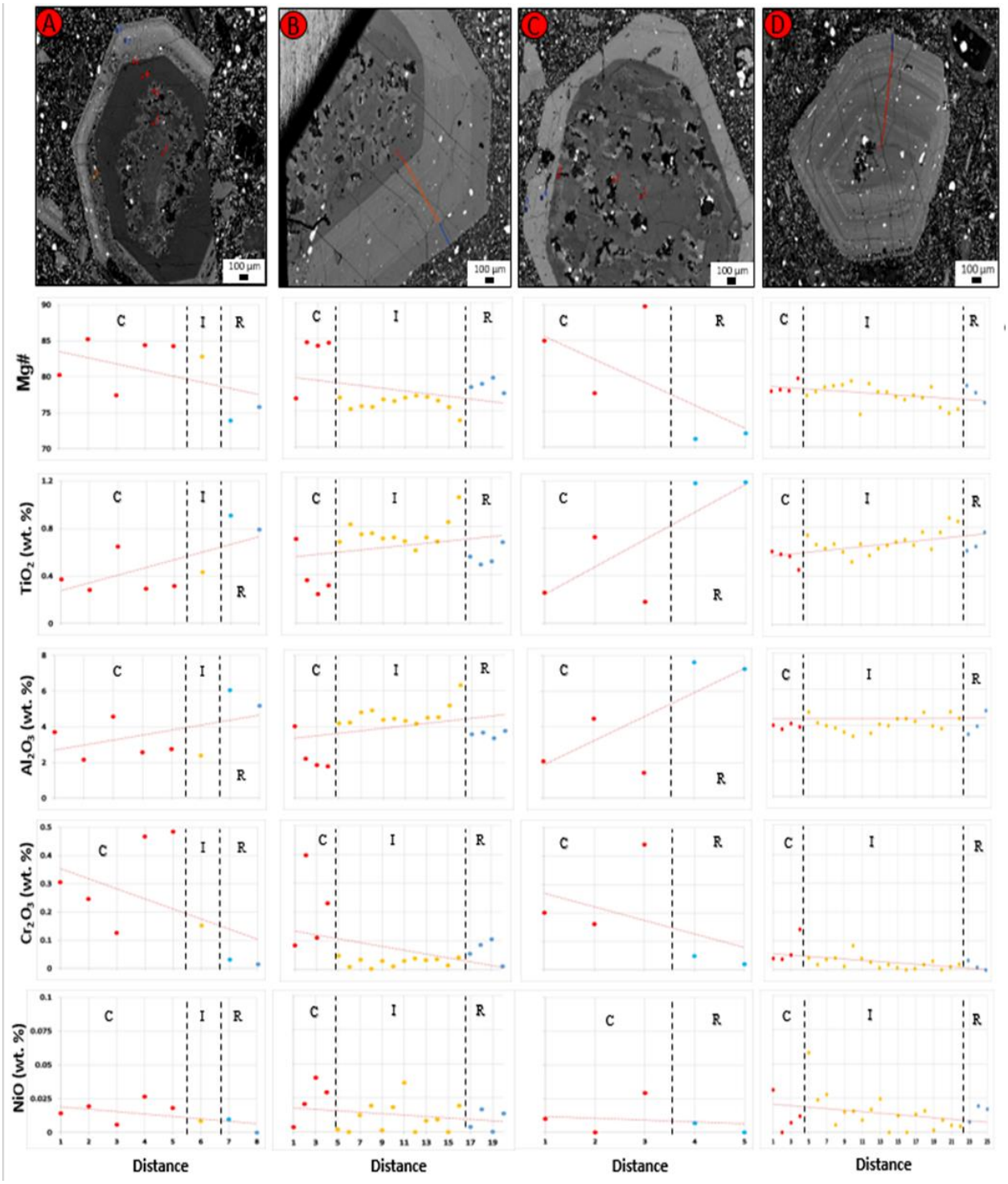

Figure 39: Lamprophyre J06 of the Bull Mountain Range. (A) crystal 1A, (B) crystal 2A, (C) crystal 5A, and (D) crystal 8A. Mineral chemistry data for Mg#, TiO_2, Al_2O_3, Cr_2O_3, and NiO plotted versus distance on select pyroxene crystals.

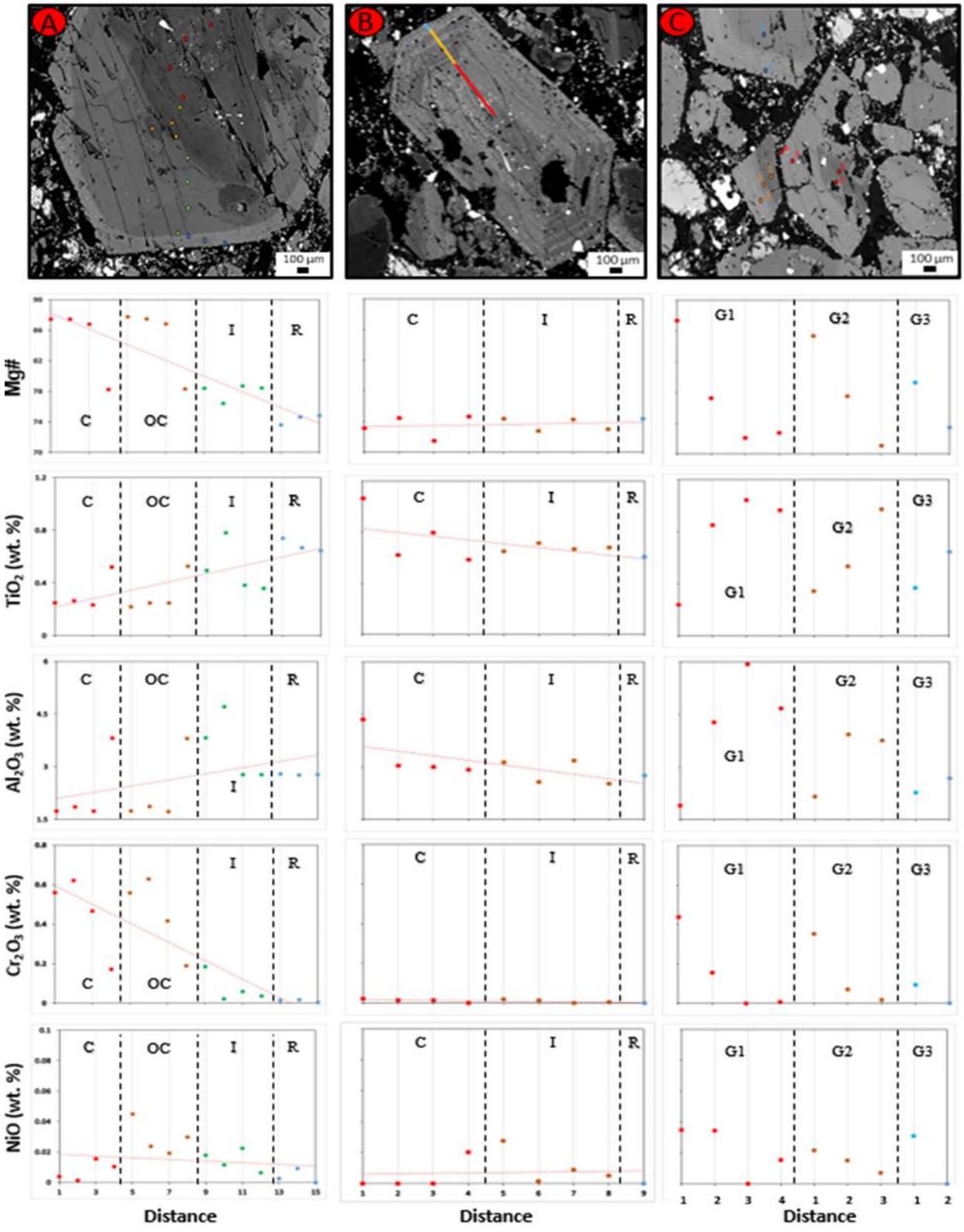

Figure 40: Lamprophyre J12 of the Bull Mountain Range. (A) crystal 1A, (B) crystal 3A, (C) crystal 4A. Mineral chemistry data for Mg#, TiO2, Al203, Cr2O3, and NiO plotted versus distance on select pyroxene crystals.

(4D. ii) Highwood Mountains Lamprophyre Mineral Chemistry

The BSE image of Highwood Mountain lamprophyre slide J18 (sannaite), crystal 1A (Fig. 41) is euhedral and has a fine-grained reaction rim when in contact with the groundmass. The crystal depicts a dimgrey colored inner core with a darker darkslategrey colored outer core that is subhedral in shape. There exist dimgrey areas around spongy texture melt pockets. The core is rich with acicular apatite crystals. Patchy zoning exists within the darker inner core and the intermediate zone and rim show concentric oscillatory zoning. Concentric zoning alters from dimgrey to lighter grey bands. The outer rim is inclusion rich and lighter dark grey in color. The ternary diagram depicts a crystal of diopside composition that experiences regression and progression with regards to Fe content. From points 1 to 2, the crystal slightly increases in Fe content. At point 3, inside the darker colored darkslategrey outer core, the composition regresses and becomes more Mg rich. The composition of point 4 is close to those of points 1 and 2 inside the core. The rest of the pyroxene composition progresses towards a more Fe rich diopside but there is a slight regression at points 5 and 7 on the dimgrey bands of the concentrically zoned rim. Along the analytical traverse (Fig. 50 a), the Mg#, Na_2O, and NiO decrease from core to rim. TiO_2 and Al_2O_3 both increase from core to rim. There is a strong contrast from core to outer core compositional values. The rim of the crystal is enriched in Cr_2O_3 compared to the core. This crystal is classified as normal zoned with respect to Fe:Mg, but Cr_2O_3 and Na_2O are anomalous,displaying discontinuous trends along the analytical traverse.

The BSE image from crystal 2A of the same lamprophyre (Fig. 42), shows a euhedral crystal featuring complex zonations and a faint reaction rim along the margins of the crystal. A dimgrey colored inner core exists with a darker darkslategrey colored subhedral outer core. Spongy textured melt pockets are confined to the lighter dimgrey portions of the core but does exists within the intermediate zone to a lesser extent. This crystal is complexly zoned because both patchy zoning and signs of

concentric zoning are present within the core. The intermediate and rim of the crystal is concentrically zoned with darkslategrey and dimgrey alternating bands. Points 9-11 represent some sort of presumed parasitic growth off the side of the main host crystal (points 1-8). The core of the parasitic crystal is dimgrey, grading into an intermediate concentrically zoned darkslategrey to grey banded region. The rim is dimgrey, rich with inclusions, and has a faint reaction rim along the crystal margin when in contact with the groundmass. The ternary diagram shows that points 1 and 2 within the core are of similar diopsidic composition. Point 3 (within the darkslategrey outer core region) shows signs of regression, decreasing in Fe content and increasing slightly in Mg content. From the intermediate zone to the rim, the Fe content of the pyroxene oscillates from regression to progression with regards to Fe content. The outermost rim of the host crystal is the most Fe rich diopsidic portion of the crystal. The parasitic crystal behaves similar to the host crystal on the pyroxene ternary diagram and on the analytical traverse (Fig. 50 b). The traverses show that Mg#, Na_2O, Cr_2O_3, and NiO decrease from core to rim. TiO_2 and Al_2O_3 increase from core to rim but experience oscillation within the data. The outer core seems to spike in Mg# and decrease in TiO_2 and Al_2O_3 content compared to the rest of the core. The crystal is classified as being normally zoned (but does feature sections of reverse zoning as evident by points 2 -3) and features discontinuous and oscillatory zoning.

The BSE image of crystal 4A from the same lamprophyre (Fig. 43) hosts a euhedral pyroxene crystal featuring complex zonations and a faint reaction rim along the margins of the crystal. This crystal is similar to J18 2A but has more elongated areas of spongy textured melt pockets within its core. The innermost anhedral core is darkslategrey and point 2 along the traverse is within a zone of concentric zoning with abnormal anhedral boundaries and is oscillating from grey to dimgrey thin bands. Point 3 exists within a bleb of spongy texture and is darkslategrey in color similar to the anhedral shaped innermost core (point 1). The outermost portion of the core is darkslategrey and the core rim shows signs of slight rounding. The concentrically zoned intermediate segment of the crystal alternates

between dimgrey to grey bands. The rim of the crystal is banded with grey to silver grey colors. There exists a distinct reaction rim around the pyroxene crystal. Acicular apatite is found in every zone of the crystal from core to rim. The pyroxene composition as shown by the ternary diagram depicts an overall progression towards a more Fe rich diopsidic composition from core to rim of this crystal. The concentrically zoned anhedral bleb within the core (point 2) is more Fe rich than other points of analysis within the core. The intermediate and rim portions of the crystal show alternating phases of increased Mg content verses a decrease in Mg content and in increase in Fe. Point 9, is what seems to be a tabular shaped partially included crystal of olivine given its fracture pattern and Mg rich and Ca deficient composition, given point 9's location on the ternary diagram. Along the analytical traverse (Fig. 50 c) the Mg#, Cr_2O_3, and NiO content decrease from core to rim. TiO_2, Al_2O_3, and Na_2O increase from core to rim. TiO_2 and Al_2O_3 fluctuate greatly in the intermediate zone along the traverse. Given the criteria above, this crystal is classified as a normal oscillatory zoned diopside.

The last crystal analyzed from lamprophyre J18 is 6a (Fig. 44). This crystal exhibits an inner core that is ovate and rounded displaying patchy zoning and faint spongy texture growth. The innermost core is dimgrey in color. Point 2 is near a lighter zone of spongy texture and is grey in color. Point 3 in the outer core is darkslategrey. The core margin is rounded in shape. There is a large portion of the crystal that is composed of concentrically zoned alternating bands. The first intermediate zone (green traverse) displays signs of spongy texture. Intermediate and rim zones are partitioned by dimgrey bands where the beginnings of spongy texture melt pockets are present. Bands alternate from grey to dimgrey in color. The outermost portion of the crystal is dark grey in color. It should be noted that points 9-14 along the traverse may be on a parasitic growth similar to other crystals from this thin section. This is perceived from the position of melt pockets around the perimeter of the parasitic crystal as well as fracture patterns. This parasitic growth of pyroxene displays continuous zoning with the host crystal, which is different than other parasitic grains observed within the same lamprophyre. The ternary

diagram depicts this crystal experienced many normal and reverse zoning events in terms of pyroxene diopside composition. The core decreases in Fe content from inner to outer core and then increases in Fe content in the first intermediate zone. The second intermediate zone decreases in Fe content. The rim increases in Fe content then regressively decreases in Fe diopsidic composition at the crystal boundary. Along the analytical traverse (Fig. 50 d), the Mg# increases slightly from core to rim, with changes in concentration at boundaries between the intermediate portions. This is present of both intermediate portions (blue and green traverse). TiO_2, Al_2O_3, Na_2O, Cr_2O_3, and NiO decrease overall from core to rim. This crystal displays both normal and reverse zoning behavior (inverse), with oscillatory and step zoning habits along the traverse.

A second lamprophyre from the Highwood Mountains analyzed was J24 (sannaite). The BSE image of crystal 1a (Fig. 46) exhibits a euhedral crystal with a faint (~10 µm) reaction rim of biotite surrounding the pyroxene crystal. The core exhibits minor spongy texture with apatite inclusions. The Inner core is grey with a dim grey outer core. The rim is grey in color and is riddled with inclusions, micas, and small pockets of spongy texture. The pyroxene composition ternary diagram for this sample shows that the inner core (red points 1-3) is diopsidic in composition. The outer core (yellow points 4-6) regresses towards a more Mg rich pyroxene. At the rim of the crystal there is a shift towards a more Fe rich diopside composition. Point 8 was excluded because the data shows that it is chemically different from all other points, thus an inclusion was probably hit by the microprobe. Along the analytical traverse (Fig. 51 a), Mg# decreases slightly while Cr_2O_3 increases slightly from core to rim. TiO_2 and Na_2O content decrease from core to rim. Curiously enough, Al_2O_3 content increases from core to rim. This crystal exhibits both normal and reverse zoned behavior (with regards to Cr_2O_3) but is ultimately classified as normal zoned with step zoning characteristics within the compositional data.

The BSE image from lamprophyre J24, crystal 4A (Fig. 47) depicts a tabular, euhedral pyroxene crystal with a defined core region, abundant inclusions, and a reaction rim at the crystal boundary. The

core displays spongy texture and faint patchy zoning and spongy texture. The innermost core is dimgrey. The lighter colored grey portion of the core is confined by a darkslategrey outer core. The crystal has a dimgrey colored intermediate zone with a rim that has small distinct grey bands. There are resorbed margins along the edge of the crystal. Where the pyroxene crystal comes into contact with the groundmass, fine grained biotite's are prevalent on the pyroxene margin. The ternary diagram shows the crystal from the center of the core to middle of the core (point 1 to 2) increasing in Ca content crossing the 50% margin (yellow line on the ternary diagram). However, this spike in Ca content could be attributed to the microprobe mixing pyroxene analysis with apatite inclusions. The outer core becomes more Mg rich. The intermediate zone becomes more Fe rich and the outer most portion of the rim regresses slightly in regard to Fe content. Much like crystal 1A, this crystal (4A) displays anomalous traverse data. From the analytical traverse (Fig. 51 b), one can see that Mg#, NiO, TiO_2 and Al_2O_3 increase from core to rim. Al_2O_3 and TiO_2 oscillate in the traverse data. Point 3 was excluded from analysis because the Fe content measured at that spot along the transect is anomalously high when compared to the rest of the pyroxene analysis from the same thin section. The Fe spike could be attributed to a magnetite inclusion (which is fairly common in spongy texture zones), but it is most likely an inclusion of biotite that was hit by the microprobe beam because of the extremely high level of Al at that particular point. Regardless of what phase point 3 is, by its position on the ternary diagram, it is definitely not diopsidic in composition. This crystal displays reverse zoning which shifts to normal behavior (Inverse), and this pyroxene exhibits oscillatory and step zoning characteristic of the data.

Crystal 6A of the same lamprophyre (Fig. 48) is a euhedral pyroxene displaying a complex core structure and abundant spongy texture melt pockets within the intermediate segment of the crystal. An oddity for sure, an irregular shaped circular-rounded mass of darkslategrey inner core exists. Between these circular core 'blebs' is a spongy textured, patchy zoned dimgrey core region. It should be noted that spongy texture is also present within the intermediate and rim sections of the crystals in greater

size and quantity. The intermediate dimgrey zones contain some patchy zoning and darker darkslategrey banding that are euhedral shaped at their margin with the rim. The rim contains grey bands along the rim. The ternary diagram shows the dark colored inner core is less Fe diopsidic in composition and the crystal progressively becomes more Fe rich in diopside composition. There is significant regression towards a more Mg rich pyroxene composition along zones of spongy texture in the intermediate region of the crystal. Point 7, along the lighter colored rim, displays an Fe rich composition close to that of hedenbergite, rather than diopside. The analytical traverse displays (Fig. 51 c) Mg#, Cr_2O_3, Na_2O, and NiO content decreasing from core to rim, while TiO_2 increases slightly from core to rim. Based on Fe and Mg composition crystal 6a is classified as a normal patchy zoned pyroxene crystal.

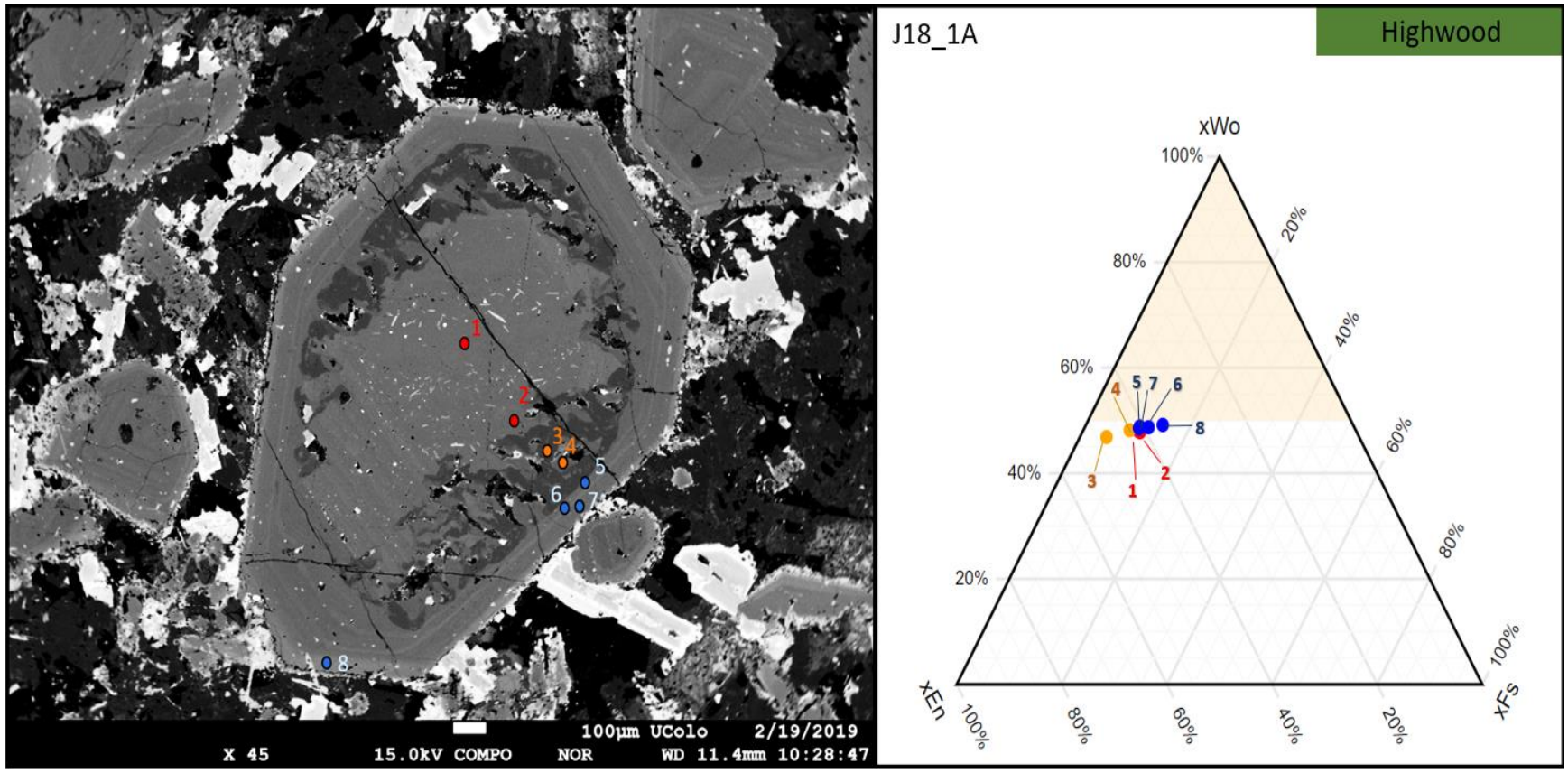

Figure 41: BSE and Ternary Diagram for the analytical traverse from core to rim across pyroxene crystal 1A, Slide J18, from the Highwood Mountains.

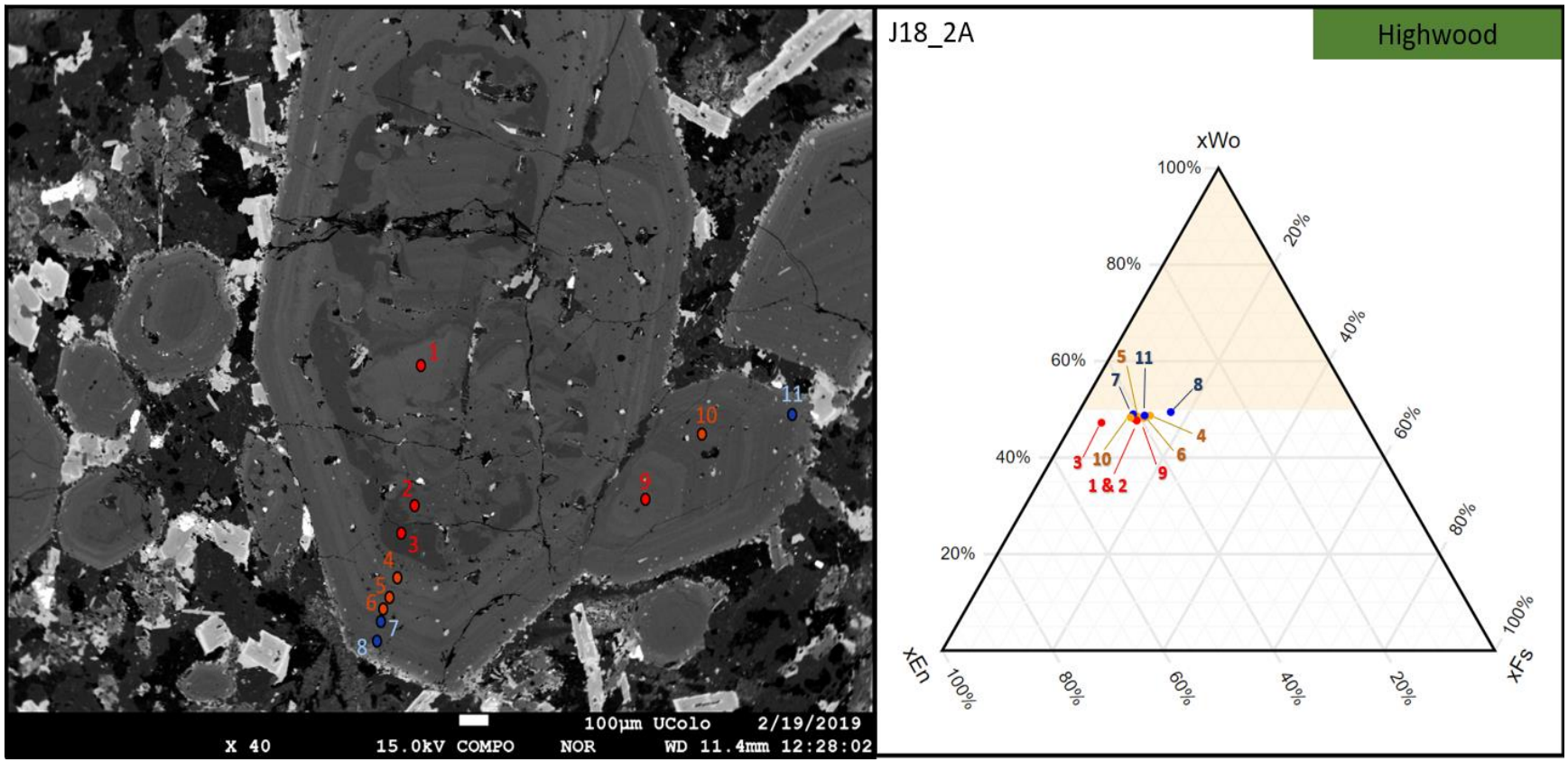

Figure 42: BSE and Ternary Diagram for the analytical traverse from core to rim across pyroxene crystal 2A, Slide J18, from the Highwood Mountains.

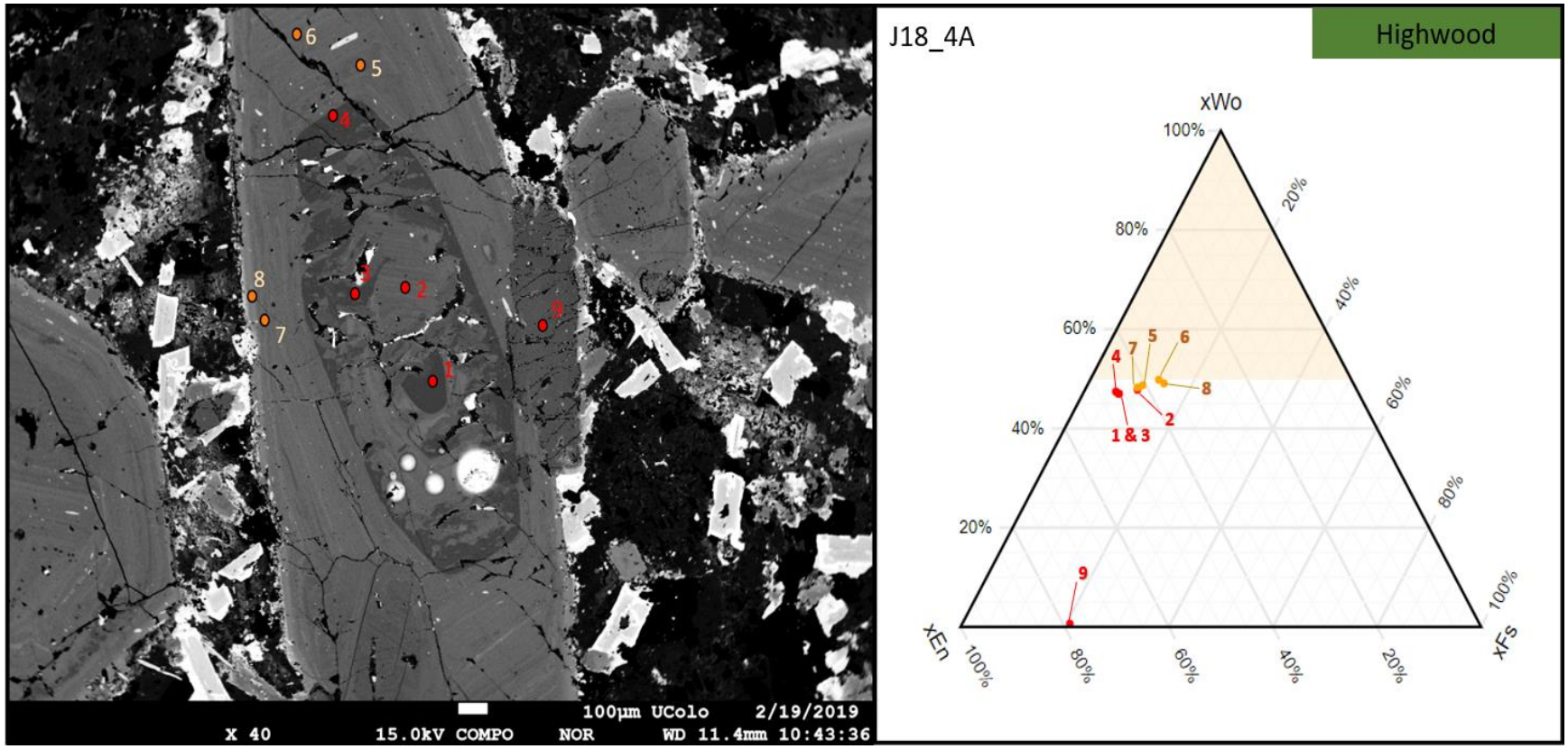

Figure 43: BSE and Ternary Diagram for the analytical traverse from core to rim across pyroxene crystal 4A, Slide J18, from the Highwood Mountains.

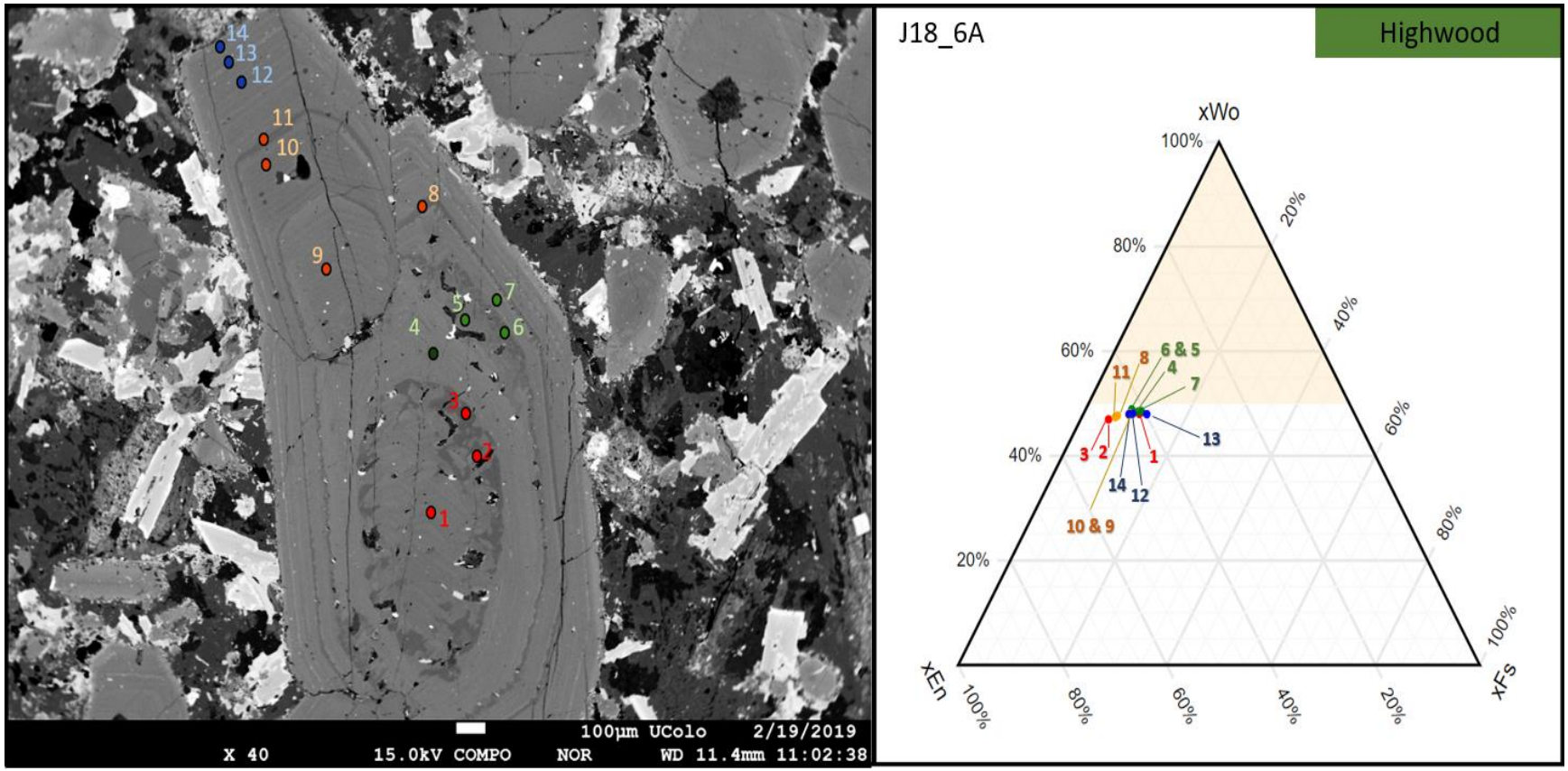

Figure 44: BSE and Ternary Diagram for the analytical traverse from core to rim across pyroxene crystal 6A, Slide J18, from the Highwood Mountains.

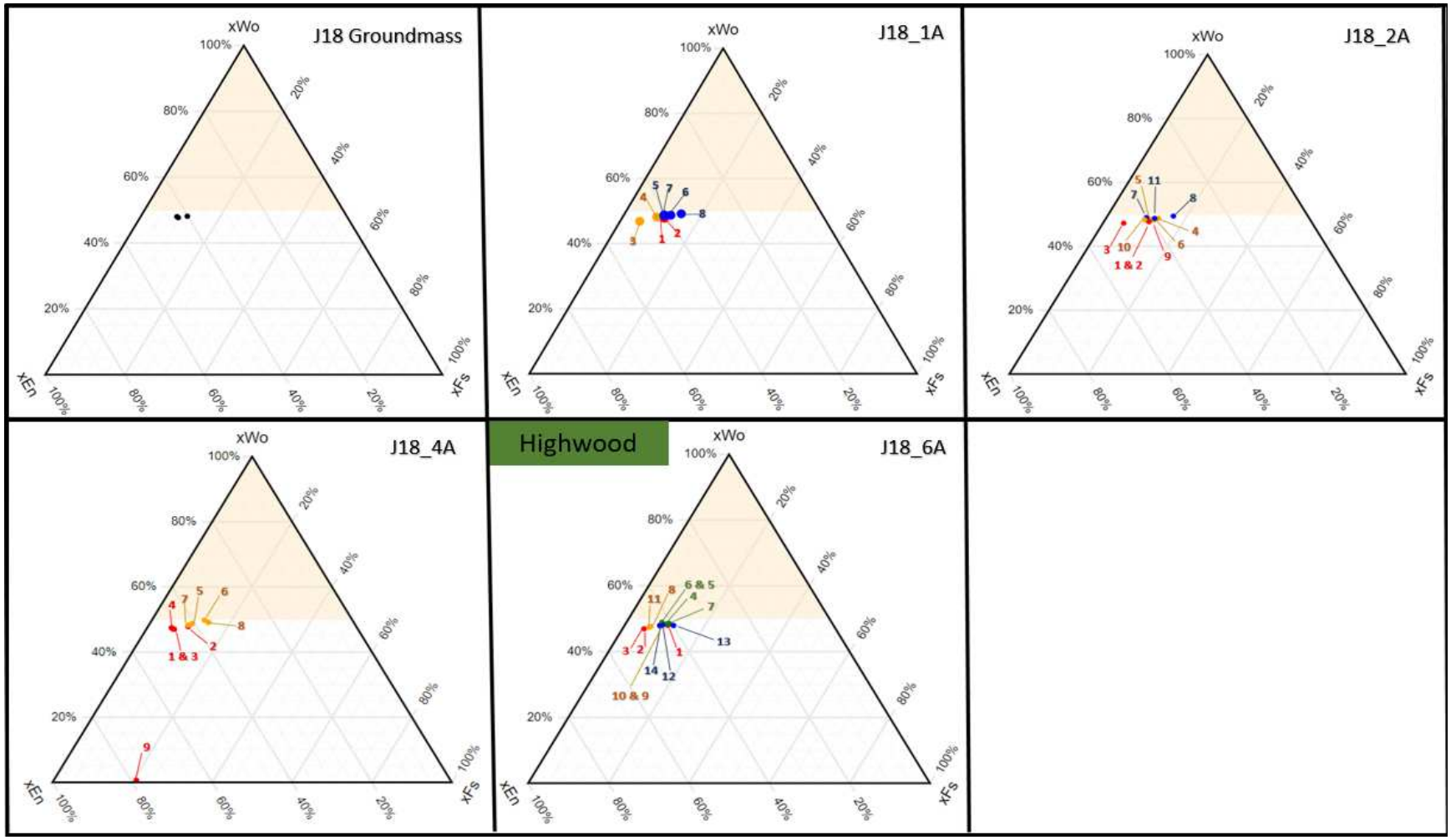

Figure 45: Compilation of pyroxene ternary diagrams from lamprophyre J18 of the Highwood Mountains.

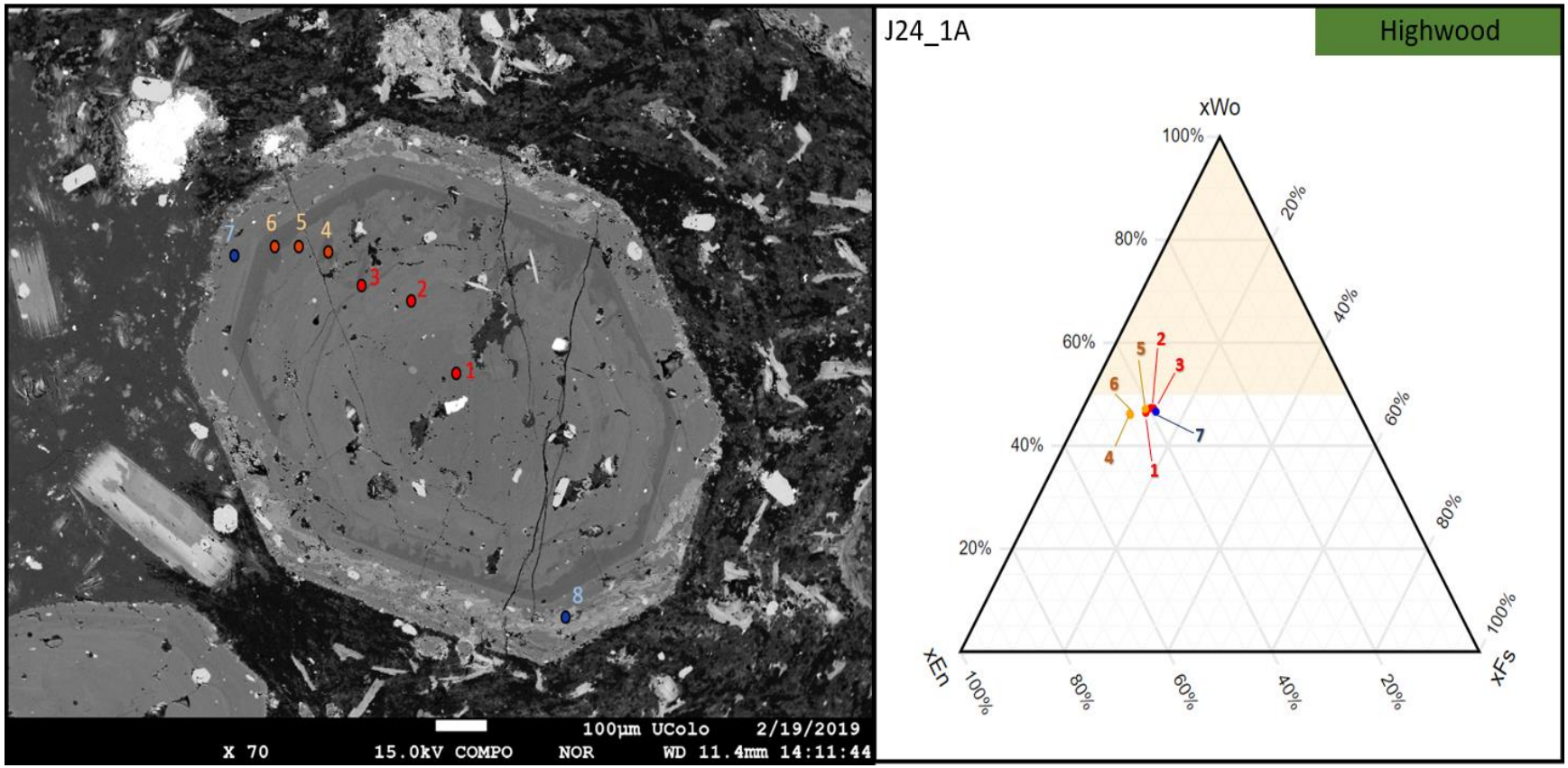

Figure 46: BSE and Ternary Diagram for the analytical traverse from core to rim across pyroxene crystal 1A, Slide J24, from the Highwood Mountains.

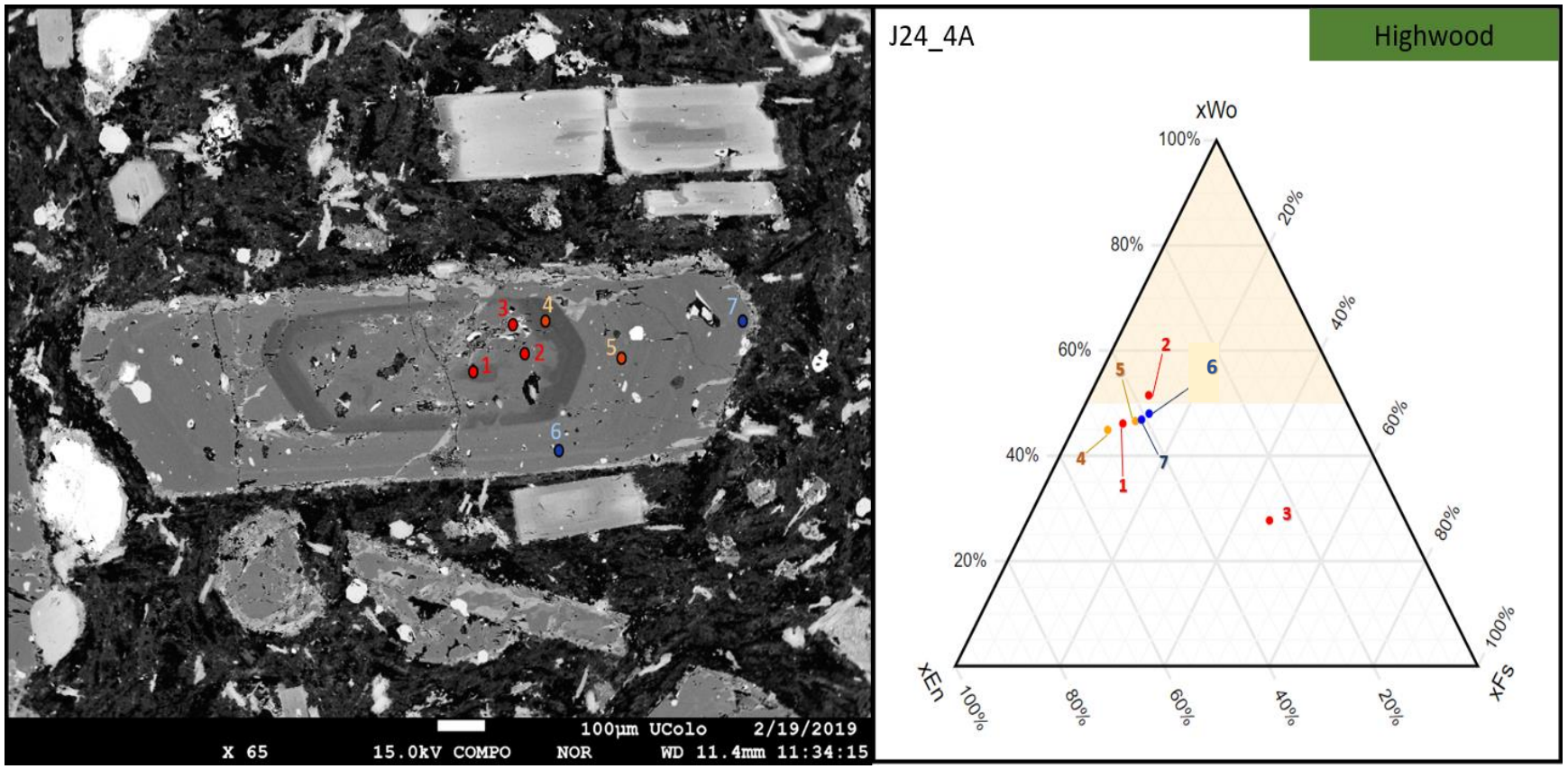

Figure 47: BSE and Ternary Diagram for the analytical traverse from core to rim across pyroxene crystal 4A, Slide J24, from the Highwood Mountains.

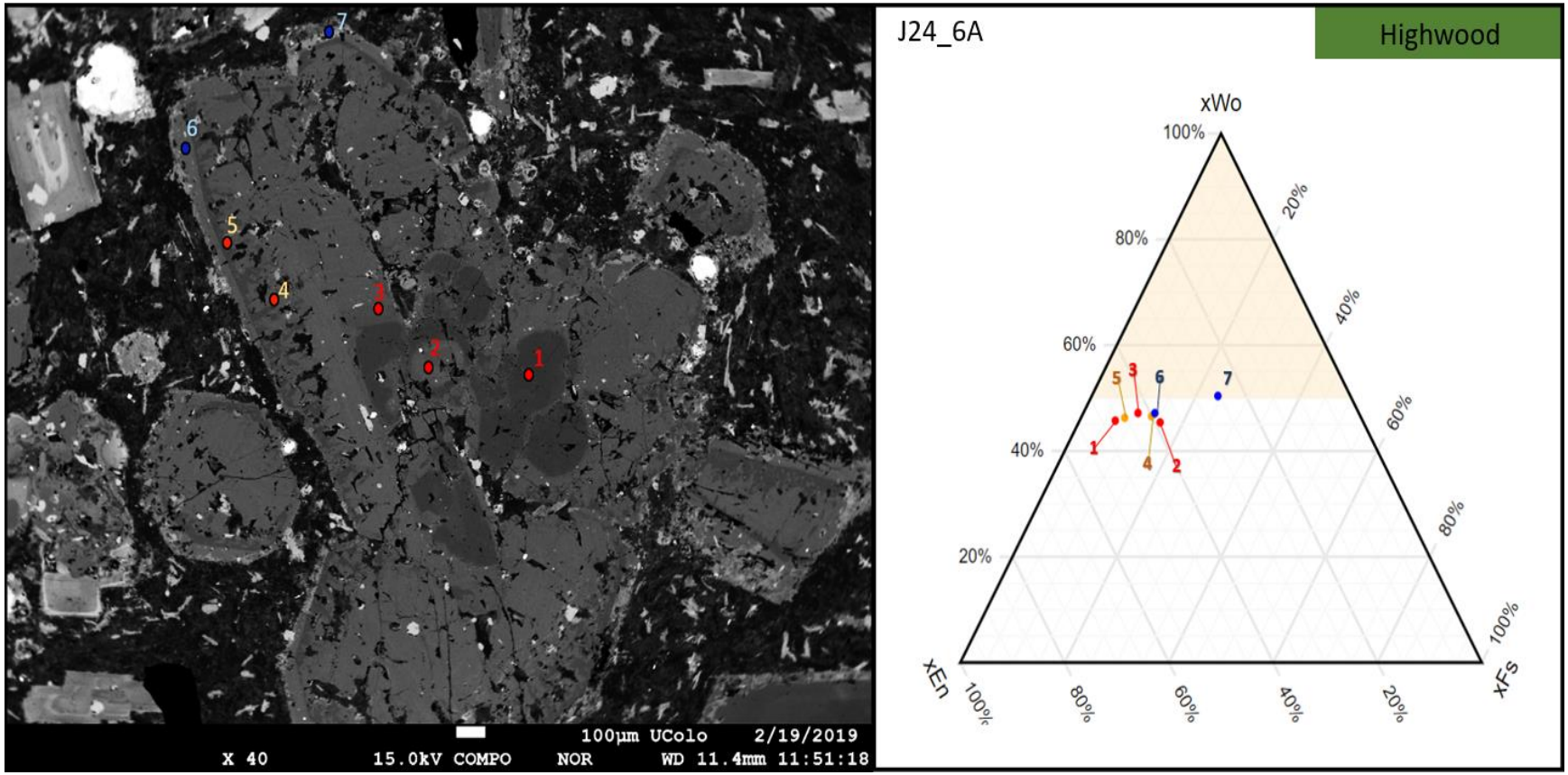

Figure 48: BSE and Ternary Diagram for the analytical traverse from core to rim across pyroxene crystal 6A, Slide J24, from the Highwood Mountains.

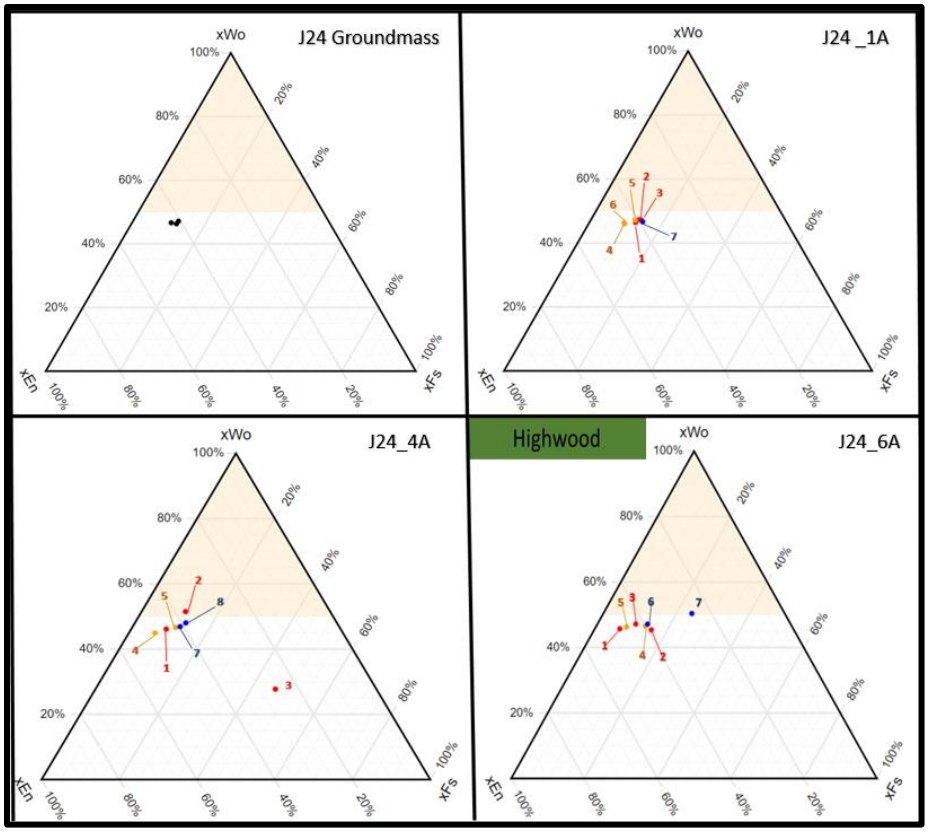

Figure 49: Compilation of pyroxene ternary diagrams from lamprophyre J24 of the Highwood Mountains.

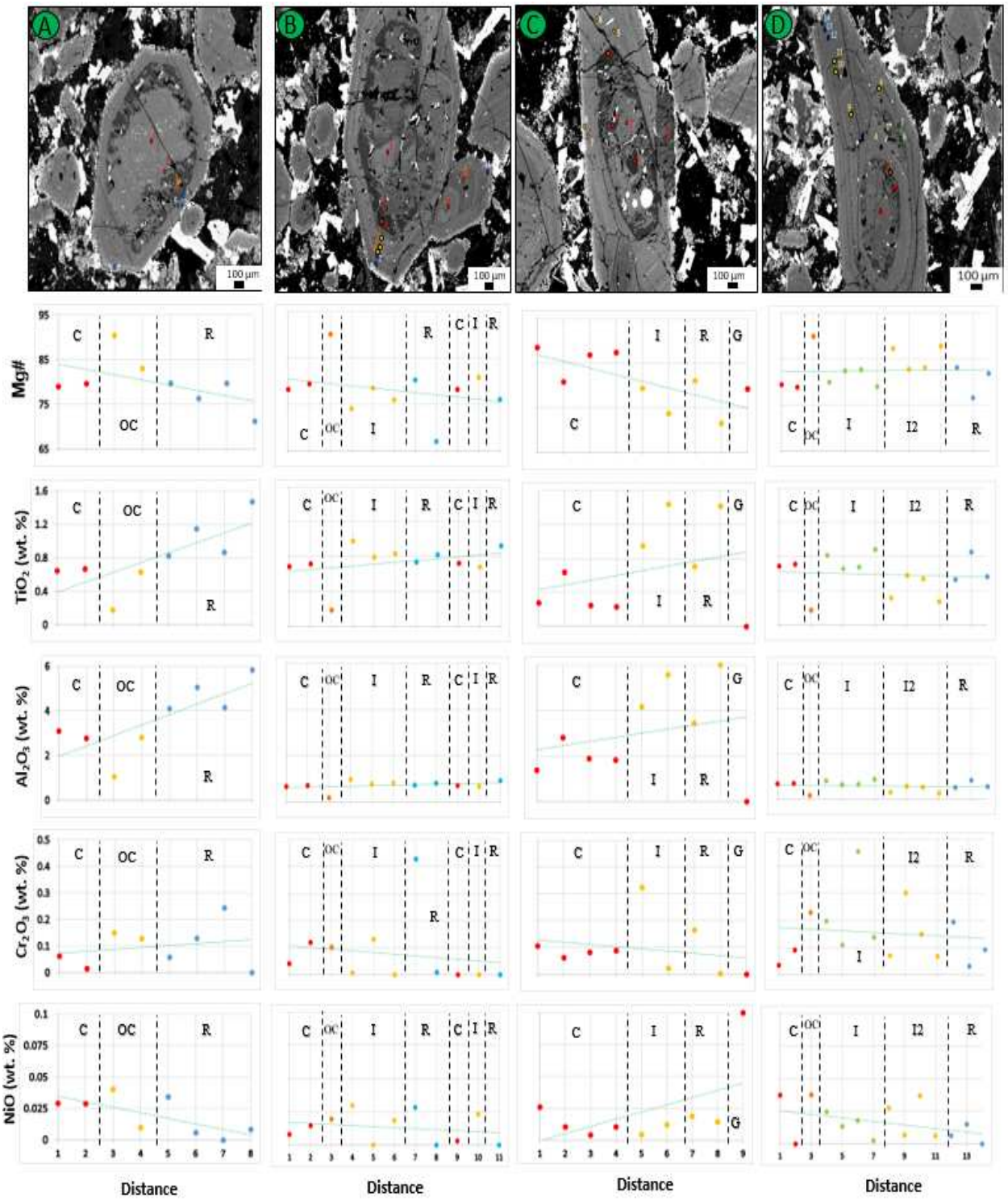

Figure 50: Lamprophyre J18 of the Highwood Mountain Range. (A) crystal 1A, (B) crystal 2A, (C) crystal 4A, (D) crystal 6A. Mineral chemistry data for Mg#, TiO2, Al203, Cr2O3, and NiO plotted versus distance on select pyroxene crystals.

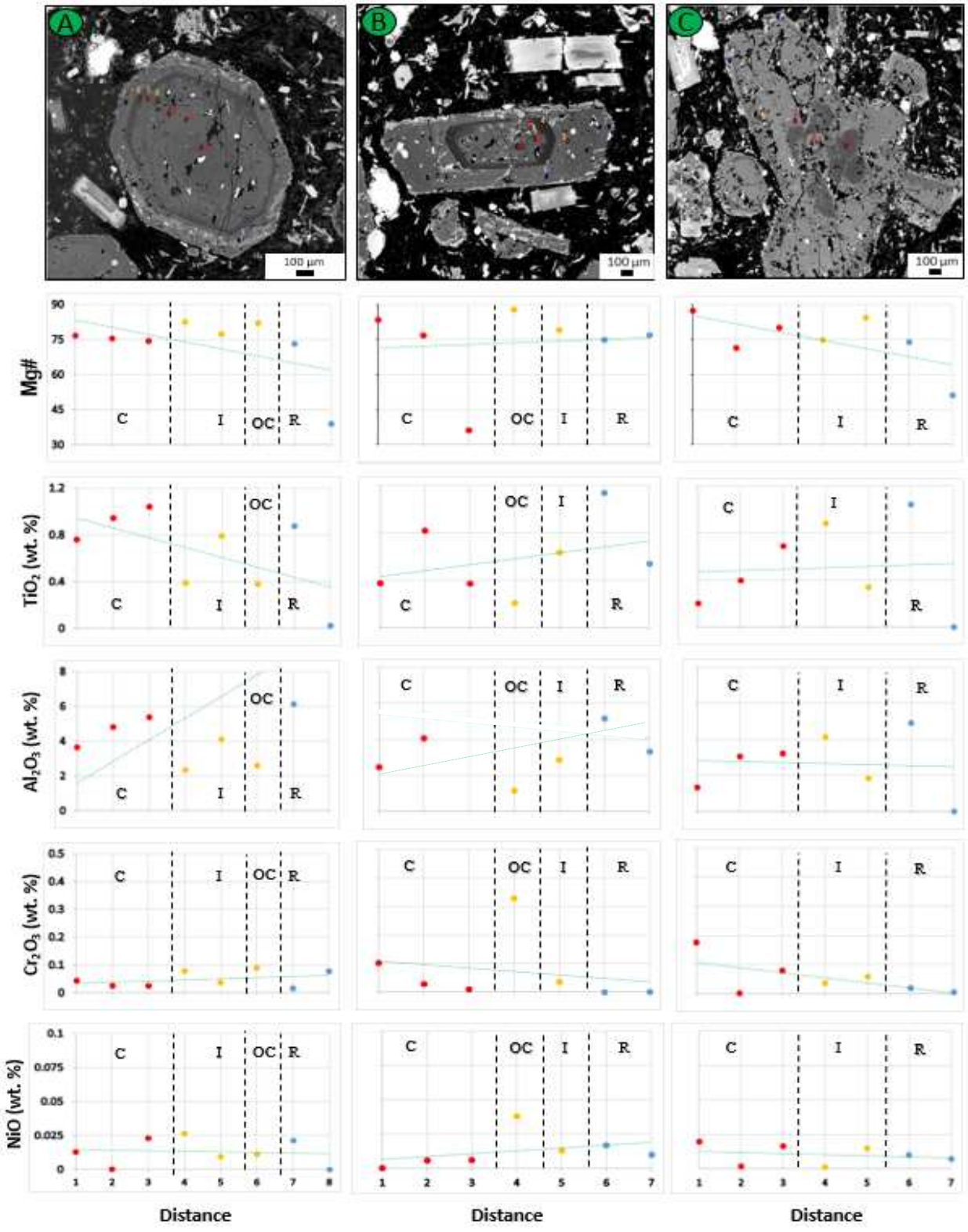

Figure 51: Lamprophyre J24 of the Highwood Mountain Range. (A) crystal 1A, (B) crystal 4A, (C) crystal 6A. Mineral chemistry data for Mg#, TiO2, Al203, Cr2O3, and NiO plotted versus distance on select pyroxene crystals.

(4D. iii) Crazy Mountain Lamprophyre Mineral Chemistry

The BSE image of Crazy Mountain lamprophyre slide J_32_3 (monchiquite), crystal 2A (Fig. 52) is subhedral, patchy zoned, and shows signs of resorption along the rim of the crystal. The crystal has an anhedral shaped darkslategrey core region with an intermediate zone displaying patchy zonation and abundant spongy textured melt pockets. Patchy zonation ranges from light grey to grey. There appears to be remnants of an outer dimgrey colored zonation that has been corroded and no longer exists on every side of the crystal. From the pyroxene composition ternary diagram one can see that the core becomes more Mg rich towards the outer core. The patchy zoned intermediate zone becomes progressively more Fe rich. The analytical traverse (Fig. 56 a) depicts Mg#, Al_2O_3, and Na_2O content decreasing overall from core to rim. The data strongly fluctuates in the intermediate zone with respect to Al_2O_3 and TiO_2. TiO_2 and NiO content increase from core to rim. Sharp dips in the traverse occur at the boundary between the core, intermediate zone, and the rim. It is unusual that TiO_2 and Al_2O_3 do not mirror each other along the compositional traverses. This crystal is classified as a normal zoned crystal (based on Fe and Mg content) experiencing oscillatory and patchy zoning.

Within the same lamprophyre crystal 4A (Fig. 53) is subhedral and complexly zoned. Edges look truncated and corroded. The crystal exhibits a darker dimgrey core with a concentrically zoned intermediate region alternating from bands of grey to bands of dimgrey. Grey bands preferentially contain pronounced spongy texture. The rim is concentrically zoned and alternates from grey to dimgrey bands. Light colored bands in the rim have spongy texture similar to the intermediate zone. The pyroxene composition ternary diagram shows that all points plot within the diopside field. The composition of the crystal becomes increasingly Fe rich from the core to the intermediate zone. The rim (blue traverse) decreases in Fe content relative to the intermediate segment of the crystal. Along the analytical traverse (Fig. 56 b), the Mg#, TiO_2, and Na_2O content increase from core to rim. Al_2O_3, Cr_2O_3, and NiO decrease from core to rim. Al_2O_3 and TiO_2 data show characteristic patterns of oscillatory

zoning. The exact type of zoning within this pyroxene crystal does not match up with any sort of compositional standard set forth in Rock (1991) but does show signs of both normal and reverse zoning (inverse). Based off the ternary diagram and analytical traverse the crystal is defined as discontinuous and oscillatory zoned.

The second lamprophyre from the Crazy Mountains analyzed with the microprobe was crystal J36 (sannaite). The BSE image of crystal 3a (Fig. 54) depicts a subhedral crystal with concentric zoning and a resorbed crystal boundary. A darkslategrey inner rounded core is surrounded by concentrically zoned bands of dimgrey and darkslategrey repeated banding. The rim is inclusion rich and is darkslategrey in color. Spongy texture melt pocket growth exists near points 2 and 3 outside of the inner core. Mineral inclusions exist in every portion of the crystal except for the innermost region of the core. The pyroxene composition ternary diagram depicts Fe content decreasing from the inner core to the outer core. The intermediate zone increases in hedenbergite content except for the darker darkslategrey bands (point 5) which regress towards a more Mg rich pyroxene composition with similar levels to that of the inner core. The rims composition is similar to that of the inner core. Along the analytical traverse (Fig. 56 c), the Mg# and Al_2O_3 content increase from core to rim in an oscillatory fashion. TiO_2 and Na_2O decrease from core to rim. Cr_2O_3 and NiO signatures mirror that of Mg# but to a lesser extent. It is strange that the innermost core and the outermost margin of the rim display discontinuous peaks of elevated Mg#, Cr_2O_3, and NiO content. This crystal is a normal to reverse zoned (inverse) diopside crystal displaying both discontinuous and oscillatory features along the analytical traverse.

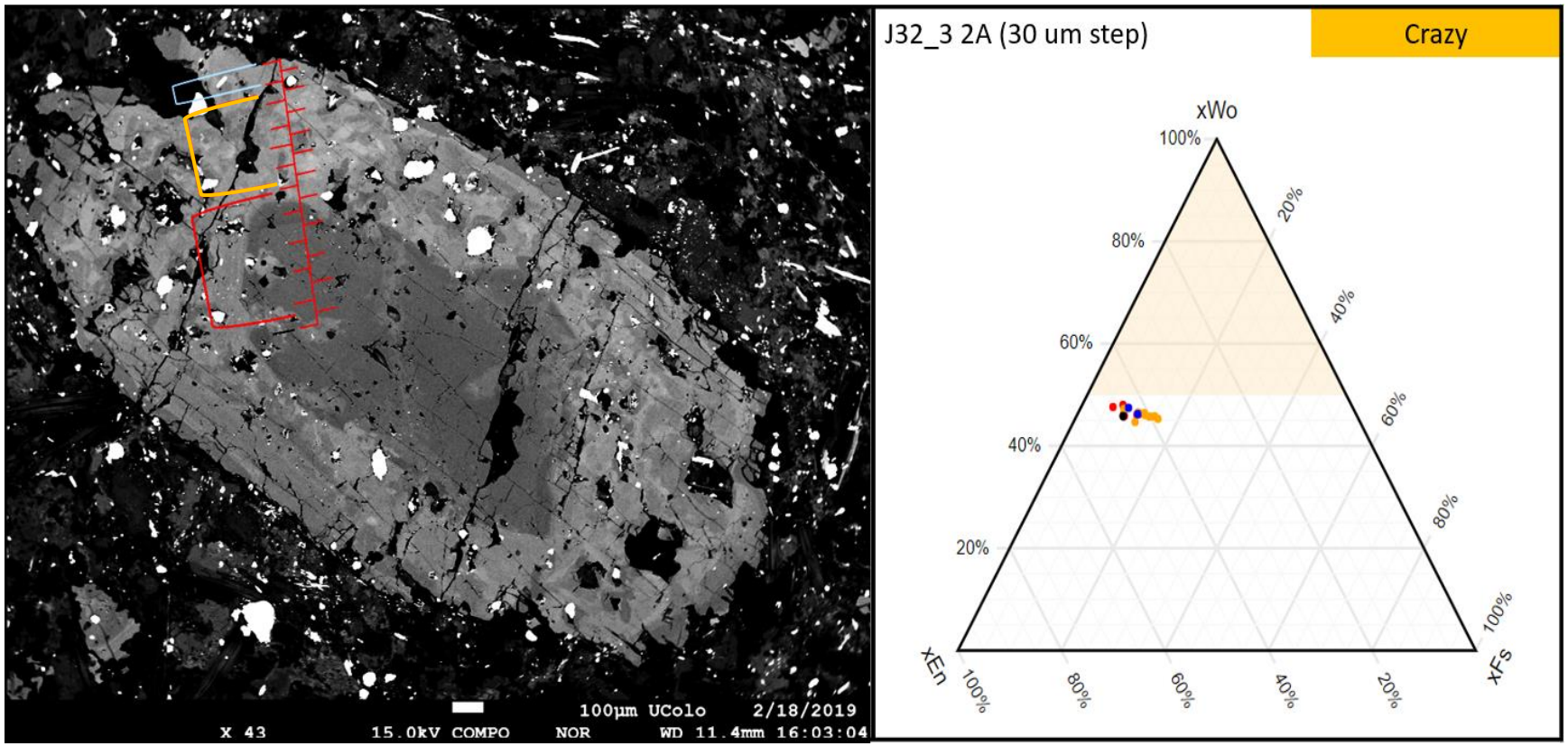

Figure 52: BSE and Ternary Diagram for the analytical traverse from core to rim across pyroxene crystal 2A, Slide J32_3, from the Crazy Mountains. Traverse utilized a 30-micron step.

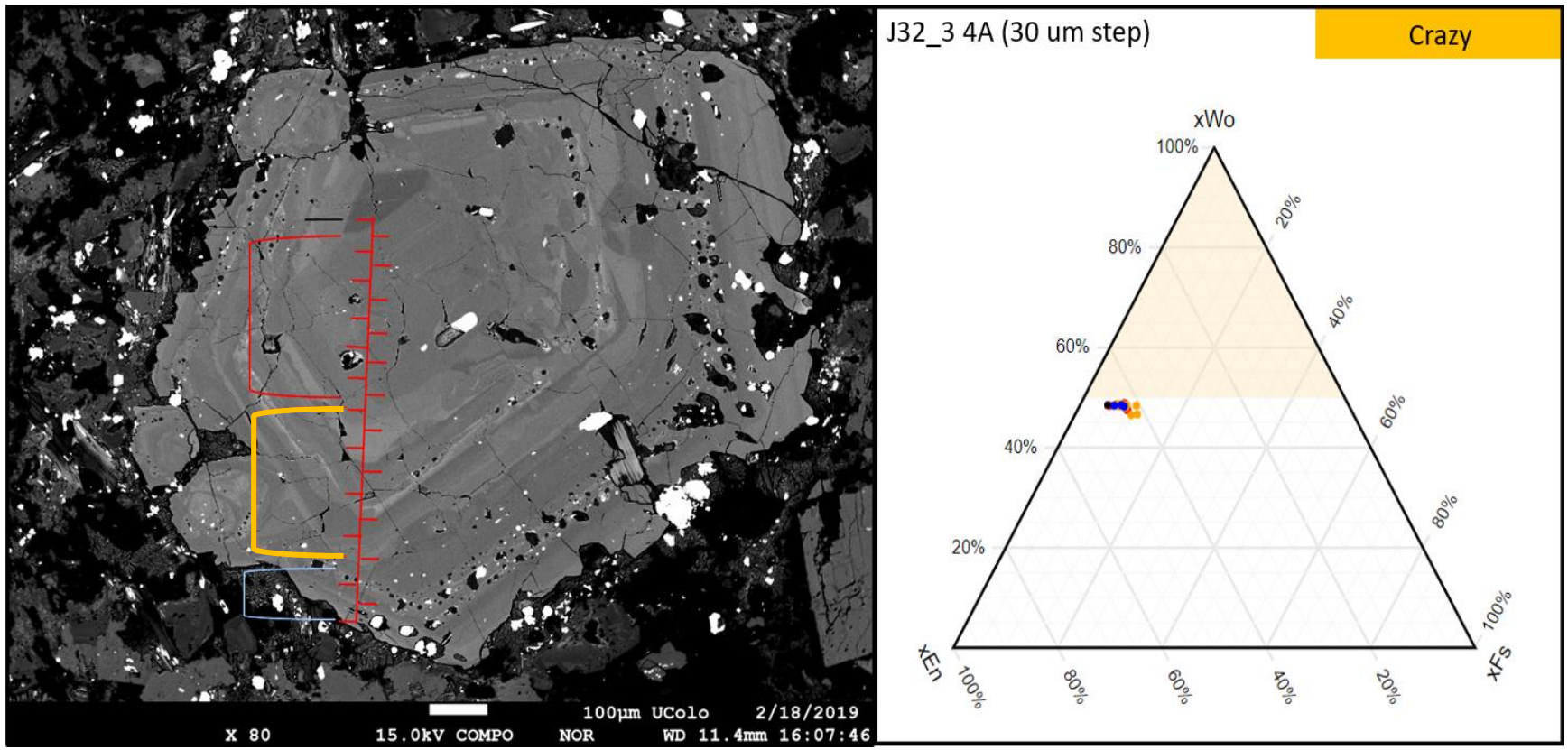

Figure 53: BSE and Ternary Diagram for the analytical traverse from core to rim across pyroxene crystal 4A, Slide J32_3, from the Crazy Mountains. Traverse utilized a 30-micron step.

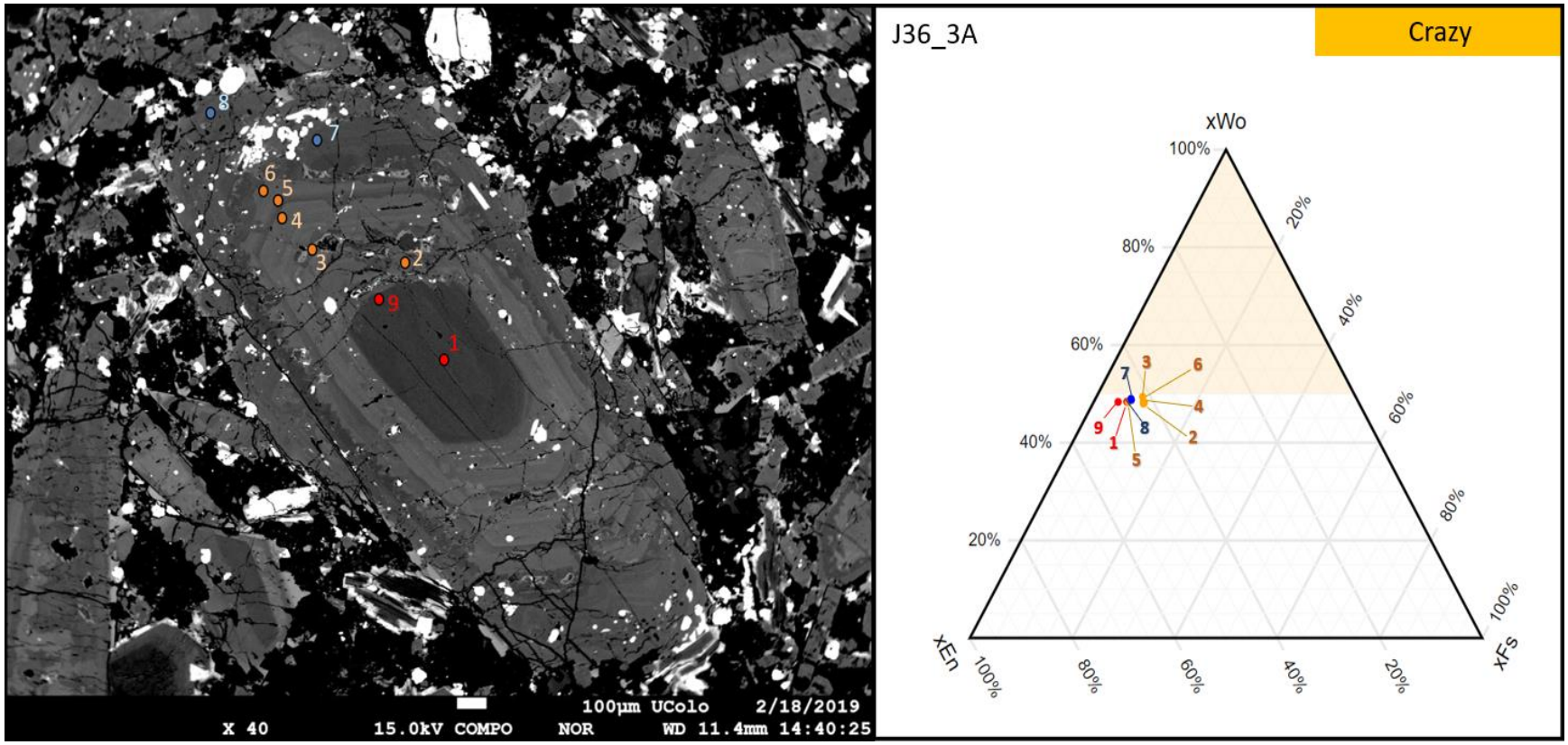

Figure 54: BSE and Ternary Diagram for the analytical traverse from core to rim across pyroxene crystal 3A, Slide J36, from the Highwood Mountains

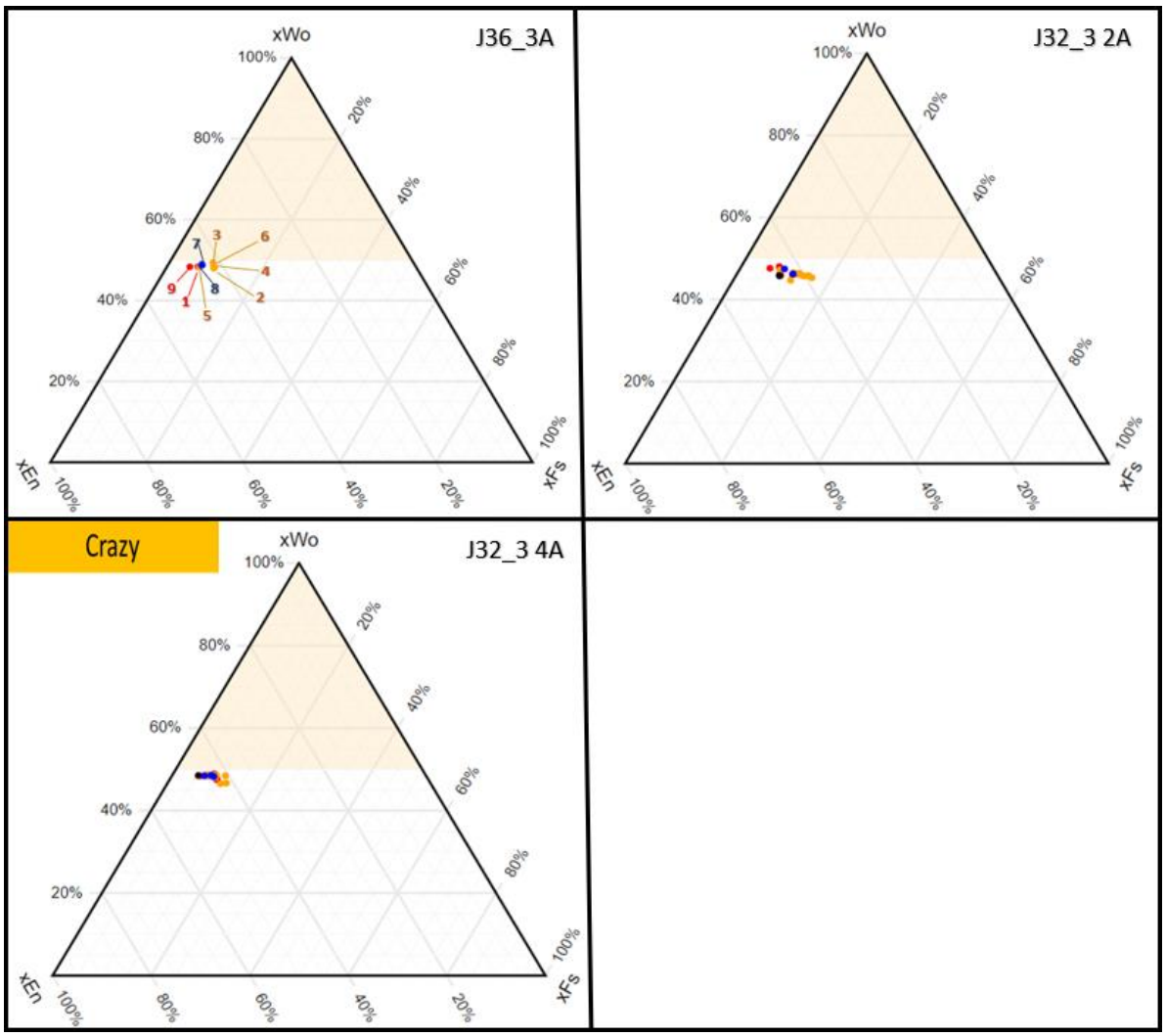

Figure 55: Compilation of pyroxene ternary diagrams from lamprophyre J32_3 and J36 of the Crazy Mountains.

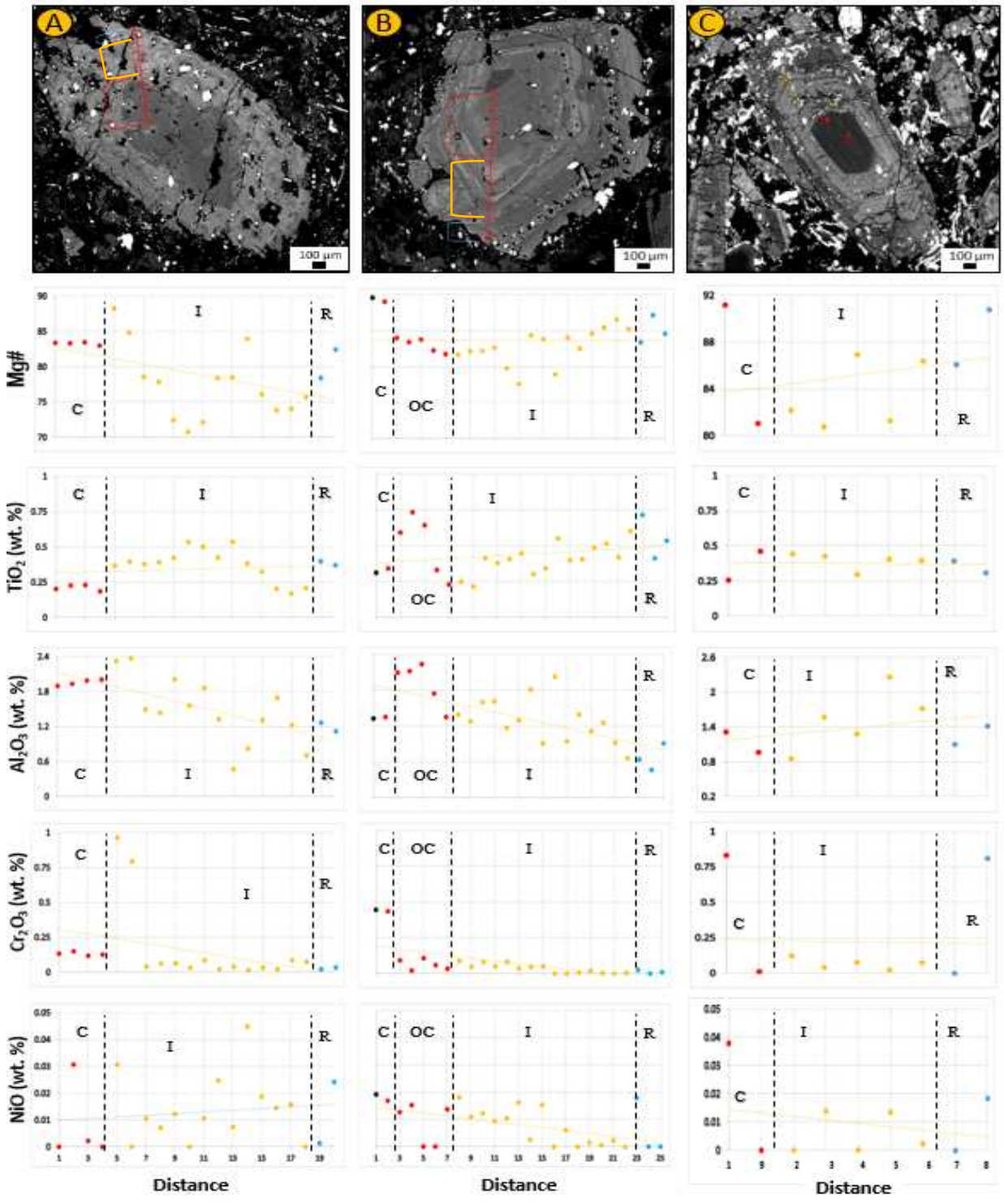

Figure 56: Lamprophyre J32_3 (A and B) and J36 I of the Crazy Mountain Range. (A) crystal 2A, (B) crystal 4A, (C) crystal 3A. Mineral chemistry data for Mg#, TiO2, Al203, Cr2O3, and NiO plotted versus distance on select pyroxene crystals

(4D. iv) Yogo Dyke Lamprophyre Mineral Chemistry

A sample collected from the Yogo Dyke Lamprophyre, termed 'Yogo' (ouachitite) in this study, was analyzed with an electron microprobe on select pyroxene crystals within the thin section. The BSE image of crystal 1A (Fig. 57) depicts a euhedral crystal with a broad silver-grey core. The core exhibits faint signs of early-stage spongy texture melt pockets, and even more so near the rim. The transition from core to rim is a subhedral boundary and the gainsboro-grey colored rim, outside of the outer core, displays melt pockets encircling the entire core. The pyroxene compositional ternary diagram shows the pyroxene increasing in Mg# from core to outer core (point 1 to 2 along the traverse) and the rim decreasing in Mg content and increasing in Ca content. Along the analytical traverse (Fig. 62 a), the Mg#, Cr_2O_3, and NiO content decrease from core to rim. TiO_2, Al_2O_3, and Na_2O increase from core to rim. Most of the compositional data show a constant trend aside from Cr_2O_3 content. This crystal is classified as a normally zoned pyroxene.

Crystal 4A of the same lamprophyre (Fig. 58) hosts an irregularly shaped anhedral crystal with pervasive spongy texture from core to rim. The crystal has a darker, broad grey core that hosts few melt pockets ~300 µm in length. Point 2 is a light grey colored irregular shaped, anhedral patch in the core devoid of melt pockets. The rim contains darker colored grey portions and lighter margins along crystal boundary. It is bizarre that the rim does not exhibit a uniform grey coloration. Thus, it is possible that this crystal is actually an aggregate of different crystals that recrystallized together at one point in this magma's history. The ternary diagram shows that points (1, 3, and 4) have similar compositions, but the light grey colored portion of the core (point 2) is more Fe rich in composition than the others. Ca enrichment exists within this pyroxene based off the data crossing the 50% Ca threshold on the ternary diagram. The analytical traverse behaves anomalously (Fig. 62 b) depicting point 2 decreasing in Mg #, TiO_2, Al_2O_3, Cr_2O_3, and NiO, while drastically increasing in Na_2O content. Overall, from core to rim, the Mg#, NiO, Cr_2O_3, TiO_2, Al_2O_3, and Na_2O content all slightly increase from core to rim. The classification of

zonation type of this pyroxene crystal does not accurately match up with perquisites from Rock (1991), thus this crystals zoning type is unknown.

Crystal 5A of the Yogo thin section (Fig. 59) is characterized by a subhedral pyroxene with some resorbed edges and a broad zone of spongy textured melt pockets. There is a dark grey core containing a heavy volume of spongy textured melt pockets. Light-colored silver-grey areas around the melt pockets exist. There is little change in coloration from core to rim unlike other crystals from this study. The pyroxene compositional ternary diagram expresses an inner core that is an Fe depleted diopside residing inside the spongy textured core and increases outside the spongy textured core. Point 3 regresses and decreases in Fe content to similar levels of the innermost core. The crystal then progressively increases in Fe content moving towards the rim. Ca enrichment exists within this pyroxene based off the data crossing the 50% Ca threshold on the ternary diagram. Along the analytical traverse (Fig. 62 c), the Mg#, Cr_2O_3, and NiO content decrease from core to rim. TiO_2, Al_2O_3, and Na_2O content increase from core to rim. The data along the traverse features sharp increasing or decrease in values from the core to outer core margin. From these criteria, this crystal is classified as a normal discontinuous zoned diopside pyroxene. A partially resorbed anhedral coarse-grained biotite is along the margin of the pyroxene crystal with a defined dark inner core and lighter barium rich rim (see Fig. 59).

The last crystal analyzed from Yogo was crystal 6A. The BSE image of 6A (Fig. 60) depicts a euhedral pyroxene crystal that has a parasitic growth attached to it. The Euhedral host crystal is characterized by a darker dimgrey inner core, a dim grey colored outer continuously zoned core, and a lighter dark grey colored rim with minor oscillatory zoning. The margins zonations have a subhedral margin. The parasitic growth exhibits its own unique coloration variation visible on the BSE. The innermost core of the parasitic section is lighter in color (grey), with a darker dimgrey outer core, and gradational boundary with the lighter dark grey rim exists. Spongy texture only exists in a segment of pyroxene that connects the host crystal (points 1-3) to the parasitic growth (points 4-7). The

compositional ternary diagram shows that the inner core is depleted in Fe content. The composition increases in Fe content within the intermediate zone. The outermost rim decreases in Mg content and increases in Ca content. The parasitic growth follows suite with the host data but to a lesser extent. Along the analytical traverse (Fig. 62 d), the Mg# and Na_2O content decrease from core to rim, while TiO_2, Al_2O_3, Cr_2O_3, and NiO increase from core to rim. The traverse of the parasitic crystal is similar to the host. This crystal is characterized by normal zonation.

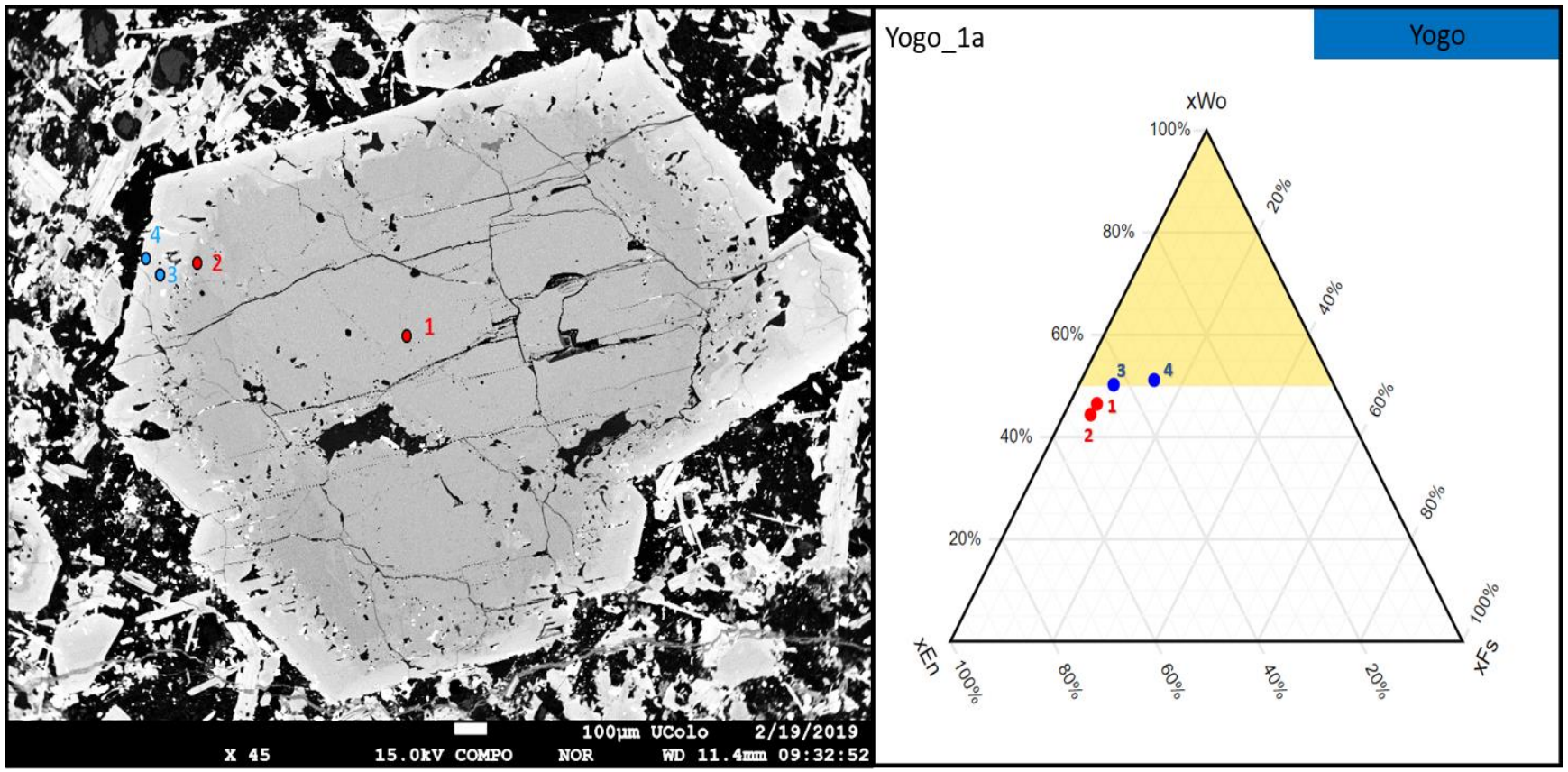

Figure 57: BSE and Ternary Diagram for the analytical traverse from core to rim across pyroxene crystal 1A, Slide Yogo, the Yogo Dyke Lamprophyre.

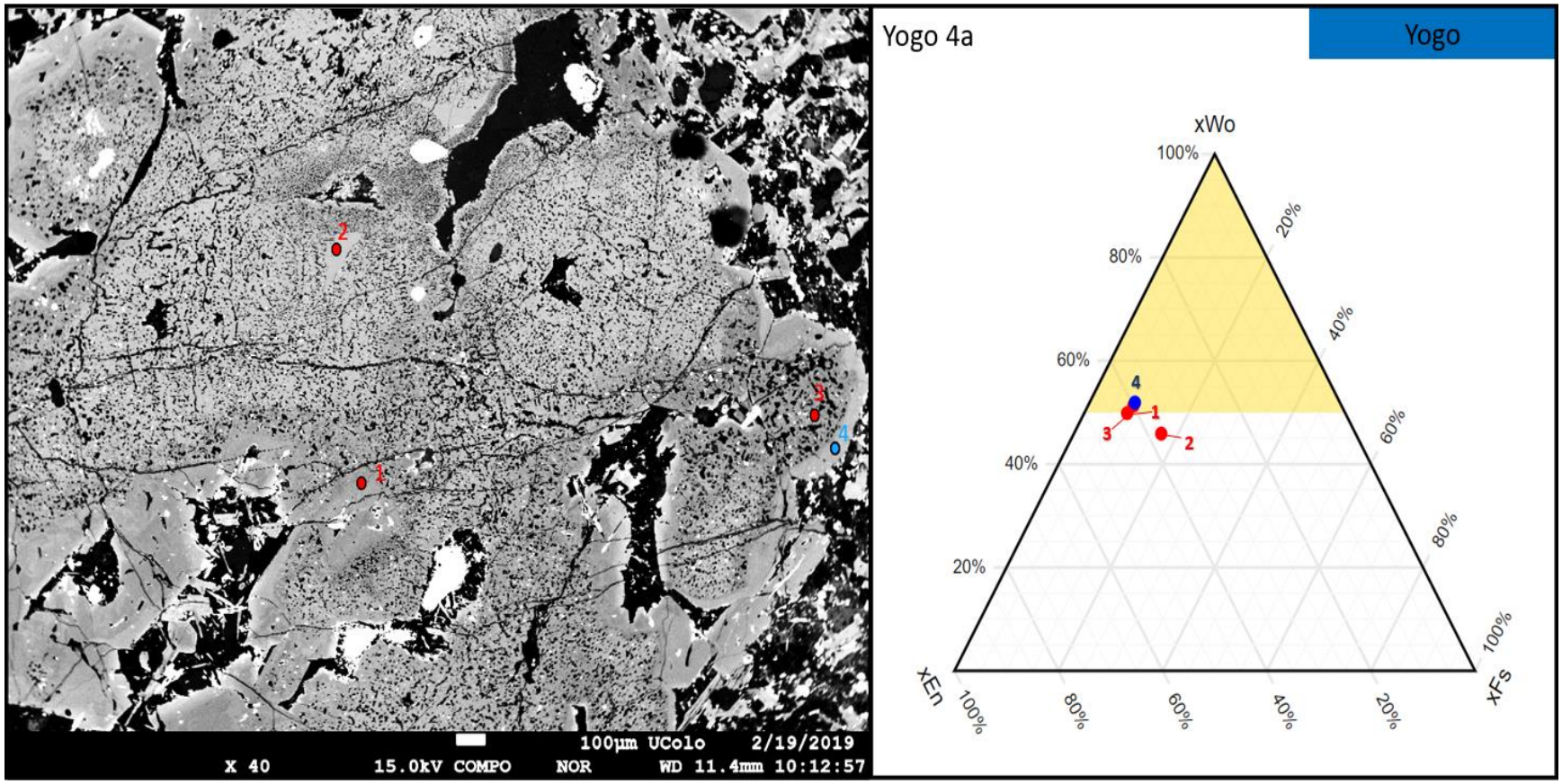

Figure 58: BSE and Ternary Diagram for the analytical traverse from core to rim across pyroxene crystal 4A, Slide Yogo, the Yogo Dyke Lamprophyre.

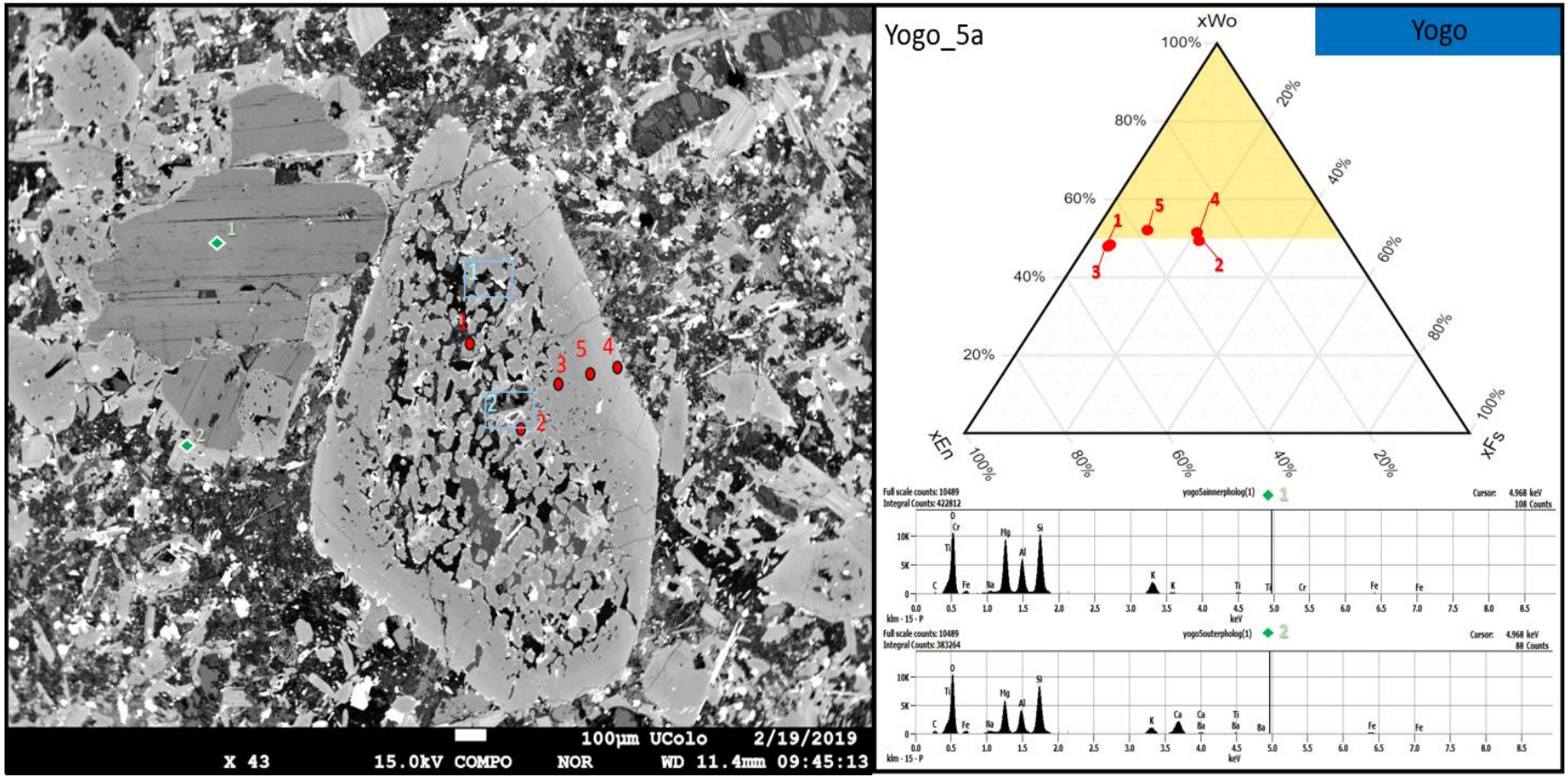

Figure 59: BSE and Ternary Diagram for the analytical traverse from core to rim across pyroxene crystal 5A, Slide Yogo, the Yogo Dyke Lamprophyre. Blue boxes correspond to melt pockets on Figure 15 (e and f).

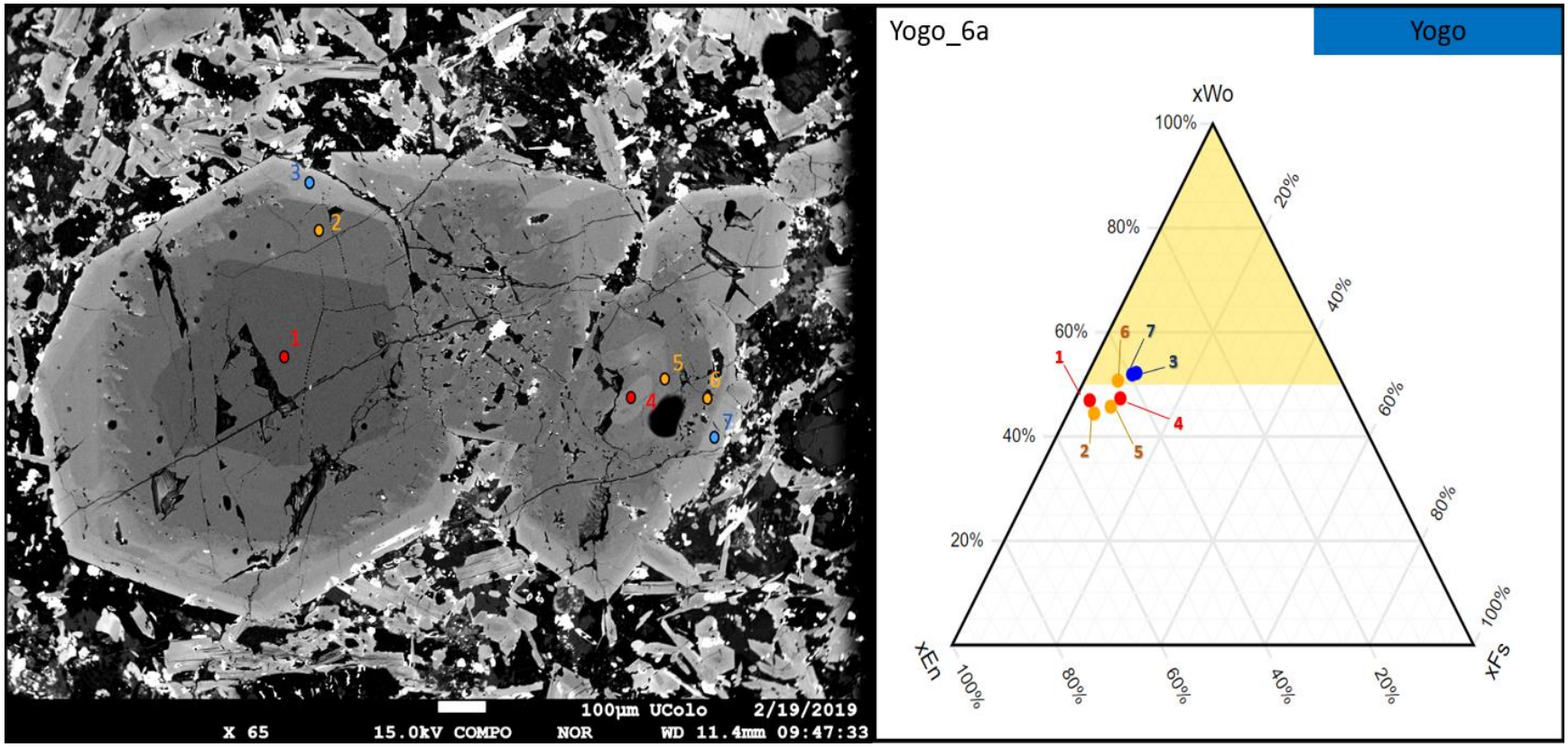

Figure 60: BSE and Ternary Diagram for the analytical traverse from core to rim across pyroxene crystal 6A, Slide Yogo, the Yogo Dyke Lamprophyre.

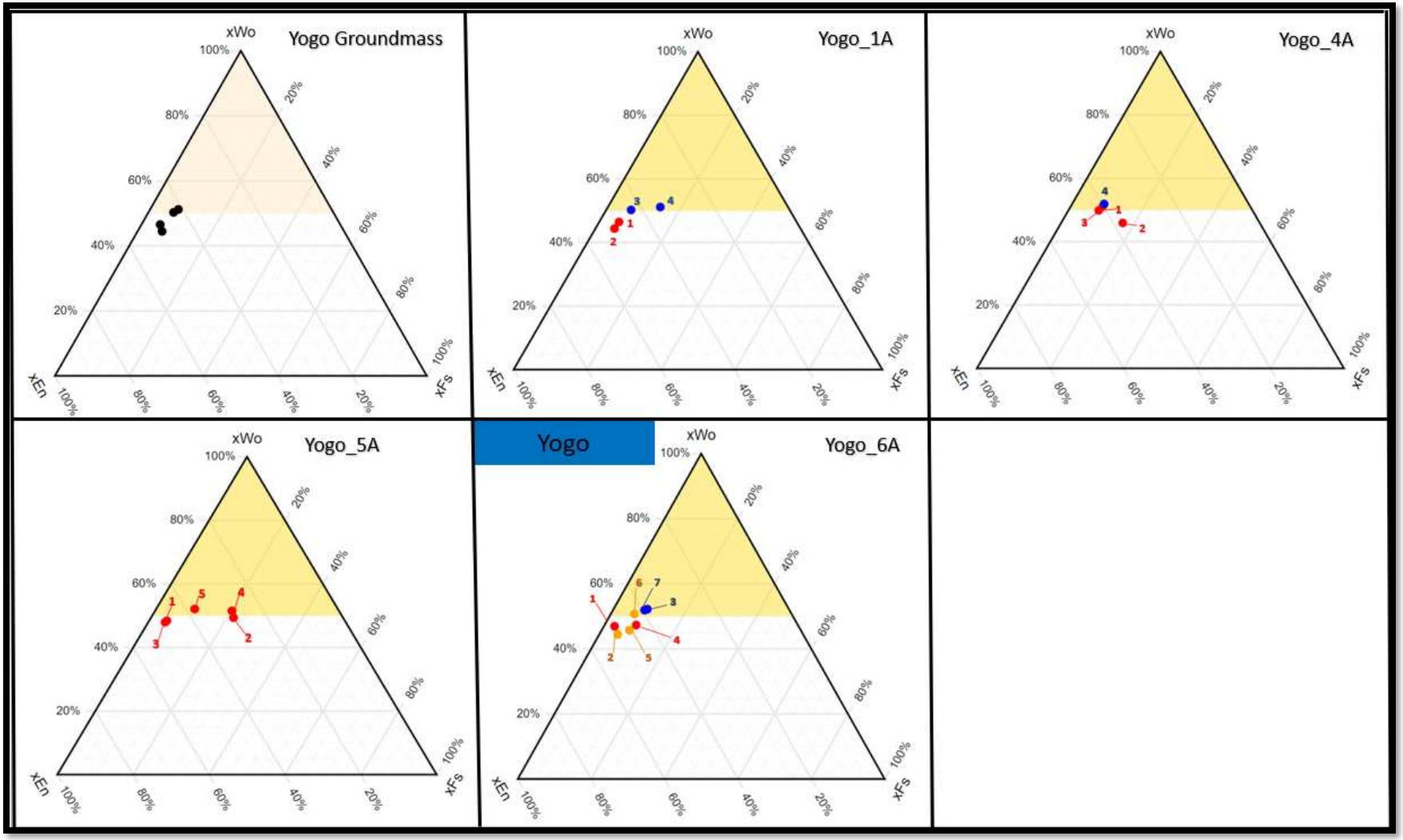

Figure 61: Compilation of pyroxene ternary diagrams from lamprophyre Yogo of the Yogo Dyke Lamprophyre.

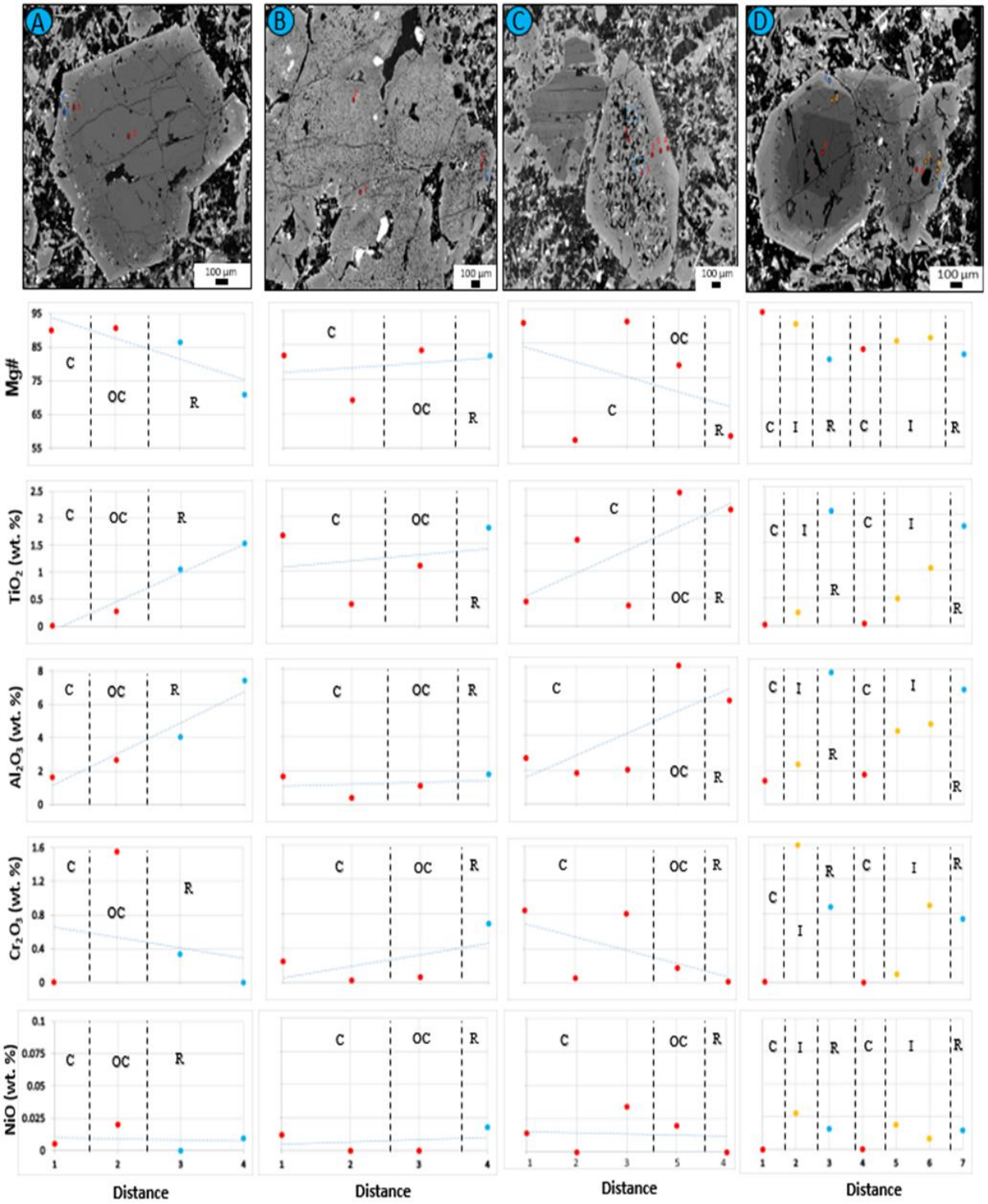

Figure 62: Lamprophyre YOGO of the Yogo Sapphire Dyke. (A) crystal 1A, (B) crystal 4A, (C) crystal 5A, (D) crystal 6A. Mineral chemistry data for Mg#, TiO2, Al203, Cr2O3, and NiO plotted versus distance on select pyroxene crystals.

(4D. v) DS Plots

A useful way to discriminate between clinopyroxene compositions is to use a cation index summary (termed DS) by O'Brien and others (1988). The DS is the sum of those cations in which diopside is enriched minus the sum of cations that are enriched in salite and is a measure of the extent of Fe substitution relative to diopside composition. The formula for DS = (Si + Cr + Mg + Ca) – (Ti + Al + Fe + Mn + Na) in cation proportions based off of six oxygens per formula unit (O'Brien et al., 1988). Salite is now an outdated term referring to an Fe rich diopside pyroxene. Regardless of the outdated name, the principle remains the same. Figure 63 depicts Al_2O_3, TiO2, CaO, and Mg# vs DS plots for each suite of the Central-Montana alkalic province studied. The data is representative of all the analytical traverse data captured during microprobe studies of clinopyroxenes including core, intermediate, and rim data. Red data plots originate from Bull Mountain, the green originates from the Highwood Mountains, the yellow from the Crazy Mountains, and finally the blue is from the Yogo Dyke lamprophyre (Fig. 62).

Within the Bull Mountain lamprophyre samples, the highest DS value measured in diopside is 3.6, and the lowest value measured is 2.6. The range of the Bull Mountain DS data is 1.0. The Highwood Mountain diopsides DS max value is 3.7, the lowest is 2.8, and the range is 0.9. The Crazy Mountain lamprophyre pyroxene traverses give a max DS value of 3.6, a minimum DS of 2.9, and thus a range of 0.7. The Yogo lamprophyre dyke diopsides exhibit a maximum DS value of 3.7, a minimum of 2.8, and a range of 0.9. Across the CMAP the DS value ranges are very similar.

Overall, the DS plots show good linear correlations (not for all elements in all suites), but as is typical of lamprophyres, there are some peculiar outliers. Al_2O_3 content within the pyroxenes seems to be correlated with the changing composition of diopside to a more Fe rich diopside, except for the samples from the Crazy Mountains (R^2=0.09). TiO_2 follows suite with Al_2O_3, however, the pyroxene samples from the Crazy Mountains show no correlations with a DS component (R^2=0.01). CaO in Bull Mountain, Highwood Mountain, and the Yogo Dyke appears to be strongly correlated with the shifting

composition of the pyroxene crystals except for pyroxene samples analyzed from the Crazy Mountains. The Mg# values from each region do appear to be strongly correlated with the hedenbergite substitution relative to diopside, displaying strong linear correlations.

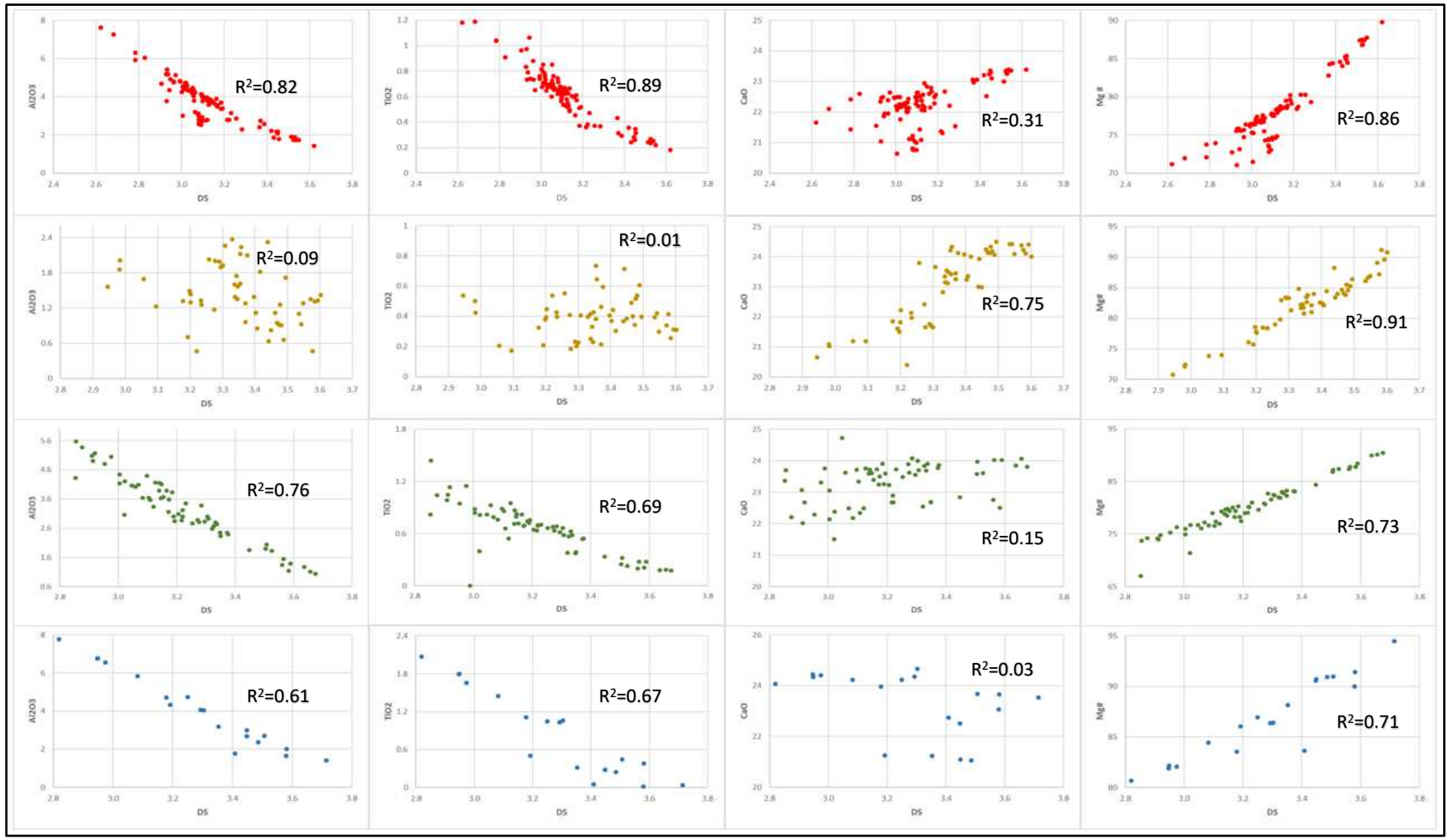

Figure 63: Variations of Al_2O_3, TiO_2, CaO, and Mg# for samples analyzed via microprobe from every field area from this study. DS= (Si + Cr + Mg + Ca) – (Ti + Al + Fe + Mn + Na) based on six oxygens and is a measure of the extent of Fe diopside substitution relative to diopside. R^2 correlation values are presented for each plot.Bull Mountin in red,.Crazy Mountains in yellow, Highwood Mountains in green, and Yogo Dyke in blue.

(4D. vi) CMAP Pyroxene Geothermobarometry

The ability to calculate the depths and temperatures that magmas partially crystallize is important when testing hypothesis of magma transport and evolution (Putirka et al., 2003). The temperature and pressure of crystallization of clinopyroxene was calculated in this study using the geothermobarometers of Putirka et al. (2003) and Putirka (2008) The models' calibrations are based on jadeite crystallization and the jadeite ($Na(Al,Fe^{3+})Si_2O_6$) – diopside ($CaMgSi_2O_6$) + hedenbergite ($CaFe^{2+}Si_2O_6$) exchange equilibria. The mineral chemistry data of clinopyroxenes from lamprophyres originating from each calc-alkaline to alkaline magmatic center focused on during the duration of the study were used to approximate the temperature (T) and pressure (P) of crystallization. For the sake of keeping unity with the rest of this study, yellow datum represents clinopyroxene from the Crazy Mountains, red datum is from the Bull Mountain range, green datum is from the Highwood Mountains, and finally, blue datum originates from clinopyroxene of the Yogo dyke lamprophyre. The formulas for temperature (Kelvins) and pressure (kilo-bars) of clinopyroxene crystallization are listed below and solving both equations simultaneously yields values needed to determine the P and T of each clinopyroxene traversal point.

$$P(\text{kbar}) = -88.3 + 2.82\times10^{-3}T(\text{K})\ln\left[\frac{[\text{Jd}^{\text{cpx}}]}{\left[\text{Na}^{\text{liq}}\text{Al}^{\text{liq}}\left(\text{Si}^{\text{liq}}\right)^2\right]}\right] + 2.19\times10^{-2}T(K) - 25.1\ln[\text{Ca}^{\text{liq}}\text{Si}^{\text{liq}}] + 7.03[\text{Mg}'^{\text{liq}}] + 12.4\ln[\text{Ca}^{\text{liq}}]$$

$$\frac{10^4}{T(\text{K})} = 4.60 - 4.37\times10^{-1}\ln\left[\frac{\left[\text{Jd}^{\text{cpx}}\text{Ca}^{\text{liq}}\text{Fm}^{\text{liq}}\right]}{\left[\text{DiHd}^{\text{cpx}}\text{Na}^{\text{liq}}\text{Al}^{\text{liq}}\right]}\right] - 6.54\times10^{-1}\ln[\text{Mg}'^{\text{liq}}] - 3.26\times10^{-1}\ln[\text{Na}^{\text{liq}}] - 6.32\times10^{-3}[P(\text{kbar})] - 0.92\ln[\text{Si}^{\text{liq}}] + 2.74\times10^{-1}\ln[\text{Jd}^{\text{cpx}}]$$

Components within the equations above are as follows. Terms like Al^{liq} refer to the cation fraction of $AlO_{1.5}$ in the liquid. Mg'^{liq} is the cation fraction ratio of MgO^{liq}/ (MgO^{liq} + FeO^{liq}). Jd^{cpx} is the mole fraction of jadeite within clinopyroxene, and pyroxene cations are calculated on 6 O atoms, and Jd is the lesser of

Na or ^{IV}Al. Where ^{IV}Al = 2 – Si; (^{VI}Al = Al – ^{IV}Al). If done correctly, cations should sum to 4. Calculations procedure after is listed below.

1. Jd = ^{VI}Al or Na, whichever is less.
2. If excess ^{VI}Al exists after Jd formation, CaTs ($Ca^{IV}\ Al^{VI}\ AlSiO_6$) = ^{VI}Al – Jd
3. If ^{VI}Al > CaTs, CaTi ($CaTiAl_2O_6$) = [^{IV}Al – CaTs]/2
4. CrCaTs ($CaCr_2SiO_6$) = Cr/2
5. DiHd ($CaFmSi_2O_6$) = Ca – CaTi – CaTs – CrCaTs

$DiHd^{cpx}$ is the mole fraction of diopside + hedenbergite, EnFs = enstatite + Ferrosilite, CaTs is the Ca-Tschermakite component, Fm = FeO + MgO ($CaFmSi_2O_6$ represents Ca(Fe, Mg)Si_2O_6, and Jd is jadeite). The liquid composition used in the calculation is equivalent to whole rock analysis from a known lamprophyre from each section available from previous works (Data from De Witt et al. 1996; Henderson et al., 2012; Gauthier, 1995; and Dudas, 1991.) The thermometer and barometry equations above can be used to calculate the temperature to a precision of ± 30 °C and the pressure to ± 1.5 kbar (Putirka, 2008). Note that there are few instances where negative values of P were calculated, but Putirka (2008) argues that these values should not be ignored because they may reflect the error that results when predicting a value that is essentially zero.

Aside from the standard error associated with the denotation of the clinopyroxene barometric models from Putirka and others (2003) and Putirka (2008), other sources of error might influence the calculated barometry values. The barometry calculation considers the composition of the parent melt, and in this study a representative whole rock analysis from each region of the CMAP was selected from previous authors work and used as a proxy for melt composition because it is assumed lamprophyres are close to primitive source melt compositions. Error could arise if the chosen liquid composition was not in fact representative of the parent liquid. Another source of error that cannot be ruled out is the volume of analysis collected from the microprobe beam during analytical traverses. The electron beam

of the microprobe penetrates the clinopyroxene surface by a few microns, it is possible that inclusions within the crystal not visible under the petrographic microscope or BSEs could inadvertently be struck during microprobe sessions. Although this could be ruled out by checking the stoichiometry of isolated analyses that display anomalous values.

Clinopyroxene barometry (converted from kbar to depth [km]) from across the CMAP is plotted on statistical box and whisker plots (Fig. 64). The median of Bull Mountain depth profiles is 59 km and the inter quartile range (IQR) is 6.6 km. There are several outliers within the Bull Mountain barometry profiles that are roughly within 40 – 20 km depth. The median of the Highwood Mountains depth profiles is 44 km while the IQR is 9.4 km. Several outliers exist within the Highwood data, one group is between 24- (-5) km, and one km datum plots at 120 km. The median of the Crazy Mountain barometry depth profiles is 29 km and the IQR is 29.1 km. The median from barometric depth profiles from Yogo is 49 km while the IQR is 18.6 km.

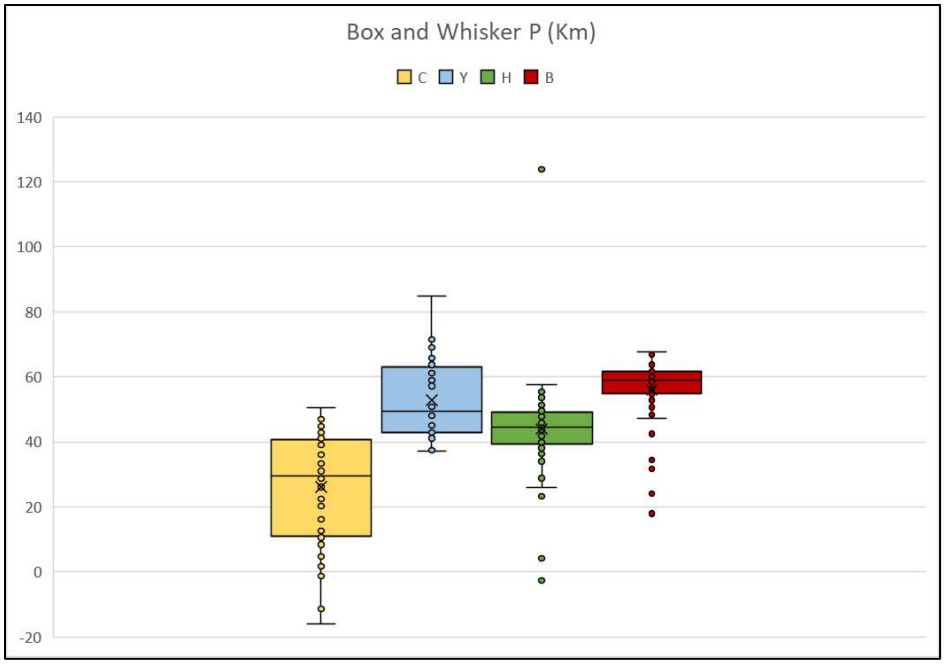

Figure 64: Box and Whisker Plots Depth of Crystallization

The equations above yielded T and P values present on Figure 65. There appears to be strong positive linear trends from lamprophyre clinopyroxene data of each region, and these trends are isolated from one another. All localities have cluster of data at 10 to 16 kbar, likely near the Moho transition, and some localities have significant spread of data to lower pressures. For example, the Crazy Mountain clinopyroxenes are characterized by much lower pressures and lower temperatures. Highwood Mountain clinopyroxenes crystallized at greater pressure and temperatures than those from the Crazy Mountains. Bull Mountain/Golden Sunlight clinopyroxenes crystallized at greater pressure and temperatures than clinopyroxenes from both the Crazies and Highwoods. Bull Mountain/Golden Sunlight pyroxenes display linear trends but with more spread of data (possibly outliers). Yogo Dyke clinopyroxenes display the greatest temperatures and pressures than all other clinopyroxenes from other regions of this study. In general pressure and temperature of clinopyroxene crystallization follows this progression Yogo>Bull>Highwood>Crazy.

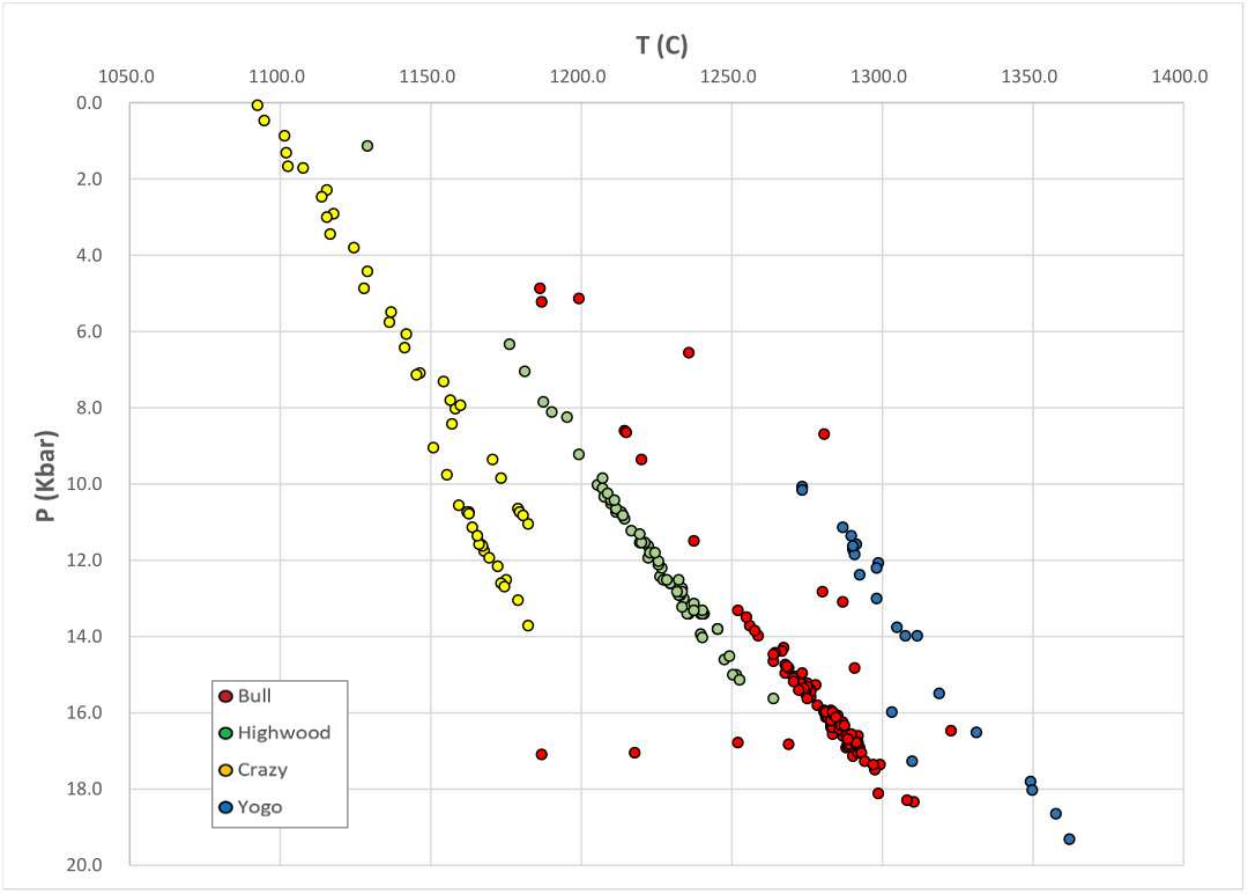

Figure 65: Barometry and Thermometry of Clinopyroxenes from Lamprophyres from Bull Mountain/Golden Sunlight (Red), Highwood Mountains (Green), Crazy Mountains (Yellow), and the Yogo Dyke Lamprophyre (Blue). Pressure is reported as kbars and temperature as degrees Celsius. Calculations after Putirka et al. (2003) & Putirka (2008).

Clinopyroxenes from Bull Mountain/Golden Sunlight lamprophyres crystalized over a pressure range of ~18 to 5 kbars (66 – 19 km) and at temperatures of 1160 °C to 1325 °C (Fig. 65, Fig. 66). The innermost core of J06_1A crystalized at 17.1 kbar (63 km). Point 2 and 3 crystalized at 11.5 kbar (42 km) and 18.1 kbar (67 km) respectively and are adjacent to spongy texture melt pocket. It is unusual that points 2 and 3 display vastly different pressure data because they are both contained within the inner core's patchy zoned core. Point 6 is contained within the intermediate region exhibiting spongy texture and crystalized in the lower crust at 8.6 kbar (32 km). The outermost rim (point 8) crystalized at similar conditions to the innermost core (Point 1), crystalizing at 16.9 kbar (62 km).

Crystal 2A of the same sample displays an innermost core of 16.3 kbar (60.3 km) while the rim is 4.8 kbar (17.8 km). Point 2 within the core crystalized at 5.1 kbar (19km), very similar to Point 20 (outer

rim). This is unusual because on the BSE image (Fig. 31) there seems to be no significant change in zonation, no possible contamination due to a melt pocket near the microprobe analysis point. The analytical transect at point 2 shows a step zoned typical behavior with drastic change in composition over a short distance (compare 76 to 85 Mg#, 0.1 to 0.4 Cr_2O_3). There is a large stretch of transect points 5 – 16 that all plot within the 1.5 kbar range of uncertainty, plotting between ~16 to 17 kbar, these points along the BSE are contained within the oscillatory zoned intermediate region. The rim points (17-20) crystalized at much lower pressure than the intermediate or core regions.

Barometry from crystal 5A of the same sample displays an innermost core which crystalized at 14.6 kbar (54 km) while the outermost rim crystalized at greater pressures of 17.3 kbar (64 km). Point 2 crystalized at 16.7 kbar (62 km) and resides inside of a lighter colored patchy zoned area adjacent to a melt pocket. Point 3 resides at the edge of the core and crystalized at 13.3 kbar (49 km), this is the lowest recorded pressure from this crystal. Point 3 corresponds to the highest Mg#, lowest TiO_2 and Al_2O_3, highest Cr_2O_3 and NiO composition along the transect. Points 4 and 5 plot within the range of uncertainty but display the greatest pressures of crystallization at the rim of the crystal.

Pressure data from crystal 8A of the same sample displays a range of data from core to rim, all of which are between 16.4 (61 km) to 14.3 kbar (53 km) points 11 and 21 respectively. The BSE image of this crystal shows a concentric oscillatory zoned pyroxene, and unfortunately the precision of the analysis is not good enough to discern any useful information from other than the fact that little variation occurred with regards to crystallization pressure and depth. It is interesting that regions of crystals with oscillatory zoning display pressure data that coincides within the range (1.5 kbar) of uncertainty.

Two clinopyroxene crystals analyzed from lamprophyre J12 of Bull Mountain/Golden Sunlight were analyzed via geobarometry. The first crystal 1A hosts an innermost core that crystalized at 5.2 kbar (19 km) with an outer rim that crystalized at 15.9 Kbar (59 km). At point 4, near the outer core margin

the pressure of crystallization is 16.8 kbar (62 km), the highest of the entire crystal, which also coincides with significant drop in Mg# and Cr_2O_3 and sharp increase in Al_2O_3 and TiO_2. Points 7, 5, and 6 all reside within the outer core and display lower pressures of crystallization than the intermediate and core regions. A noteworthy feature of this crystal is the inner core being the lowest pressure point. The crystal could be viewed as a foil to J06_2A, although this crystal does not display abundant spongy texture or concentric/oscillatory zoning (Fig. 35).

The last crystal analyzed from lamprophyre J12 is sector/oscillatory zoned crystal 3A. The greatest pressure exists in the innermost core at 17 kbar (63 km) and the lowest is at the outermost rim with 16 kbar (59 km). At first glance, the barometry data shows a progressive rate of crystallization with regard to depth, but this range of data falls within the error of uncertainty.

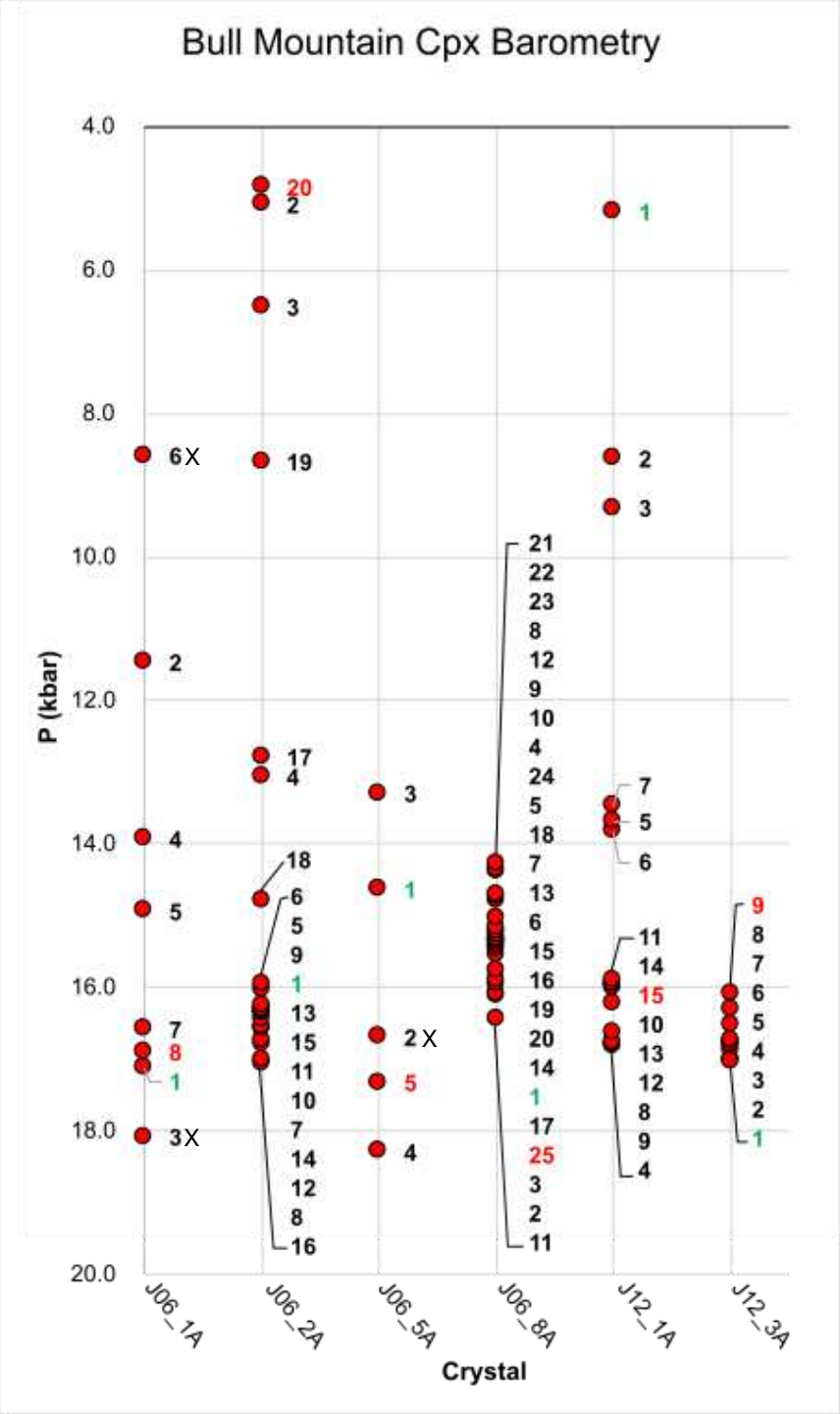

Figure 66: Barometry of Clinopyroxenes from Bull Mountain/Golden Sunlight lamprophyres J06 and J12. Pressure (P) scale is in kbars. Green points represent the innermost core analyzed and the red points represent the outermost rim analyzed. These numbered points also correspond to analytical traverses present in section 7D.i.

Clinopyroxenes from lamprophyres of the Highwood Mountains crystalized over a pressure range of ~16 to 1 kbars (59 – 4 km) and at temperatures of 1130 °C to 1260 °C (Fig. 65, Fig. 67). All barometry data for clinopyroxenes of the Highwoods are present on Figure 67. Select pyroxenes within the groundmass of lamprophyre J18 crystallized at ~10.2-10.8 kbar (38 - 40 km). Groundmass pyroxenes from lamprophyre J24 crystallized at ~12.8-15.1 kbar (47 km-56 km).

The first pyroxene crystal analyzed from lamprophyre J18 is crystal 1A. The innermost core and the outermost rim (points 1 and 8) both crystalized at 13.40 kbar (50 km). Point 3 is located within the darker outer core in patchy zoned areas surrounded spongy textured melt pockets and it displays the lowest pressure at 8.1 kbar (30 km) which also corresponds to a decrease in Fe composition of the diopside (Fig. 41) and the highest Mg# value given for the entirety of the crystal at 90 Mg#. Point 4 is within lighter patchy zoned segments adjacent to the melt pocket and crystalized at 11.2 kbar (41 km). Points 5, 6, and 7 within the rim are within the margins of uncertainty (range from 11.6 kbar (43 km) to 12.7 kbar (47 km)). Point 8 hosts the most Fe rich hedenbergite composition within the crystal as well as the highest TiO_2 and Al_2O_3 content. It is unusual that the innermost core and rim both crystalized at 13.4 kbar (50 km) in addition to the mineral composition variations between the two points along the analytical transect.

Barometry data from crystal 2A of the same lamprophyre displays an inner core that crystalized at 13.4 kbar (50 km) and the outer rim (point 8) crystalized at 14 kbar (52 km). Similar to crystal 1A the core and rim data coincide with statistical uncertainty. It should be noted that on Figure 67, points 9, 10, and 11 correspond to the parasitic growth. The core (point 9) and the rim of the growth (point 11) both crystalized at 12.5 kbar (46 km). The intermediate region of the parasitic growth (point 10) crystalized at 10.3 kbar (38 km). Point 2 within the core plots within uncertainty of Point 1 but point 3 within the darker outer core of the crystal crystallized at 7.8 kbar (29 km) and corresponds to increase in Mg#, Cr_2O_3, NiO and a decrease in Fe, TiO_2 and Al_2O_3 content along the transect when compared to the inner

core (Fig. 42 and 50). Points 4, 5, and 6 are within the crystal's intermediate region and range in crystallization pressure data from 15 kbar (56 km) to 13.2 kbar (49 km). Point 7 within the rim crystalized at 11.5 kbar (43 km) and corresponds to a spike in Mg#, Cr_2O_3, and NiO content along the transect compared to the intermediate region of the crystal.

Another pyroxene crystal analyzed (4A) displays an inner core that crystalized at 7 kbar (26 km) and an outer rim that crystalized at 13.1 kbar (48 km). It is unusual that the innermost core crystalized at lower pressures than the rim, as this unlike to the other pyroxene crystals analyzed from the same lamprophyre. Point 2 of the core crystalized at 11.9 kbar (44 km) and is within a lighter colored anhedral segment of the core and corresponds to a decrease in Mg# and an increase in Fe, TiO_2, and Al_2O_3 content. Points 1, 3, and 4 are all within the core and plot identical compositions of the pyroxene on the ternary diagram, and unlike point 2, they are confined to darker patchy zoned areas. Point 3 crystalized at 10.8 kbar (40 km) while point 4 crystalized at 10.7 kbar (40 km). Points 5 – 8 are within the oscillatory zoned intermediate and rim regions. Points 5 and 7 both plot at 11.5 kbar (43 km) whereas points 6 and 8 crystallized at 13 kbar (48 km). On the analytical traverse these points behave similarly to one another with respect to mineral composition.

The last pyroxene crystal analyzed with geobarometry from the same lamprophyre was 6A. It should be noted that both 6A and 2A contain parasitic growths, but 6A's growth displays continuous oscillatory zoning whereas 2A does not. The innermost core crystalized at 12.6 kbar (47 km) while the outermost rim crystalized at 10.6 kbar (39 km). Point 2 of the core shares the same pressure of crystallization but point 3 at the outer core drastically lowers and crystalized at 9.2 kbar (34 km). On the analytical transect point 3 also corresponds to a sharp increase in Mg# and Cr_2O_3 content, and decrease in Fe, TiO_2, and Al_2O_3 content (Fig. 50). From points 4 to 11 (the distance of the intermediate zones) the range of crystallization pressure is from (12.2 kbar (45 km) to 6.3 kbar (23 km)). Point 11 crystallized at 6.3 kbar (23 km) and is within the oscillatory concentrically zoned segment of the crystal, this particular

point does not follow the trend of other crystals with oscillatory zoning wherein most of the crystallization depths are fairly consistent. Point 13 is the second to last recorded point along the analytical traverse and crystallized at 12.10 kbar (45 km). Point 13 also exists within a lighter colored band of zoning and hosts the most Fe rich composition of the entire crystal.

Three clinopyroxene crystals from lamprophyre J24 of the Highwood Mountains were analyzed via geobarometry. The first crystal is 1A and the innermost core crystalized at 12.8 kbar (47 km) while the outermost rim crystalized at 15.6 kbar (58 km). Points 2 and 3 within the inner core of the traverse record increasing crystallization pressure with 13.3 kbar (49 km) and 13.8 kbar (51 km) respectively. At Point 4, what the author has termed the intermediate section of the core, the crystal displays its lowest crystallization pressure with 11.3 kbar (42 km).

The second crystal analyzed from the same lamprophyre was pyroxene crystal 4A. The innermost core crystalized at 12.9 kbar (48 km) while the outermost rim crystalized at 14.6 kbar (54 km). Note that there are two anomalous pressure crystallization data within this crystal that were omitted from Figure 67 because these points greatly skewed the presentation of the data, but these points will instead be discussed here. The first, point 3 as discussed in the microprobe analysis section (7D. ii) could be representative of an Fe rich biotite or Fe rich magnetite inclusion that was struck with the microprobe during the analytical traverse. Point 3 recorded a crystallization pressure of 33.5 kbar (124 km). Because of the position of point 3 on the ternary diagram coupled with an incredibly high crystallization pressure, this datum point was omitted from the clinopyroxene barometry. Another anomalous value which could not be explained is point 2 along the traverse located within the lighter colored portion of the crystals core. This point recorded a crystallization pressure of -0.7 kbar. On the ternary diagram for this crystal (Figure 47), this point plots above the diopside field and is enriched in Ca. Thus, it is likely that the microprobe analyzed an inclusion of apatite. Point 6 exists within a lighter

colored thin band, crystalized at 13.4 kbar (50 km), and is the most Fe, TiO_2, and Al_2O_3 enriched portion of the crystal.

The final crystal analyzed from this lamprophyre was pyroxene crystal 6A. The innermost core crystalized at 9.8 kbar (36 km) and the outermost rim recorded crystalized at 13.4 kbar (50 km). Based off the position of the points along the transects on Figure 67, there exists fluctuating crystallization pressures from core to rim which aligns with Fe diopside composition fluctuating in a similar manner (Fig. 48). Note that point 2 within a lighter colored patch of the inner core displays the greatest crystallization depth at 14.5 kbar (54 km). This point is also the most Fe rich portion of this pyroxene crystal. Point 7 exists within a lighter colored band near the rim which is full of inclusions. Its location on the ternary diagram (Fig. 48) alludes to accidental analysis of an inclusion. Barometric calculations gave crystallization result of 1.1 kbar (4 km). These data and the point's location on the ternary diagram raise some skepticism regarding its validity. The data was excluded from Figure 65 as it would skew the data and presentation but was untouched on Figure 67.

Figure 67: Barometry of Clinopyroxenes from Highwood Mountain lamprophyres J18 and J24. Pressure (P) scale is in kbars. Green points represent the innermost core analyzed and the red points represent the outermost rim analyzed. These numbered points also correspond to analytical traverses present in section 7D. ii.

Clinopyroxenes from lamprophyres of the Crazy Mountains crystalized over a pressure range of ~14 to 0 kbar (52 to 0 km depth in the crust) and at temperatures ranging from 1180 °C to 1090 °C (Fig. 65, Fig. 68). Two pyroxenes were analyzed from lamprophyre J32_3. The innermost core of crystal 2A crystalized at 10.6 kbar (39 km) while the outermost rim crystalized at 12.5 kbar (46 km). There is little variation in crystallization depth within the core from points 1-4 (10.6 kbar (39 km) to 11 kbar (41 km)) and all points plot within margins of uncertainty. Point 5 is the first point within the intermediate region of the pyroxene crystal and crystallized at 2.87 kbar (11 km) and is associated with an increase in Mg#, TiO_2, Al_2O_3, Cr_2O_3, and NiO content along the analytical traverse. Although no concentric oscillatory zoned bands exist within this pyroxene the composition along the traverse seems to fluctuate in an oscillatory fashion. This behavior is mirrored by points (5-18) and range in crystallization depth from 0.82 kbar (3 km) to 13 kbar (48 km). It should be noted that the highest (Point 14, 13 kbar (48 km)) and lowest pressures (Point 18, 0.82 kbar (3 km)) recorded exist within this intermediate zone. Compared to the rest of the other pyroxene crystals analyzed during this study from other regions of the Central-Montana alkalic province, the pyroxenes of the Crazies display evidence of crystallizing at much shallower depths.

The last crystal analyzed from the same lamprophyre (4A) displays an innermost core that crystalized at 9 kbar (33 km) and an outermost rim that crystalized at 11.4 kbar (42 km). Keeping with the trend of crystal 2A there exist four points that crystallized at extremely low pressures. These are: Point 7, 0.02 kbar (<1 km); Point 14, 0.45 kbar (2 km); Point 11, 1.27 kbar (5 km); and Point 13, 2.44 kbar (9 km). All the points listed above are within the intermediate region of the crystal, with the exception of point 7 which is located at the margin of the outer core intermediate boundary. It should be noted that the points from the intermediate region have associated uncertainty given the clustering of the data. Two data points within the core and two within the intermediate region calculated negative geobarometric values. These points are not visible on Figure 70, but their data will be discussed here.

These points are: Point 6, -0.3 kbar; Point 8, -2.7 kbar; Point 12, -3.1 kbar; and Point 10, -4.3 kbar. The presence of negative pressure values is discouraging, even more so that these points along the analytical traverse do not show anomalous compositional values; and the fact that nearly all the points on the ternary diagram show realistic trends of progression (normal zoning) of the diopside with respect to Fe content (hedenbergite) and a regression (reverse zoning) in the intermediate and core regions. One would expect anomalous values similar to other pyroxenes observed during the course of this study. One explanation could stem from the selection bias associated with how the microprobe analysis points were selected as opposed to the analytical 30 micron step the computer used to generate in this analytical traverse data. A pre-selected line was drawn on the crystal during the microprobe analysis, and every 30 microns an analysis would be taken. Most other microprobe analysis from this study was carried out by single spot analysis chained over the course of the mineral with irregular micron intervals between each point in hopes of avoiding mineral inclusions, fractures, or melt pockets. Thus, it is possible that the negative values of the data collected from this pyroxene could be contaminated by inclusions along the traverse.

One pyroxene crystal (3A) of lamprophyre J36 was analyzed and depicts an innermost core that crystalized at 7.1 kbar (26 km) and an outermost rim that crystalized at 3 kbar (11 km). Similar to other pyroxenes from the Crazies, this crystal hosts crystallization depths that are very shallow compared to the rest of the data. In this crystal though, all the low-pressure data exists within the rim of the crystal in point 7, 3.42 kbar (13 km); Point 9, 3 kbar (11 km); and Point 8, 1.63 kbar (6 km). This behavior is unique to this one pyroxene crystal as the other pyroxenes from the Crazies display intermediate region data points with low pressure values. Points 2, 3, 4, 5, and 6 range from 4.8 kbar (18 km) to 8.3 kbar (31 km) and correspond to enrichment of Fe diopside composition (hedenbergite) on the ternary diagram (Fig. 54).

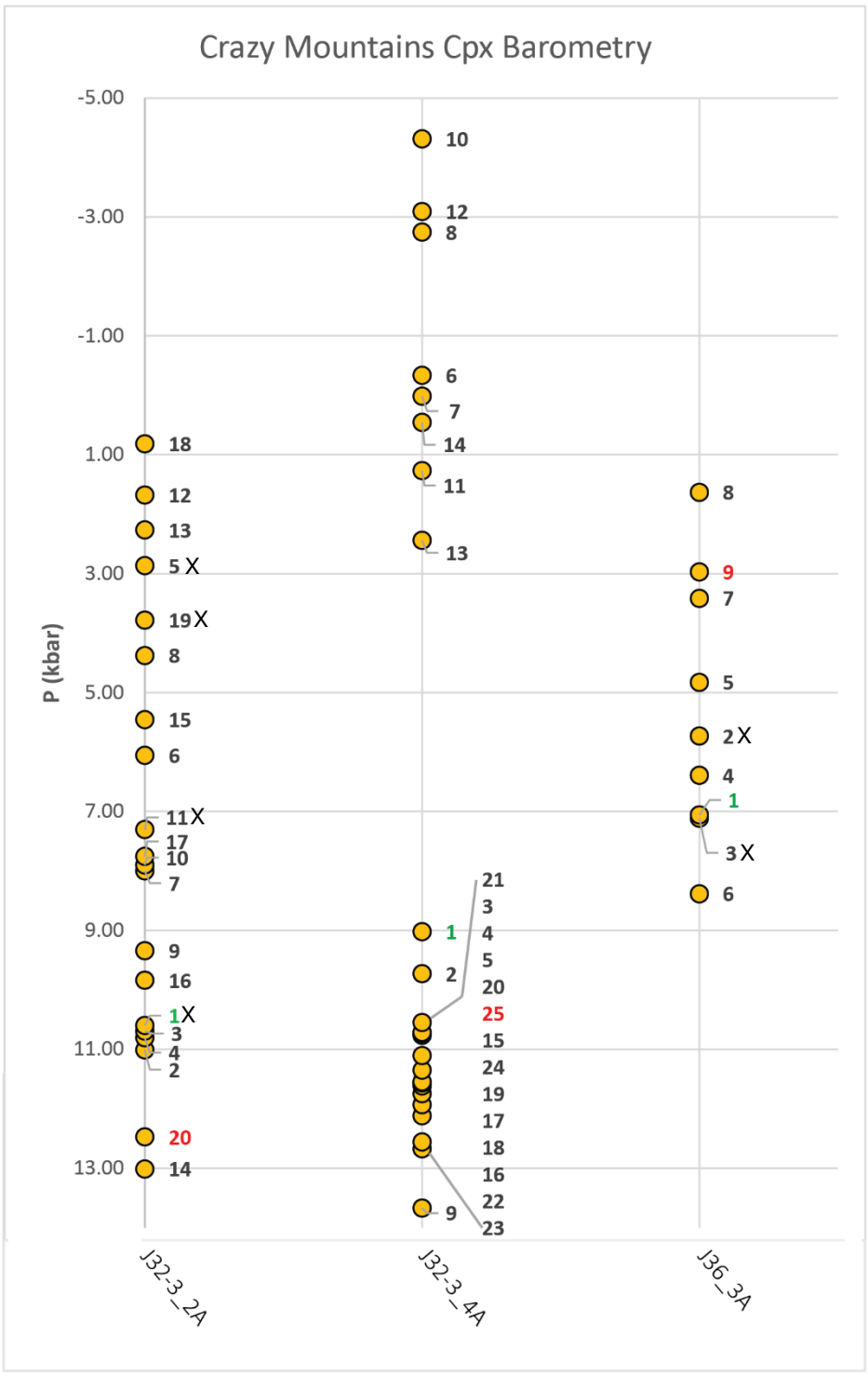

Figure 68: Barometry of Clinopyroxenes from Crazy Mountain lamprophyres J32_3 and J36. Pressure (P) scale is in kbars. Green points represent the innermost core analyzed and the red points represent the outermost rim analyzed. These numbered points also correspond to analytical traverses present in section 7D.iii.

Clinopyroxenes from the Yogo Dyke lamprophyre crystalized over a pressure range of ~19 to 10 kbar (70 to 37 km depth in the crust) and at temperatures ranging from 1275 °C to 1360 °C (Fig. 65, Fig. 69). Select groundmass pyroxenes were analyzed in addition to the crystals which were the target of this study. The groundmass pyroxenes crystalized at 10.11-18 kbar (37-67 km). Four pyroxene crystals analyzed originate from one thin section called 'Yogo' in other sections of this work. Within crystal 1A the innermost core crystalized at 14 kbar (52 km) and the outermost rim also crystalized at 14 kbar (52 km). Point 2 within the outer core crystalized at 18.6 kbar (67 km), the greatest pressure recorded in this crystal. Point 3 of the rim crystalized at 10 kbar (37 km) and is the lowest pressure recorded as the crystal crystallized. Point 3 also corresponds to Ca increase in the pyroxene whereas Point 4 depicts the richest Fe composition. It should be noted that the scale of pressure kbar values are much higher than other regions of this study.

Crystal 4A of lamprophyre Yogo hosts an inner core (Point 1) with pervasive spongy texture that crystalized at 11.1 kbar (41 km) and an outermost rim (Point 4) that crystalized at 11.4 kbar (42 km). Point 2 exists within a lighter colored patchy zoned section of the melt pocket rich core which crystalized at 23 kbar (85 km). Point 3 crystalized at 11.8 kbar (44 km), but because Points 1, 3, and 4 plot with little variation there is a considerable amount of uncertainty involved with these data.

Crystal 5A of the same lamprophyre displays an inner core that crystalized at 13.7 kbar (51 km) and an outer rim that crystalized at 16 kbar (59 km). Note that Point 4 is actually the outermost rim and point 5 is farthest extent of the outer core. Point 2 resides outside of the core region rich with spongy texture melt inclusions and crystallized at 17.2 kbar (63 km). Point 3 and 5 show crystallization at lower pressures with 13 kbar (48 km) and 12. 1 (45 km) kbar respectively. This crystal is the only one from Yogo that depicts the rim crystalizing deeper than the core without any issues of uncertainty between the two points unlike that of crystal 4A.

The final crystal analyzed from the Yogo lamprophyre is crystal 6A. The innermost dark core (Point 1) of 6A crystalized at 12.4 kbar (46 km) while the lighter rim (Point 3) crystalized at 12 kbar (44 km) within the margin of uncertainty. Point 2 shows the dimgrey intermediate/outer core region crystalized at 17.8 kbar (66 km). It should be noted that crystal 6A possesses a parasitic growth which was also analyzed (Points 4-7). On figure 69, there are two sets of red and green numbers for easy differentiation between the host crystal and the parasitic growth. Point 4 is the core of the parasitic growth that crystalized at 15.5 kbar (57 km) and the outermost rim of the growth (Point 7) crystalized at 11.5 kbar (43 km). It is unusual that the parasitic growth behaves differently than the host in regard to crystallization pressure, yet the rim of the growth and the host have almost identical Ca rich pyroxene composition (Figure 60).

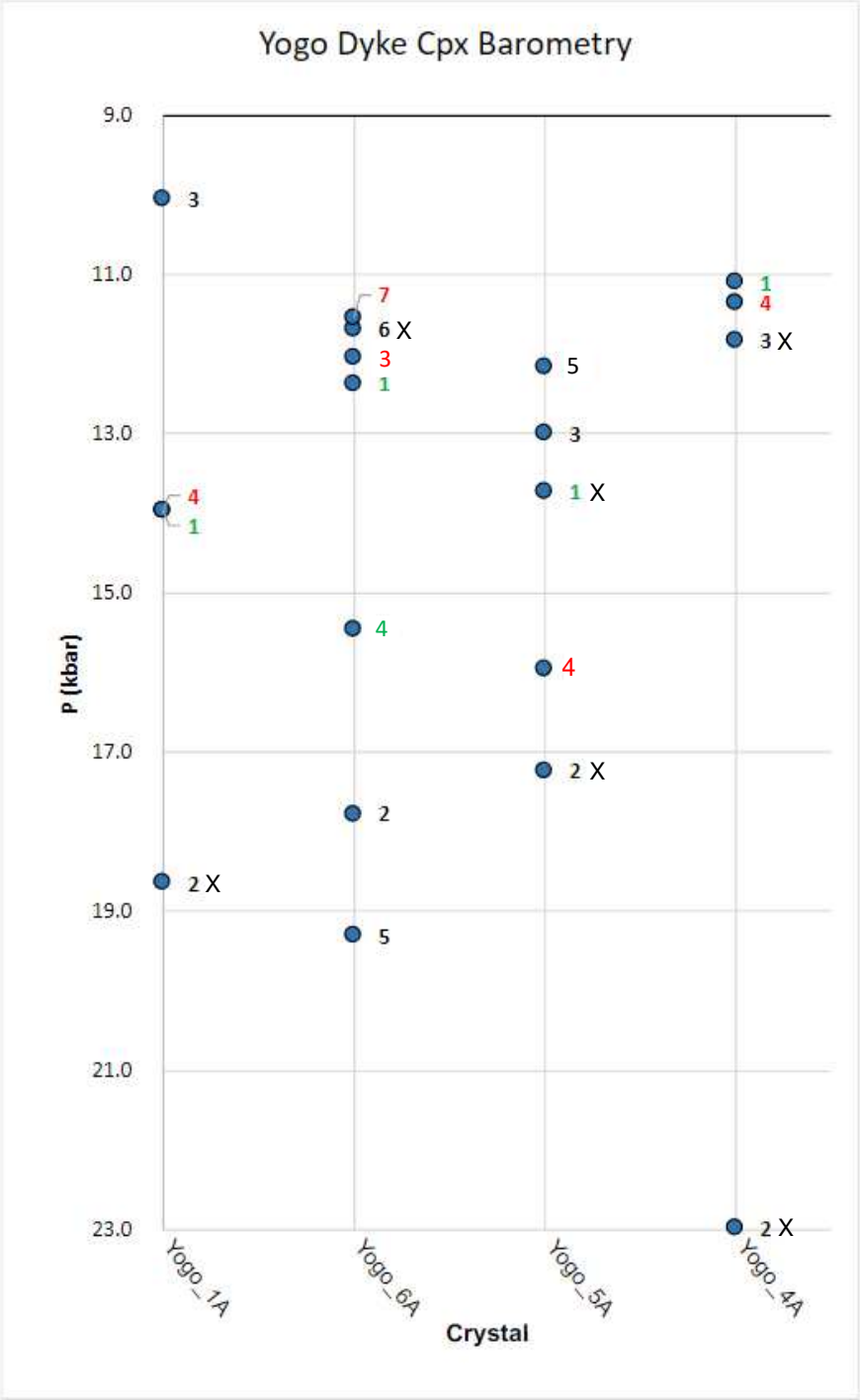

Figure 69: Barometry of Clinopyroxenes from the Yogo Dyke lamprophyre. Pressure (P) scale is in kbars. Green points represent the innermost core analyzed and the red points represent the outermost rim analyzed. These numbered points also correspond to analytical traverses present in section 7D. iv.

(5) Discussions

(5A) Petrology of the CMAP

As previously mentioned, not all of the rocks collected and analyzed during this study are petrographically lamprophyres, and to assess their validity additional geochemical analysis are needed. The igneous rocks collected do however possess "lamprophyric properties". Lamprophyric rocks investigated in this study are generally dyke rocks that are mesocratic to melanocratic rocks of porphyritic texture which contain essential biotite, and/or amphibole (hornblende), clinopyroxene, and olivine. The lamprophyric properties of these rocks are further supported by the presence of globular structures (ocelli), resorption features on mafic crystals, and crustal xenoliths. Thus, the lamprophyric rocks collected from this study were classified by current IUGS standards using observed modal mineralogy within thin sections with emphasis on light colored constituents and predominant mafic minerals (Le Maitre et al. 1989; Le Bas and Streckeisen, 1991; Strekeisen, 2021; Geologyscience.com, 2021).

From the lamprophyre classification scheme proposed by Rock (1991) all lamprophyric rocks observed during this study were calc-alkaline (shoshonitic), alkaline, or ultramafic lamprophyres. No lamproite or kimberlite lamprophyric rocks were observed. Using Table 1 and Figure 1 when analyzing mineral modalities and assemblages from thin sections, the following lamprophyric rock types discussed below were observed from Bull Mountain/Golden Sunlight, Highwood Mountains, Crazy Mountains, and the Yogo Dyke.

(1) ***Minettes (CAL)*** are porphyritic calc-alkaline igneous rocks with alkali feldspar crystals (also in groundmass) with essential biotite and diopsidic augite ± olivine. Biotite and augite are often present as accessories within the finer groundmass.

(2) ***Vogesites (CAL)*** are porphyritic calc-alkaline igneous rocks named after their type locality from Vosges, of northern France. Alkali feldspar crystals are more abundant than plagioclase (also within the groundmass). Essential mafic minerals are diopsidic augite and hornblende ± olivine. Often augite and biotite exist within the groundmass, but coarse crystals of biotite are uncommon.

(3) ***Spessartites (CAL)*** are porphyritic calc-alkaline igneous rocks named after their type locality from the Spessart Mountains of Germany. Of the lighter constituents, plagioclase is more abundant than alkali feldspar (also within the groundmass). Contains essential coarse mafic minerals of diopsidic augite and hornblende ± olivine.

(4) ***Kersantites (CAL)*** are porphyritic calc-alkaline igneous rocks named after their type locality from Kersanton, France. Plagioclase is more prevalent than alkali feldspar (also within the groundmass). Essential mafic minerals are biotite and diopsidic augite ± olivine.

(5) ***Sannaites (AL)*** are porphyritic alkaline igneous rocks named after rocks discovered in the Fen Igneous Complex of Sannavand, Sweden. These rocks contain alkali feldspar and feldspathoids (in lesser amounts) with essential diopsidic augite (usually Ti rich) and brown hornblende ± olivine.

(6) ***Monchiquites (AL)*** are porphyritic alkaline igneous rocks named after Sierra de Monchique in the south of Portugal. These rocks are dominated by olivine, augite (usually Ti rich), and brown colored hornblende. Feldspars are absent and glass/feldspathoids exist within the groundmass.

(7) ***Ouachitites (UML)*** are rare porphyritic ultramafic igneous rocks named after the Oauchitas Mountains of Arkansas, USA. These rocks contain forsteritic olivine, diopsidic augite, biotite (phlogopite), and amphibole set in a matrix of similar assemblage. Carbonates and feldspathoids occur within the groundmass.

Nine thin sections were created from lamprophyric rocks from Bull Mountain/Golden Sunlight. Four are classified as minettes, three as vogesites, and two as kersantites. Sixteen thin sections from the Highwood Mountains were analyzed. Nine are classified as vogesites, three as sannaites, two as spessartites, and two as minettes. Twenty-one thin sections from the Crazy Mountains were analyzed, with one section bearing no observable lamprophyric properties. From the Crazies, ten are classified as monchiquites, five as vogesites, three as kersantites, and two as sannaites. The section analyzed from the Yogo Dyke is classified as an ouachitite, in agreement with Gauthier (1995) and Palke and others (2016).

It should be noted that only calc-alkaline lamprophyres are present in the Late Cretaceous aged suite analyzed from Bull Mountain/Golden Sunlight. The Early Tertiary aged rocks, the Highwood Mountains, much like the Crazies, are a mixture of calc-alkaline and alkaline lamprophyres. The Crazies have a greater abundance of alkaline lamprophyres, predominately monchiquites, than the Highwood Mountain suite. While the Early Tertiary Yogo dyke is the only ultramafic lamprophyre classified in this study.

(5B) Petrography of the CMAP

Rocks analyzed during this study with the 'Glistening Porphyry' characteristic of lamprophyres are dark grey to grey green in color in fresh samples, while weathered samples are brown to red in color. Thin sections and BSEs depict porphyritic and panidiomorphic textures across all locations of the CMAP. The petrographic characteristics of lamprophyric rocks of the CMAP are summarized in Table 4. The dominant mafic phases are clinopyroxene and biotite with lesser olivine, all of which ranged in size from a few centimeters in length to microcrystalline (<10 μm) matrix constituents. Another petrographic texture worthy of note is the common occurrence of cumulophyric and glomerophyric clusters of mafic minerals. The frequency of observed disequilibrium features (rounding and resorption, spongy texture, embayment) in mafic phases is as follows clinopyroxene>biotite>olivine>hornblende. Few coarse

leucocratic constituents such as plagioclase or alkali feldspar are observed (with exception of J28, see photograph 8, Appendix D), but they are readily apparent within the matrix. Leucocratic ocelli were observed in every region of the CMAP, with the circular structures being most common within the monchiquite lamprophyric rocks of the Crazy Mountains.

Table 5: Summary of Petrography from Lamprophyric Rocks of the CMAP

	Minette (CAL)	**Vogesite (CAL)**	**Spessartite (CAL)**	**Kersantite (CAL)**	**Sannaite (AL)**	**Monchiquite (AL)**	**Ouachitite (UML)**
Cpx	M*G	M*G	M*G	(M*)	M*G	M*G	M*G
Ol	(MIG)	M(I)	MG(I)	GI	(M)GI	(MG)I	(G)
Bt	M*GI	(M*)GI	(M*GI)	M*G(I)	M*GI	(M*I)G	M*G
Hbl			(M)	(MG)	(M)	M	
Pl	(G)	(G)	G	G		(G)	
Af	(M)G	(M)G	(G)	(G)	G		G
Foids		G			G	G	G
Ap	I	I	I		I	I	I
Cal	I (G)	G		G(I)	G	G	G
Fe-ore	GI	GI	G	G	G	G	GI
Oc	G	G		G		G	G

*Key: Cpx = clinopyroxene; Ol = olivine; Bt = biotite/phlogopite; Hbl = hornblende; Pl = plagioclase; Af = alkali feldspar; Foids = feldspathoids (leucite); Ap = apatite; Cal = carbonates; Fe-ore = opaque-oxides; Oc = ocelli structures. G= groundmass; M= macrocryst; I = inclusions; ( ) = rare; * = mineral displays disequilibrium features i.e. spongy texture*

Hornblende is generally one of the most bountiful mafic phases within lamprophyres (Rock,1991), but it was found to be less abundant than the other mafic minerals in rocks of the Bull Mountain/Golden Sunlight, Highwood Mountains, and the Yogo dyke. The Crazy Mountain monchiquites are the only rocks with abundant hornblende. Interpreted mafic xenolithic enclaves (Fig. 23 c) observed within the Highwoods held greater amounts of clustered amphiboles. It is possible that samples completely lacking hornblende but that do contain clinopyroxene crystals displaying cores with microcrystalline patchworks of pyroxenes, opaques, and feldspars originate from hornblende that became unstable and was subsequently overgrown by clinopyroxenes; and in this case, it is likely the hornblende originated from country rocks or from an earlier magma that crystallized amphiboles (Streck, 2008).

Rock (1991) describes characteristic zonation of phlogopite/biotite macrocrysts of lamprophyric rocks as having pale yellow cores and transitioning to a reddish-brown pleochroic rim. While this was observed in all regions of the CMAP (most apparent in the Highwood rocks), the inverse was also observed as well. Both coarse and groundmass scale micas can be bent in rocks of every region of the CMAP. In most samples one can find only a hand full of visible bent crystals, but in the Crazies and Highwoods in particular, the feature was a more common occurrence. Biotite macrocrysts of Bull Mountain/Golden Sunlight displayed internal kinked zones of differing birefringence (Fig. 18 (f)). Biotite is the most common phase found partially or completely enclosed within porphyritic pyroxene crystals. Micas caught in disequilibrium with the melt are identified by pervasive spongy texture, resorbed boundaries, and opaque reaction rings. Biotite itself is a common alteration mineral which is often itself replaced by chlorite. Chloritization occurs often in association with carbonates.

Olivine is visible within rocks of every location of the CMAP as a major mafic phase present as macrocrysts or smaller microcrystalline varieties with the groundmass. Tabular, granular, pseudo-hexagonal shaped shells of opaque crystals form around altered olivine, and when completely replaced Iddingsite, pyroxenes, white micas, opaques, serpentine, chlorite, or carbonates were identified as replacement minerals. These granular shaped replacement features are interpreted as olivine crystals caught in total disequilibrium with the melt. Other olivine macrocrysts in disequilibrium are enshrouded in biotite + pyroxene + opaques reaction rims but are not completely replaced. Curiously though, in a few cases where stable olivine macrocrysts were not observed in the matrix, fresh olivine was present as enclosed inclusions within pyroxene megacryst grain boundaries. Even the healthiest idiomorphic olivine macrocrysts are commonly rimmed by dark brown biotite.

Apatite inclusions are visible within melt pockets and as inclusions in clinopyroxene cores intermediate/mantles, and the rim of crystals in all rocks of the CMAP but was most prevalent in the Highwood and Crazies lamprophyric rocks. Apatite crystals display acicular needle like, to equant, to

tabular shapes. Apatite was a common occurrence in concentric growth bands and oscillatory zoned segments host pyroxene crystals. This suggests apatite saturation conditions throughout the host pyroxene growth history (Ubide et al. 2019). Interestingly, apatite inclusions are most abundant in sector zoned clinopyroxenes.

In keeping with the enigmatic nature of lamprophyric rocks, no site from the CMAP has clinopyroxenes that behave with uniform textures. In addition, even within a single thin section, pyroxene macrocrysts are not uniform in regard to zonations and textural features. Euhedral stubby prisms to long tabular macrocrysts are the most common habit observed aside from microcrystalline varieties within the matrix. Coarse glomerocrystic pyroxene masses were identified wherein pyroxene is found radiating outward from a central host crystal in a star like pattern, where the cores contain patchy zonations, and are most visible in rocks of the Highwoods and Bull Mountain/Golden Sunlight. Mineral inclusions (biotite, olivine, apatite) within clinopyroxene macrocrysts suggest new magmas promoted heterogeneous nucleation of clinopyroxene and other minerals on pre-existing clinopyroxene crystals (Kirkpatrick, 1977). Pyroxene zoning from every site of the CMAP varies from slight zonations to heavily or complexly zoned as seen by differing birefringences. Complex zonations are the norm rather than the exception. Pyroxenes displayed a range of internal zoning patterns from: concentric, patchy, oscillatory, or sector zoning. Sector zoning is most abundant in rocks of the Highwoods and Bull Mountain/Golden Sunlight. Disequilibrium features are best preserved in clinopyroxene compared to the other mafic phases within lamprophyric rocks of the CMAP.

Under Ideal conditions if a crystal is in equilibrium with the melt, the composition of the mineral adjusts to lower temperatures and the crystal will be homogeneously zoned. Evidence of homogeneous zoned pyroxenes is nonexistent within these lamprophyric rocks, the pyroxene crystals are chemically zoned caught in the process of disequilibrium with the melt. A unique occurrence of all pyroxenes across the CMAP is the presence of patchy zoning. Patchy zoning, as opposed to clear growth bands, in

macrocrysts of the CMAP is often associated with spongy texture but this is not always the case (Table 5). Patchy zoning textural relationships of crystals can be difficult to interpret, but in all macrocrysts across the CMAP the lighter zones of patchy zoning are associated with lower Mg# values compared to darker zoned areas within the same areas that display higher Mg# values.

Table 6: Macrocryst Type BSE and Petrographic Textural Features

	Type	B1	B2	B3	B4	B5	B6	H1	H2	H3	H4	H5	C1	C2	C3	Y1	Y2	Y3	Y4
Shape	Euhedral crystal	✓	✓			✓	✓	✓	✓	✓						✓		✓	✓
	Subhedral crystal			✓	✓						✓	✓		✓	✓				
	Rounded/Anhedral crystal												✓				✓		
	Truncated crystal	✓																	
	Sector zoned crystal		✓				✓												
	Parasitic growths w/ continous zoning								✓										
	Parasitic growths w/ disontinous zoning																		✓
Core	Dark core		✓	✓		✓	✓			✓			✓	✓	✓	✓			✓
	Light Core	✓					✓	✓	✓		✓	✓					✓	✓	
	Darker outer core	✓	✓			✓		✓	✓	✓	✓	✓	✓		✓	✓	✓		✓
	Lighter outer core													✓					
	Patchy Zoned Core	✓	✓	✓				✓	✓				✓	✓			✓	✓	
	ST limited to inner core	✓			✓							✓						✓	
	ST pervasive through entire core		✓	✓							✓						✓	✓	
	ST limited to outer core							✓	✓	✓			✓						
	Inclusion rich core	✓			✓		✓	✓	✓		✓							✓	
	Irregular shaped core					✓				✓		✓					✓		
	Euhedral core/mantle boundary	✓																	
	Subhedral core/mantle boundary		✓					✓	✓	✓	✓			✓	✓		✓		
	Rounded core/mantle boundary			✓	✓	✓						✓	✓					✓	
Mantle	Dark mantle					✓		✓						✓					✓
	Light mantle		✓	✓					✓	✓	✓			✓	✓	✓	✓	✓	
	Oscillatory zoned mantle		✓		✓		✓	✓	✓	✓				✓	✓				
	Patchy zoned mantle					✓							✓				✓		
	Inclusion rich mantle			✓	✓		✓				✓	✓	✓	✓	✓	✓			
	Inclusion rich bright bands						✓							✓					
	ST growth in isolted bands of mantle						✓							✓					
	ST pervasive through entire mantle											✓	✓				✓		✓*
	ST limited to core/mantle boundary	✓																	
	ST limited to mantle/rim boundary															✓			✓
Rim	Dark rim		✓									✓	✓		✓				
	Light rim	✓		✓	✓	✓	✓	✓	✓	✓				✓		✓	✓	✓	✓
	Resorbed crystal margin				✓			✓	✓	✓			✓	✓	✓				
	Reaction rim							✓	✓	✓									
	Inclusion rich rim			✓	✓		✓								✓				✓
	ST limited to isolated bands of rim				✓						✓	✓		✓					
	ST limited to outer rim				✓		✓			✓									
	Oscillatory zoned rim			✓							✓	✓							
	Patchy zoned rim										✓		✓		✓				✓

Note that colors of types correspond to which region of the CMAP the Types originate from. Red = Bull Mountain/Golden Sunlight, Green = Highwood Mountains, Yellow = Crazy Mountains, and Blue = Yogo Dyke. ST = Spongy Texture, (*) on Y4 corresponds to ST present in parasitic growth and not the host.

(5C) Clinopyroxene Mineral Chemistry of the CMAP

Due to modal abundance and the complex zonations captured within clinopyroxene macrocrysts, they were the mafic phase selected as the main focus of the mineral chemistry portion of this study. The various types of habits, features, and textures of pyroxenes from the CMAP are discussed below after the methods of Barton and others (1982) and Ubide and others (2014). Hereafter clinopyroxene macrocrysts from each region of the CMAP will be distinguished into "Types" and referred to as Type B1, Type H2, etc. These macrocryst Types are segregated by textural features observed from BSEs and under the petrographic microscope, see Table 5.

Clinopyroxenes of all Types from every region of the CMAP are classified as diopside, Fe rich diopside, Ca rich diopside, or augite. Ca rich diopsidic composition (implying crossing over the top diopside field on Fig. 70) was found in pyroxenes of the Highwoods and Yogo Dyke, with Yogo having a greater proportion. All pyroxenes of the Crazies are strictly diopsides. The only region with significant augite composition is Bull Mountain/Golden Sunlight. Note there are select outlier data which are discussed in previous chapters and may be mineral inclusions.

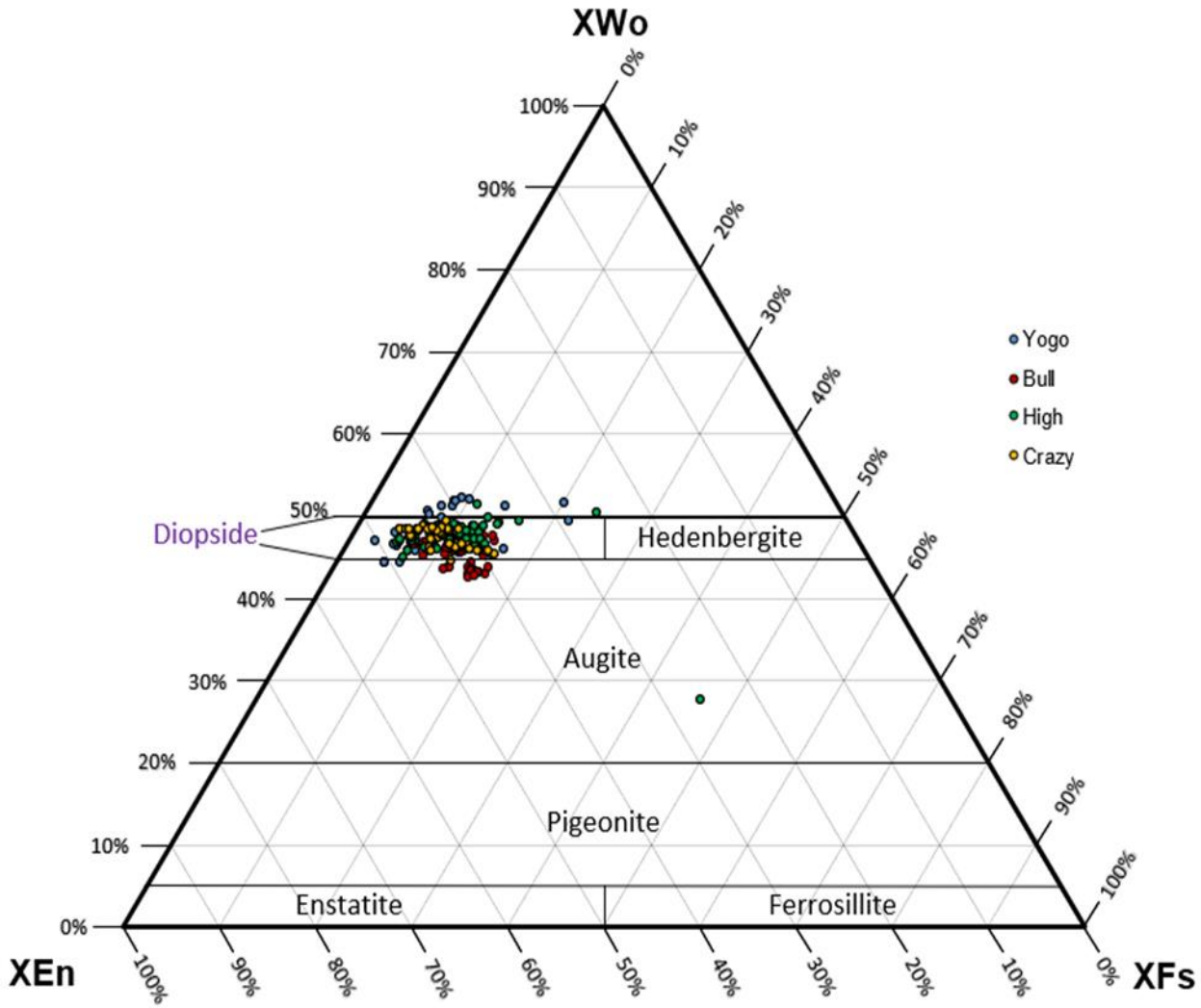

Figure 70: Pyroxene Ternary Diagram of the CMAP

Macrocryst Type mineral chemistry compositional ranges (Mg#, XFs (Ferrosillite Number)), calculated geothermobarometry values (P in kbars and T in °C), and analytical zoning trends of traverses are summarized on Table 6. Bivariate element compositional and Fe^{2+}/Fe^{3+} plots versus Mg# for all macrocryst Types are available on Figure 71.

In lamprophyric rocks (vogesite and minette) from Bull Mountain/Golden Sunlight six distinct Types of clinopyroxene macrocrysts were deduced from BSE and petrographic analysis. Type B1 (J06_1A), B2 (J06_2A), B3 (J06_3A), B4 (J06_8A), B5 (J12_1A), and B6 (J12_3A) range in Mg# between 90

and 71, with ferrosillite contents in the range of Fs_{5-18}. B Type macrocrysts are characterized as mostly normally zoned (with exception of B6) displaying oscillatory and discontinuous trends along analytical traverses. From the bivariate plots (Fig. 71) B Type macrocrysts are enriched in Cr_2O_3 and FeO (Fig. 72) and relatively lower in SiO_2 than other Types of the CMAP.

In sannaites from the Highwood Mountains four distinct Types of clinopyroxene macrocrysts were deduced from BSE and petrographic analysis. Type H1 (J18_1A), H2 (J18_2A,4A), H3 (J18_4A), H4 (J24_1A,4A), H5 (J24_6A), range in Mg# between 90 and 67, with ferrosillite contents in the range of Fs_{5-17}. Note that unlike other regions of the CMAP some Types (H2 and H4) represent pyroxenes that are nearly identical in regard to observable textures, habit, dissolution features. In attempts to confirm the authors interpretation of near identical macrocrysts, these Types were segregated in regard to mineral chemistry and geothermobarometry data to investigate if these crystals are as similar as they seem on BSEs and under the petrographic microscope. These Types have been separated as H2 (J18_2A), H2-1 (J18_6A) and H4(J24_1A), H4-1(J24_4A) respectively on Figure 71, Figure 78, and Table 6. H Type macrocrysts are mostly normally zoned with some displaying both normal and reverse zoning (inverse) trends. Analytical traverses display oscillatory, discontinuous, and unique step zoning, with the latter being most visible with Highwood lamprophyric rocks compared to others from the CMAP. H Type macrocrysts are slightly enriched in TiO_2 and CaO (Figs. 71 and 72). Compositional data from H Type macrocrysts seem to behave similarly to B Types of the Bull Mountain/Golden Sunlight suite.

In monchiquites and sannaites from the Crazy Mountains three distinct Types of clinopyroxene macrocrysts were deduced from BSE and petrographic analysis. Type C1 (J32-3_2A), C2 (J32_4A), and C3 (J36_3A) range in Mg# between 90 and 71, with ferrosillite contents in the range of Fs_{5-16}. C Type macrocrysts are defined as normal or inversely zoned with oscillatory or discontinuous analytical zoning trends. Similar to other variation diagrams discussed earlier in this works, the Crazy Type data on the bivariate compositional Type diagrams (Fig. 71) tend to behave like their namesake and are easily

discriminated when compared to other regions of the CMAP by the greater range of compositions. C Type macrocrysts exhibit lower values of TiO_2, Al_2O_3, CaO, and Fe^{2+}/Fe^{3+} than other Types of the CMAP. In addition, Na_2O levels are significantly higher than all other Types of the CMAP.

In the Yogo Dyke lamprophyre (ouachitite) four distinct Types of clinopyroxene macrocrysts exist. Type Y1 (Yogo 1A), B2 (Yogo 4A), B3 (Yogo 5A) Y4 (Yogo 6A) range in Mg# between 94 and 57, with ferrosillite contents in the range of $Fs_{3\text{-}22}$. In accordance with other Types of the CMAP, Y Type macrocrysts are defined as normally zoned. Discontinuous zoning analytical traverse trends are present in Y3 but this could be explained by fewer data in the Yogo Y Type traverses that could make the discontinuous sharp jumps in composition more obvious. Y Type macrocrysts host the most ultramafic signatures with elevated Mg#, TiO_2, Al_2O_3, Cr_2O_3, and CaO levels along with the lowest SiO_2 and FeO composition of all Types of the CMAP (Figs. 71 and 72).

Table 7: Summary of Type Composition, Geothermobarometry Statistical Analysis, and Analytical Zoning Characteristics (determined by electron microprobe analysis).

	Composition		Geothermobarometry					Zoning (Analytical)					
Type	Mg #	XFs (ferrosilite)	P (km) ± 5.5 Range	P (km) ± 5.5 Mean	P (km) ± 5.5 σ	P (km) ± 5.5 IQR	T (°C) ± 30	Normal	Reverse	Inverse	Oscillat-ory	Discon-tinous	Step
B1	85-74	$Fs_{8\text{-}14}$	67-32	54	12	13	1298-1214	✓			✓	✓	
B2	85-74	$Fs_{8\text{-}14}$	63-18	52	15	13	1291-1186	✓			✓	✓	
B3	90-71	$Fs_{5\text{-}15}$	68-49	59	8	10	1310-1252	✓				✓	
B4	80-75	$Fs_{11\text{-}14}$	61-53	57	2	2	1322-1264	✓					
B5	88-74	$Fs_{8\text{-}18}$	62-19	52	13	11	1288-1186	✓				✓	✓
B6	75-71	$Fs_{6\text{-}15}$	63-60	62	1	1	1251-1187		✓		✓		
H1	90-71	$Fs_{5\text{-}15}$	50-30	44	6	5	1239-1190	✓				✓	
H2	90-67	$Fs_{5\text{-}17}$	56-29	47	8	7	1251-1190	✓			✓	✓	✓
H2-1	90-77	$Fs_{5\text{-}12}$	47-23	40	6	7	1229-1175			✓	✓		✓
H3	88-71	$Fs_{6\text{-}15}$	48-26	41	7	5	1237-1181	✓			✓		
H4	82-73	$Fs_{10\text{-}14}$	58-42	48	5	5	1263-1219	✓					✓
H4-1	88-74	$Fs_{7\text{-}13}$	54-(-3)	50	38	13	1247-1117			✓	✓		✓
H5	87-71	$Fs_{7\text{-}16}$	54-4	40	17	13	1249-1128	✓					
C1	88-71	$Fs_{6\text{-}16}$	48-3	27	14	24	1182-1101	✓			✓		✓
C2	90-78	$Fs_{5\text{-}12}$	51-(-16)	28	22	38	1182-1059			✓	✓	✓	
C3	90-81	$Fs_{5\text{-}10}$	31-6	20	8	13	1156-1102		✓		✓	✓	✓
Y1	91-71	$Fs_{5\text{-}14}$	69-37	52	13	8	1357-1102	✓					
Y2	84-69	$Fs_{8\text{-}17}$	85-41	53	21	12	1394-1286			✓			
Y3	91-57	$Fs_{4\text{-}22}$	64-45	53	8	11	1309-1297	✓				✓	
Y4	94-81	$Fs_{3\text{-}9}$	71-43	53	12	18	1362-1289	✓					

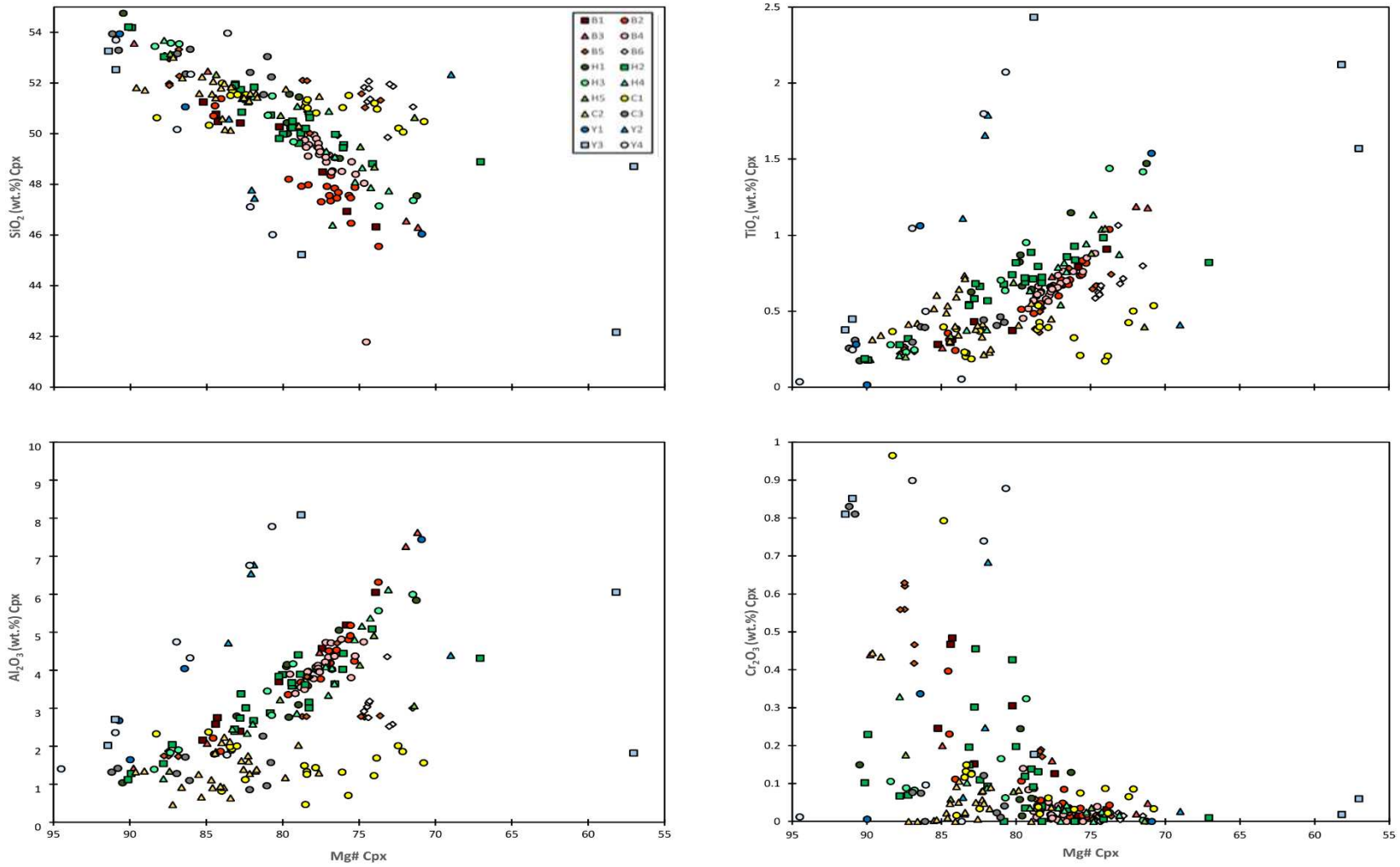

Figure 71: Clinopyroxene Elemental Bivariate Diagrams vs. Mg# by Macrocryst Type

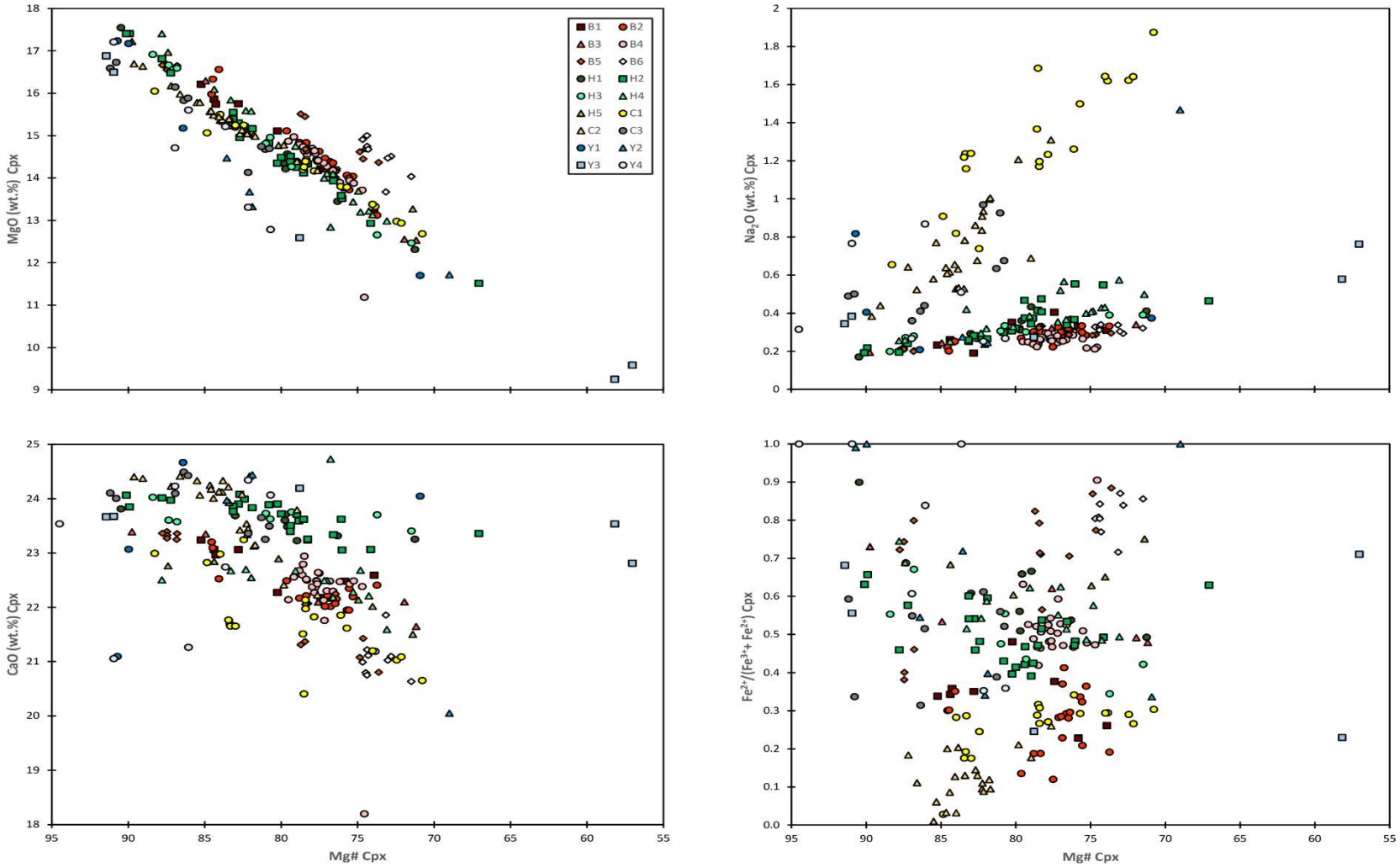

Figure 71 (Cont.): Clinopyroxene Bivariate Diagrams vs. Mg# by Macrocryst Type

Individual macrocryst Types can be differentiated as phenocrysts, antecrysts, or xenocrysts on the basis of zoning, textural, and mineral chemistry evidence captured within crystals. Davidson and others (2007), Streck (2008), Ubide and others (2012), and Menezes and others (2015) add to the discussion of macrocrysts in lamprophyres by incorporating this term 'antecryst'. They summarize, "… [an antecryst] refers to a specific crystal type that differs from those identified as phenocrysts (larger early-crystalized phases that are in equilibrium with the liquid) and xenocrysts (crystals that are foreign to the magmatic liquid and have no genetic association with it)." Therefore, antecrysts are crystals that did not crystallize directly from the host magma, but still maintained a genetic connection within that same system. They postulate that antecrysts may be an indication of a previous stage of magmatic evolution, and because of this they may no longer be in chemical equilibrium with the fractionated liquid that carries them. Antecryst microtextures include zoned clinopyroxene (Ti-rich rims and partially corroded cores), mineral inclusions within clinopyroxene cores, and biotite coronas surrounding macrocrysts (Menezes et al., 2015).

B1, B2, and B3 macrocrysts are interpreted as antecrysts while B4 and B5 are interpreted as xenocrysts and B6 could be interpreted as xenocrystic or phenocrystic. All B Type macrocrysts except B5 and B6 display corroded core regions with spongy texture. From core to rim, B (1-4) Type macrocrysts host rims that are enriched with Ti when compared to their cores, although B2 oscillatory mantle region is significantly more enriched than both core and rim segments. As one would expect Al_2O_3 follows this oscillatory trend. Type B (1-5) defines Mg# decreasing normal zoning trends most likely originating from progressive crystal fractionation of a primitive magma composition becoming more evolved. Curiously, sector zoned B6 Type macrocrysts define Mg# increasing from core to rim (with decrease in TiO_2 and Al_2O_3). Sector zoned B6 hosts the lowest Mg# values of the Bull Mountain/Golden Sunlight suite, and on the bivariate Type diagrams (Fig. 71) B6 can be discriminated from the other B Type macrocrysts by lower Al_2O_3, Cr_2O_3, and CaO composition. Curiously, B6 plots above the other B Types along the

trendline for MgO composition. In regard to Fe^{2+}/Fe^{3+} ratios, B6 is significantly elevated compared to other B Type macrocrysts. B6 is likely either a phenocryst or a xenocryst because its zoning and composition are different than other B Types, but additional geochemical data is needed to determine this. B6 displays fewer signs of disequilibrium features when compared to other B Types but does host small pockets of spongy texture within isolated bands of the mantle. Presumed xenocryst (B4) Mg# ranges from 80 to 75, there is little variation in TiO_2 and Al_2O_3 composition, and the outer rim B4 displays a partially resorbed margin. Further evidence of another xenocryst exists (B5) due to the patchy zoning pervasive from core to mantle segments.

Both H2 and H4 Types do not behave erratically on the bivariate diagrams, thus the author's interpretation based off textural features that multiple macrocrysts (J18_2A and J18_6A, Type H2) and (J24_1A and J24_4A, Type H4) be grouped together. Unlike other regions of the CMAP, no H Type macrocryst significantly discriminates itself from the others on bivariate diagrams (Fig. 71). H (1-4) Types are interpreted as antecrysts given the presence of spongy textured cores, micaceous reaction rims, and TiO_2 rim enrichment (Menezes et al. 2015). An interesting feature of H (1-3) Types is the presence of subhedral/subrounded grain boundary between the core and mantle regions associated with an increase in Mg#. Patchy zoning is present at the center of the cores (typically associated with spongy texture, except for H1 where the inner core is devoid of melt pockets and instead, they reside inside the outer core) often rich with inclusions surrounded by a high Mg# darker outer core in BSEs. Type H (1-3) macrocrysts exhibit Mg# decreasing normal discontinuous, oscillatory, and step zoning trends most likely originating from progressive crystal fractionation. An interesting feature observed from H (2 and 4) is the presence of both normal and reverse zoning taking place over broad oscillatory mantle regions characterized by fine banding.

H2 Type macrocrysts (presumed antecrysts) are similar to types 1, 3, and 4, but differ in that they host 'parasitic growths of clinopyroxene' which are themselves continuously zoned with their

respective host's banding. Where the parasitic growth and the host come in contact with one another spongy texture worm-like chains are observed alongside a suture looking fracture pattern. Curiously though, in H2 the inner cores of this growth hold nearly identical Mg# values as the host's innermost core, but in crystals of nearly identical textural features (H2-1) the growth depicts elevated Mg# values compared to its host. H5 is interpreted as xenocrystic because the crystal contains primitive signatures (Mg# 87) within its irregular rounded patchy zoned core. In addition, spongy textured melt pockets are found in every region of the macrocryst, and the crystal shape is subhedral compared to the other Types which are all euhedral. The form of the irregular darker core is similar to cumulophyric texture wherein crystals would clump together from a central point.

C1 is interpreted as xenocrystic and is completely anhedral and ovate. The crystal is clearly out of equilibrium with the groundmass because C1 displays resorbed crystal margins, abundant inclusions, and pervasive patchy zoning from core to rim. The crystal is normally oscillatory zoned with regards to the analytical traverse and decrease in Mg# from core to rim. Spongy texture exists within the outer core and is pervasive through the crystal mantle. C2 is also a xenocryst and originates from the same thin section as C1, yet their textural features and analytical traverse trends vary greatly. C2 is subhedral and displays patchy and oscillatory zoning on BSEs and both normal and reverse zoning compositional trends (inverse). The dark inner core is primitive having Mg# of 90 and is surrounded by patchy zoning that shifts from fine to coarse oscillating banding. It should be noted that these bands are not "healthy" and patchy zoning seems to overprint the bands in some locations within the mantle. Inclusions are rich within these bands and spongy texture are most prevalent in coarse bands (>100 um) along the partially resorbed rim. Unlike C1, the compositional data trends are more progressive rather than step zoned implying the macrocryst is in the process of re-equilibration through diffusion. Interestingly, both C1 and C2 xenocrysts behave similar on bivariate diagrams (Fig. 71). C3 is an antecryst. Compared to C1 and C2, Type C3 exhibits low Al_2O_3, Na_2O, and Fe^{2+}/Fe^{3+}ratios on bivariate diagrams. C3 is reverse oscillatory

zoned with increasing Mg#, and Al_2O_3, while TiO_2 and Cr_2O_3 oscillate but ultimately do not vary greatly from core to rim. The darker inner core has nearly identical Mg#, TiO_2, Al_2O_3, and Cr_2O_3 concentrations as the dark patchy zoned resorbed rim. Much like C2, C3 hosts unhealthy fine and coarse bands comprising the crystals mantle. Spongy textured melt pockets are absent from C3, thus the crystal could be a phenocryst, because melt pockets and TiO_2 enriched rims are nonexistent.

Y1, Y3, and Y4 Types are interpreted as antecrysts. All of these macrocryst Types have euhedral grain boundaries, normal zoning defined by decreasing Mg#, and TiO_2 enriched rims. Y (1-3) Types are characterized by high Cr_2O_3, with highest concentrations recorded as 1.6, 0.8, and 1.6 wt. % oxide respectively. Curiously, Y1 and Y3 Type traverses depict Cr_2O_3 content decreasing from core to rim, while Y4 increases from core to rim. The presumed parasitic growth of Y4 mirrors all compositional trends of the host crystal. It should be noted that Y1, Y3, and Y4 Types display spongy texture melt pockets, but those pockets are not pervasive throughout the entire crystal in contrast to Y2. Y2 is a presumed xenocryst because the traverse composition differs from all other Types of the Yogo Dyke lamprophyre. Y2 shows the most disequilibrium features with pervasive spongy texture accompanied with patchy zoning throughout the entire crystal, large melt pockets (>1 mm in length) and rounding of the crystal margin. This macrocryst is inversely zoned with Mg#, TiO_2, Al_2O_3, Cr_2O_3, NiO, increasing from core to rim. Interestingly, point 2 along the traverse has increased Na_2O content (up to 1.5 %) and Fe^{2+}/Fe^{3+} ratios compared to other Y Types. Curiously, the other Types host darker core regions (high Mg# and low Fe) while Y2 displays the opposite with an unusually bright/light core (low Mg# and high Fe) on the BSE (Fig. 58).

The diversity of zonations present within clinopyroxene Types of the CMAP are indicative of changes in open system magmatic processes and are discussed below. B (1-4) and H (1-5) macrocrysts with spongy textured cores are evidence of the crystal being out of equilibrium with the melt, and later growing from the melt. If these macrocrysts were out of equilibrium with the melt the whole duration of

its crystallization history, one would expect pervasive spongy texture, resorbed grain boundaries, rounding, or visible reaction rims, as seen in macrocryst C1.

B4 and B5 Types originate from section J24 and in all of these macrocryst Types there exists reversal of zoning from the inner to outer core. Reverse zoning trends on analytical traverses are attributed to open system magmatic processes such as magma recharge and contamination (Streck, 2008). Whereas the more abundant normal zoning trend of clinopyroxene macrocrysts from the CMAP is likely an indication of a progressive crystal fractionation sequence of primitive sourced magmas becoming more evolved.

Sector zoning such as found within B6 is controlled by the crystallographic structure of the mineral as well as its growth rate related to varying degrees of magma undercooling when the crystal is out of equilibrium. In a study of major and trace elements within sector zoned clinopyroxene, Ubide and others (2019) state that, "[sector zoning] is strongly dependent on the charge/size of a given cation and its ability to charge-balance the clinopyroxene structure after incorporation of Al^{3+}in tetrahedral substitution for Si^{4+}."

Streck (2008) argues that patchy zoning of macrocrysts could be indicative of xenocrysts with complex growth histories. Tomiya and Takahashi (2005) and Streck and others (2007) assert that patchy zoning can result from (1) step zoned crystals with originally homogenous core areas caught in the process of slowly being eliminated by intra-crustal diffusional processes, or (2) melt-crystal re-equilibration processes of originally unzoned crystals. More precisely, this re-equilibration could occur when single crystals are suspended in melt that they are not in equilibrium with, or where crystals interact with melt from cracks or small channels along magmatic reservoir margins (Streck, 2008). Pervasive patchy zoning could also be generated when a crystal is in the process of re-equilibrating with the melt through diffusion or when crystallization into open spaces of skeletal crystals produces compositions different from the skeletal crystal host (Streck, 2008). To differentiate between these two

processes the analytical traverse is analyzed at points pertaining to patchy zones. In the case of C1 and Y2, step zoning is observed along this compositional transition, thus crystal growth within a skeletal host is the most probable origin (Stewart and Pearce, 2004). When macrocrysts of from the same region of the CMAP are discriminated on bivariate diagrams, C3 separates from C1 and C2, the processes involved in crystallization are likely very different owing to the injection of a more primitive magmas.

Step zoning observed in Highwood macrocrysts (H2 and H4) within normally zoned crystals might be an indication of a more complex growth history involving open system processes, similar to patchy zoning (Streck, 2008). Observable small scale reverse zoning within single crystals can manifest as growth bands located along the core to rim transect and have been interpreted as an indication of growth from more mafic rich (high Mg#) magmas after initially growing from more differentiated and silicic magmas (Streck, 2008). Within macrocrysts with broad mantles displaying oscillatory zoning fine banding on the scale of <10-40 μm is thought to be largely kinetically controlled, but more precisely it is observable feedback between growth and diffusion in the melt, whereas concentric coarser bands are thought to reflect more dynamic magma processes. For example, oscillatory zoning can occur due to growth of a crystal during convection within a magma chamber where the crystal experiences continuous changes in pressure and temperature, but coarse bands with spikes in Mg# values could be attributed to prolonged mixing events. The presence of differing populations of macrocrysts within a single thin section (H2 and H2-1 for example) with varying Mg# values within parasitic growth cores likely records different mixing and recharge events. Macrocryst xenocrysts with cumulophyric textures, like those found in H5, could be evidence that the macrocryst originally started growing in a primitive melt, was later caught in disequilibrium with the melt, that eventually re-equilibrated and continued growth only to be subjected to disequilibrium conditions at a later point.

Unexpectedly clinopyroxenes from each region of the CMAP have varying ferric-ferrous ratios and discrimination fields from each suite are clearly visible (Figs. 73, 74, and 75). The similarities

observed of lamprophyric rocks from Bull Mountain/Golden Sunlight and the Highwood Mountains on compositional bivariate diagrams are not replicated with respect to ferrous-ferric ratios. Traditionally as magmas crystalize mafic minerals (olivine and clinopyroxene) where Mg^{2+} and Fe^{2+} are preferred within the crystal lattice, the melt will increasingly become enriched in Fe^{3+}/Fe^{2+} and oxygen fugacity will increase; but in minette magmas the opposite exists where phlogopite contains predominately ferric iron and has higher Fe^{3+}/Fe^{2+} ratios than the bulk rock, thus, the residual liquid is driven towards lower ferric/ferrous ratios as phlogopite is crystallized early out of the melt (Carmichael, 1991). More primitive mafic melt composition is often attributed where Mg#, Cr, and Ni are high, but magmas of more magnesian composition can correspond to other factors such as an increase in oxygen fugacity reducing the amount of Fe^{2+} of the melt (Streck, 2008). Lamprophyres and minettes have elevated Fe^{3+} /Fe^{2+} ratios up to five log units higher than MORBs (Carmichael, 1991). However, the differing ferrous/ferric ratios of clinopyroxenes across the CMAP demonstrate that lamprophyric rock redox states are determined substantially by source regions (Carmichael, 1991). More questions arise. If these rocks are of similar age, from the Late Cretaceous to Early Eocene times, and from the same volcanic province, why do they show differing ferric-ferrous pyroxene compositional trends from one another?

Note that select groundmass clinopyroxene analyses are present on table 4. Unfortunately, only groundmass clinopyroxenes EMPA exist for the Highwood Mountains (J24 & J18) and Yogo dyke. The mean Mg# is 78.1 within sample J24, while the mean Mg# is 80.5 for sample J18. Note that anomalous stoichiometry values are present in crystal 3 of J18, visible within the Total Cation vs Ideal Cation values (4.52 Total compared to 4.00 Ideal). The mean Mg# for the Yogo dyke groundmass clinopyroxenes is 87.4 and as expected the Yogo groundmass crystals are enriched in Cr oxide compared to those from the Highwood Mountains.

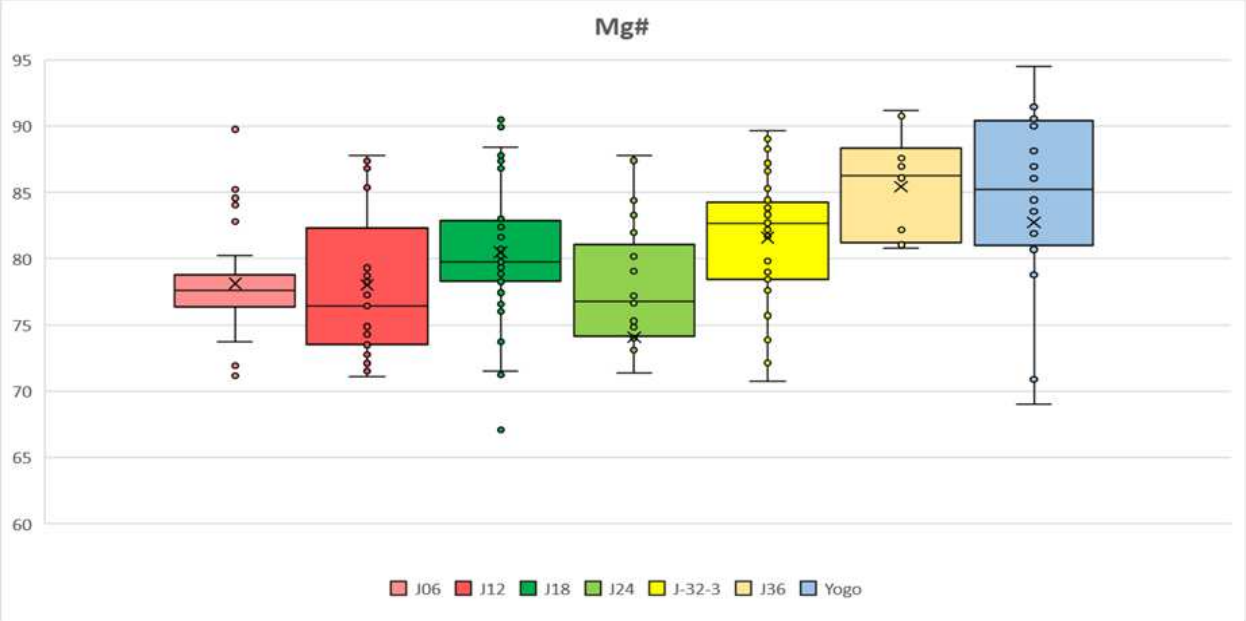

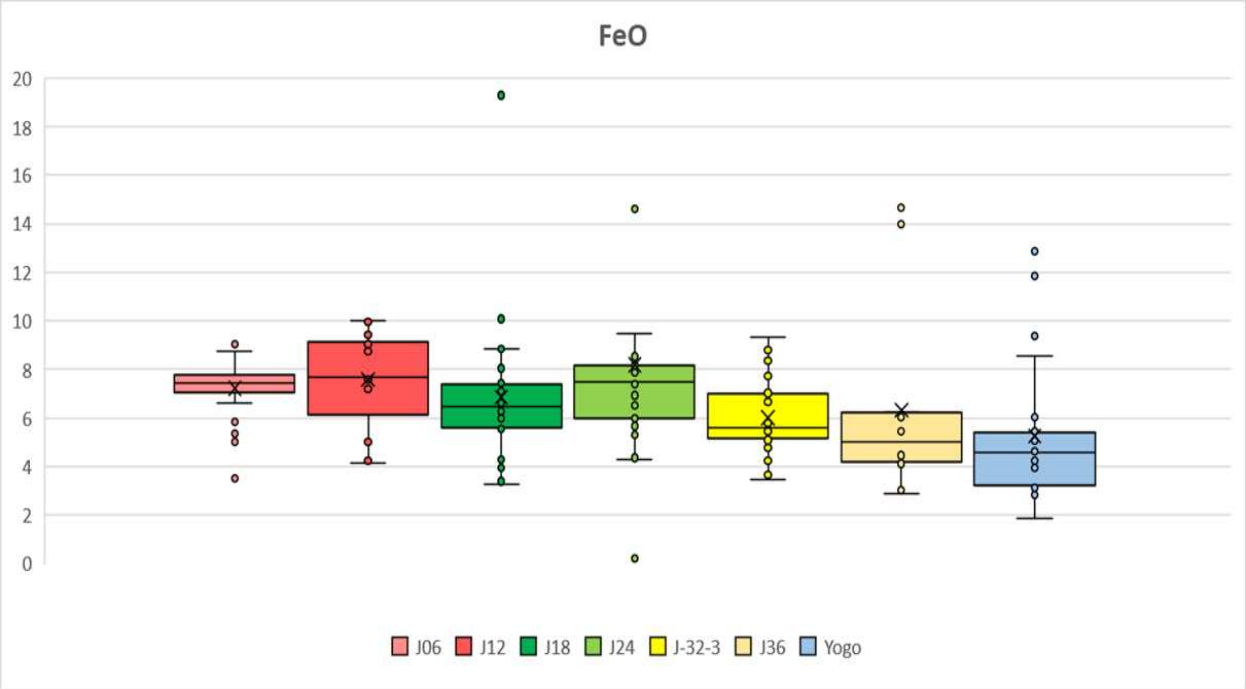

Figure 72: Box and Whisker Plots (Mg# and FeO)

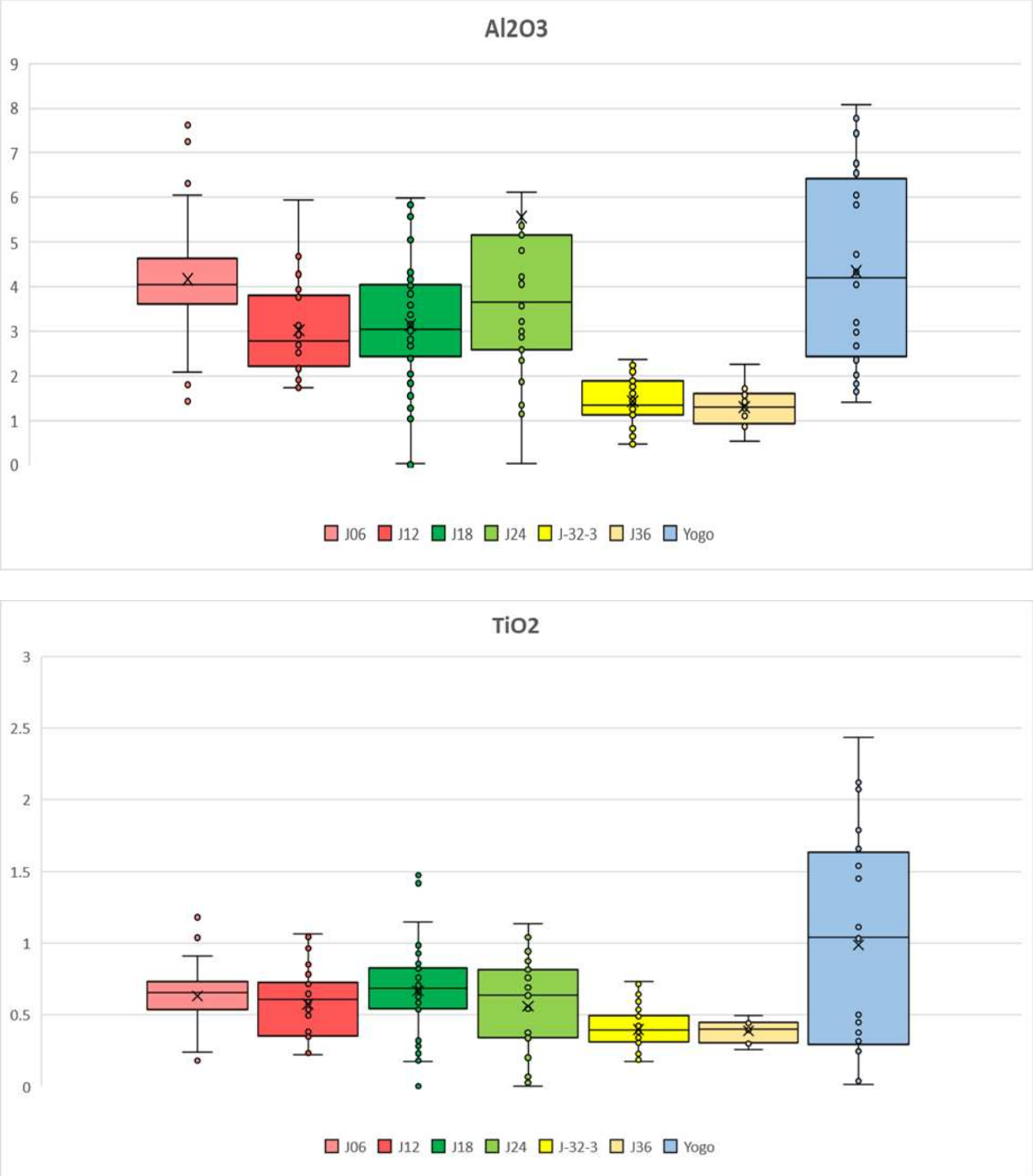

Figure 72 (Cont.): Al_2O_3 and TiO_2 Box and Whisker Plots

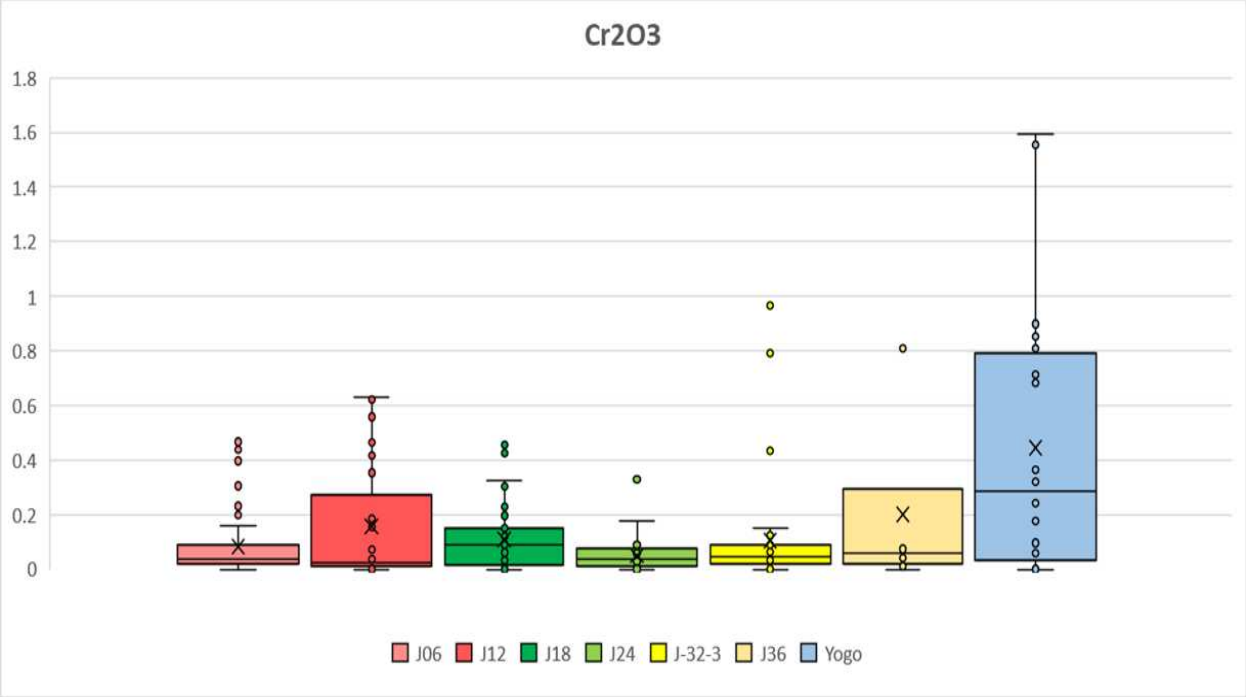

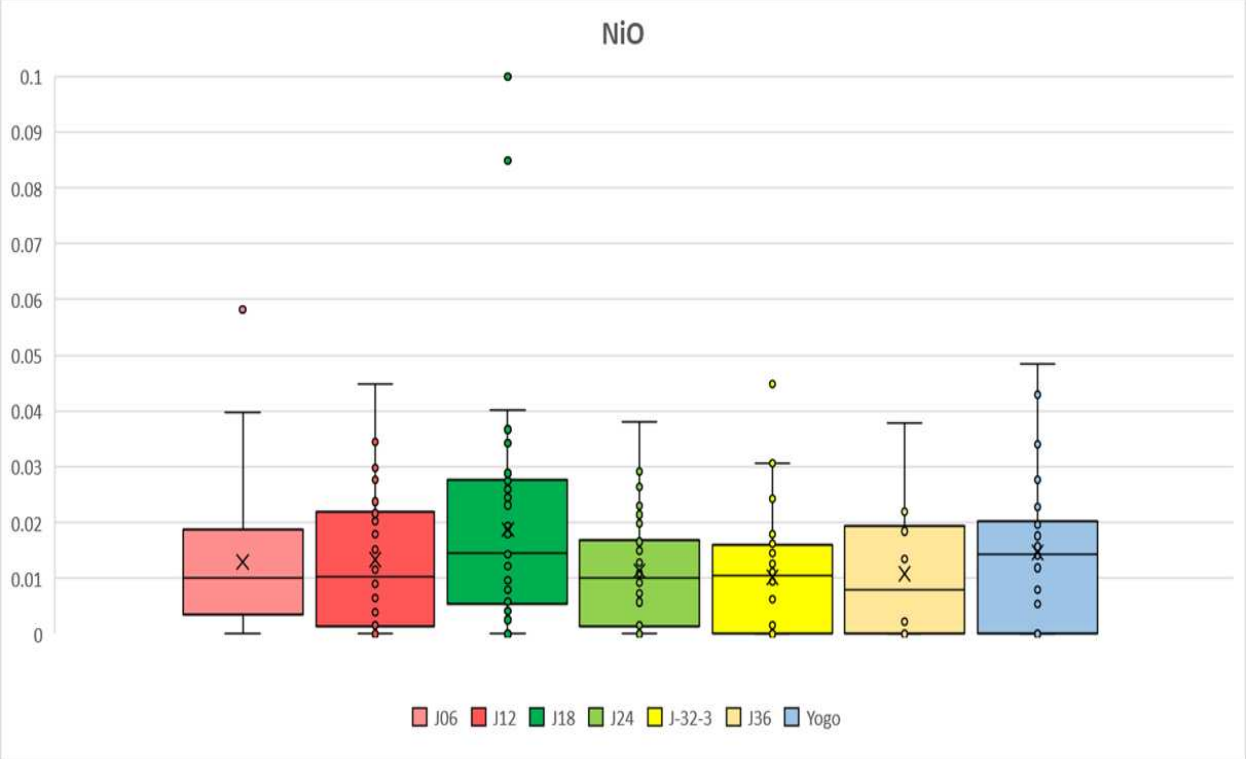

Figure 72 (Cont.): Cr_2O_3 and NiO Box and Whisker Plots

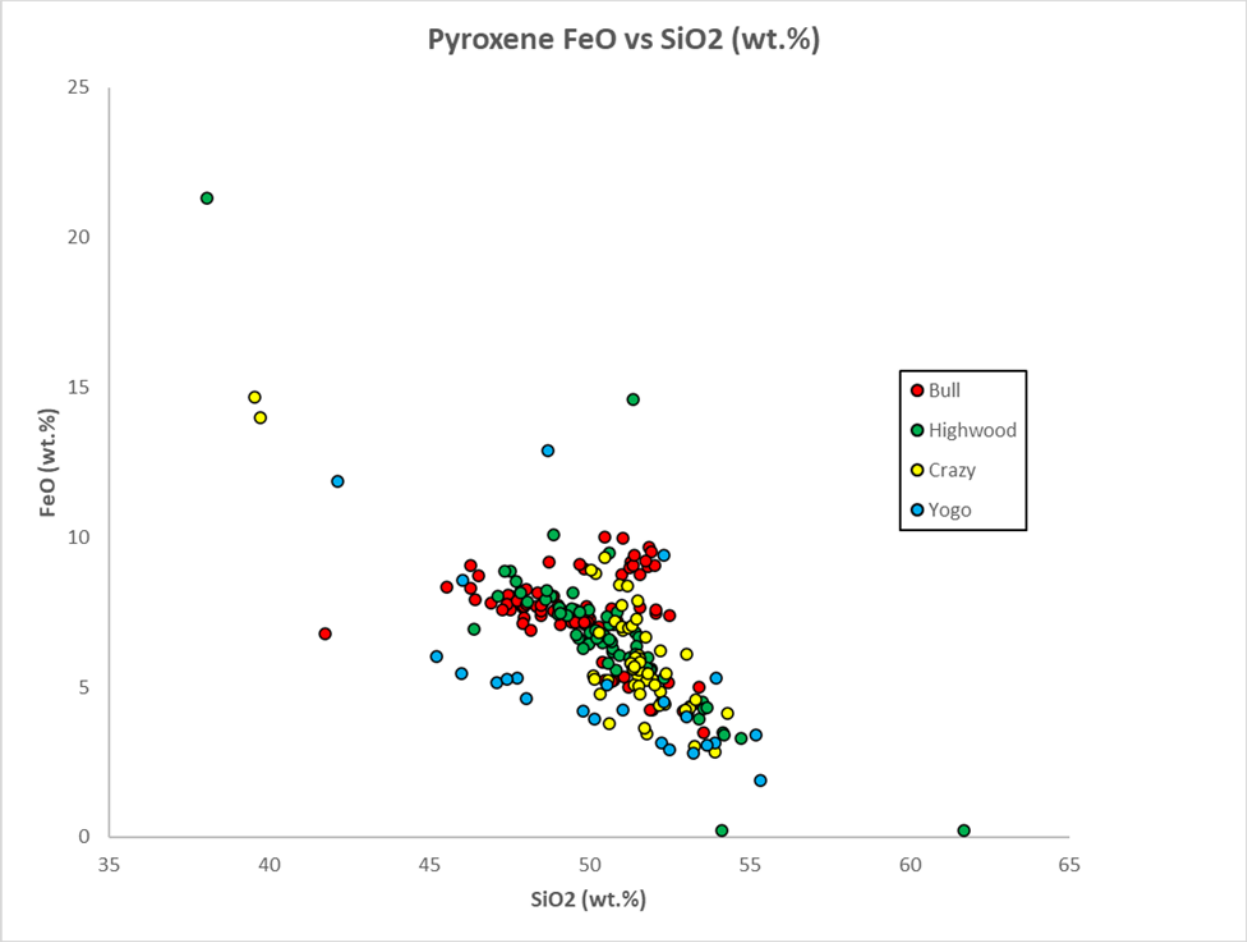

Figure 73: Pyroxene FeO vs SiO_2 (wt.%) Variation Diagram

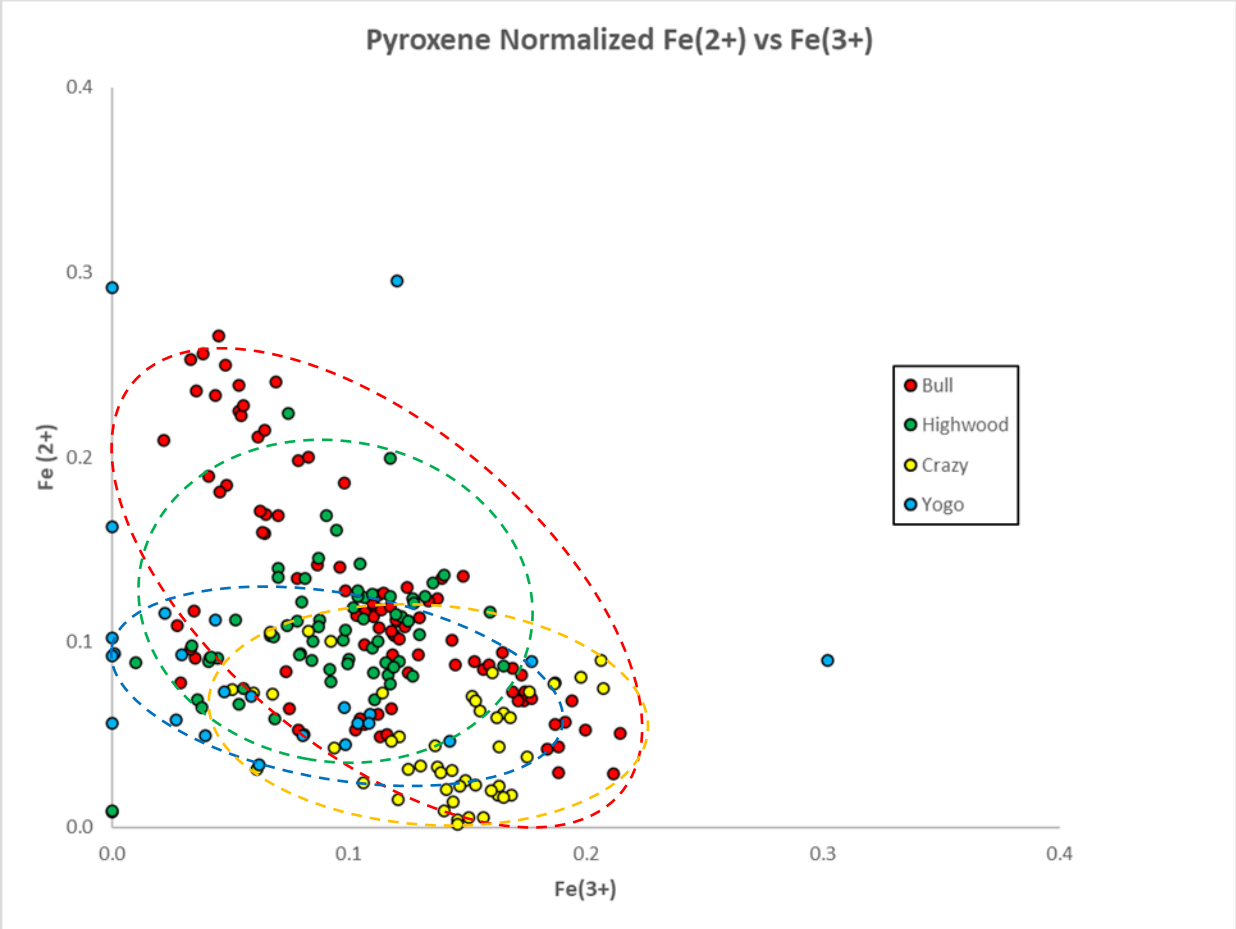

Figure 74: Clinopyroxene Normalized Fe^{2+} vs Fe^{3+} by Region of the CMAP

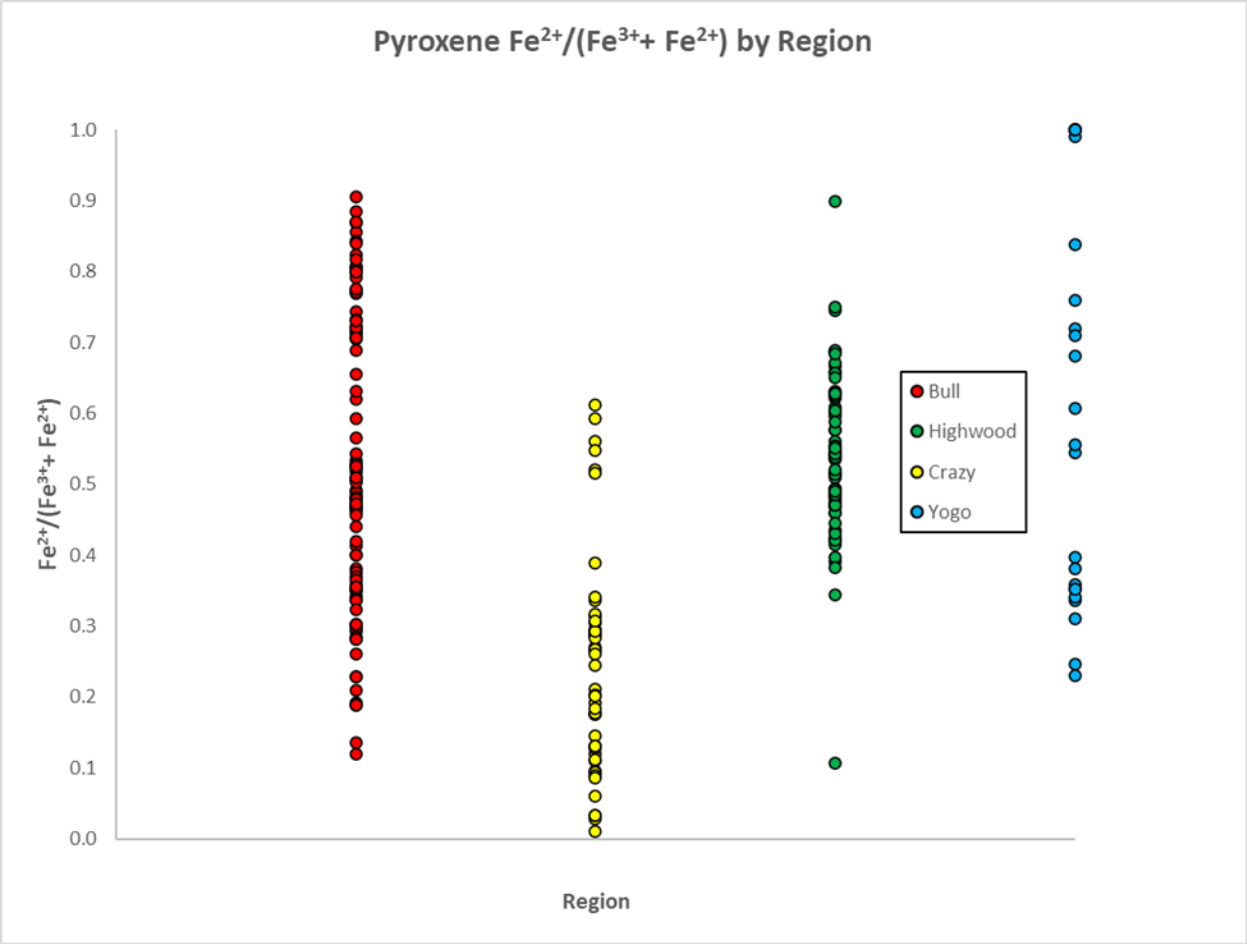

Figure 75: Clinopyroxene $Fe^{2+}/(Fe^{3+}+Fe^{2+})$ Variation of the CMAP

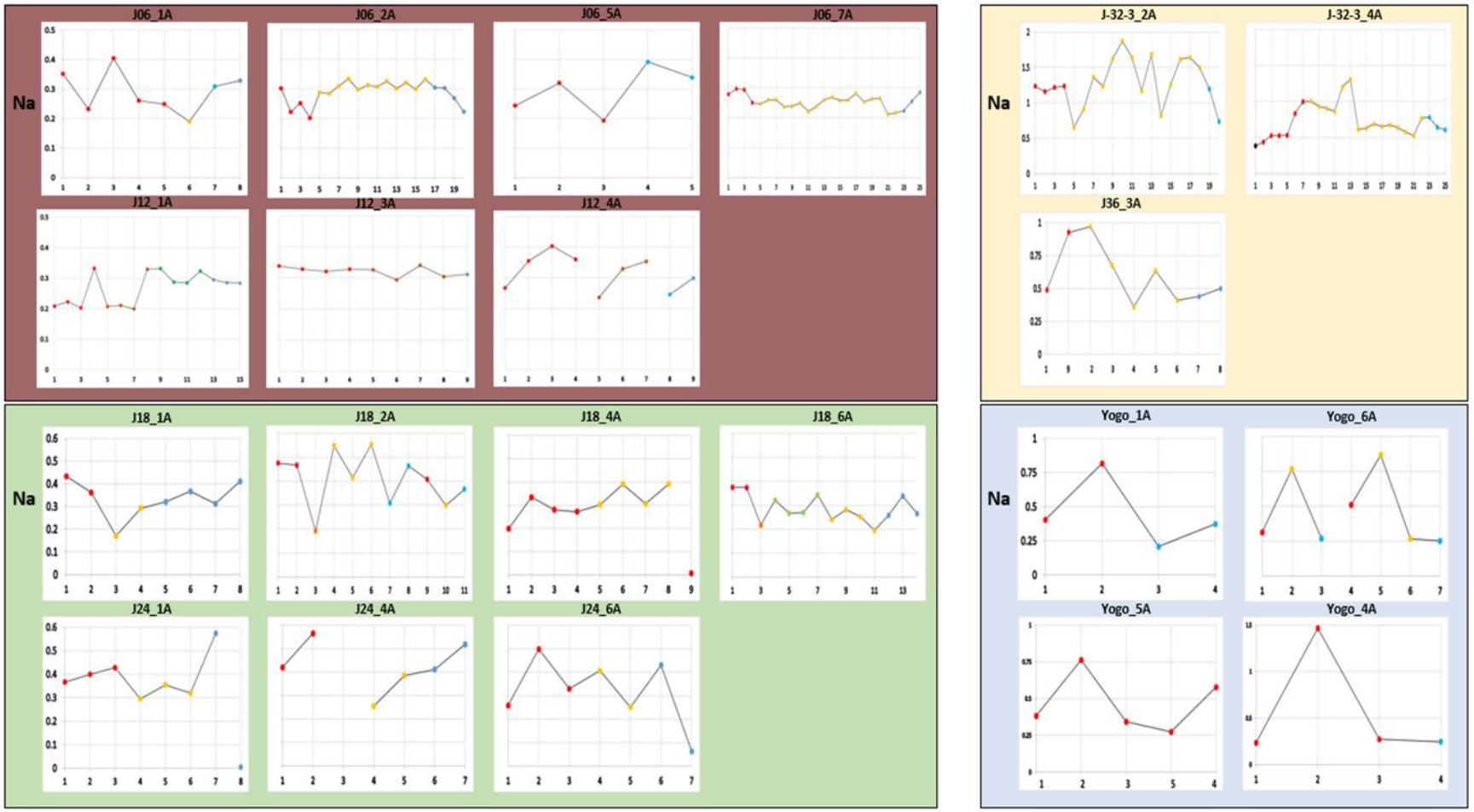

Figure 76: Na_2O vs Distance analytical traverses for each crystal analyzed from this study. Note that Bull Mountain crystals are within the red border, Highwood Mountain crystals are within the green border, Crazy Mountain crystals are within the yellow border, and the Yogo Dyke crystals are within the blue border.

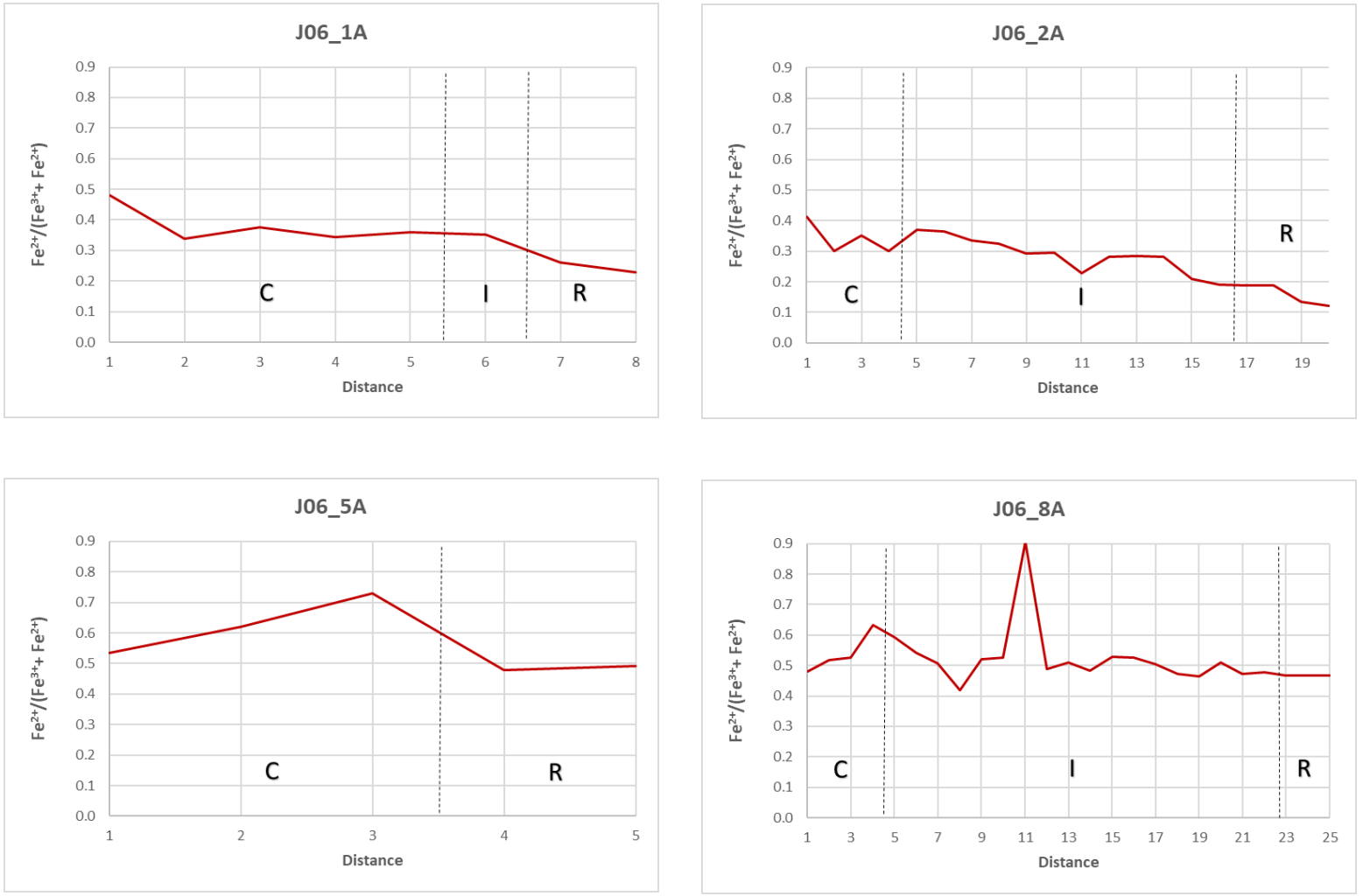

Figure 77: $Fe^{2+}/(Fe^{3+}+Fe^{2+})$ across analytical traverses from J06 (Bull Mountain/Golden Sunlight)

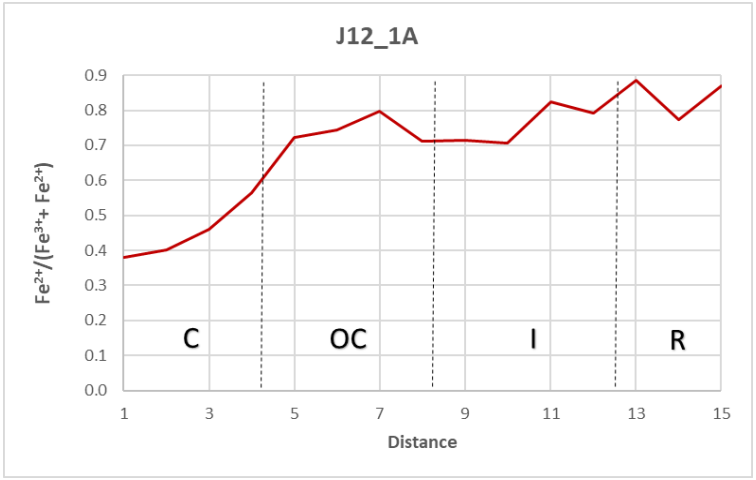

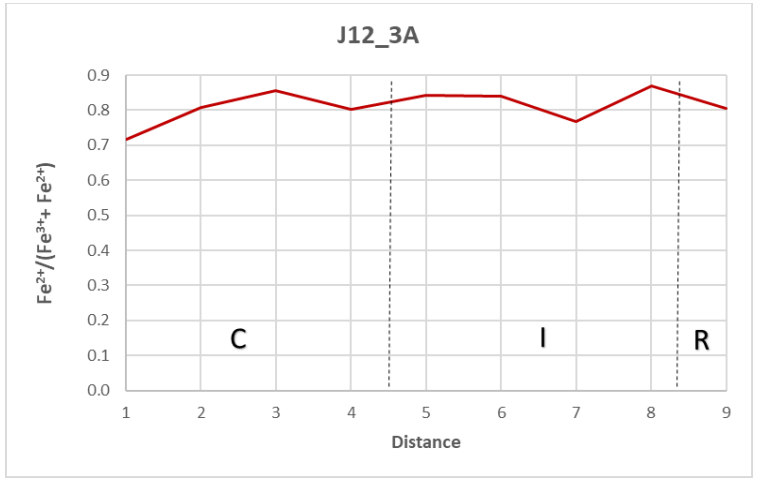

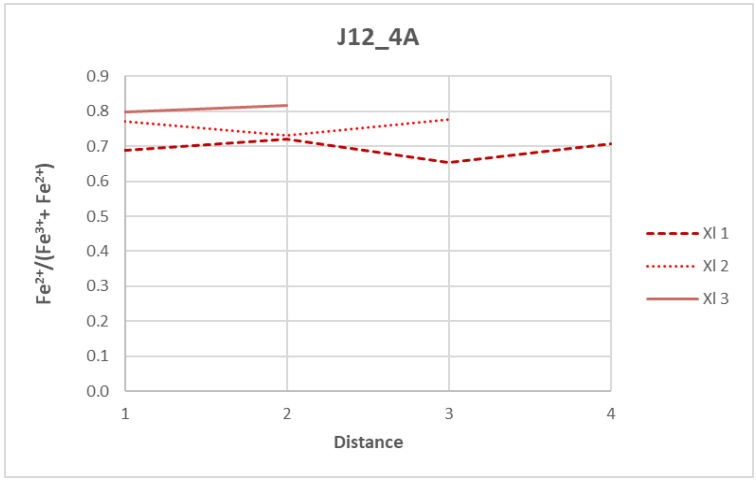

Figure 77 (Cont.): $Fe^{2+}/(Fe^{3+}+Fe^{2+})$ across analytical traverses from J12 (Bull Mountain/Golden Sunlight)

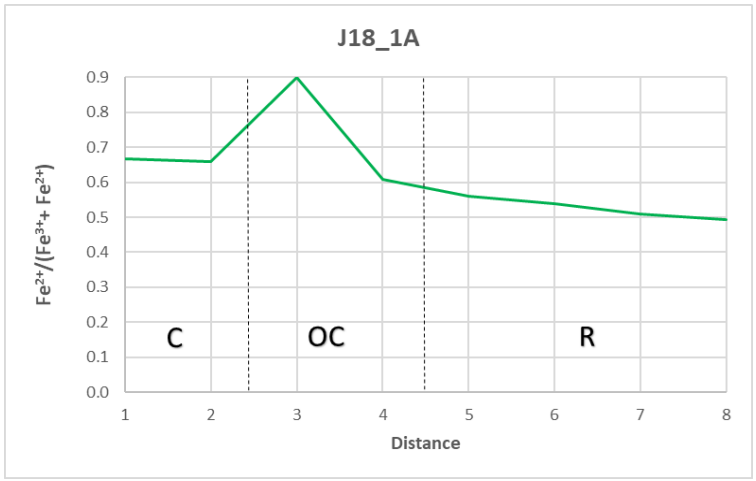

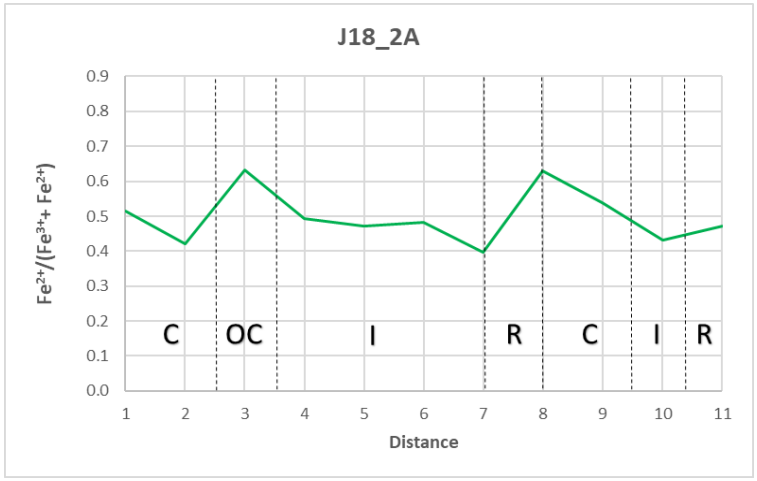

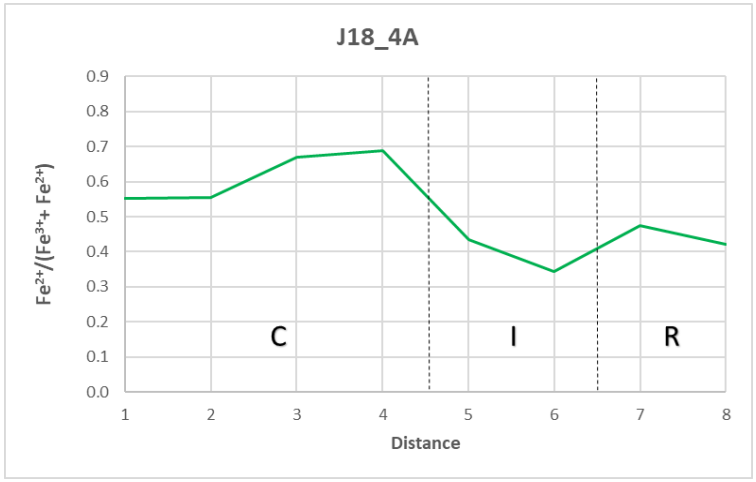

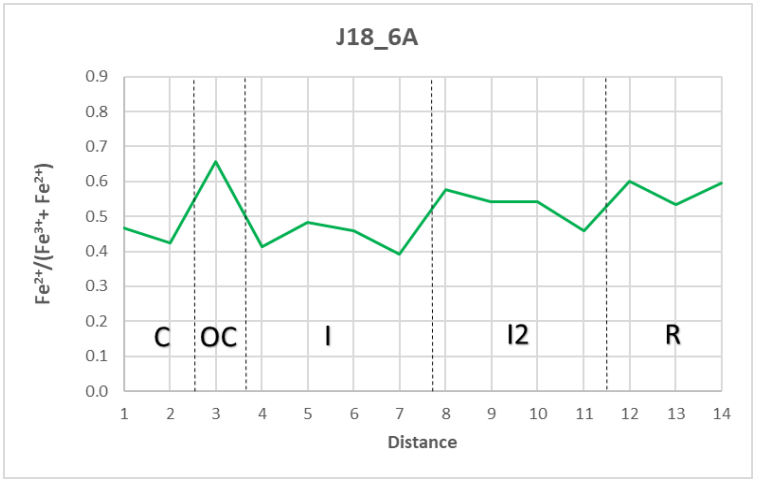

Figure 77 (Cont.): $Fe^{2+}/(Fe^{3+}+Fe^{2+})$ across analytical traverses from J18 (Highwood Mountains)

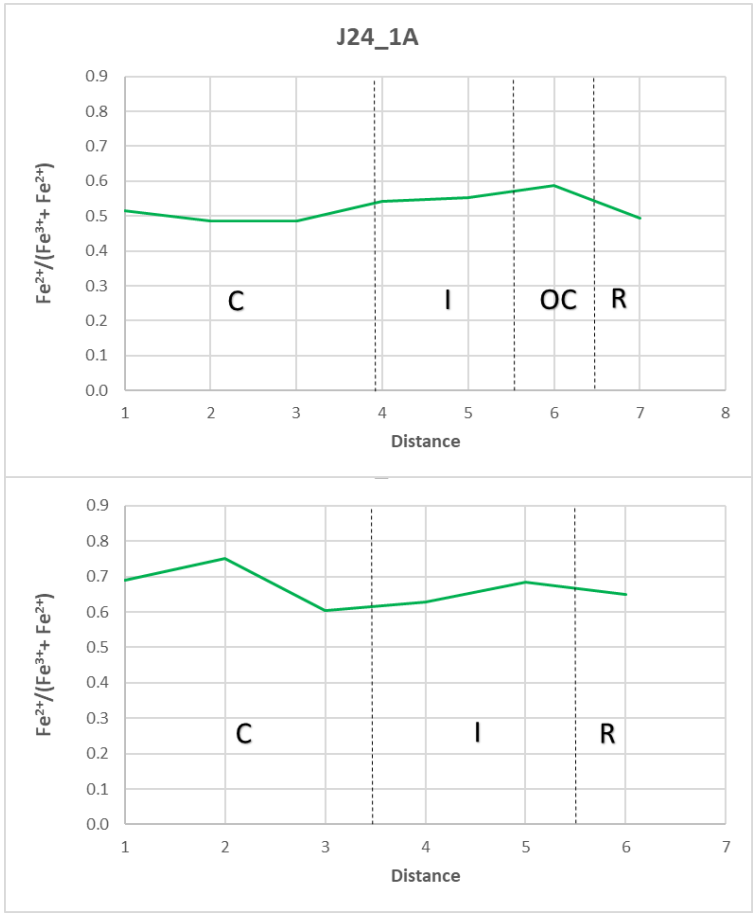

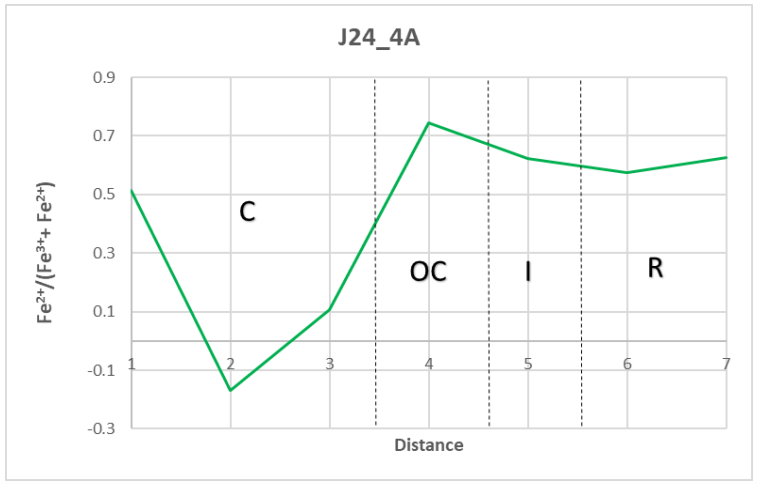

Figure 77 (Cont.): $Fe^{2+}/(Fe^{3+}+Fe^{2+})$ across analytical traverses from J24 (Highwood Mountains)

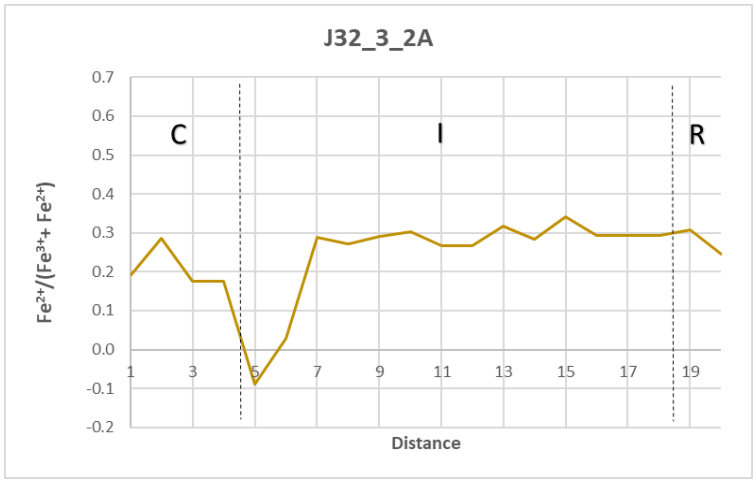

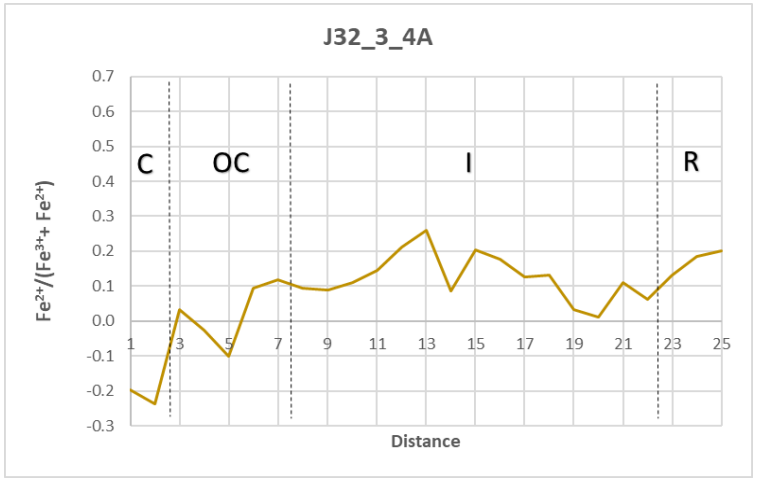

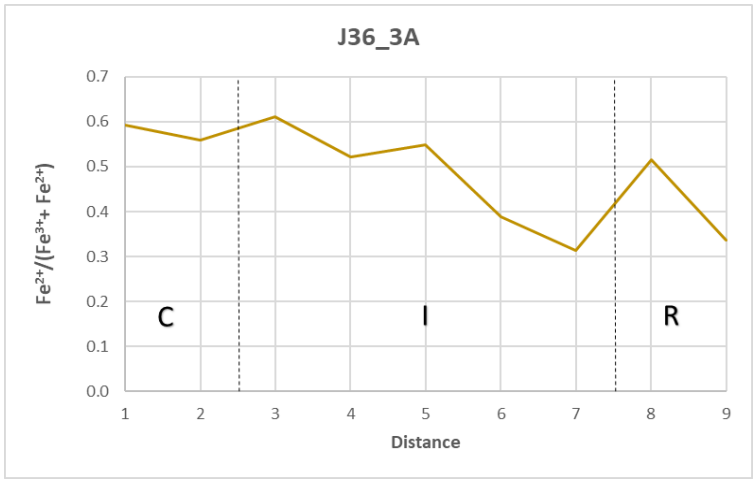

Figure 77 (Cont.): $Fe^{2+}/(Fe^{3+}+Fe^{2+})$ across analytical traverses from J32_3 and J36 (Crazy Mountains)

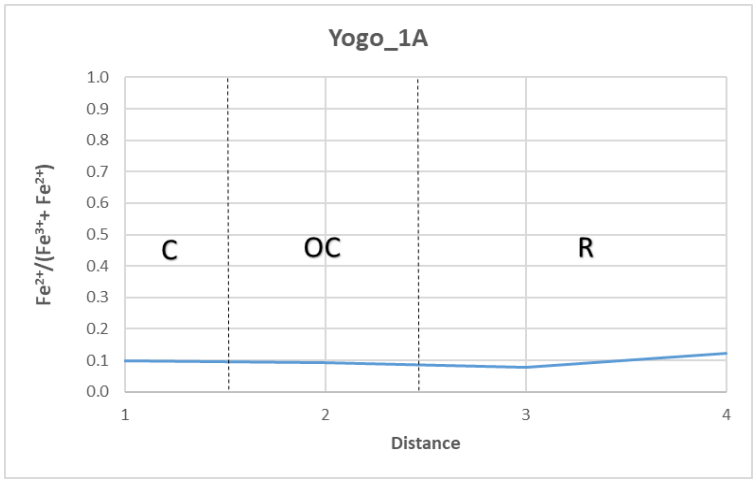

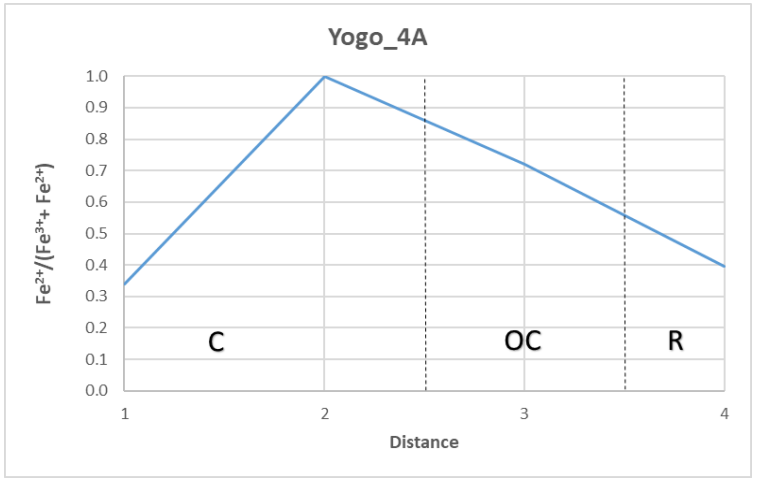

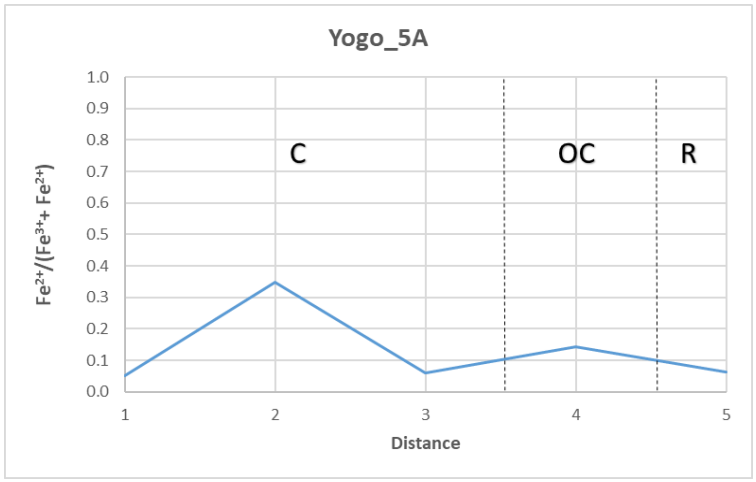

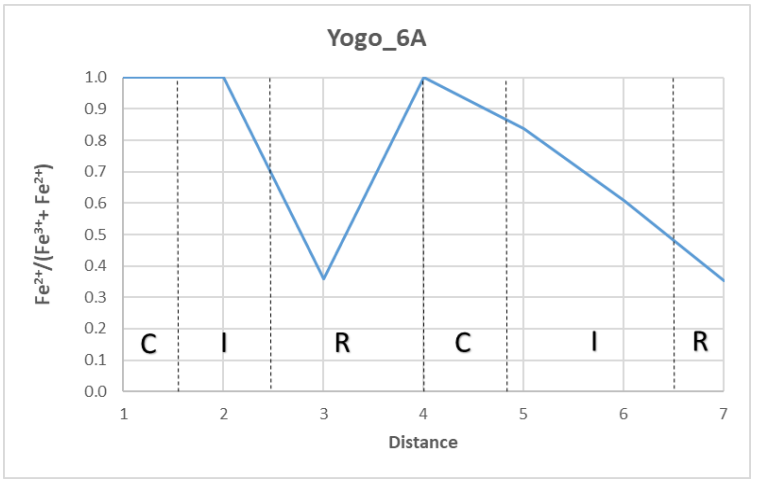

Figure 77 (Cont.): $Fe^{2+}/(Fe^{3+}+Fe^{2+})$ across analytical traverses from the Yogo Dyke

(5D) Clinopyroxene Geobarometry of the CMAP

Within barometric and thermometer pyroxene equations and models of Putirka and others (2003) and Putirka (2008) used within this study, FeO is used rather than Fe_2O_3 because it is assumed that Fe^{2+} is the preferred state of iron within the clinopyroxene structure. Clinopyroxene only barometry and thermometry models of Putirka and others (2003) and Putirka (2008) have been applied to quantify crystallization depth and temperatures of clinopyroxene macrocrysts from every region of the CMAP. B Type macrocrysts have a calculated mean crystallization depth of 56 km (± 5.5), a standard deviation of 10 km (± 5.5), a crystallization depth inter-quartile range (IRQ) of 7 km (± 5.5), and a temperature range of 1322 - 1186 °C (± 30). H Type macrocrysts have a calculated mean crystallization depth of 42 km (± 5.5), a crystallization depth standard deviation of 10 km (± 5.5), a crystallization depth IRQ of 9 km (± 5.5), and a temperature range of 1263 - 1117 °C (± 30). C Type macrocrysts have a calculated mean crystallization depth of 26 km (± 5.5), a crystallization depth standard deviation of 18 km (± 5.5), a crystallization depth IRQ of 29 km (± 5.5), and a temperature range of 1182 - 1059 °C (± 30). While the Y Type macrocrysts of Yogo Dyke have a calculated mean crystallization depth of 53 km (± 5.5), a crystallization depth standard deviation of 13 km (± 5.5), a crystallization depth IRQ of 19 km (± 5.5), and a temperature range of 1394 - 1102 °C (± 30) (See Table 7 for Individual Type Statistical Analysis).

Figure 78 displays all macrocryst Type crystallization depths with an estimated lower crust depth of 45 km for southwestern Montana as modeled by Porter and others (2016). In general, across the CMAP (Fig. 78), clinopyroxene macrocrysts are equivalent to lower crustal/upper mantle crystallization depths. Bull Mountain/Golden Sunlight B Type macrocrysts and the Highwood Mountains H Type macrocrysts display similar lower crustal/upper mantle depth trends but B Types crystalized at greater depths (+10 km) compared to H Types. Some Crazy Mountain C Types appear to have crystallized within much shallower lower crustal to surface levels and Y Types of Yogo Dyke record crystallization depths primarily within the upper mantle.

The interpretation of B4 and B6 as xenocrysts is supported by crystallization depths of those macrocryst Types when compared with the other antecrysts (B1, B2, B3). B5 was interpreted as a xenocryst based off of textural and compositional features, but the range of crystallization depths profile is more similar to that of the antecrysts than the xenocrysts. Additional geochemical analysis may be required to properly determine if there exists a genetic relationship of Type B5 to the others within the same suite.

As noted in Section 7D. vi there are few instances where negative values of P were calculated with H4-1 and C2 being the main offenders. These negative crystallization depth values likely reflect the error resulting when a result is zero (Putirka, 2008), thus it can be assumed that these depths likely correspond to crystallization at or near the surface during dyke emplacement. In C2 a coarse grain of biotite (~100 μm) and many apatite inclusions are entirely enclosed within a lighter colored band near the rim. This suggests that the melt promoted diverse nucleation conditions where clinopyroxene, biotite, and apatite growth occurred on the 'host' clinopyroxene crystal. Since both apatite and biotite incorporate incompatible elements, this might suggest a later stage of crystallization wherein they were integrated into C2 during the last stages of magmas ascent.

The authors interpretation that macrocrysts H2 and H2-1 belong to the same Type is supported by the crystallization depths of these macrocrysts which are very similar, however, the interpretation of H4 and H4-1 belonging to the same Type seems incorrect as the two macrocrysts vary greatly in pressure of crystallization (Table 7). This is unexpected as H4 and H4-1 exhibit near identical textures on BSEs and similar compositional trends on ternary diagrams (Fig. 46 and 47). H4 is classified as normally zoned while H4-1 is reversely zoned. Thus, it is even stranger that H4-1 and H5 have similar crystallization depth results when the two macrocrysts have different shape, habit, zoning, and disequilibrium features. The alternative explanation is that H4-1 should be classified as a xenocryst.

Y2 is a presumed xenocryst, and this is supported by the crystallization depth recorded along point 2 along the traverse, within the core, at 85 km (23 kbar). Compared to other Y type macrocrysts (Fig. 78), Y2 behaves distinctly different than other Y Type macrocrysts which are interpreted as antecrysts. Curiously, comparing crystallization depths to locations along the crystal analytical traverses, point 2 of each Type from Yogo (Fig. 62), exists within their outer cores. These outer core points all crystallized at greater depths than the inner cores. This suggest recharge and mixing of a primitive source when the rim crystallized.

It should be noted that macrocryst Types with spongy textured cores do not discriminate themselves against Types that do not exhibit spongy texture along the crystallization depth profiles. For example, both B1, B2, and B3 host numerous melt pockets within their spongy textured cores, but B5, which has no visible or pervasive signs of spongy texture plots within the same range as the other Types. This is true of Y Type macrocrysts from Yogo Dyke. Thus, changing pressure conditions does not seem responsible for the generation of spongy textured melt pockets within clinopyroxenes, instead the culprit is likely the macrocrysts emergence into a changing chemical environment.

Select clinopyroxene matrix barometric values are present on Figure 78. Within the Highwoods two different matrix mean crystallization depths are present. J18 (≈39 km) and J24 (≈51 km) and Yogo (≈51 km) crystallization depths are represented by horizontal bars segmented between macrocryst depth profiles. For the Yogo dyke the crystallization depth of the matrix clinopyroxene is near the shallowest depths recorded for the macrocrysts. This trend is not apparent within the Highwood matrix clinopyroxenes as they plot nearer the center of macrocryst depth results.

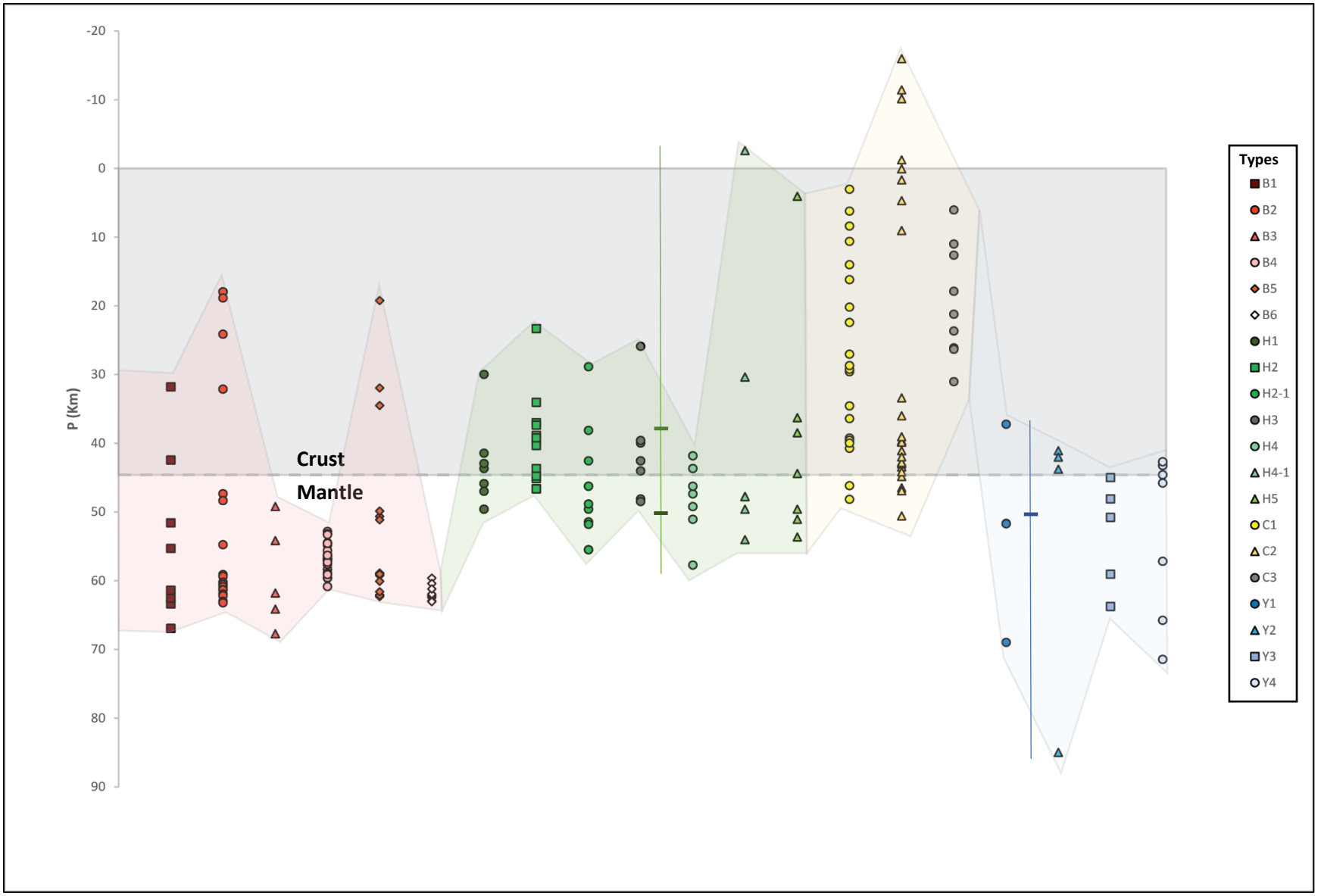

Figure 78: CMAP Clinopyroxene Macrocryst Type Depth of Crystallization

(5E) Petrogenesis

Lamprophyric rocks of the CMAP host clinopyroxene, more precisely diopsides with lesser augite, macrocrysts with complex zoning and disequilibrium features. Clinopyroxene is known to be stable at crustal and upper mantle conditions and composition is highly sensitive to pressure, temperature, and melt water content (Ubide et al. 2014). Open system processes changes are recorded in these macrocrysts regardless of if they are classified as phenocrysts, antecrysts, or xenocrysts. The only way to uncover which magmatic processes influenced the crystals, in theory, is by a whole suite of geochemical tools (major and trace element along with isotope compositions) (Rollinson, 2013). In this study textural observations are available from BSEs and under the petrographic microscope, as well as clinopyroxene mineral chemistry analytical traverses collected by electron microprobe. Clinopyroxene macrocrysts of this study display intricate optical zoning associated with complex compositional variations across core to rim analytical traverses. To compare clinopyroxene macrocryst assemblages from across the four different study areas of the CMAP, the macrocrysts were divided into Types based off of similar petrographic observations. B Types = Bull Mountain/Golden Sunlight, H Types = Highwood Mountains, C Types = Crazy Mountains, and Y Types = Yogo Dyke (see Tables 6 and 7). This is necessary because much like the heterogeneity of lamprophyric dyke swarms, the clinopyroxene macrocrysts assemblages within a single thin section can vary greatly. Thus, the enigma of lamprophyre petrogenesis could potentially be unraveled by understanding the magmatic processes recorded within this dominant mafic phase of the CMAP. Evidence for the three petrogenetic models (Mantle Metasomatism, Prostka, and Cogne) within lamprophyric rocks of the CMAP are discussed below.

Harker variation diagrams of whole rock composition for lamprophyric rocks of the CMAP do not share a single variation trend with a traditional alkali basalt, this likely means that these lamprophyric rocks petrogenesis cannot be explained by a single fractionation process. Macrocryst Type variation diagrams support this as simple fractionation of pyroxene, but cannot explain the compositional

variations observed within the lamprophyric rocks of the CMAP. As is typical of lamprophyres, multiple magmatic processes play a role in controlling magma composition. C Type macrocrysts record the shallowest mean crystallization depths within the entirety of the CMAP. In addition, differing ferric-ferrous ratios (most pronounced in the Crazies) likely mean that the parent magmas of these lamprophyric rocks are significantly different than in other areas of this study, or that their petrogenesis is far more complex than in other regions.

One must first consider the structural and tectonic settings that greatly influenced the southwestern region of Montana, in particular the CMAP, in regard to emplacement of Late Cretaceous to Early Eocene plutonism and volcanism with which the lamprophyric rocks of this study are temporally associated with. Both calc-alkaline and alkaline magmatism are present in the CMAP (du Bray et al. 2006; du Bray et al. 2012). The Boulder Batholith and its satellite plutons, and related volcanic rocks of Late Cretaceous age are a record of arc magmatism that formed in an evolving thrust wedge during contractional deformation, as opposed to the extensional regime that was present in the Cenozoic as the result of the Cordilleran arc collapse (Scarberry et al. 2020).

Maria and Luhr (2008) argue that lamprophyre melts could be the “essence” of subduction zone related geochemistry. du Bray and Harlan (1996) assert that compositional similarities between alkaline dyke swarms within the Crazy Mountains and the Big Timber stock are consistent with mantle dominated genesis within a subduction related volcanic arc setting. Crazy Mountain dyke swarms on ternary AFM diagram ($Na_2O + K_2O$ – FeOT- MgO) trends are similar to those of Cascade volcanic arc rocks and approximate calc-alkaline signatures (du Bray et al., 2006). Crazy Mountain lamprophyric rocks are predominately alkaline (namely monchiquites and sannaites) and clinopyroxenes caught in the process of disequilibrium display unique compositional trends not similar to signatures present elsewhere within the CMAP. C Type clinopyroxene macrocrysts record normal, reverse, and inverse zoning and lower values of TiO_2, Al_2O_3, CaO, and Fe^{2+} /Fe^{3+} ratios than clinopyroxene Types from other regions of the

CMAP. In addition, Na_2O levels are substantially higher than all other Types of the CMAP. These variations confirm that the parent magma of these lamprophyric rocks is significantly different than other areas of this study. C Type macrocrysts are interpreted as xenocryst and antecrysts that crystallized within much shallower lower crustal depths than other Types of the CMAP.

The Crazy Mountain dyke swarms are contemporaneous with the Big Timber Stock within the Crazy Mountain Basin and have variations manifesting from a single magmatic reservoir source based off age, field relationships, and similar petrographic and geochemical features (du Bray et al., 2006). The magma intrusions and dykes across the Crazy Mountains likely originate from a single diapiric shaped magma reservoir and those dykes represent all stages of compositional evolution of the magma (du Bray et al., 2006). The clinopyroxene xenocrysts and antecrysts identified in this study all vary in composition, zoning, and resorption features. The crystallization depths ranging from 51 km to the surface likely represent xenocrysts torn from the plumbing system of this diapiric magma reservoir as lamprophyric melt made its way to the surface where it was emplaced. The abundance of hornblende, biotite, and apatite crystals both as macrocrysts (excluding apatite) and as inclusions within resorbed spongy textured clinopyroxenes confirms that these minerals crystallized early within the petrogenesis of these lamprophyric rocks and that the primary melt had an enriched composition. This gives credence to a heavy metasomatic influence. Eocene aged magmatism within the Crazy Mountains and its associated dykes represent renewed volcanic arc magmatism following shallow subduction and record the eastern most extent of arc magmatism during Early Tertiary igneous activity and its subsequent westward trending migration as a response to steepening subduction of the Farallon plate along the western edge of North America (du Bray et al., 2006). The remelting of the subducting slab could release hydrous metasomatic fluids at great depths or metasomatism could result from hydrous fluid flow in the mantle at the time of magma formation which could generate a hydrous lamprophyric melt responsible for the observed sannaites and monchiquites.

Within the Bull Mountain/Golden Sunlight lamprophyric rocks (vogesites and minettes) the cores of clinopyroxene antecrysts and xenocrysts display high Mg# values (90-80). B Type macrocrysts are enriched in Cr_2O_3 and FeO and lower in SiO_2 composition compared to other macrocryst Types of the CMAP. Bull Mountain clinopyroxene xenocrysts and antecrysts display a wide variety of textural, resorption, and compositional features which is why there is a greater number of macrocrysts Types in the Bull Mountain suite than any other of the CMAP. Normal zoning is most common within antecrysts, and presumed xenocrysts, likely indicating a progressive crystal fractionation sequence of a primitive sourced magma becoming more evolved in a magma chamber at or near the Moho, or during the lamprophyric melt ascension. B Type antecrysts and xenocrysts crystallized near the lower crust-mantle boundary and fractionation of source melts must have taken place at greater depths than macrocrysts derived from the Highwoods or the Crazies. Glomerocryst clusters of pyroxenes (with biotite) are common and indicate that clinopyroxene and phlogopite must have played an essential role relative to the chemical evolution of the parent magma (du Bray et al. 2006).

Geochemical signatures of the Boulder Batholith and its satellites are consistent with genesis originating from subduction and continental arc magmatism processes associated with high convergence rates and shallow subduction angle (du Bray et al. 2012). Through radiogenic isotopic and geochemical variations of the Boulder batholith and its satellite intrusions, du Bray and others (2012) identified no compelling evidence of involvement of a subducted slab component in the genesis of those igneous rocks, but rather assimilation of crustal components by mantle derived magmas. Few presumed crustal xenoliths are entrained within lamprophyric rocks of Bull Mountain/Golden Sunlight, but this would be expected to be a rare occurrence and their absence does not lend enough evidence to support the felsic and mafic mixing of components essential to the Cogne model of petrogenesis. However, evidence of diffusional exchange exists within abundant patchy zoning usually encompassing spongy texture, but not always the case, wherein Mg# decreases in lighter patchy zones. Tomiya and Takahashi

(2005) and Streck and others (2007) assert that patchy zoning can result from crystals with originally homogenous cores caught in the process of slowly being eliminated by intra-crustal diffusional processes. The complexity observed within the macrocrysts (especially sector zoned crystals) of Bull Mountain/Golden Sunlight likely spawns from injections of more primitive magmas into the magma chamber that was becoming progressively more evolved. Note the estimated depth of the Boulder Batholith, on Figure 79, after Houston and Dilles (2013) when compared to the barometric estimates of clinopyroxenes originating from lamprophyric rocks of this study. These estimates imply the possibility of a deeper magma reservoir beneath the batholith wherein the clinopyroxene xenocrysts and antecrysts must have crystallized from. The presence of clusters of antecrysts indicates that magma reservoirs may have been partly crystallized crystal melt mushes (Ubide et al. 2014). Thus, multiple recharges and subsequent mixing coupled with entrainment of primitive High Mg# antecrysts or xenocrysts occurred during magma ascent. The Prostka and Cogne hybridization models of petrogenesis seems most applicable to lamprophyric rocks of Bull Mountain/Golden Sunlight.

As discussed earlier there is significant overlap in compositional data from Late Cretaceous B Type macrocrysts and Eocene aged H Type antecrysts and xenocrysts. This similarity exists within whole rock variation diagrams, crystallization depth profiles, and zoning characteristics. The crystallization depths of H Type macrocrysts plot nearer to the lower crustal-upper mantle boundary but are not as deep as B Types. This is evident within the mean crystallization depth of H Types recorded at 42 km compared to 56 km of B Type macrocrysts. The Mg# values for H Type macrocrysts are most similar to B Type and are mostly normally zoned with step zoning compositional trends on traverses that record complex growth histories. Compared to other lamprophyric rocks from the CMAP the Highwood clinopyroxene macrocrysts are enriched in TiO_2 and CaO. The Highwoods contain the greatest proportion of macrocrysts displaying both normal and reverse zoning characteristics. This small scale shifting over the course of the core to rim traverse likely indicates growth from more mafic rich (high

Mg#, low Fe) magmas after initially growing from more differentiated or evolved magmas. Presumed parasitic growths are most common in H Type antecrysts, besides recharge and mixing events, it is unclear what these unique features represent.

Spongy textured melt pockets are most common within the cores, primarily the outer cores of H Type antecrysts. O'Brien and others (1988) analyzed disequilibrium features in diopside from mafic phonolites (termed minettes in that study due to the presence of biotite phenocrysts) and determined that they were the result of multiple episodes of magma mixing. Another area studied within the CMAP, the Bearpaw Mountains, by Macdonald and others (1992) suggested that similar magma mixing events explained the disequilibrium textures found in minettes. Henderson and others (2012) classified pyroxene phenocrysts that had distinct pale diopsidic pyroxene cores and thin concentric bands occurring within mantles as xenocrysts or antecrysts that were genetically related to the host magma. Henderson and others (2012) suggest that strongly zoned, Ti and Al rich pyroxenes with zones of olivine inclusions, should be classified as antecrysts, that were carried up from depth along with Mg-rich olivine during adiabatic (isothermal) rise through the lithosphere to the crust. Henderson and others (2012) suggest that volatile rich minettes were rapidly extracted from the source region and quickly transported through the lithosphere and crust. A common occurrence in lamprophyric rocks of the Highwoods is bent and deformed biotites. Rapid ascent, like what is common of kimberlitic magmas could account for the bent/stressed micas and the brecciated diopside crystals found within minette lamprophyres (Henderson et al., 2012). Radiometric isotope and trace element research have concluded that the formation of magmas involved the interactions between different sources, including Archaean asthenopsheric mantle material and subduction related potassic metasomatic events in the lithosphere (Henderson et al., 2012). The presence of phlogopite, apatite, and hornblende give credence to metasomatic fluids interacting with lamprophyric melts. Given the abundant step zoning trends implying magma mixing and the macrocryst assemblages, as well as the general overlap and resemblance to

compositional trends from Bull Mountain lamprophyric rocks, a similar magmatic plumbing system is expected (Fig. 78). Hybridization (i.e., the Prostka Model) of primitive and felsic melts within a lower crustal magma reservoir coupled with fractionation and multiple mixing/recharging events could generate antecryst assemblages that cycle through stages of equilibrium and disequilibrium during rapid magma ascent.

The Yogo Dyke lamprophyre's macrocryst barometry offers no evidence of crystallization in the crust. The ultramafic signatures of the Yogo Dyke are preserved within the clinopyroxene antecrysts that crystallized from low silica melts. Yogo clinopyroxenes are elevated in TiO_2, Al_2O_3, Cr_2O_3, and CaO levels along with the lowest SiO_2 and FeO values compared to other macrocrysts of the CMAP. Antecrysts crystallized within a magma reservoir that hosts the deepest plumbing system within the CMAP (Fig. 79). Evidence for this exists within the world-renowned xenocrystic sapphires that are entrained within the ouachitite dyke (Meyer and Mitchell, 1988). Significant magma mixing events are implied from reverse zoning and Mg# spikes along traverses. The abundant pervasive spongy texture and disequilibrium features preserved within clinopyroxenes suggests hybridization as the catalyst for lamprophyric melts.

In general, barometric calculations show that clinopyroxene macrocrysts crystalized in the lower crust near the mantle crust-mantle boundary (Fig. 78 and 79). The crystallization depth of macrocrysts across the CMAP follow this trend: Yogo>Bull Mtn.>Highwood Mtn.>Crazy Mtn. The inferred depth of magmatic plumbing and reservoirs must therefore follow this trend. Clinopyroxene xenocrysts are derived from fractionated primitive source melts at greater depths within the upper mantle. B and Y Type clinopyroxene antecrysts display resorbed spongy textured cores and have the highest Mg# cores, and thus must have crystallized from a more primitive melt. Mg# spikes along the analytical traverses may be results of recharge of primitive magma and are most commonly observed at the outer core/mantle and mantle/rim crystal boundary. Evidence for recharge and mixing events are present within every region of the CMAP, the exact number of recharge events is unknown, but in the case of

the Highwood macrocryst Types, two or possibly three events are interpreted within H2 Types. Normal zoned antecrysts are the product of fractionation within magma reservoirs. Reverse zoned macrocrysts allude to a more primitive influx of magma mixing with lamprophyric melt at depth. The majority of clinopyroxene crystals from the CMAP are interpreted as antecrysts because it is impossible to tell which crystals are cognate with the melt without additional geochemical studies.

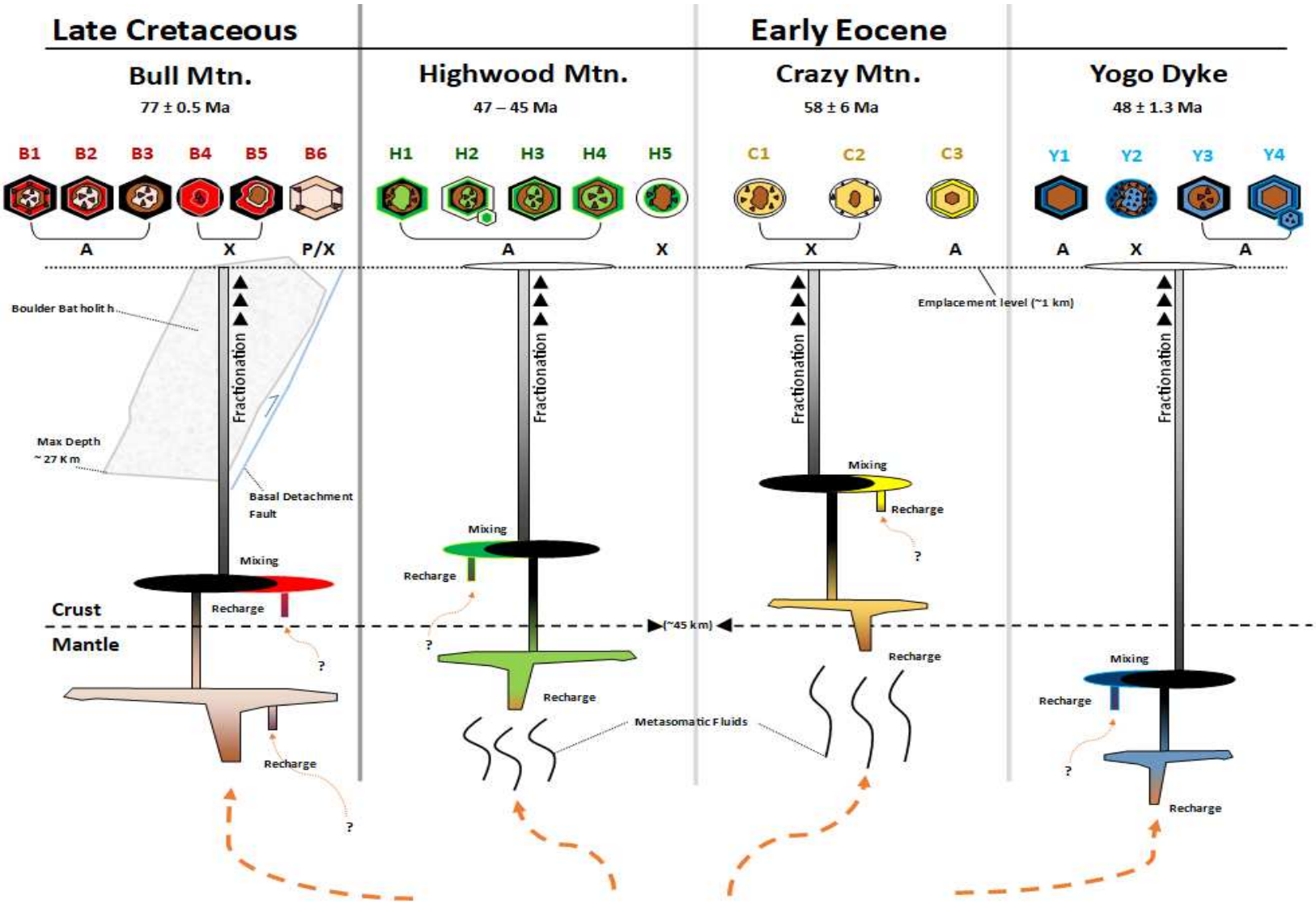

Figure 79: Conceptual Schematic of Magmatic Processes of the CMAP. Clinopyroxene macrocryst Type stratigraphy is shown along with inferred plumbing systems related to each region of the CMAP. Hexagons represent clinopyroxenes within equilibrium with the melt. Rounded and irregular shapes represent macrocrysts in disequilibrium with the melt. Purple specks triangular shapes represent resorbed spongy textured areas. A = Antecryst, P = Phenocryst, X = Xenocryst. (After Ubide et al. 2014; Ubide et al. 2019).

(5F) Conclusions & Future Implications

Ever since early prospecting days miners used lamprophyres as an exploration tool for discovering economic deposits, nowadays this uncommon rock type has been linked spatially and in time to numerous hydrothermal gold deposits across the world (Rock, 1991). Two of the four regions of this study (Bull Mountain/Golden Sunlight and Yogo Dyke) are well known economic deposits that are associated with hydrothermal activity and lamprophyres from these sites were collected in a reconnaissance and mineral chemistry study. Lamprophyric rocks originating from CMAP magmatic complexes are primarily dyke rocks with panidiomorphic and porphyritic textures that contain essential mafic phases of biotite and clinopyroxene (± olivine and hornblende). These mafic phases range in size from a few centimeters in length to microcrystalline (<10 μm) matrix constituents. The abundant clinopyroxene macrocrysts within lamprophyric rocks of the CMAP were the primary focus for electron microprobe analysis presented within this study. Clinopyroxenes from the CMAP are primarily diopside or augites that are complexly zoned and commonly display disequilibrium features such as spongy textured melt pockets. Lamprophyric rocks host ocelli, bent biotite, and complexly zoned mafic macrocrysts. Samples collected and studied from the Late Cretaceous Bull Mountain/Golden Sunlight mining operations are found to be predominately minette > vogesite > kersantite varieties of lamprophyres. Whereas the Highwood Mountains lamprophyric rocks of Eocene age are classified as vogesites > sannaites > minnettes ≈ spessartites. Crazy Mountain (Crazies) lamprophyric rocks of Eocene age host the largest suite of alkaline lamprophyres and are classified as monchiquites > vogesites > kersantites > spessartites. The world renown sapphire-bearing Yogo dyke lamprophyre of Eocene age is classified as an ouachitite. The similarities and differences between lamprophyric rocks and clinopyroxene composition, textural features, and barometry from each region of the CMAP are summarized on tables 8 and 9.

Clinopyroxenes from the CMAP (excluding the Crazy Mountains) are classified as antecrysts or xenocrysts that crystallized near the lower crust – mantle boundary (12 kbar ≈ 45 km) as estimated from barometric models. Barometric mean estimates of the pressure of crystallization for clinopyroxenes are as follows: Bull Mountain/Golden Sunlight = 15.1 ± 1.5 kbar (56 km), Highwood Mountains = 11.4 ± 1.5 kbar (42 km), Crazy Mountains = 7.1 ± 1.5 kbar (26 km), Yogo Dyke = 14.3 ± 1.5 kbar (53 km). Using geophysical depth estimates combined with hornblende geobarometry Houston and Dilles (2013) estimate the maximum depth of the Boulder Batholith to be approximately 27 km. When compared to the barometric estimates of clinopyroxenes originating from Bull Mountain/Golden Sunlight lamprophyric rocks of this study, the clinopyroxene estimates imply the possibility of a deeper magma reservoir beneath the Batholith wherein the clinopyroxene xenocrysts and antecrysts must have crystallized at great depths (Fig. 79). Thus, it is possible that the lamprophyric rocks within Bull Mountain/Golden Sunlight are a record of a deeper plumbing system and reservoir for the Boulder Batholith than previously thought. A genetic link of lamprophyres to epithermal gold and porphyry copper-gold deposits is well known (Rock, et al. 1987, 1988, 1989; Rock and Groves, 1988; Wyman and Kerrich 1988, 1988 b, 1989) and perhaps in the future lamprophyres could be used as a guide in further economic exploration within the Boulder Batholith and the surrounding CMAP.

When comparing lamprophyres from the CMAP to Hawaiian alkali basalts, lamprophyres do not follow standard fractionation trendlines implying a more complex genetic history than simple crystal fractionation. The erratic behavior of clinopyroxene compositions on bivariate diagrams from across the CMAP shows that multiple complex open system magmatic processes are likely at play when controlling lamprophyric magma composition. Drastically different compositional variations of Crazy Mountain clinopyroxenes compared to others of the CMAP confirm that the parent magma of lamprophyric rocks originating from the Crazies is likely significantly different other areas of this study. Enriched primary melts from the Crazies and the Highwoods likely had a heavy metasomatic influence. There exists

evidence for multiple recharge and mixing events exists within the analytical traverses of all lamprophyric rocks of the CMAP. Hybridization of mafic and felsic magmas likely influenced the petrogenesis of lamprophyric rocks from Bull Mountain/Golden Sunlight, the Highwood Mountains, the Crazy Mountains, and the Yogo Dyke Lamprophyre.

This is very much a reconnaissance study and for a more thorough investigation of the similarities and dissimilarities of lamprophyric textures and mineral chemistry from each region of the CMAP, the author suggests a much broader study wherein more lamprophyric rocks are sampled and collected. If circumstances would allow (i.e., fresh, non-altered, samples), it would be best to get an even distribution of lamprophyric rocks to analyze. A shortcoming of this study is the uneven spread of samples collected from each region. LA-ICP-MS work is standard for analyzing trace elements within lamprophyric rocks as seen in Ubide and others (2012, 2014, 2019). Trace element signatures of macrocryst mafic phases would be an invaluable tool for comparing with whole rock and trace element geochemistry of lamprophyric rocks from the CMAP as trace elements give insight into open system magmatic processes.

Pyroxene seemed the obvious crystal to focus on during this study because of its occurrence in nearly every lamprophyric rock within the CMAP, but a new study focusing on different macrocryst assemblages of biotite/phlogopite, amphiboles, olivine could prove useful. In addition, very few studies researching lamprophyric petrogenesis rely on analysis from a single mafic macrocryst population (clinopyroxene in the case of the study), most incorporate all major mafic phases as well as groundmass analysis. EMP work on cognate mica phases, as seen in Pandey and others (2017), wherein those authors analyzed both clinopyroxenes and biotite in attempt to determine the composition of host lamprophyres within the Eastern Dharwar Craton of southern India seems more useful than just a single mineral study. A multi-phase study was beyond the scope of this study, nonetheless, a field study

prioritizing multiple mafic constituents would aid in potentially figuring out a petrogenetic origin of the lamprophyric rocks within the CMAP.

Table 8: Summary of Lamprophyric and Clinopyroxene Variations for Bull Mountain/Golden Sunlight and the Highwood Mountains.

Bull Mountain/Golden Sunlight (Late Cretaceous)	
Petrology (IUGS)	Minnette > Vogesite > Kersantite
Notable Lamprophyric Petrographic Features	Panidiomorphic and Porphyritic, Cumulophyric and Glomerophyric clusters, ocelli, bent Bt
Notable Cpx Textural Features	Twinning, Anhedral and Euhedral Cpx macrocryst populations, Bt and opaques reaction rims, Disaggregated rims, Pervasive ST or ST patchy zoned cores, Sector zoning, Enclosed Bt and carbonates
Cpx Classification	Diopside - Augite
Cpx Composition	↑ (Cr_2O_3 and FeO)
Cpx Mean Mg#	Mg# 78.1
Cpx Analytical Zoning	Normal (B1-5), Reverse (B6), abundant oscillatory and discontinous zoning
Cpx Mean Crystallization Pressure/Depth	15.1 (Kbar ± 1.5) ≈ 56 (Km ± 5.5)
Cpx σ Crystallization Pressure	2.9 (Kbar)
Cpx Mean Crystallization Temperature	1273.1 (°C ± 30)
Antecryst Types	B1, B2, B3
Phenocryst Types	B6?
Xenocryst Types	B4, B5, B6
Petrogenesis	Hybridization

Highwood Mountains (Early Eocene)	
Petrology (IUGS)	Vogesite > Sannaite > Minnette ≈ Spessartite
Notable Lamprophyric Petrographic Features	Panidiomorphic and Porphyritic, Cumulophyric and Glomerophyric clusters, abundant ocelli, abundant bent Bt
Notable Cpx Textural Features	Euhedral Cpx macrocrysts, Abundant Ap and fluid inclusions in mantle bands, Continiously zoned parasitic growths, ST patchy zoned cores or ST confined to mantle bands, Sector zoning, Bt reaction rims, Enclosed Bt and Ol
Cpx Classification	Diopside
Cpx Composition	↑ (CaO)
Cpx Mean Mg#	Mg# 78.8
Cpx Analytical Zoning	Normal (H1-5), Inverse (*H2-1 & *H4-1), abundant oscillatory and step zoning
Cpx Mean Crystallization Pressure/Depth	11.4 (Kbar ± 1.5) ≈ 42 (Km ± 5.5)
Cpx σ Crystallization Pressure	2.8 (kbar)
Cpx Mean Crystallization Temperature	1220.7 (°C ± 30)
Antecryst Types	H1, H2, H3, H4
Phenocryst Types	-
Xenocryst Types	H5
Petrogenesis	Hybridization and Mantle Metasomatism

Note: ST = Spongy Textured Melt Pockets, Bt = Biotite, Ol = Olivine, Cpx = Clinopyroxene, Hbl = Hornblende, Ap = Apatite

Table 9: Summary of Lamprophyric and Clinopyroxene Variations for the Crazy Mountains and the Yogo Dyke Lamprophyre.

Crazy Mountains (Early Eocene)	
Petrology (IUGS)	Monchiquite > Vogesite > Kersantite > Spessartite
Notable Lamprophyric Petrographic Features	Porphyritic, Cumulophyric clusters, abundant xenoliths, ocelli, bent Bt, abundant metasomatic phases
Notable Cpx Textural Features	Anhedral and Euhedral Cpx macrocryst populations, Rounded internal grain boundaries, Abundnant Ap inclusions, Resorbed or diaggregated rims in Anhedral Cpx, Groundmass ST Cpx, Enclosed Ol - Bt - Hbl, ST highly variable in Cpx
Cpx Classification	Diopside
Cpx Composition	↑ (Na_2O) ↓ (TiO_2, Al_2O_3, CaO, and Fe^{2+}/Fe^{3+} ratios)
Cpx Mean Mg#	Mg# 82.4
Cpx Analytical Zoning	Normal (C1), Reverse (C3), Inverse (C2), abundant oscillatory zoning
Cpx Mean Crystallization Pressure/Depth	7.1 (Kbar ± 1.5) ≈ 26 (Km ± 5.5)
Cpx σ Crystallization Pressure	4.8 (Kbar)
Cpx Mean Crystallization Temperature	1142.6 (°C ± 30)
Antecryst Types	C3
Phenocryst Types	-
Xenocryst Types	C1, C2
Petrogenesis	Hybridization and Mantle Metasomatism

Yogo Dyke (Early Eocene)	
Petrology (IUGS)	Ouachitite
Notable Lamprophyric Petrographic Features	Panidiomorphic and Porphyritic, ocelli, bent Bt
Notable Cpx Textural Features	Anhedral and Euhedral Cpx macrocrysts, Ca content increase at rims, Parasitic growths with discontinous zoning, Pervasive ST or ST inner cores, Ap inclusions, Groundmass ST Cpx
Cpx Classification	Diopside - Ca rich Diopside
Cpx Composition	↑ (TiO_2, Al_2O_3, Cr_2O_3, and CaO) ↓ (SiO_2 and FeO)
Cpx Mean Mg#	Mg# 82.7
Cpx Analytical Zoning	Normal (Y1, Y3, Y4), Inverse (Y2) zoning
Cpx Mean Crystallization Pressure/Depth	14.3 (Kbar ± 1.5) ≈ 53 (Km ± 5.5)
Cpx σ Crystallization Pressure	3.4 (Kbar)
Cpx Mean Crystallization Temperature	1310.9 (°C ± 30)
Antecryst Types	Y1, Y3, Y4
Phenocryst Types	-
Xenocryst Types	Y2
Petrogenesis	Hybridization

Note: ST = Spongy Textured Melt Pockets, Bt = Biotite, Ol = Olivine, Cpx = Clinopyroxene, Hbl = Hornblende, Ap = Apatite

Many of the lamprophyric rocks collected from this study contain pyroxenes laden with inclusions of apatite, and a few contain what appear to be melt inclusions (more prevalent in Highwood samples). Analyzing glass inclusions from olivine phenocrysts from minettes of the Mexican Volcanic Belt, Maria and Luhr (2008) interpreted calc-alkaline lamprophyres as the product of partial melting of phlogopite-pyroxenite veins within a mantle wedge by partial melting of peridotite wall rock. Given the tectonic history of southwestern Montana, with shifts from convergence to extensional regimes, an inclusion analysis study could give insight into lamprophyre petrogenesis. Melt and fluid inclusions present within pyroxenes from the Highwoods could be important in determining magmatic evolution of the lamprophyres, specifically, identifying volatile phases that may be locked within those inclusions. In addition, data from an inclusions study could provide another source for pressure/crystallization calculations.

The presence of sector zoning within lamprophyres could potentially be explored for the application of thermobarometric modelling due to the effects of sluggish crystallization kinematics associated with pyroxene growth (Ubide et al., 2019). Some authors use the program MELTS to calculate the evolutionary history of the host melt and the progression of phase crystallization (Menzes et al. 2015). The importance of a detailed study involving whole rock geochemical data could be a useful tool if another study were to be undertaken on lamprophyric rocks from the CMAP.

Another possible study could be centered on analyzing phases within melt pockets. Sulfides and rare phases were found within the cores of clinopyroxene within melt pockets and these phases could be analyzed with spectrometry analysis to determine their identity. It is assumed that the melt pocket interiors are synonymous with the matrix based off of textural observations but a detailed study within the melt pockets could confirm this. In addition, lamprophyres within the Golden Sunlight Mine are contemporaneous with gold mineralization and a detailed melt pocket mineralogy study within

pyroxenes could add to the discussion of whether or not lamprophyres could be the source of Au and rare economic minerals, as suspected by Rock (1991).

References

Armstrong, J. T. 1988. Quantitative Analysis of Silicates and Oxide Minerals: Comparison of Monte-Carlo, ZAF and Phi-Rho-Z Procedures. Microbeam Analysis, pg. 239 – 246.

Barton, M., Varekamp, J.C., and Van Bergan, M.J. 1982. Complex Zoning of Clinopyroxenes in the Lavas of Vulsini, Latium, Italy: Evidence for Magma Mixing. J. Volcanol. Geotherm. Res. 14, pg. 361-388.

Bedard, J., Ludden, J., and Francis, D. M. 1988. Petrology and Pyroxene Chemistry of Monteregian Dykes: The Origin of Concentric Zoning and Green Cores in Clinopyroxenes from Alkali Basalts and Lamprophyres. J. Petrol., V. 28, pg. 355-388.

Berger, B. R., Hildenbrand, T. G., and O'Neill, J. M. 2011. Control of Precambrian Basement Deformation Zones on Emplacement of the Laramide Boulder Batholith and Butte Mining District, Montana, United States: U.S. Geological Survey Scientific Investigations Report 2011-5016, pg. 1-29.

Bevins, R. E., Kokelaar, B. P., and Dunkley, P. N. 1984. Petrology and Geochemistry of Lower to Middle Ordovician Igneous Rocks in Wales: A Volcanic Arc to marginal Basin Transition. Proc. Geol. Ass. V. 95, pg. 337-347.

Blundy, J. and Cashman, K. 2008. Petrologic Reconstruction of Magmatic System Variables and Processes. Rev. Mineral Geochem, V. 69, pg. 179-249.

Bowen, N. L. 1928. The Evolution of the Igneous Rocks. Princeton University Press.

Burchfiel, B. C., and Davis, G. A. 1975. Nature and Controls of Cordilleran Orogenesis, Western United States: Extensions of an Earlier Synthesis. American Journal of Science, V. 275-A, pg. 363-396.

Carmichael, I. S. E. 1991. The Redox States of Basic and Silicic Magmas: A Reflection of their Source Regions? Contributions to Mineralogy and Petrology, V. 106, pg. 129-141.

Chadwick, R. A. 1981. Chronology and Structural Setting of Volcanism in Southwestern and Central Montana. In Montana Geological Society Field Conference and Symposium Guidebook to Southwest Montana, pg. 141-148.

Claybaugh, S. E. 1952, Corundum Deposits of Montana: U. S. Geological Survey Bulletin 983, pg. 100.

Cogne, J. 1962. La Sizunite (Cap Sizun, Finistere) et le Probleme de L'origine des Lamprophyres. Bull. Soc. Geol. Fr., V. 7 (IV), pg. 141-156.

Currie, K. L. and Ferguson, J. 1970. The Mechanism of Intrusion of Lamprophyre Dykes Indicated By "Offsetting" of Dykes. Tectonophysics, V. 9, pg. 525-535.

Dahy J.P. (1988) The geology and igneous rocks of the Yogo sapphire deposit and the surrounding area, Little Belt Mountains, Judith Basin County, Montana. Master's thesis, Montana College of Mineral Science and Technology.

Dahy, J. P. 1991. Geology and Igneous Rocks of the Yogo Sapphire Deposit, Little Belt Mountains, Montana. In D.W., Bake and R.B, Eds. Guidebook of the Central Montana Alkalic Province: Geology, Ore Deposits and Origin. Montana Bureau of Mines and Geology Special Publication 100, Missoula, Mt, pg. 45-54.

Davidson, J. P., Morgan, D. J., Charlier, B. L. A., Harlou, R., Hora, J. M. 2007. Microsampling and Isotopic Analysis of Igneous Rocks: Implications for the Study of Magmatic Systems. Annual Review of Earth and Planetary Sciences, V. 35, pg. 273-311.

Downes, M. J. 1974. Sector and Oscillatory Zoning in Calcic Augites from M. Etna, Sicily. Contributions Mineral Petrology, V. 47, pg. 187-196.

DeWitt, E., Foord, E. E., Zartman, R. E., Pearson, R. C., and Foster, F. 1996. Chronology of Late Cretaceous Igneous and Hydrothermal Events at the Golden Sunlight Gold-Silver Breccia Pipe, Southwestern Montana. U.S. Geological Survey Bulletin 2155, pg. 1-45.

du Bray, E. A., Harlan, S. S., and Wilson, A. B. 2006. Petrology of the Crazy Mountains Dike Swarm and Geochronology of Associated Sills, South-Central Montana. USGS Professional Paper 1715, pg. 1-26.

du Bray, E. A., Aleinikoff, J. N., Lund, K. 2012. Synthesis of Petrographic, Geochemical, and Isotopic Data from the Boulder Batholith, Southwest Montana. USGS Professional Paper 1793, pg. 1-46.

Dudas, F. O., 1991. Petrogenesis and Mantle Source of Igneous Rocks in the Crazy Mountains, Montana: University Park, Pennsylvania State University, Ph. D. thesis, pgs. 442.

Dudas, F. O. 1991. Geochemistry of Igneous Rocks from the Crazy Mountains, Montana, and Tectonic Models for the Montana Alkalic Province. Journal of Geophysical Research, V. 96, pg. 13261-13277.

Fisera, M. 1974. Bronzite-Olivine Minette from Brloh in the Pisek Area. Cas Mineral Geol, V. 19, pg. 71-76.

Foley, S. and Peccerillo, A. 1992. Potassic and Ultrapotassic Magmas and Their Origin. Lithos, V. 28, pg. 181-185.

Foster, F. 1991. Geology and General Overview of the Golden Sunlight Mine, Jefferson Country, Montana. In the Association of Exploration Geochemists 15th International Geochemical Exploration Symposium Field Trip Guidebook to Mineral Deposits of Montana, pg. 26-36.

Foster, F. and Childs, J. F. (1993) An Overview of Significant Lode Gold Systems in Montana, and their Regional Geologic Setting. Explor. Mining. Geol., V. 2 (3), pg. 217-244.

Frey, H. M. and Lange, R. A. 2011. Phenocryst Complexity in Andesites and Dacites from the Tequila Volcanic Field, Mexico: Resolving the Effects of Degassing vs. Magma Mixing. Contrib. Mineral Petrol, V. 162, pg 415-445.

Gaschnig, R. M., Vervoort, J.D., Lewis, R.S., and Tikoff, B. 2011. Isotopic Evolution of the Idaho Batholith and Challis Intrusive Province, Northern US Cordillera. Journal of Petrology, V. 52, pg. 2397-2429.

Gauthier, G. 1995. Mineralogy, Geochemistry, and Geochronology of the Yogo Dike Sapphire Deposit, Montana. Thesis, The University of British Columbia. pg. 1-287.

Geologyscience.com. 2021. Lamprophyre. https://geologyscience.com/rocks/lamprophyre

Ginibre, C., Worner, G., and Kronz, A. 2007. Crystal Zoning as an Archive for Magma Evolution. Elements, V. 3, pg. 261-266.

Gümbel, C. W. Von. 1874. Die Paleolithischen Eruptivgesteine des Fichtelgeberges. Franz München.

Guylaine, G. 1995. Mineralogy, Geochemistry, and Geochronology of the Yogo Dike Sapphire Deposit, Montana. Thesis. University of British Columbia.

Hamilton, W., and Myers, B. 1974. Nature of the Boulder Batholith of Montana. GSA Bulletin, V. 85 (3), pg. 365-378.

Harlan, S. H. 1996. Timing and Emplacement of the Sapphire-Bearing Yogo Dike, Little Belt Mountains, Montana. Economic Geology, V. 91, pg. 1159-1162.

Hatch. F. H., Wells, A. K., and Wells, M. K. 1972. *Petrology of Igneous Rocks*. Murby, London.

Hearn, B. C. Jr. 1989. Montana High-Potassium Igneous Province: Crazy Mountains to Jordan, Montana. Field trip Guidebook T346.

Henderson, C. M. B., Richardson, F. R., and Charnock, J. M. 2012. The Highwood Mountains Potassic Igneous Province, Montana: Mineral Fractionation Trends and Magmatic Processes Revisited.

Hobbs, W., Griggs, A. B., Wallace, R. E., and Campbell, A. B. 1965. Geology of the Coeur d'Alene District, Shoshone County, Idaho, U.S. Geological Survey Professional Paper 478, pgs. 139.

Houston, R. A., and Dilles, J. H. 2013. Structural Geologic Evolution of the Butte District, Montana. Economic Geology, V. 108, pg. 1397-1424.

Kerrich, R. and Wyman, D. A. 1994. The Mesothermal Gold-Lamprophyre Association: Significance for an Accretionary Geodynamic Setting, Supercontinent Cycles, and Metallogenic Processes. Mineralogy and Petrology, V. 51, pg. 147-172.

Kirkpatrick, R. J. 1977. Nucleation and Growth of Plagioclase, Makaopuhi and Alae Lava Lakes, Kilauea Volcano, Hawaii, Geol. Soc. Am. Bull, V. 88, pg. 78-84.

Klepper, M. R., Weeks, R. A., and Ruppel, E. T. 1957. Geology of the Southern Elkhorn Mountains, Jefferson and Broadwater Counties, Montana. U.S. Geological Survey Professional Paper 292, pgs. 82.

Klepper, M. R., Robinson, G. D., and Smedes, H. W. 1971. On the Nature of the Boulder Batholith. Geol. Soc. America Bull., V. 82, pg. 1563-1580.

Korzeb, S. L., Scarberry, K. C., and Zimmerman, J. L. 2018. Interpretations and Genesis of Cretaceous Age Veins and Exploration Potentialfor the Emery Mining District, Powell County, Montana. Montana Bureau of Mines and Geology Bulletin 137, pg. 1-49.

Larson, E. S. 1940. Petrographic Province of Central Montana. Geol. Soc. America Bull., V. 51, pg. 887-948.

Larsen, L. H. and Simms, F. E. 1972. Igneous Geology of the Crazy Mountains, Montana- A Report of Work in Progress. Montana Geological Society. 21st Annual Conference, pg. 135-139.

Le Bas, M. J. and Streckeisen, A. L. 1991. The IUGS Systematics of Igneous Rocks. Journal of the Geological Society, London., V. 148, pg. 825-833.

Le Maitre, R. W, Bateman, P., Dudek, A., Keller, J. 1989. A Classification of Igneous Rocks and Glossary of Terms: Recommendations of the International Union of Geological Sciences Subcommission on the Systematics of Igneous Rocks. Blackwell Scientific Publications, Oxford.

Luhr, J. F. and Carmicheael, I. S. E. 1980. The Colima Volcanic Complex, Mexico: Part I. Postcaldera Andesites from Volcan Colima. Contrib. Mineral. Petrol., V.71, pg., 343-372.

Luhr, J. F. and Carmicheael, I. S. E. 1981. The Colima Volcanic Complex, Mexico: Part II. Late Quaternary Cinder Cones. Contrib. Mineral. Petrol., V. 76, pg. 127-147.

Ma, G. S. K., Wang, K.-L., Malpas, J., Iizuka, Y., Xenophontos, C., Turkmani, A. A., Chan, G. H.-S., Usuki, T., and Chan, Q. H.-S. 2015. Melt Pockets in Spongy Clinopyroxenes in Mantle Xenoliths from the Plio-Quaternary Al Ghab Volcanic Field, NW Syria: Implications for the Metasomatic Evolution of the Lithosphere. The Earth's Heterogeneous Mantle, Springer International Publishing Switzerland, pg. 205-257.

Macdonald, R., Upton, B. G. J., Collerson, K. D., Hearn, B. C., Jr., and James, D. 1992. Potassic Mafic Lavas of the Bearpaw Mountains, Montana: Mineralogy, Chemistry, and Origin. Journal of Petrology, V. 33, pg. 305-346.

Maria, A. H., and Luhr, J. F. 2008. Lamprophyres, Basanites, and Basalts of the Western Mexican Volcanic Belt: Volatile Contents and a Vein-Wallrock Melting Relationship. Journal of Petrology, V. 49, pg.2123-2156.

Marvin, R. F., Witkind, I. J., Keefer, W. R., and Mehnert, H. H. 1973. Radiometric Ages of Intrusive Rocks in the Little Belt mountains, Montana. Geol. Soc. Amer. Bull., V. 84, pg. 1977-1986.

Marvin, R. F., Hearn, B. C. Jr., Mehnert, M. H., and Meritt, V. M. 1974. K-Ar Ages of Selected Tertiary Ingeous Rocks in Southwestern Montana. Isochron West, V. 10, pg. 10-17.

Marvin, R. F., Hearn, B. C. Jr., Mehnert, H. H., Naeser, C. W., Zartman, R. E. and Lindsey, D. A. 1980. Late Cretaceous – Paleocene- Eogene Igneous Activity in North-Central Montana. Isochron/West, V. 29, pg. 5-25.

Menezes, S. G., Azzone, R. G., Enrich-Rojas, G. E., Ruberti, E., Gagliarani, R., Barros-Gomes, C., and Chmyz, L. 2015. The Antecryst Compositional Influence on Cretaceous Alkaline Lamprophyre Dykes, SE Brazil. The Brazilian Journal of Geology, V. 45, pg. 79-93.

Menzies, M. A. 1983. Mantle Ultramafic Xenoliths in Alkaline Magmas: Evidence for Mantle Heterogeneity Modified by Magmatic Activity. Continental Basalts and Mantle Xenoliths, pg. 92-110.

Meyer, O. A. and Mitchell, R. H. 1988. Sapphire Bearing Ultramafic Lamprophyre from Yogo, Montana: a Ouachitite. Canadian Mineralogist, V. 26, pg. 81-88.

Mining.com. March 23, 2021. https://www.mining.com/barrick-sees-win-win-strategy-in-golden-sunlight-mine-closure-project/

Mitchell, R. H. 1985. A Review of the Mineralogy of Lamproites. Tr. Geol. Soc. S. Afr., V. 88, pg. 411-438.

Mitchell, R. H. 1994a. Suggestions for Revisions to the Terminology of Kimberlites and Lamprophyres from a Genetic Viewpoint. Proc. 5th Int. Kimberlite 1, pg. 15-26.

Mitchell, R. H. 1994. The Lamprophyre Facies. Mineralogy and Petrology, V. 51, pg. 137-146.

Mitchell, R. H., and Bergman, S. C. 1991. Petrology of Lamproites. New YorkPlenum.

Müller, D., Stumpfl, E. F., Taylor, W. R. 1992. Shoshonitic and Alkaline Lamprophyres with Elevated Au and PGE Concentrations from the Kreuzeck Mountains, Eastern Alps, Austria. Mineral Petrology, V. 46, pg. 23-42.

Müller, D. and Groves, D. I. 2016. Potassic Igneous Rocks and Associated Gold-Copper Mineralization. Cham, Switzerland

Mychaluk, K.A. 1992. Geology of the Vortex Mine, Utica, Montana. Bachelor's thesis, University of Calgary. pgs. 35.

Nelson, S. T, and Montana, A. 1992. Sieve-Textured Plagioclase in Volcanic Rocks Produced by Rapid Decompression. American Mineralogist, V. 77, pg. 1241-1249.

O'Brien, H. E., Irving, A. J., and McCallum, I. S. 1988. Complex Zoning and Resorption of Phenocrysts in Mixed Potassic Mafic Magmas of the Highwood Mountains, Montana. American Mineralogist, V. 73, pg. 1007-1024.

O'Brien, H. E., Irving, A. J., and McCallum, I. S. 1991. Eocene Potassic Magmatism in the Highwood Mountains, Montana: Petrology, Geochemistry and Tectonic Implications. Journal of Geophysical Research, V. 96, pg. 4539-4556.

O'Brien, H. E., Irving, A. J., McCallum, I. S., and Thirwall, M. F. 1995. Geochimica et Comochimica Acta, V. 59, pg. 4539-4556.

Olson, N. H., Dilles, J. H., Kallio, I. M., Horton, T. R., and Scarberry, K. C. 2016. Geologic Map of the Ratio Mountain 7.5' Quadrangle, Southwest Montana. Montana Bureau of Mines and Geology EDMAP-10, scale 1:24,000.

Oyer, N., Childs, J., Mahoney, J. B. 2014. Regional Setting and Deposity Geology of the Golden Sunlight Mine: An Example of Responsible Resource Extraction. The Geological Society of America, Field Guide 37, pg. 115-144.

Pandey, A., Chalapathi Rao, N. V., Chakrabarti, R., Pandit, D., Pankaj, P., Kumar, A., and Sahoo, S. 2017. Petrogenesis of a Mesoproterozoic Shoshonitic lamprophyre Dyke from the Wajrakarur Kimberlite Field, Eastern Dharwar Craton, Southern India: Geochemical and Sr-Nd isotopic Evidence for a Modified Sub-continental Lithospheric Mantle Source. Lithos, V. 292-293, pg. 218-233.

Palke, A. C., Renfro, N. D., and Berg, R. B. 2016. Origin of Sapphires from a Lamprophyre dike at Yogo Gulch, Montana, USA: Clues from their Melt Inclusions. Lithos, V. 260, pg. 339-344.

Parsons, W. H. 1942. Origin and Structure of the Livingston Igneous Rocks, Montana. GSA Bulletin, V. 53 (8), pg. 1175-1186.

Pearce, J. A. 1983. Role of the Sub-Continental Lithosphere in Magma Genesis at Active Continental Margins. Continental Basalts and Mantle Xenoliths. Shiva, Nantwich, pg. 230-249.

Peccerillo, A. 1992. Potassic and Ultrapotassic Rocks: Compositional Characteristics, Petrogenesis, and Geologic Significance. Episodes, V. 15, pg. 243-251.

Perring, C. S., Rock, N. M. S., Golding, S. D., and Roberts, D. E. 1989. Criteria for the Recognition of Metamorphosed or Altered Lamprophyres: A Case Study from the Archaean of Kambalda, Western Australia. Precambrian Research, V. 43, pg. 215-237.

Peterson, T. D. 1992. Early Proterozoic Ultrapotassic Volcanism of the Keewatin Hinterland, Canada. Proc 5th International Kimberlite Conference.

Pirsson, L. V. 1895. Complementary Rocks and Radial Dykes. American Journal of Science, V. 50, pg. 116-121.

Porter, R., Y. Liu, and W. E. Holt. 2016. Lithospheric Records of Orogeny Within the Continental U.S., Geophys. Res. Lett., 43.

Prostka, H. J. 1973. Hybrid Origin of the Absarokite-Shoshonite-Banakite Series, Absaroka Volcanic Field, Wyoming. Geological Society of America Bulletin, V. 84, pg. 697-702.

Prelevic, D., Foley, S. F., Cvetkovic, V., and Romer, R. L. 2004. Origin of Minette by Mixing of Lamproite and Dacite Magmas in Veliki Majdan, Serbia. Journal of Petrology, V. 45, pg. 759-792.

Putirka, K. D., Ryerson, F. J., and Mikaelian, H. 2003. New Igneous Thermobarometers for Mafic and Evolved Lava Compositions, Based on Clinopyroxene + Liquid Equilibria. Am Mineral, V. 123, pg. 1542-1554.

Putirka, K. D. 2008. Thermometers and Barometers for Volcanic Systems. Reviews in Mineralogy & Geochemistry, V. 69, pg. 61 – 120.

Reynolds, M. W. 1979. Character and extent of Basin-Range Faulting, Western Montana. In *Basin and Range Symposium*. Edited by G.W. Newman and H.D. Goode. Rocky Mountain Association of Geologists, pg. 185-193.

Richter, D. H., and Moore, J. G. 1966. Petrology of the Kilauea Iki Lava Lake, Hawaii. U.S. Geol. Surv. Prof. Paper 537-B, B1-B26.

Ridley, J. 2021. Pres. A New Look at the Sapphire-Bearing Yogo Lamprophyre Dike, MT. MBMG CON.

Roberts, A. E. 1963. The Livingston Group of South-Central Montana, Short Papers in Geology and Hydrology. U.S. Geological Survey Professional Paper 475-B, pg. B86-B92.

Robinson, G. D., Klepper, M. R., and Obradovich, J. D. 1968. Over-lapping Plutonism, Volcanism, and Tectonism in the Boulder Batholith Region, Western Montana. Geol. Soc. America Mem., 16, pg. 557-576.

Rock, N. S. 1977. The Nature and Origin of Lamprophyres: Some Definitions, Distinctions, and Derivations. Earth Science Reviews, V. 13, pg. 123-169.

Rock, N. S. 1979. Petrology and Origin of the Type Monchiquites and Associated Lamprophyres of Serra de Monchique, Portugal. Trans. R. Soc. Edinburgh, V. 70, pg. 149-170.

Rock, N. S. 1981. How Should Igneous Rocks be Grouped? Geologic Magazine, V. 118, pg. 449-461.

Rock, N. S. 1984. The Nature and Origin of Calc-Alkaline Lamprophyres: Minettes, Vogesites, Kersantites, and Spessartites. Trans. R. Soc. Edinburgh: Earth Sciences, V. 74, pg. 193-227.

Rock, N. S. 1987. The Nature and Origin of Lamprophyres: An Overview. Geological Society Special Publications, No. 30, pg. 191-226.

Rock, N. S. 1989. Kimberlites as Varieties of Lamprophyres: Implications for Geological Mapping, Petrological Research and Mineral Exploration. Spec. Publ. Geol. Soc. Aust, V. 14, pg. 46-59.

Rock, N. S. 1991. Lamprophyres. Blackie Glasgow and London, Van Nostrand Reinhold 115 Fifth Avenue New York, New York.

Rock, M. S. and Groves, D, I. 1988. Do Lamprophyres Carry Gold as Well as Diamonds? Nature, V. 332, pg. 253-255.

Rock, N. M. S., Duller, P., Haszeldine, R. S., and Groves, D. I. 1987. Lamprophyres as Potential Gold Exploration Targets. Geol. Dept. & Univ. Extension, Univ. W. Aust, V. 11., pg. 271-286.

Rock, N. M. S., Groves, D. I., and Perring, C. S. 1988. Gold, Lamprophyres and Porphyries: A new Genetic Model: Geol. Soc. Australia Abstracts, No. 22, pg. 307-312.

Rock, N. M. S., Groves, D. I., Perring, C. S. and Golding, S. D. 1989. Gold, Lamprophyres, and Porphyries: What Does Their Association Mean? Econ. Geol. Monograph, V. 6, pg. 601-617.

Rollinson, H. 2013. *Using Geochemical Data: Evaluation, Presentation, Interpretation*. Longman Scientific and Technical, England, pgs. 352.

Scarberry, K. C. 2016. Geologic Map of the Sugarloaf Mountain 7.5' Quadrangle, Deer Lodge, Jefferson, and Powell Counties, Montana. Montana Bureau of Mines and Geology. Open File Report 674. Scale 1:24,000.

Scarberry, K. C. 2016. Geologic Map of the Wilson Park 7.5' Quadrangle, Southwestern Montana. Montana Bureau of Mines and Geology. Geologic Map 66. Scale 1:24,000.

Scarberry, K. C., Yakovlev, P. V., and Schwartz, T. M. 2020. Mesozoic Magmatism in Montana. MBMG Special Publication 122: Geology of Montana, vol 1: Geologic History, pg. 1-30.

Shore, M., and Fowler, A. D. 1996. Oscillatory Zoning in Minerals; a Common Phenomenon. Canadian Mineralogy, V. 34, pg. 1111-1126.

Smedes, H. W. 1966. Geology and Igneous Petrology of the Northern Elkhorn Mountains, Jefferson and Broadwater Counties, Montana. U.S. Geological Survey Professional Paper 510, pgs. 116.

Smedes, H. W., Klepper, M. R., and Tilling, R. I. 1988. Preliminary Map of Plutonic Units of the Boulder Batholith, Southwestern Montana. U.S. Geological Survey Open-File Report 88-283, scale 1:200,000.

Smith, H. G. 1946. The Lamprophyre Problem. Geological Magazine, V. 83 (4), pg. 165-171.

Spry, P. G., Foster, F., Truckle, J. S., Chadwick, T. H. 1997. The Mineralogy of the Golden Sunlight Gold-Silver Telluride Deposit, Whitehall, Montana, USA. Mineralogy and Petrology, V. 59, pg. 143-164.

Stewart, M. L., and Pearce, T. H. 2004. Sieve-Textured Plagioclase in Dacitic Magma; Interference Imaging Results. American Mineralogist, V. 89 (2-3), pg. 348-351.

Streck, M. J., Leeman, W. P., Chesley, J. 2007. High-Magnesian Andesite from Mount Shasta: A Product of Magma Mixing and Contamination, not a Primitive Mantle Melt. Geology, V. 35, pg. 351-354.

Streck, M. J. 2008. Mineral Textures and Zoning as Evidence for Open System Processes. Reviews in Mineralogy and Geochemistry, V. 69, pg. 595-622.

Streckeisen, A. 1979. Classification and Nomenclature of Volcanic Rocks, Lamprophyres, Carbonatites and Melilitic Rocks. Geology, V. 7, pg. 331-335.

Strekeisen, A. 2021. *Lamprophyres*. Alexstrekeisen.it. alextrekeisen.it/English/vulc/lamprophyres.php

Tilling, R. I., Klepper M. R., and Obradovich, J. D. 1968. K-Ar Ages and Time Span of Emplacement of the Boulder Batholith, Montana. American Journal of Science, V. 266, pg. 671-689.

Tomiya, A., and Takahashi, E. 2005. Evolution of the Magma Chamber Beneath Usu Volcano Since 1663: a Natural Laboratory for Observing Changing Phenocryst Compositions and Textures. Journal of Petrology, V. 46, pg. 2395-2426.

Ubide, T., Arranz, E., Lago, M., Gale, C., Larrea, P. 2012. The Influence of Crystal Settling on the Compositional Zoning of a Thin Lamprophyre Sill: A Multi-Method Approach. Lithos, V. 132-133, pg. 37-49.

Ubide, T., Gale, C., Arranz, E., Lago, M., and Larrea, P. 2014.Clinopyroxene and Amphibole Crystal Populations in a Lamprophyre Sill from the Catalonian Coastal Ranges (NE Spain): A Record of Magma History and a Window to Mineral-Melt Partitioning. Lithos, V. 184-187, pg. 225-242.
Ubide, T. Gale, C., Larrea, P., Arranz, E., Lago, M., and Tierz, P. 2014. The Relevance of Crystal Transfer to Magma Mixing: A Case Study in Composite Dykes from the Central Pyrenes. Journal of Petrology, V. 55-N. 8, pg. 1535-1559.

Ubide, T., Gale, C., Larrea, P., Arranz, E., and Lago, M. 2014. Antecrysts and their Effect on Rock Compositions: The Cretaceous Lamprophyre Suite in the Catalonian Coastal Ranges (NE Spain). Lithos, V. 206-207, pg. 214-233.

Ubide, T., Mollo, S., Zhao, J. X., Nazzari, M., and Scarlato, P. 2019. Sector-zoned Clinopyroxene as a Recorder of Magma History, Eruption Triggers, and Ascent Rates. Geochemica et Cosmochimica Acta, V. 251, pg. 265-283.

Ubide, T., Caulfield, J., Brandt, C., Bussweiler, Y., Mollo, S., Di Stefano, F., Nazzari, M., and Scarlato, P. 2019. Deep Magma Storage Revealed by Multi-Method Elemental Mapping of Clinopyroxene Megacrysts at Stromboli Volcano. Frontiers in Earth Science, V. 7:239.

Vuke, S. M., Porter, K. W., Lonn, J. D., and Lopez, D. A. 2007. Geologic Map of Montana. Montana Bureau of Mines and Geology Geologic Map 62

Winston, D. 1986. Paleotectonics and sedimentation in the Rocky Mountain Region, United States. American Association of Petroleum Geologists, V. 41, pg. 87-118.

Winter, J. D. 2010. Principles of Igneous and Metamorphic Petrology 2nd Ed. New York: Prentice Hall.

Weed, W. H. 1893, The Laramie and the Overlying Livingston Formation in Montana. U.S. Geological Survey Bulletin 105, pgs. 68.

Weed, W. H., and Pirrson, L. V. 1895. Highwood Mountains of Montana. Geol. Soc. Am. Bull, V. 6, pg. 389-422.

Wyman, D. A., and Kerrich, R. 1988. Alkaline Magmatism, Major Structures and Gold Deposits: Implications for Greenstone Belt Gold Metallogeny. Economic Geology, V. 83, pg. 454-461.

Wyman, D. A., and Kerrich, R. 1988 b. Lamprophyres a Source for Gold. Nature, V. 332, pg. 209-210.

Wyman, D. A., and Kerrich, R. 1989. Archean Shoshonitic lamprophyres associated with Superior Province Gold Mineralization: Distribution, Tectonic Setting, Noble Metal Abundance and Significance for Gold Mineralization. Econ. Geol. Monograph, V. 6, pg. 661-667.

Appendices

A. Modal Mineralogy of Thin Sections from Study

Sample Collected & Name	Matrix	Olivine	Pyroxenes	Biotite (mica)	Feldspar	Foids	Oxides	Carbonates	Notable Accessory Minerals	Notable Textural/Dissolution Features
Bull Mountain Range Lamprophyres (BML)										
J-03 (Vogesite)	53		36	1	2		8			spongy texture, step zoning
J-06 (Vogesite)	45	1	48				6			spongy texture, complexly zoned px
J-09 (Minette)	55		15	25			5			
J-09-1 (Minette)	56		10	20			9	5		
J-10 (Kersantite)	50		25	12			8	5		
J-10-1 (Kersantite)	60		20	10			6	4		
J-12 (Vogesite)	20	4	38	1	30		7			spongy texture, complexly zoned px
J-13 (Minette)	55		20	15			10			bent bt
J-29 (Minette)	64		5	22			4	5		bent bt, heavily altered phenos (olv and px)
Highwood Mountain Range Lamprophyres (HML)										
J-14 (Spessartite)	24	5	35		30		6			flow alignment
J-15 (Spessartite)	30		45		25					
J-16 (Vogesite)	54	6	40							spongy texture
J-17 (Vogesite)	40	5	40	1	14					stepped zoning of px
J-18 (Sannaite)	35	10	43	10		2				spongy texture, complexly zoned px
J-19 (Minette)	60	5	20	15						
J-20 (Minette)	75		15	10						xenoliths, bent bt
J-21 (Vogesite)	42	8	45				5		analcime in pyx blebs	spongy texture
J-22 (Sannaite)	54	1	38			2	5			
J-23A (Vogesite)	58		30			.	7		(5) altered Olivines to opaque and blue birefringent mineral, analcime in pyx blebs	spongy texture, step zoning pyx, complexly zoned px
J-23B (Vogesite)	48		35				10		opaque acicular fine grained mineral, (7) altered olivines to opaques and a blue birefringent min	spongy texture, step zoning pyx
J-24 (Damkjernite/Sannaite)	35		30	18	8	1	6	2		spongy texture, complexly zoned px
J-25 (Vogesite)	52		25	15	6		2			spongy texture, step zoning pyx
J-26 (Vogesite)	55		39				5	1		2 different populations of pyx, one equigranular
J-27 (Vogesite)	56	5	36				3		apatite in px crystals	matrix full of rounded, high relief crystals, spongy texture, contact
J-28 (Vogesite)	32	4	31	11	14		6	2		spongy texture
Crazy Mountain Range Lamprophyres (CML)										
J-30 (Kersantite)	73		2	10			5	2	8 Hornblende	strongly zoned bt
J-31 (Kersantite)	75		4	12			4	5		bent bt
J-31-1 (Kersantite)	67		10	20				1	2 Hornblende	contact
J-32-1 (Monchiquite)	50	5	25	15		1	4			bent bt, spongy texture
J-32-2 (Monchiquite)	66		15	5		8	2	4		bent bt

Sample Collected & Name	Matrix	Olivine	Pyroxenes	Biotite (mica)	Feldspar	Foids	Oxides	Carbonates	Notable Accessory Minerals	Notable Textural/Dissolution Features
Crazy Mountain Range Lamprophyres (CML) cont										
J-32-3 (Monchiquite)	46		20	12			6	16		spongy texture
J-32-C (Vogesite)	55		30	10			5			strongly zoned bt
J-33-1 (Vogesite)	50	10	36				4			very coarse olivine
J-33-2 (Vogesite)	70		10	8			2	10		bent Bt
J-34 (Not lamp)	89		2				8	1	apatite	few coarse crystals
J-35 (Monchiquite)	64		5	2	1	12	3	1	12 Hornblende, apatite	leucite growth along fractures, 2 distinct groundmass ocelli populations
J-36 (Sannaite)	37	2	40	12		4	5			zonation in bt, complexly zoned px
J-37 (Monchiquite)	50		10	1		3	3	5	28 Hornblende	
J-37-C (Monchiquite)	65		30				5		apatite	margin of contact with country rock, flow alignment, spongy texture
J-38 (Vogesite)	44	5	35	12			4		apatite	spongy texture, very coarse olv phenos
J-39 (Monchiquite)	58		30	9		2	1			spongy texture, bent bt
J-39-1 (Monchiquite)	82			5			5	8		Bt banded replacement
J-40 (Monchiquite)	66		25	8			1			margin of contact with country rock, bent bt, Spongy texture
J-41 (Monchiquite)	86		9			2	1	2		few megacrysts
J-42 (Vogesite)	58		36		1		5		abundant altered olivine (yellow)?	spongy texture, heavy replacment
J-43 (Spessartite)	43	16	32				9			spongy texture
Other Collected Lamprophyres										
Yogo (Ouachitite)	59		20	15			5	1		complexly zoned px, bent bt
17B702 (Kersanite)	75		5	20					Hornblende, Clinozoisite	
J-11 (Broadway) (Kersantite)	53		40				7			strongly altered crystals
J-44a (Spessartite)	59	20	2	2	6	1	10		(6) Hornblende	intergrowth of ol and hbl, patchy zoning
J-44b (Minette)	55	5	14	16			10		abundant altered yellow mineral	Fe rich bt in groundmass
J-44CD (Spessartite)	66	5	8			4	12	5	abundant altered yellow mineral	few coarse crystals
J-45 (Vogesite)	41		8				1	12	(Several blebs with low relief/low birefringence minerals) (8)	very altered px phenos (30)
J-45-1 (Minette)	51	2	18	8			1		(Several blebs with low relief/low birefringence minerals) (5)	very altered px phenos (15)

B. Select Hand Sample Descriptions

- J03 (Bull Mountain)
    - Displays a mottled or knobby texture where pyroxene crystals have fallen out during weathering. Groundmass is green to dark grey in color. Euhedral dark grey to black colored pyroxene is present and is .2 to 1 cm in length. Sample is porphyritic and panidiomorphic. Minor phlogopite is present but is less abundant than the dominant pyroxene. Mica is less than .1cm in width. Sample appears partially weathered but some pyroxene crystals display cleavage and fresh faces.
- J06 (Bull Mountain)
    - Sample is dark grey to black in color within the groundmass. Fresh books of dark colored biotite are present and are subhedral to euhedral. Biotite is on average .2 to .3 cm in width. Pyroxene is grey to black in color and is euhedral and medium to coarse grained. Typical 90 – 90 pyroxene cleavage is visible on the largest of crystals. There are .2 to .5 cm sized green colored blebs of prismatic looking crystals, presumably altered olivines. Sample is porphyritic and panidiomorphic. Hydrochloric acid dropped on an irregular shaped white colored bleb effervesced, thus, there must be some calcite present. Sample is very fresh and there is no sign of pervasive alteration.
- J09 (Bull Mountain)
    - Sample displays the typical 'glistening porphyry' texture with .25cm to 1.1 cm sized biotites that are pseudo-hexagonal in shape. Books of mica are also present. Groundmass is light grey to light tan in color. Sample is porphyritic. There are green anhedral shaped green blebs that appear to be altered. White circular crystals of plagioclase are present and are .1cm in length. Leucite is present and appears circular in shape and is <1 cm in width. Sample may be altered but the biotites are in excellent

condition. Green colored subhedral pyroxenes are present ranging in size from .2 cm to .8 cm in width. There are circular shaped, anhedral green minerals that are rimmed by a .1 cm wide rim that is red to dark brown in color. Sample has some quartz veining present that are <.1 cm in width.

- J12 (Bull Mountain)
    - Sample is dark grey in color within the groundmass. Sample is panidiomorphic with euhedral, black colored pyroxenes abundant in the groundmass ranging in size from .1 cm to .5 cm. From hand lens there appears to be some zonation within some of the pyroxene crystals as there is a color change in the rim of some crystals. Biotite is present and is .1 cm to .2 cm in width and is dark black in color. HCL on white blebs effervesced, calcite is present in some form. There is also a subhedral and boxy shaped amber to dark brown colored crystal that appears fractured, size ranges from .1 cm to .25 cm. Sample appears largely unaltered.
- Yogo
    - Sample is light grey to medium grey in color within the groundmass. Sample has abundant white, circular crystals .1 cm to .2cm in width, presumably leucite. There is also lime green colored mineral that is able to be scratched, irregularly shaped, and is presumably analcime. Mica is present and is lighter in color, tabular, and on average .2 cm in width. From afar the rock displays a salt and pepper or specular texture due to abundant micas within the groundmass. There is also fresh, prismatic, green colored olivine that is subhedral. White .2 to .4 cm sized angular blebs are present and effervesce with HCL. Calcite may be present. White colored plagioclase about .1 cm to .2 cm in size is present. Sample appears fresh but may be slightly altered.
- J18 (Highwood)

- Groundmass is light grey to dark grey in color. Sample is panidiomorphic with abundant euhedral dark grey colored pyroxenes present. Pyroxene is .1 cm to .4 cm in size and 90 -90 cleavage is clearly visible. Dark colored biotite is present in the groundmass and is <.1 cm in size. Leucite is present as .1 cm rounded nodules. Plagioclase is also in the groundmass as white colored .1 cm sized crystals. Sample may be slightly altered as there are green shaped blobs (.2 cm) in size rimmed by red to brown colored minerals. White (.3 cm) sized globular structures are visible in hand sample.

- J22 (Highwood)
  - Groundmass is light grey to green colored. Sample is panidiomorphic. Dark grey colored pyroxene is present and is euhedral and is .1 to .6 cm in length. Black colored biotite are present, some are pseudo hexagonal but most are not. Biotite is on average .1 cm in size. Sample appears mottled or knobby where crystals must have weathered out. Oblate shaped, white colored plagioclases are present in minor abundance and are .1 to .2 cm in size.
- J24 (Highwood)
  - Massive groundmass is light grey in color and the sample is porphyritic and panidiomorphic. Dominant crystals are light colored grey euhedral pyroxene crystals. These crystals display 90-90 cleavage and are .2 cm to 1.3 cm in size. There may be two population of pyroxene crystals because there are smaller (.1 cm) sized euhedral blocky shaped pyroxene crystals within the groundmass. Phlogopite is present in the groundmass but is extremely fined grained (<.1cm) and is tan in color. Anhedral to subhedral white colored plagioclase crystals are present and range in size from .3 cm to 1 cm. Sample displays mottled texture where larger crystals have weathered out.
- J26 (Highwood)

- Massive groundmass light grey to dark grey in color. There are few crystals visible to the naked eye other than black colored biotite ranging in size from <.1cm to .4 cm. fine grained black colored amphibole is present and is anhedral to subhedral. Pyroxene is also present and is dark grey in color, euhedral, and .1cm to .2 cm in length. .1cm fine grained circular blebs of a white mineral are present, presumably leucite. Sample appears to be unaltered and displays minor signs of mottling or weathering.

- J28 (Highwood)
  - Dark grey colored massive groundmass. Sample is porphyritic and panidiomorphic. Dark grey, euhedral, zoned pyroxene is present. Pyroxene is .2 cm to .7 cm in size. Fine grained mica is present in groundmass (<.1 cm to .1 cm) and is black in color. Euhedral plagioclase is present and displays long, rectangular, white colored crystals ranging in size from .2 to .5 cm. There appears to be some flow alignment features as the pyroxene and plagioclase are all aligned by their longest axis. There appears to be some amorphous red colored alteration mineral present. Sample is mottled and knobby due to weathering.

- J-32-1 (Crazy)
  - Sample is massive and is light green to light grey in color. The groundmass is full of very fine grained (<.1 cm) sized tan to white colored micas. 1 to 2 cm sized angular xenoliths are present. Fine grained black to tan colored euhedral mica is present ranging in size from .2 to .7 cm. Anhedral black colored amphibole or pyroxene is present and is fine to medium grained. There are abundant .1 cm sized acicular needed shaped black crystals throughout the entire groundmass. First sample where biotite and phologopite are both present.

- J-32-3 (crazy)
    - Sample is massive and light grey to dark grey in color. Few macrocrysts are present but the groundmass houses abundant tan colored micas that are very fine grained (<1. Cm). Minor medium grained pyroxene is present as dark colored subhedral crystals. Globular shaped, fine grained, red oxidized crystals are present in the groundmass.
- J36 (Crazy)
    - Sample is porphyritic and panidiomorphic. The massive groundmass is dark grey in color. The largest macrocrysts are euhedral, medium to coarse grained, grey colored pyroxenes displaying typical pyroxene cleavage. Pyroxene crystals are .2 cm to .8 cm in size. There appears to be both biotite and phlogopite in this sample, or at least two different colored micaceous crystals. Some micas display zonation with darker exteriors and lighter colored cores. Micas are subhedral but some are pseudo hexagonal and range in size from .2 to .4 cm. Some are arranged into micaceous books displaying nice tabular cleavage. Sample is mottled and knobby due to weathering out of larger crystals. It should be noted that this sample is extremely crumbly and brittle to the touch. There are few signs of alteration.
- J40 (crazy)
    - Sample is porphyritic and panidiomorphic. The massive groundmass is dark grey in color. Macrocrysts of biotite and pyroxene are visible on the surface. Biotite is dark black in color and is euhedral and is .2 to .7 cm in size. Pyroxene is prismatic and needle shaped, and some of the smaller crystals appear to be aligned along their longest C-axis. Possible signs of flow alignment. Pyroxene crystals range in size from .1 cm to .5 cm. There appears to be some minor olivine. Olivine is green and prismatic, more often rounded and is .1 to .2

cm in size. Micaceous book cleavage is present, and the surface appears mottled or knobby due to weathering. Sample does not appear to be altered.

- J43 (Crazy)
    - Sample is porphyritic and panidiomorphic. Massive groundmass is light grey to tan in color. The major phase and macrocrysts is pyroxene. Pyroxenes are euhedral, fine to medium grained and oriented in the same direction. Flow alignment may be present. Black colored fine-grained mica (.1 cm) is present in the groundmass. .4 cm sized white circular features are present displaying mineral growth from along a circular cavity, these could be ocelli. Globular shaped irregular white colored blebs are present (.2cm in size) and do not effervesce with HCL.

C. Select Thin Section Descriptions

- J03 (Bull Mountain)
    - Sample is porphyritic with pyroxene crystals being the dominate crystals set in a microlitic matrix composed of glass, plagioclase, opaques, and very fine to fine grained pyroxene material. Modal percentages for this sample are as follows: Matrix (50), pyroxene (36), biotite (2), feldspar (4), and oxides (8). Pyroxene is predominately clinopyroxene, but there are few orthopyroxenes present but to a lesser extent within the groundmass. Pyroxene crystals are subhedral, medium to very coarse grained, and show signs of corrosion and resorption along their rims. The inside of the pyroxene crystals displays spongy texture (sieve). The degree of spongy texture varies per crystal. In some crystals, the texture resides in the core, but in others it is pervasive throughout the core to the edge of the crystals rim. Concentric zoning and sector zoning are present in the pyroxenes in cross polarized light. Within the spongy texture, melt pockets are present. Mineralogy within the melt pockets contains glass, pyroxene, biotite, opaques, acicular apatite, and chlorite. Biotite is very fine to fine grained and is anhedral to subhedral. The crystals reside along the margins of the pyroxene crystals and are also scattered throughout the groundmass, but the largest biotite crystals are adjacent to phenocryst macrocrysts. Biotite is dark red to brown in color, probably high in Fe and Ti content. feldspar (probably sanidine) crystals reside in the matrix but there are a few crystals that are fine to medium sized. Carlsbad twinning is visible, and the crystal faces are commonly “dirty” and splotchy. Plagioclase crystals in the matrix are microlitic and very fine grained. Apatite is present as fine-grained needled inclusions in the cores of pyroxene phenocrysts but also is visible within the matrix. Opaques are subhedral to euhedral, fine to medium grained, and are hexagonal shaped. Opaques are present within the groundmass, melt pockets of

pyroxenes, and within irregularly shaped blebs of an altered mineral clusters. These clusters were presumably olivines, as they display relict signs of classic olivine fractures and prismatic habit, now replaced by white micas and opaques. These alteration globular structures are fine to medium grained.

- J06 (Bull Mountain)
    - Sample is porphyritic with a very fine grained hypocrystalline groundmass (containing both glass and minerals). Modal percentages for this sample are as follows: Matrix (45), olivine (5), pyroxene (44), oxides (6), with minor apatite, chlorite, biotite, and plagioclase. Pyroxene crystals are subhedral to euhedral, medium to very coarse grained, display exsolution lamella, and are complexly zoned. Pyroxene is present as macrocrysts, fine grained broken and truncated aggregates, or as cumulophyric clusters. Pyroxene crystals display spongy texture, and three types can be determined from this sample. One, where the spongy melt pockets are only present in the core, two, where the spongy texture is only in the rim of the grain, or three, where the entire crystal displays pervasive spongy texture from core to rim. Melt pockets form string or snake like chains and are confined to banded portions of pyroxene crystals, alternatively, the melt pockets are also present as irregularly shaped rounded blebs and patches. Melt pocket mineralogy includes: biotite, chlorite, quartz, apatite, plagioclase, glass, opaques, and olivine (?). A couple of melt pockets show undulated quartz pockets. Pyroxenes are inclusion rich and some of them may contain fluid or melt inclusions in the core and intermediate zones of crystals. Inclusions follow linear patterns and form chains along banded margins within the crystals. Olivine is fine to medium grained, anhedral, corroded, and clearly out of equilibrium with the melt. Olivine is fractured, often overprinted by alteration minerals, and is surrounded by a corona of high relief, serrated minerals, and opaques. Opaques

are very fine to fine grained, cubic or hexagonal shaped, and are often surrounded by a halo or corona of minerals similar to the olivine crystals. Biotite is fine grained, anhedral, often associated with chlorite, and lies near the margins of pyroxene crystals. Apatite is found as fine grained long acicular needles within pyroxene cores and within the groundmass.

- J09 (Bull Mountain)
    - Sample is porphyritic and contains a microlitic fine grained groundmass of plagioclase and sanidine with minor carbonate. Major modal mineralogy is as follows: matrix (55), pyroxene (15), biotite (25), and opaques (5). Pyroxene crystals are medium grained to coarse grained, subhedral to euhedral, display spongy texture, and show signs of corrosion/resorption. Fractures are prevalent in all of the pyroxene crystals and are full of mica or carbonate infillings. Along the margin of the pyroxene there is a ring of fine grained opaques and tiny aggregates of pyroxenes enveloping the pyroxenes. Within some pyroxene crystals, inclusions of fine to medium grained biotite exists and can also be found along the margins of pyroxene crystals. Biotite is very fine grained to coarse grained. There are two types of biotite present. One displaying anhedral, globular crystal margins, with darker color in plane polarized light. The other exhibiting zonations, anhedral to subhedral shape, lighter in color, hosts a plethora of enclosed crystals, and is rimmed by fine grained cubic opaque crystals. All biotite shows signs of corrosion and disaggregation. In this sample there exists a large population of altered crystals displaying relict columnar and crystal habit. There is a dark opaque rim around each of these and the interior is full of disaggregated crystal fragments of high order white minerals (micas and calcite). Perhaps these used to be olivines? The dark alteration minerals described are all equigranular. Opaques in the groundmass are very fine grained and display cubic

habit. It should be noted that there is a considerable amount of carbonate within the groundmass of this sample. Sample shows signs of previous alteration.

- J12 (Bull Mountain)
    - Sample is porphyritic, panidiomorphic, and displays seriate textured plagioclase. Major modal mineralogy is as follows: matrix (19), olivine (5), pyroxene (38), Biotite (1), feldspar (30), and oxides (7). Pyroxene crystals are fine to coarse grained, with a large population of medium sized crystals. Pyroxene is euhedral, often displays spongy texture, twinning, and is rich with fine grained apatite inclusions. Smaller fine-grained pyroxene exists in the groundmass and is subhedral and occasionally disaggregated. Spongy texture and melt pockets are more common in the coarser pyroxene crystals but are not exclusive to coarse crystals. Spongy texture patches occur in the intermediate zone of crystals or completely blanket some pyroxenes. Melt pocket mineralogy includes: pyroxene, plagioclase, biotite, opaques, glass, and some yellowish colored alteration mineral. Olivine is fine to medium grained, subhedral, and shows signs of alteration and corrosion. Olivine is also present as fine-grained enclosed crystals within larger pyroxene crystals. Coronas around olivine is present but much rarer in this sample compared to other bull mountain lamprophyres. This olivine must be fresher than the others and relatively unaltered. Biotite is dark red to brown in color (high Fe and Ti), anhedral, and occasionally enclosed within pyroxene crystals. Plagioclase is anhedral to euhedral, very fine to medium grained, present as microlites, and commonly displays Carlsbad twinning. Opaques are very fine to fine grained, display cubic habit, and are commonly found as inclusions within pyroxene crystals.

- J18 (Highwood)
    - Sample is panidiomorphic and intergranular. Modal mineralogy is as follows: matrix (35), olivine (10), pyroxene (43), biotite (10), and leucite (2). The matrix is composed of intergranular plagioclase that is fine grained, anhedral, shows signs of seritization, and is drusy or “dirty” with inclusions. Pyroxene is euhedral, fine to coarse grained, displays spongy texture, complexly zoned, and may contain melt or fluid inclusions in banded intermediate regions of crystals. Twinning and exsolution lamellae are present in pyroxenes but is rare. The degree of spongy textured melt pockets is not so destructive or overprinting to these pyroxenes. It does seem to be contained within the cores or the lighter colored banded regions of pyroxenes in their intermediate zones. There is two generation of pyroxenes, one finer within the groundmass, and the other as coarser phenocrysts. Spongy texture is absent from the finer grained pyroxene and present in the coarser phenocrysts. Olivine is subhedral, fine to medium grained, and enshrouded in a reaction rim corona of biotite and opaques. Cumulophyric masses of olivine are also present and olivine enclosure is common in coarser pyroxene crystals. Biotite is very fine to fine grained, anhedral to subhedral, commonly tabular, and occasionally zoned. Biotite color varies from extremely dark brown or red to tan. Biotite rims most phenocrysts and reactions seem likely between biotite and the other mafic phases. Leucite is anhedral to subhedral, fine grained, and found within the groundmass. Minor phases also identified include acicular apatite, chlorite, and cubic shaped oxides.
- J22 (Highwood)
    - Sample is panidiomorphic with a hypocrystalline fine grained groundmass. Modal mineralogy is as follows: matrix (54), pyroxene (38), leucite (2), and opaques (6). Pyroxene is euhedral, fine to coarse grained, displays spongy texture, complexly zoned, and displays

exsolution lamellae. Pyroxene crystals are long prismatic-rectangular shapes, stubby prisms, or arranged in star shaped growth of aggregates growing out from a central host crystal. Phenocrysts showing spongy texture also exhibit complex zoning and banding. The spongy texture is limited to lighter colored regions of the intermediate zones or the cores. Some of the pyroxene crystals are lightly colored green and others are clear in plain polarized light. Melt pockets are irregularly shaped within the spongy textured zones and the mineralogy is too fined crystal to determine. Leucite is anhedral to subhedral, fine grained, and found within the groundmass or within fractures of pyroxenes. Opaques are hexagonal or cubic shaped and fine grained. There exists pseudomorphed masses that is now totally replaced by alteration high order white minerals that retains its original euhedral shape. These features are fine to medium grained and completely rimmed by very fine-grained opaque minerals. It is possible these could at one point have been olivine. Notable accessory minerals include fine grained tabular chlorite, and subhedral elongate green colored crystals of epidote/clinozoisite. These crystals rim pyroxenes and are found throughout the groundmass. There are medium grained sized patches within the groundmass that are globular or circular shaped that contain no opaques or microlitic plagioclase, it is possible these features could be ocelli.

- J24 (Highwood)
    - Sample is porphyritic and shows sign of intense alteration. Modal mineralogy is as follows: matrix (35), pyroxene (30), biotite (18), feldspar (8), leucite (1), oxides (8), and carbonate (2). Pyroxene is euhedral, medium to coarse grained, displays exsolution lamellae, and spongy texture growth. Spongy texture and melt pockets while present, are not the norm within this sample. When present in pyroxene crystals the melt pockets are irregularly shaped blebs isolated from one another. In rare cases the melt pockets do link up to form

chain like structures. Spongy texture is common within the core and intermediate zone of crystals. Complex zonation and banding is rare within pyroxene crystals, but when present, the core is lighter in color than the rim of phenocrysts. Radial growth and star like arrangements of pyroxene crystals is common. Apatite inclusions exist as fine-grained acicular needles or tabular platy crystals within the cores of pyroxenes. Biotite (mica) is fine to medium grained, anhedral to euhedral, extremely dark red in color to colorless in plane polarized light and is commonly enclosed within or lining coarser pyroxene crystals. It seems there is two generation of mica present in this section. One is extremely dark colored (Fe Ti rich), amorphous or blocky shaped, and may be a pseudomorph of an earlier mafic phase no longer present. The other is colorless to tan colored, platy, tabular, and looks healthier or fresher displaying typical biotite or mica birds' eye extinction in cross polarized light. Some of the biotite is bent or strained and displays zonation between the rim and core of the mica phenocrysts. Feldspar is subhedral, fine to medium grained, tabular, and displays abundant Carlsbad twinning. Feldspar appears to be sanidine and shows signs of intense seritization. Leucite is fine grained, subhedral, forms equant pseudo hexagonal shaped crystals, and is common as inclusions within pyroxene crystals but is also present in alteration assemblages. Oxides present are fine grained, anhedral or subhedral forming amorphous or cubic shaped crystals. Oxides are commonly associated with biotite in this sample. Carbonate is anhedral, fine to medium grained, and occurs within the groundmass or circular shaped ocelli present throughout the section. The groundmass is hypocrystalline and dark in color, but there are irregular shaped patches of the groundmass that are lighter in color and host pyroxene, biotite, leucite, and dark brown to light orange colored alteration minerals overprinting pyroxene and biotite.

- J26 (Highwood)
    - Sample is panidiomorphic, porphyritic, and has a hypocrystalline groundmass or matrix. Modal mineralogy is as follows: matrix (53), olivine (1), pyroxene (39), biotite (2), oxides (4), and carbonates (1). Pyroxene is fine grained to coarse grained, subhedral to predominately euhedral, displays spongy texture with abundant melt pockets, complexly zoned and banding occurs, and rarely twinned. Spongy texture melt pocket shape, orientation, and behavior is very variable throughout the entire section. Types of spongy texture features within pyroxene is listed below: (1) No melt inclusions in the inner core but with spongy features within the outer core and intermediate zones of the crystals following banded lineation and zonation, (2) Pervasive spongy texture from core to rim, (3) Spongy texture and melt inclusions only along the rim margins, and (4) spongy texture only within the inner core of crystals. It should be noted that apatite is very common as inclusions within pyroxene crystals and can be tabular or acicular and needle like. Apatite is more concentrated within the core of pyroxene crystals. Some pyroxene crystals have faint green coloration in plan polarized light. Olivine is fine to medium grained, anhedral, and rimmed by opaque crystals. Biotite is present in two forms, (1) as fine grained pseudomorphs of a previous mafic phase, still retaining their euhedral crystal boundary, and as (2) where mica is very fine grained, bladed, and dispersed in the matrix. Oxides present are fine grained, anhedral or subhedral forming amorphous or cubic shaped crystals. Oxides are commonly associated with biotite in this sample. Carbonate is anhedral, fine to medium grained, and occurs within the groundmass. There are large irregularly shaped areas within the section where the groundmass becomes darker in color and finer grained. These patches generally have coarser pyroxene crystals than the rest of the thin section. Minor minerals include chlorite, leucite, and apatite.

- J28 (Highwood)
    - Sample is porphyritic with glomeroporphyritic clusters of pyroxenes and displays sign of intense alteration. Modal mineralogy is as follows: matrix (36), pyroxene (36), biotite (16), feldspar (4), oxides (6), and carbonate (2). Pyroxene is euhedral, medium to coarse grained, displays spongy texture and melt pockets, displays complex zonation and banding, and is entirely rimmed and overprinted by fine grained biotite. Pyroxene is host to blocky and acicular apatite crystals. Spongy texture and melt pockets are more concentrated in the rim and core regions of crystals. Melt pockets in pyroxenes are full of fine-grained minerals to microscopic to determine or completely full of chlorite. Pyroxene growth is radial, and star shaped and cumulophyric clusters are common. Partial enclosures of biotite within the pyroxene are also common within this section. Biotite is present as amorphous blob structures or euhedral bladed crystals. Biotite is dark red to brown in color or colorless and oxides are emplaced within or on the margin of biotite crystals. Fine grained and coarse biotite is found lining the margin of coarser pyroxene crystals. There was clearly a reaction taking place between the two phases at one point. Feldspar is subhedral, medium to coarse grained, tabular, and displays abundant Carlsbad twinning. Feldspar appears to be sanidine and shows signs of intense seritization. Fine grained biotite fragments are found enclosed within feldspar crystals. Oxides present are fine grained, anhedral or subhedral forming amorphous or cubic shaped crystals. Oxides are commonly associated with biotite in this sample. Carbonate is anhedral, fine to medium grained, and occurs within the groundmass or circular shaped ocelli present throughout the section. Accessory minerals include: chlorite, apatite, leucite, analcime, and hornblende.

- J11 (Madison)
    - Sample is porphyritic, has a cryptocrystalline groundmass, and is heavily altered. Modal mineralogy is as follows: matrix (53), pyroxene (38), biotite (2) and oxide (7). Pyroxene is subhedral, rectangular, medium to coarse grained, display exsolution lamellae, and often altered to a fine-grained light colored white micaceous mineral. Some pyroxene crystals are so altered by calcite and chlorite that only fine-grained fibrous pyroxene strands remain. Biotite is tan to colorless in plane polarized light, bent and strained, anhedral, and medium grained. Oxides are very fine grained, cubic, and associated with alteration blebs of chlorite and calcite. Alteration blebs are euhedral or amorphous, exhibiting no discernable shape. Euhedral alteration blebs were probably mafic components at one point that were completely replaced by other phases.
- Yogo Dyke
    - Sample is porphyritic and panidiomorphic. Modal mineralogy is as follows: matrix (59), olivine (10), pyroxene (20), biotite (14), oxides (5), and carbonates (1). Pyroxene is fine to coarse grained, subhedral to euhedral, displays spongy textured melt pockets that are more prevalent in the core than the rim of crystals. The coarsest pyroxene crystals are rich with apatite inclusions. There seems to be another population of coarse pyroxene crystal that is also euhedral but does not exhibit signs of spongy texture. These crystals are commonly fractured (overprinted by alteration minerals), corroded, and rimmed by biotite crystals. Fine to medium grained pyroxenes also display signs of spongy textured melt pocket growth. Ocelli is present in the form of quartz, calcite, chlorite, pyroxene assemblages and is globular in shape. Biotite is very coarse to fine grained (within the groundmass) and is euhedral to subhedral in shape. Biotite is occasionally bent and zoned. Zoning pattern is a darker core with a lighter colored rim. Partially enclosed crystals of

pyroxene are common within the coarser biotite crystals. Olivine is fine to medium grained, subhedral, and rimmed by opaques. Unfortunately, no sapphire was identified in thin section.

- J-32-3 (Crazy)
    - Sample contains phlogopite and pyroxene but is not porphyritic or panidiomorphic like most of the lamprophyric rocks from this study Coarse crystals do exist, but they are not as heavily populated as other samples from this study. Modal mineralogy is as follows: matrix (46), pyroxene (20), biotite (12), oxides (6), and carbonates (16). The groundmass is hypocrystalline and dark in color, but there are irregular shaped patches of the groundmass that are lighter in color and host pyroxene, biotite, calcite, and white micas. Pyroxene is fine to coarse grained and is sub to anhedral, commonly resorbed, and displays spongy texture within the rim and cores of crystals. Pyroxenes are also characteristically green in color and concentric and patchy zonations are present. The rims of pyroxene crystals are commonly resorbed. Biotite is commonly bladed when coarser grained and amorphous in the groundmass. Biotite is very fine to fine grained and light tan to dark red in color. Phlogopite and biotite varieties may both exist. Some mica is altered to chlorite. Oxides are subhedral to anhedral and is found in clusters or filling voids. Calcite present is dirty and ranges in size from fine grained in the groundmass to medium grained. Calcite seems to be secondary as none of it appears to be fresh or euhedral. Sample contains an unusual amount of calcite.
- J36 (Crazy)
    - Sample is porphyritic and panidiomorphic with a hypocrystalline groundmass. Modal mineralogy is as follows: matrix (37), olivine (2), pyroxene (40), biotite (12), leucite (4), and oxides (5). Enclosed crystals of pyroxene are found within coarser crystals of biotite

and the reverse is true of enclosed crystals of biotite within coarser pyroxene. Biotite is seen rimming biotite or pyroxene. Mica is using zoned with darker internal cores and lighter colored rims. Coarse mica displays resorbed, rounded edges. Pyroxene is subhedral, very coarse to fine grained, occasionally twinned, and is complexly zoned. The margins of the pyroxenes show signs of resorption and rounding. Pyroxene habit is often tabular and inclusion rich with apatite and melt (or fluid) inclusions along concentric bands that stand out from the crystal in plane polarized light. Finer grained crystals of pyroxene within the groundmass display both zoned and unzoned crystals. A unique feature of this thin section is the present of coarse biotite clusters encircling fragments of pyroxene material. Patchy zoned crystals exist with spongy texture pervasive from core to rim, these crystals are often richer with inclusions than crystals not displaying spongy texture.

D. Select Hand Sample Photographs

Photograph D1: Lamprophyre J03 in hand sample.

Photograph D2: Lamprophyre J06 in hand sample.

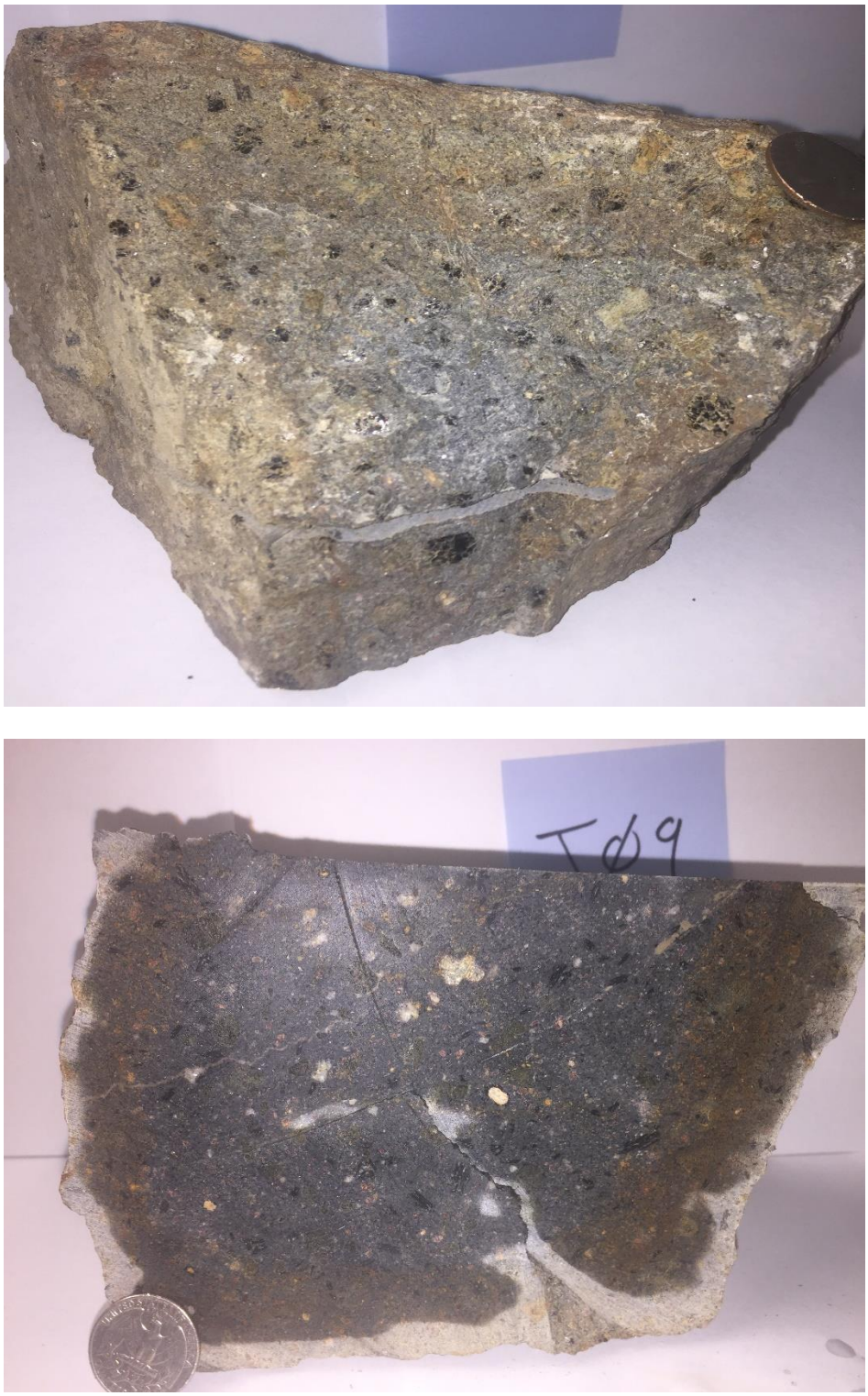

Photograph D3: Lamprophyre J09 in hand sample. Top photo is the natural rock face; the bottom photo is a cut surface sprayed with water to show the macroscopic features of the rock.

Photograph D4: Lamprophyre J12 in hand sample. Top photo is the natural rock face; the bottom photo is a cut surface sprayed with water to show the macroscopic features of the rock.

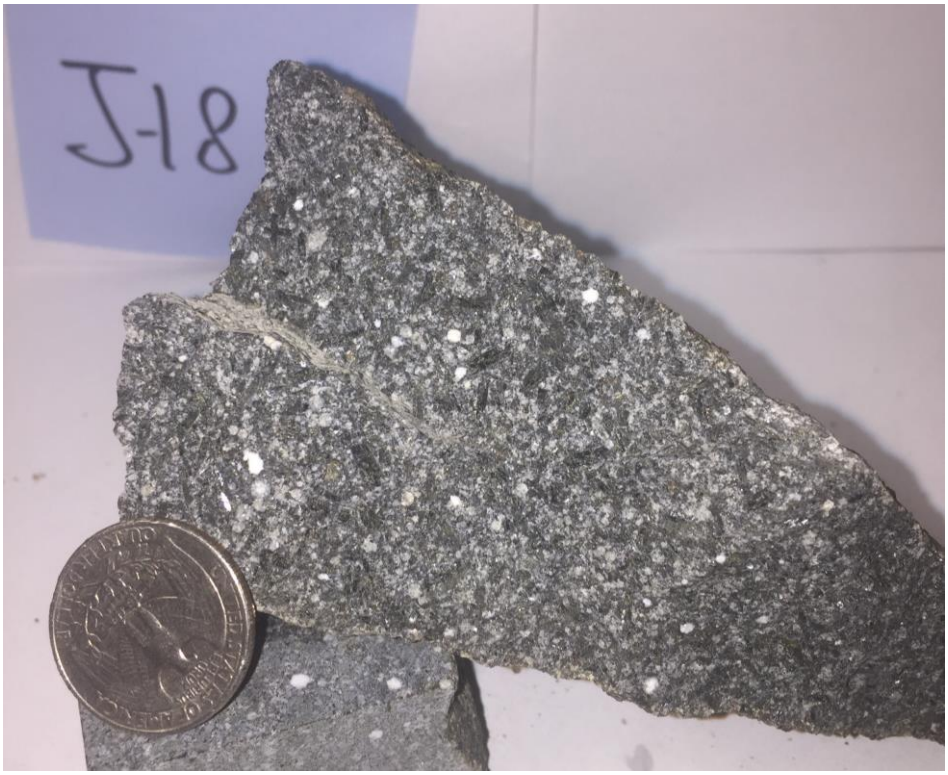

Photograph D5: Lamprophyre J18 in hand sample.

Photograph D6: Lamprophyre J22 in hand sample.

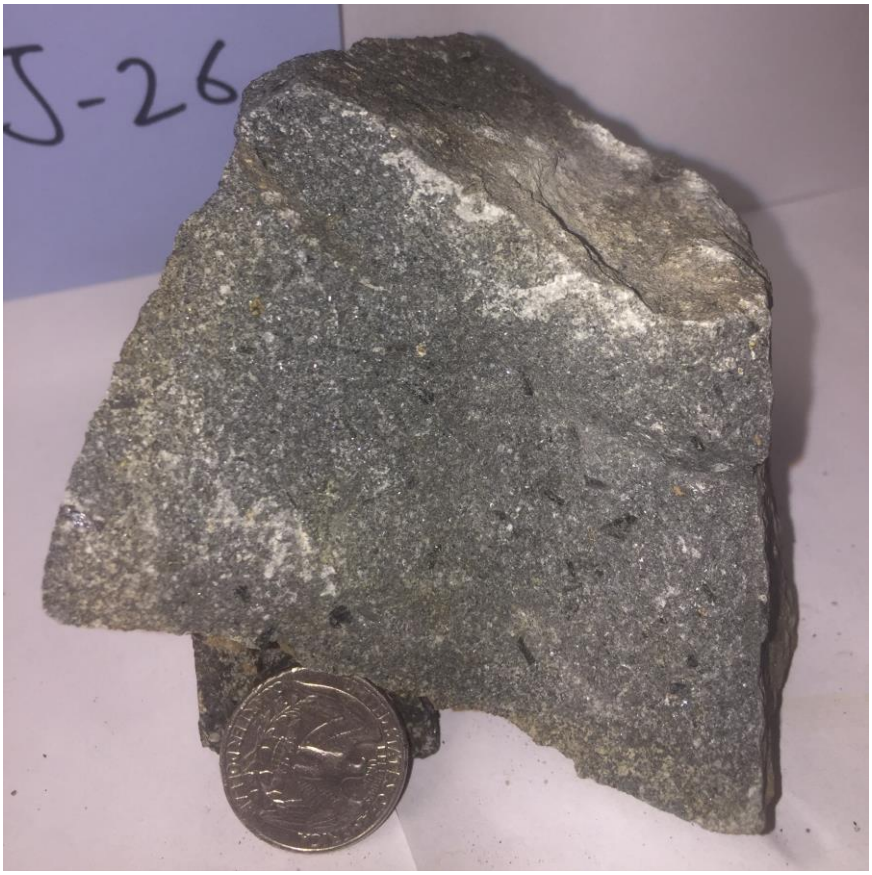

Photograph D7: Lamprophyre J26 in hand sample.

Photograph D8: Lamprophyre J28 in hand sample.

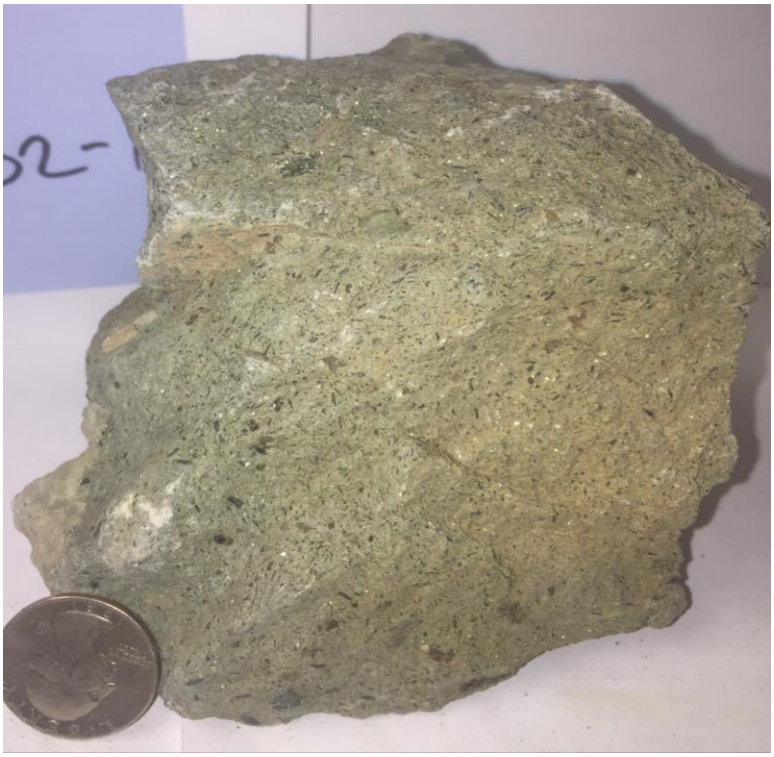

Photograph D7: Lamprophyre J22 in hand sample.

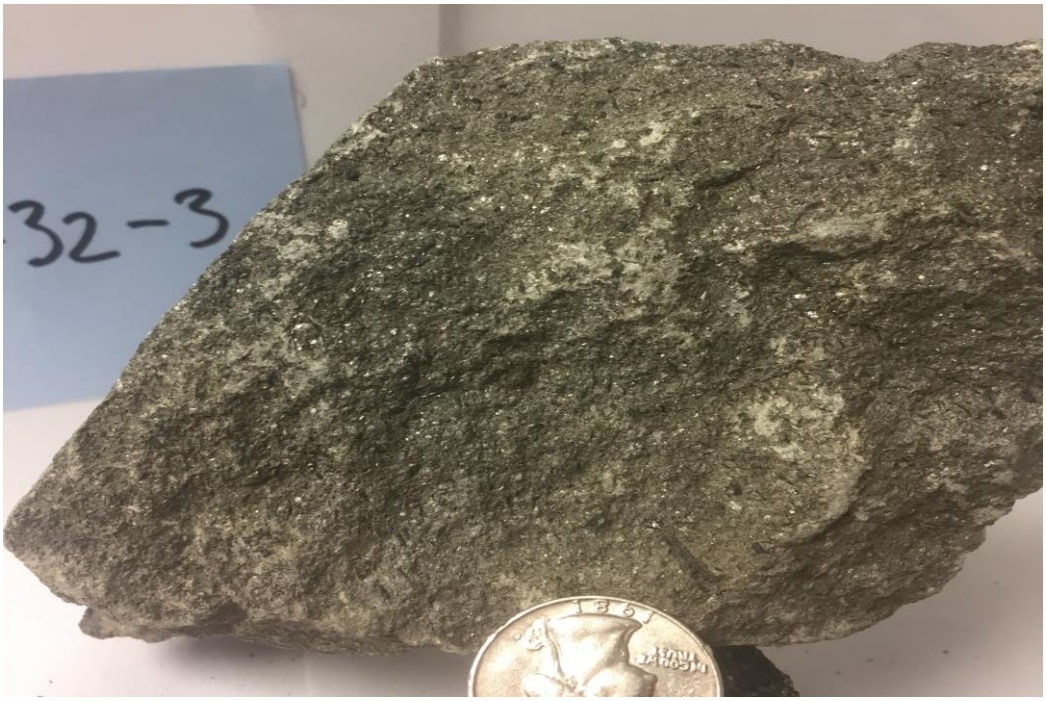

Photograph D10: Lamprophyre J32-3 in hand sample.

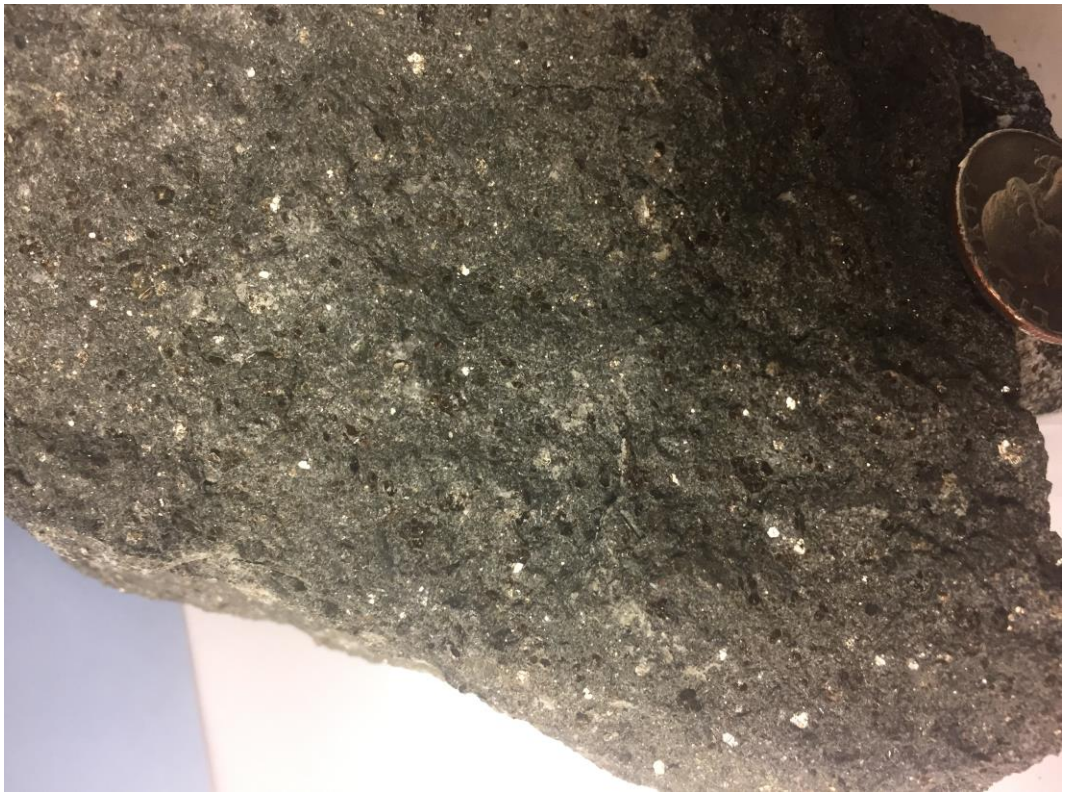

Photograph D11: Lamprophyre J36 in hand sample.

Photograph D82: Lamprophyre J40 in hand sample.

Photograph D93: Lamprophyre J43 in hand sample.

E. GPS Coordinates

Name	Latitude	Longitude	Elevation
B01	46.10561695	-112.0042268	1706.69
B02	46.1055659	-112.0059773	1726.16
B03	46.10528595	-112.0065019	1725.20
J01	46.04298142	-112.0149634	2133.52
J02	46.02169666	-112.0331158	2277.23
J03	46.00808982	-112.0349672	2232.05
J04	46.01383444	-112.0423078	2078.00
J05	45.90322919	-112.0173888	1712.70
J06	45.89236423	-112.0270183	1705.01
J07	45.9125357	-112.0127655	1712.70
J08	45.91818997	-112.016737	1970.33
J09	45.92328709	-112.0209519	1949.91
J10	45.91997791	-112.0175616	1923.23
J11	45.6956439	-112.3281971	1719.91
J14	47.36043722	-110.7296661	1328.42
J15	47.41484139	-110.6311466	1790.09
J16	47.41472857	-110.6308201	1802.82
J17	47.41487928	-110.6306968	1805.47
J18	47.41490576	-110.630592	1806.67
J19	47.41579701	-110.6294123	1841.52
J20	47.41591092	-110.62875	1851.13
J21	47.41627118	-110.6282753	1851.61
J22	47.46802281	-110.5956304	1389.22
J23	47.46872337	-110.5949176	1431.04
J24	47.4704694	-110.6040381	1366.15
J25	47.47048558	-110.6037903	1376.72
J26	47.47071315	-110.6035596	1390.18
J27	47.4707688	-110.6024359	1444.50
J28	47.47072186	-110.602094	1453.63
J29	45.92489004	-112.024312	1962.58
J30	46.16811099	-110.491041	1803.90
J31	46.16812902	-110.490876	1811.14
J32	46.22867703	-110.482092	2368.81
J33	46.22878298	-110.479801	2412.27
J34	46.39138302	-110.523516	1645.39
J35	46.29650901	-110.449866	1840.40
J36	46.29662703	-110.449602	1840.21
J37	46.28404504	-110.419087	1870.33
J38	46.28646397	-110.418796	1858.96
J39	46.29039701	-110.417889	1899.93
J40	46.29921896	-110.435745	1873.54
J41	46.30587797	-110.434407	1886.27
J42	46.31269597	-110.43295	1863.57
J43	46.41141702	-110.551862	1620.72
J44	45.66568203	-110.680346	1524.54
J45	44.96878898	-113.475289	1785.79
Lamp	45.69872693	-112.3300016	1703.57